Nanoparticle-Based Surface Modifications for Microtribology Control and Superhydrophobicity

by

Kendall Matthew Hurst

A dissertation submitted to the Graduate Faculty of
Auburn University
in partial fulfillment of the
requirements for the Degree of
Doctor of Philosophy

Auburn, Alabama
December 13, 2010

Keywords: nanoparticles, microelectromechanical systems,
tribology, stiction, thin films, superhydrophobicity

Approved by

W. Robert Ashurst, Co-Chair, Associate Professor of Chemical Engineering
Christopher B. Roberts, Co-Chair, Chair and Professor of Chemical Engineering
Ram B. Gupta, Professor of Chemical Engineering
Robert L. Jackson, Associate Professor of Mechanical Engineering

Abstract

The emergence of miniaturization techniques for consumer electronics has brought forth the relatively new and exciting field of *microelectromechanical systems* (MEMS). However, due to the inherent forces that exist between surfaces at the micro- and nanoscale, scientists and semiconductor manufacturers are still struggling to improve the lifetime and reliability of complex microdevices. Due to the extremely large surface area-to-volume ratio of typical MEMS and microstructured surfaces, dominant interfacial forces exist which can be detrimental to their operational lifetime. In particular, van der Waals, capillary, and electrostatic forces contribute to the permanent adhesion, or *stiction*, of microfabricated surfaces. This strong adhesion force also contributes to the friction and wear of these silicon-based systems.

The scope of this work was to examine the effect of utilizing nanoparticles as the basis for roughening surfaces for the purpose of creating films with anti-adhesive and/or superhydrophobic properties. All of the studies presented in this work are focused around a *gas-expanded liquid* (GXL) process that promotes the deposition of colloidal gold nanoparticles (AuNPs) into conformal thin films. The GXL particle deposition process is finalized by a critical point drying step which is advantageous to the microelectromechanical systems and semiconductor (IC) industries. In fact, preliminary results illustrated that the GXL particle deposition process can easily be integrated into current MEMS microfabrication processes.

Thin films of AuNPs deposited onto the surfaces of silicon-based MEMS and tribology test devices were shown to have a dramatic effect on the adhesion of microstructures. In the

various investigations, the apparent work of adhesion between surfaces was reduced by 2-4 orders of magnitude. This effect is greatly attributed to the roughening of the typically smooth silicon oxide surfaces which, in turn, dramatically decreases the "real are of contact" between two contacting surfaces. The studies found that AuNP thin films produced using the lowest initial concentrations of nanoparticles in solution produced estimated real contact areas of around 1%, reducing the adhesion of oxidized Si (100) surfaces from about 37 mJ/m^2 down to 0.02 mJ/m^2. In addition, the reducing in real contact area effectively reduced the coefficient of static friction between silicon-based surfaces due to the extremely high dependence of stiction on friction and wear at the microscale.

This work also investigated methods of permanently immobilizing AuNP-based films on the silicon surfaces of microstructures in order to create more mechanically robust coatings. The use of organic self-assembled monolayers (SAMs) functionalized with tail-groups known to bond to metallic surfaces were effective in producing much more durable coatings as opposed to non-immobilized AuNP films. Chemical vapor deposition (CVD) techniques were also used to coat rough AuNP films with very thin films of silica (SiO$_2$) to create a robust, rough surface. This method was also very effective in creating a durable coating which is capable of reducing the adhesion energy and friction between two microscale surfaces for extended periods of time. Similar CVD techniques were also used to begin investigating the production of alumina nanoparticle-based superhydrophobic films for use in consumer electronics.

Overall, the work presented in this dissertation illustrates that engineered nanoparticle-based surface modifications can be extremely effective in the reduction of the inherent interfacial phenomena that exist on microfabricated systems. This work is can potentially lead us into a new age of the miniaturization of mechanical and electronic devices.

Acknowledgements

First and foremost, I must thank my advisors Dr. Chris Roberts and Dr. Bob Ashurst for giving me the opportunity to work on a fundamentally new and challenging project. They were both available whenever I needed scientific advice or the occasional laughter and encouragement. I gratefully acknowledge my predecessors Madhu Anand, Chris Kitchens, Dan Obrzut, Adam Anderson, and Aimee Poda for their helpful insight and friendship. I also gratefully acknowledge my co-workers and peers in the Department of Chemical Engineering for generally making the Auburn experience more satisfying. Special thanks go to my lab-mate, Naveed Ansari, for all of the time and effort he spent fabricating and testing microdevice tribology chips of which he developed. This work would have not been possible without him.

Thanks are also owed to the faculty and staff of the Department of Chemical Engineering. It was the kindness and open arms of the faculty that convinced me to pursue my degree at Auburn University. Special thanks are given to Karen Cochran and Sue Ellen Abner who would both give up precious time during their busy days to help any student with any problems that may arise. Finally, I must thank my family for being so patient and understanding as I have pursued my education over the years. This day has been a long time coming and, thanks to their guidance, I am ready to move on to the next chapter in my life. As this chapter comes to a close, I dedicate this work to my late uncle Gregory "Ebay" Hansen (1952 – 2008) and cousin Jonathan Robert Hansen (1986 – 2009) whom my family lost during my time at Auburn. You are missed every day.

Table of Contents

List of Tables

List of Figures

CHAPTER 1

TRIBOLOGY, MEMS TECHNOLOGY AND RELIABILITY

1.1   Introduction to tribology

In his famous speech nearly fifty years ago, Richard Feynman discussed a relatively new field of science: miniaturization (Feynman 1992). Feynman talked about the potential for miniature machines, such as internal surgeons that could simply be swallowed. However, Feynman also singled out the most fundamental obstacles on the road toward miniaturization: adhesion and friction (Feynman 1992). At the nano- and micro-scale, the principal interactions between two small, contacting materials becomes increasingly important and can dominate inertial and gravitational forces usually encountered on a larger scale (Dowson 1998; Bhushan 1998). The science of studying two such contacting surfaces in relative motion is known as *tribology*, which encompasses a variety of surface interactions including friction, wear, and adhesion (Bhushan 1999).

Microtribology refers to the study of the surface interactions between two contacting, rubbing surfaces on the micro- or nano-scale. On this level, the surface interactions are driven by the surface-to-volume ratio of the surfaces in question. Burnham and Kulik (1999) described this phenomenon by comparing an ordinary pencil eraser to a residual eraser particle. A pencil eraser has dimensions on the order of 1 cm, while the radius, R, of residual particles from the eraser can be on the order of 100 μm. The surface-to-volume ratio for spherical objects equals

3/R indicating that the surface-to-volume ratio of a residual particle is 100 times greater than for the whole eraser. Burnham and Kulik (1999) go on to describe how the ratio between the attractive surface forces and the weight of a spherical particle is 10,000 times larger for a residual eraser particle, and therefore, the residual particle can be predicted to cling to a sheet of paper. This adhesion of micro- and nano-scale components is extremely important to micro-tribology as a whole, as friction and wear are strongly dependent on the level of adhesion (Bhushan 1990a).

Decades after Feynman introduced the field of miniaturization, scientists and engineers are continuing to try to improve the fields of microfluidics and microelectro-mechanical systems (MEMS). As time has passed, these researchers have become increasingly aware of the limitation discussed by Feynman in that technology on the micro-scale will be hindered until adhesion can be suppressed and the tribology of moving, contacting surfaces can be effectively controlled.

1.2   Introduction to MEMS

Microelectromechanical systems (MEMS) are a relatively new technology directly coupling miniature mechanical components with microelectronics and the semiconductor (IC) industry (Bao and Wang 1996). Typically, the core elements of a MEMS device are a sensing or actuating element and a signal transduction unit (Hsu 2002). The first successfully operating micromechanical devices, fabricated by surface-micromachining technology in 1988, were electrostatic micromotors (Fan et al. 1988; 1989). Fig. 1.1 presents an optical photograph of a polysilicon microgear at 10X magnification. To date, several types of MEMS have been introduced for commercial markets, including membrane pressure sensors (Bao and Wang 1996),

accelerometers for automobile airbag sensors (Goodenough 1991), and digital light processing (DLP) displays (Van Kessel et al. 1998). More recent commercialized applications for MEMS components include smartphones and video game controllers, such as for Nintendo Wii[TM], which utilize accelerometers to detect movement (Liu et al. 2009). Fig. 1.2 shows a scanning electron microscope (SEM) image of a commercially available MEMS accelerometer, while Fig. 1.3 illustrates digital micromirror devices used in DLP displays.

MEMS are fabricated from a variety of methods, including bulk micromachining, surface micromachining, and LIGA, a German acronym for lithography, electroplating, and molding (Madou 1997; Hsu 2002). Bulk and surface micromachining are the two most widely used methods for the production and fabrication of MEMS. Bulk micromachining involves the etching of material from bulk substrates, such as silicon wafers, to form three-dimensional microstructures (Hsu 2002). Surface micromachining, on the other hand, involves the deposition of additional layers onto bulk substrates which are then patterned and etched to create structures (Petersen 1982; Howe 1988; Muller 1990).

Fig. 1.4 presents a simplified diagram for a surface micromachining process. The starting material is generally a mono-crystalline silicon wafer, upon which an electrical isolation layer (typically silicon nitride) is deposited. A layer of polysilicon is then deposited to form the ground plane and actuation pad for the device. The polysilicon layer is patterned using lithography, and then anisotropically etched to isolate one portion of the polysilicon (actuation pad) from other portions (ground pad). A sacrificial layer of silicon oxide is then deposited over the patterned polysilicon layer. This layer serves as a "spacer" during the process, to provide gaps between the three-dimensional microstructures. The sacrificial layer is patterned and anisotropically etched forming areas for the next structural layer to anchor to the
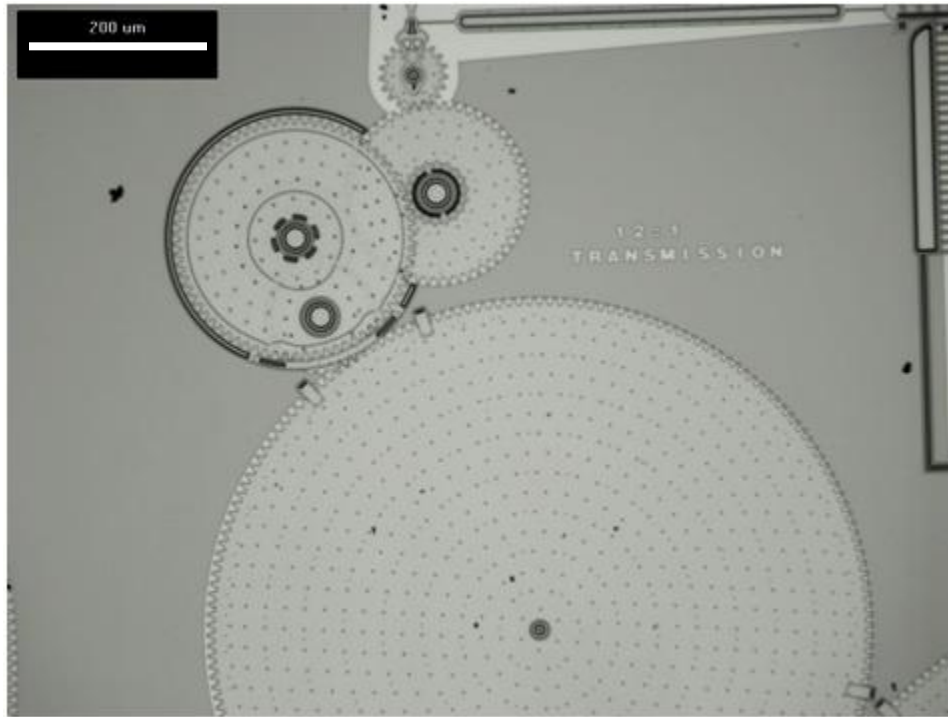
Figure 1.1. Optical microscope photograph of polysilicon microgears at 10X. The largest gear is

approximately 800 μm in length. Scale bar is 200 μm.

polysilicon ground plane. The structural polysilicon layer is then deposited, patterned, and etched to form the complete, desired microstructure. All that remains is to remove the sacrificial layer by isotropically etching with a hydrofluoric acid (HF) solution, leaving "released" and free-standing microstructures.

While the field of MEMS technology has grown to a mature stage in only a few short decades, the rapid development has also revealed bottlenecks and challenges to the advancement of the field (Petersen 1995). Today, only the simplest MEMS are used commercially while more complex devices are subject to surface phenomena that can lead to device failure. Both the production and lifetime of MEMS are limited by major reliability issues caused by strong adhesion, friction, and wear (Mastrangelo 1997; Tas et al. 1996, Komvopoulos 1996; Miller et al. 1996; Maboudian 1998; Rymuza 1999).

1.3   MEMS reliability issues

Surface and bulk micromachined MEMS and microfabricated devices typically have surface microstructures with lateral dimensions of 50-500 μm and thicknesses of 0.1-10 μm. These miniature components are also typically raised only 0.1-5 μm from the substrate surface. Due to the extremely large surface-area-to-volume ratios of such structures and components, surface and interfacial forces play an increased role in the operation of MEMS devices (Rymuza 1999; Mastrangelo 1997; Tas et al. 1996; Komvopoulos 1996; Maboudian and Howe 1997). Interactions between relatively smooth surfaces become critical and increase the probability of device failure. The most common phenomena affecting MEMS reliability are release stiction, in-use stiction, friction, and wear.
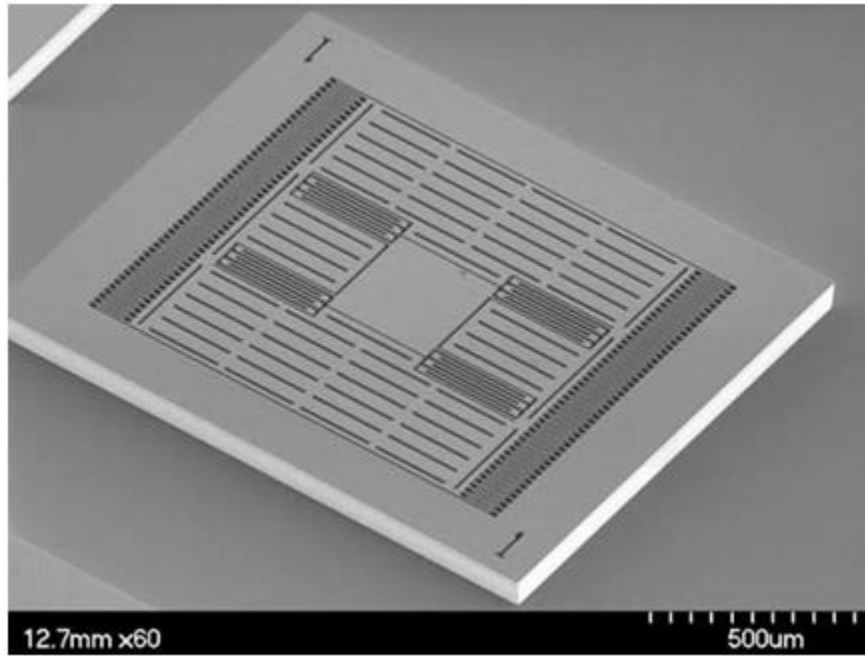
Figure 1.2. SEM image of a commercially available MEMS accelerometer designed by the

Micro and Nano Systems Laboratory at Polytechnique Montreal.
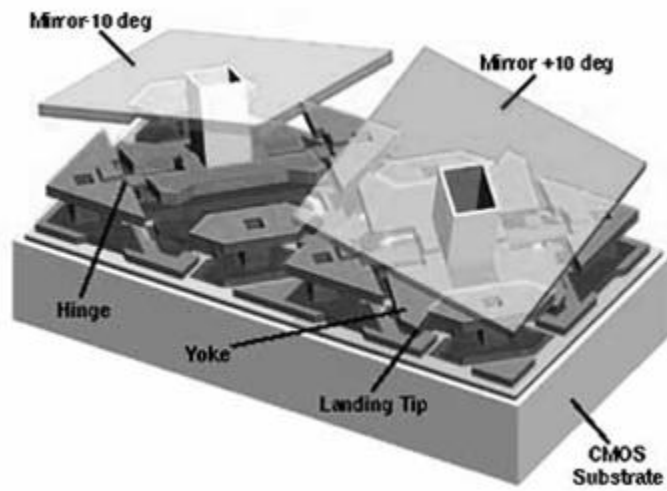
Figure 1.3. Illustration of digital micromirror devices utilized for DLP televisions

and displays, developed by Texas Instruments. The dimensions of the

square mirrors are 16 x 16 μm.
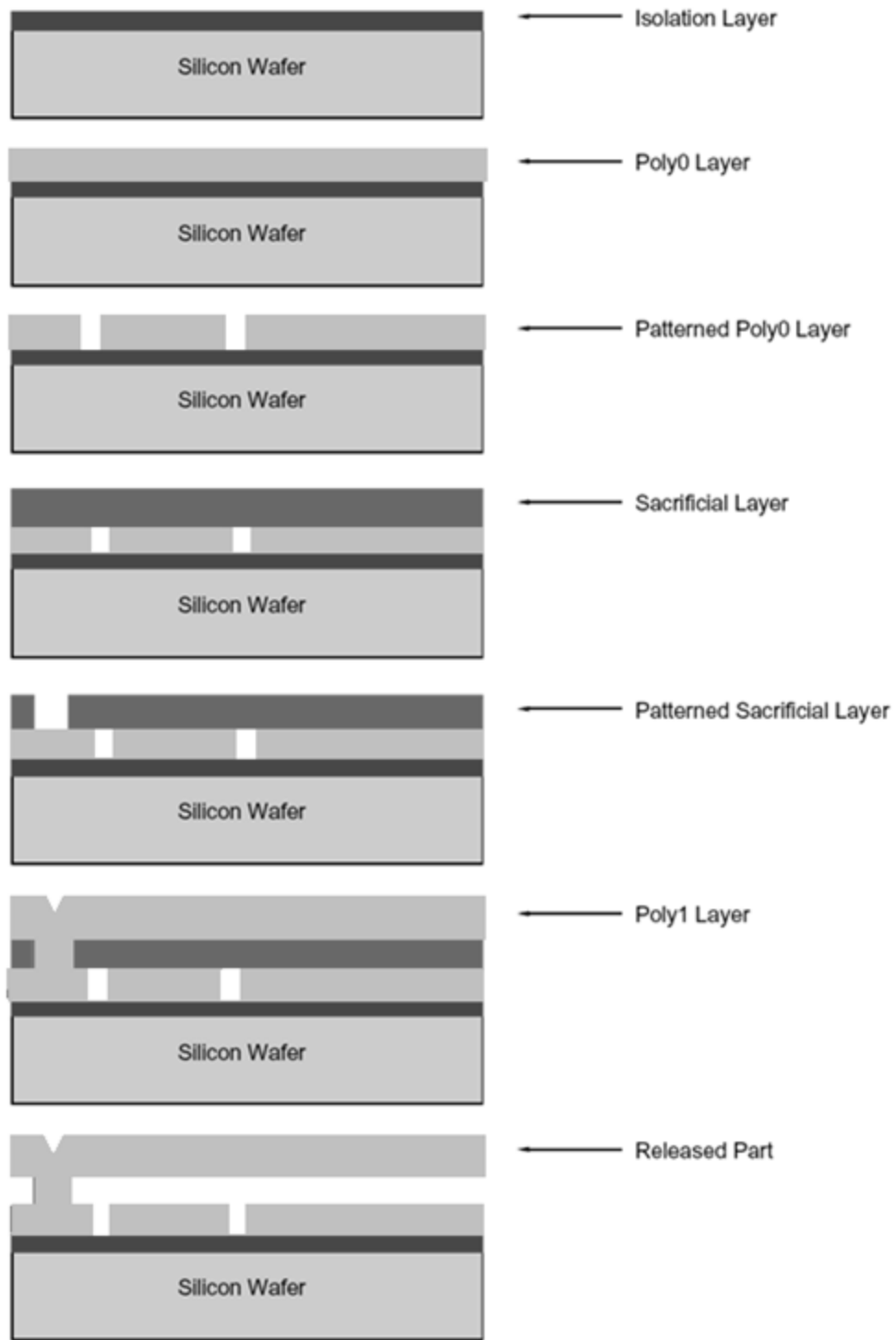
Figure 1.4. A simplified process diagram for the fabrication of a polysilicon

cantilever beam via surface micromachining.

1.3.1 Release stiction

The term *stiction* refers to the inadvertent adhesion of microstructure surfaces when they cannot overcome inherent interfacial forces such as capillary, chemical, van der Waals, or electrostatic attractions. Fig. 1.5 compares the force per area exhibited between two smooth silicon surfaces by capillary, electrostatic (applied voltage of 1 V), and van der Waals forces (Komvopoulos 2003). The figure shows that for small separation distances, these forces are much larger than the typical restoration force of a microfabricated structure.

Release stiction more specifically refers to the adhesion of microfabricated surfaces to the underlying substrate following the final sacrificial layer etching step (shown in Fig. 1.4). Following the etching of these sacrificial layers, the gaps left behind are filled with liquid. Due to the tremendous liquid capillary forces that can occur in such microscopic gaps, liquid cannot simply be allowed to evaporate and dry the surfaces (Guckel et al. 1989; Mastrangelo and Hsu 1993; Legtenberg et al. 1994). Instead, released devices are generally stored in an organic phase until measures can be taken to dry the device while avoiding such capillary forces to take over. These capillary forces are dependent on the contact angle between the liquid and solid surface in air, as shown in Fig. 1.6 for water on hydrophobic and hydrophilic surfaces.

Capillary forces can be described by the Laplace equation below (Eqn. 1.1), where γ is the liquid surface tension and θ is the contact angle.

$$P_L = P_1 - P_2 = \frac{2\gamma\cos\theta}{d} \tag{1.1}$$

Consider two parallel surfaces separated by a thin liquid layer with gap d as shown in Fig. 1.7. If the contact angle of the liquid film is less than 90°, the pressure within the liquid (P_2) will be less than that of the ambient air (P_1), resulting in a net attractive force between the two plates (Tas et al. 1996). This attractive capillary force is usually much stronger than the typical bending

9
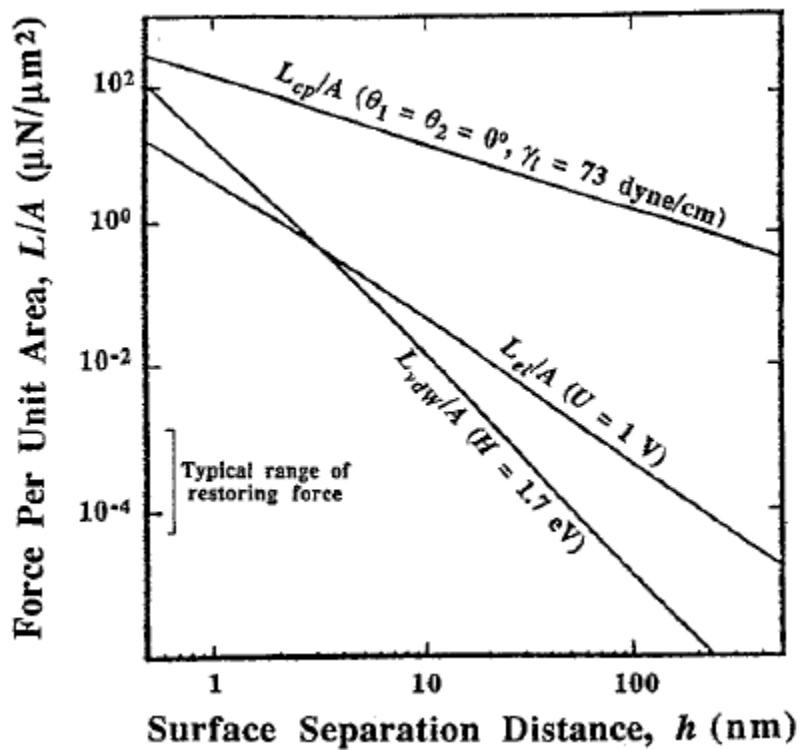
Figure 1.5. Comparison of interfacial attractive forces with surface separation between two smooth silicon surfaces (Komvopoulos 2003). F_{cp}, F_{el}, and F_{vdW} refer to capillary, electrostatic, and van der Waals forces, respectively.
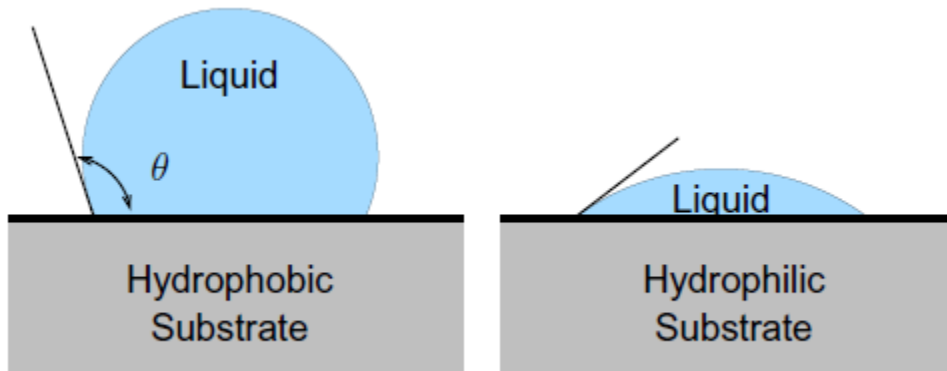
Figure 1.6. Diagram illustrating the contact angle of a water droplet on

hydrophilic and hydrophilic substrates (Ashurst 2003).
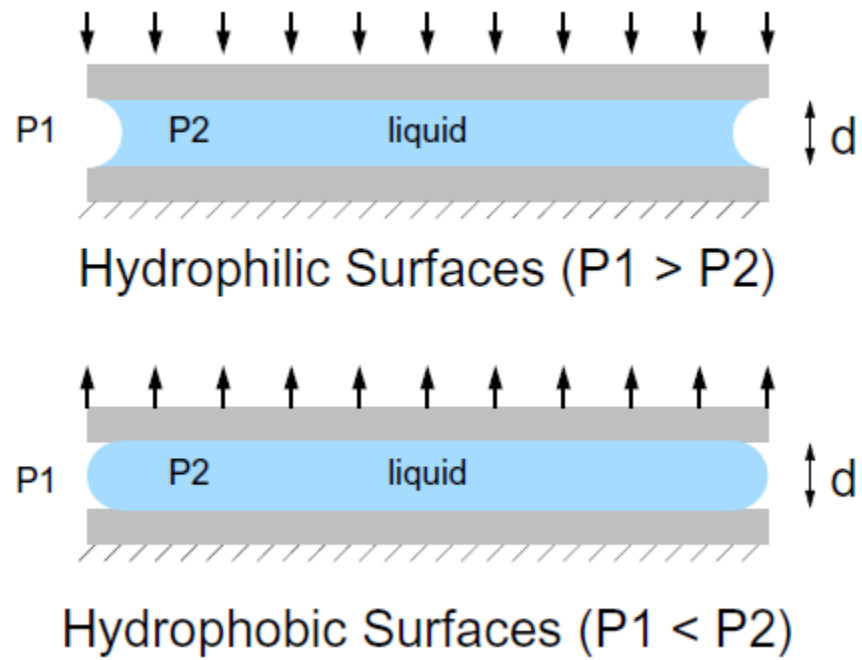
Figure 1.7. Diagram indicating the action of Laplace pressure for hydrophobic

and hydrophilic surfaces (Ashurst 2003).

restoration force of a microstructure. Therefore, structures will be pulled into contact with the underlying substrate and become permanently adhered. Alternatively, if the contact angle is greater than 90°, the Laplace pressure will result in an opposing force.

1.3.2 In-use stiction

Another adherence phenomenon is in-use stiction which refers to the permanent adhesion of microstructures during operation. In-use stiction often occurs between device components that may come into contact in an on-off fashion (RF switches, cantilever beams, etc.) or components that are continually in contact (gears). A key role in adhesion mechanisms is that of surface roughness. The root-mean-square (RMS) roughness at the bottom of released microstructures was measured by Legtenberg (1996) to be on the order of 1 to 3 nm. Due to the relative smoothness and small scale of microstructured components, large "real" areas of contact exist which, accompanied by extremely high van der Waals attractive forces, can often cause permanent adherence. Fig. 1.8 illustrates the real contact surface area between two surfaces with RMS roughness on the nanometer scale.

1.3.3 Friction and wear

In addition to the problems associated with stiction, microfabricated devices suffer from high coefficients of friction and substantial wear, especially in locations that experience high shear where massive contact pressures can be generated by moving components on rough silicon oxide surfaces (Tanner et al. 1999; Wang et al. 2002; Williams 2001). During the sliding of two surfaces, the interactions between rough asperities cause energy loss by means of elastic deformation and the formation of wear debris (Brenner 2001). For example, the hubs on

microgears become cluttered with wear debris after only a few hundred thousand cycles, as shown in Fig. 1.9, and will seldom last more than a few million cycles before becoming permanently unusable due to irreversible binding caused by increased friction (Tanner et al. 1996; Tanner 2000). The mechanism for wear in microdevices is very poorly understood, however, it is known that wear depends on mechanical contact details and environmental conditions including humidity (Tanner et al. 1999; Patton and Zabinski 2002).

1.4 Surface energy and superhydrophobicity

As briefly discussed in section 1.3.1, the very hydrophilic nature of silicon and silicon oxide materials can lead to detrimental capillary effects which can render MEMS and microdevices useless. The hydrophobicity of a surface can be directly related to the interfacial surface energies following Young's equation (Adamson and Gast 1990; Doms et al. 2008):

$$\gamma_L \cos\theta = \gamma_S - \gamma_{SL} \tag{1.2}$$

In Eqn. (1.2), θ is the contact angle of the fluid on the surface, γ_L is the liquid surface tension, γ_S is the solid surface energy, and γ_{SL} is the interfacial energy between the solid and liquid. By definition, γ_{SL} is the energy required to pull apart the two surfaces to create two distinct surfaces (one solid and one liquid). The value of γ_{SL} can be approximated from the surface energies of the separate components following (Doms et al. 2008):

$$\gamma_{SL} = \gamma_S + \gamma_L - 2\sqrt{\gamma_S \gamma_L} \tag{1.3}$$

Based on Eqns. (1.2) and (1.3), when the bare solid surface energy is higher than the solid-liquid interfacial energy ($\gamma_S > \gamma_{SL}$), the contact angle will be less than 90° and the solid surface is hydrophilic (when water is the liquid being examined). In the case of silicon-based surfaces, the surface energy is extremely high yielding a very hydrophilic surface. Therefore, one method
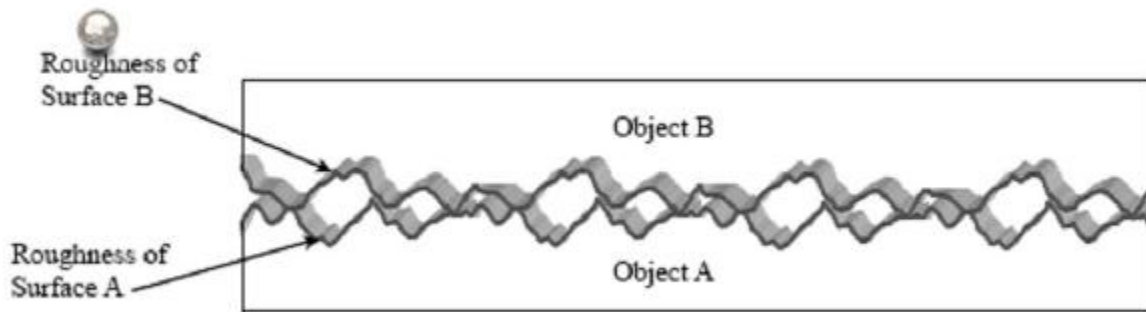
Figure 1.8. Diagram illustrating the real contact surface area between two surfaces exhibiting adhesion due to large attractive forces (Kang 2007).
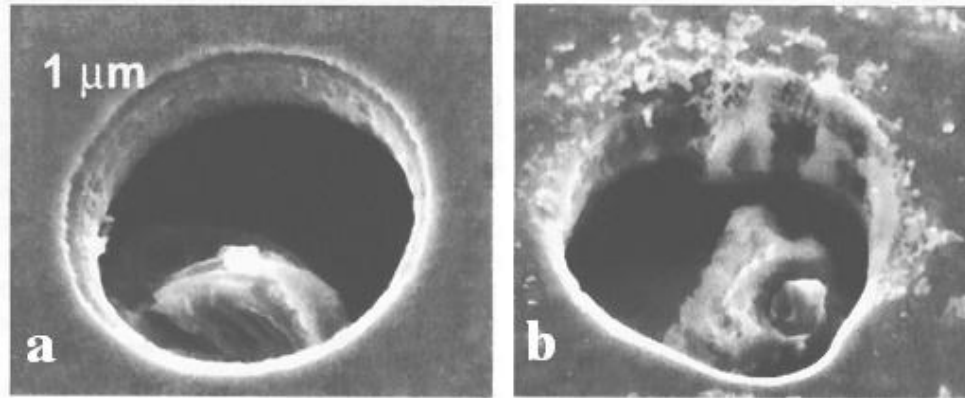
Figure 1.9. SEM images of a microengine pinhole (a) before operation and

(b) following about one-million cycles.

commonly used to reduce the hydrophilic nature of MEMS and microstructures is to significantly lower the surface energy by chemically altering the surfaces.

Another key factor influencing hydrophobicity is surface roughness. Wenzel (1936) first examined the effect of surface roughness of hydrophobicity and contact angles. Wenzel determined that if the solid-liquid interface followed the contours of a rough surface, the actual angle of contact should equal the equilibrium contact angle for a smooth surface adjusted by a roughness factor, r, as shown by Eqn. (1.4).

$$\cos \theta_W = r \cos \theta \qquad (1.4)$$

The roughness factor, r, is a ratio of the actual surface area to the projected surface area ($r > 1$ for rough surfaces).

Cassie and Baxter (1944) also examined the effect of rough surfaces on hydrophobic nature. In their work, Cassie and Baxter examined the effect of trapped air between liquid droplets and extremely rough surfaces. The Cassie-Baxter model, Eqn. (1.5), adds to the Wenzel model by taking into account a fraction of the surface ($\varphi < 1$) that a droplet of water makes contact with due to the trapped air.

$$\cos \theta_{CB} = \varphi \cos \theta + (1 - \varphi) \cos \theta_G \qquad (1.5)$$

In Eqn. (1.5), θ_G represents the contact angle between the liquid droplet and the entrapped gas. Fig. 1.10 illustrates the wetting states based on (a) apparent contact angles on smooth surfaces, (b) Wenzel contact angles, and (c) Cassie-Baxter contact angles.

Superhydrophobic surfaces, or surfaces with $\theta > 160°$, may play a vital role for the future of the MEMS industry. Such surfaces, which typically link appropriately roughened surfaces with low surface energy materials such as fluorinated compounds (Lacroix et al. 2005), have the potential to greatly reduce the surface energy of MEMS and microstructures and effectively

17
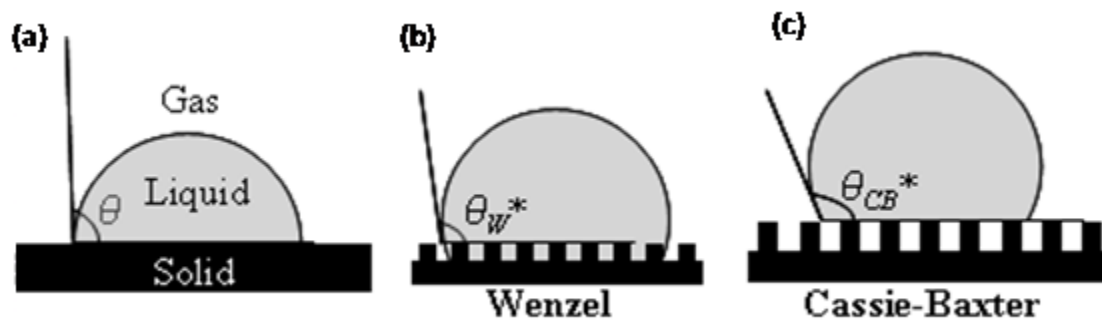
Figure 1.10. Wetting states illustrating (a) apparent contact angle, (b) Wenzel contact angle,

and (c) Cassie-Baxter contact angle.

reduce detrimental interfacial phenomena. Superhydrophobic coatings have the potential to revolutionize not only the MEMS industry, but the consumer electronics industry as well.

1.5   Objectives of this work

It is well known that the reliability issues discussed in this work are major bottlenecks to the realization of the full potential of MEMS devices. Previous attempts to improve the reliability of MEMS have shown that wear and stiction can be decreased, however, there is currently no single surface treatment that can address all reliability concerns at once. Therefore, the overall goal of this research is to develop a wear-resistant, anti-stiction coating process for MEMS while emphasizing current MEMS and microfabrication techniques. In order for a new process to be integrated into the MEMS industry, the coating must exhibit a drastic improvement in alleviating stiction and wear of microstructures and be compatible with current microfabrication processes already in use.

Based on previous work on the deposition of nanoparticles by gas-expanded liquid technology and supercritical fluid drying, the use of deposited nanoparticles as coatings on MEMS devices has been explored. As will be discussed in subsequent chapters, gas-expanded liquid/supercritical fluid processing is highly compatible with current microfabrication methods and can easily be integrated into industry. However, the intentional deposition of particles onto the surface of micromachined devices is a fundamentally new concept. Therefore, a number of fundamental studies have been explored to determine if nanoparticle coatings and films are a viable option towards increasing the lifetime of MEMS.

CHAPTER 2

ADDRESSING RELIABILITY ISSUES IN MEMS – A REVIEW

Several engineering solutions have been developed to address adhesion- and friction-related problems in MEMS. However, stiction has been identified as perhaps the single most important mode of failure in MEMS, as it is known that friction on the microscale is strongly dependent upon adhesive forces (Bhushan 1990b). As a result, numerous approaches to alleviating adhesion-related failure have been examined. The following sections provide details about some approaches used to address stiction, friction, and wear in microstructured devices.

2.1 Engineering solutions to release stiction

One type of engineering approach to release stiction is to physically or chemically alter the surface of the structures. One example of such an approach is the intentional texturization of the surfaces to reduce the real contact area (Alley et al. 1993). Houston et al. (1995) employed ammonium fluoride (NH_4F) to selectively etch certain crystallographic orientations of silicon. Since polysilicon is comprised of small, randomly oriented crystalline grains, etching these surfaces with NH_4F creates a rough, textured surface. These rough surfaces reduce the real contact area available when two contacting surfaces are brought together by capillary forces.

On the other hand, the chemical alteration of surfaces by grafting a molecular monolayer of a hydrophobic species tackles the fundamental causes of release stiction: moisture adsorption

and capillary forces (Abe et al. 1995). Self-assembled monolayers (SAMs) of various organic materials have been deposited onto microstructures in the liquid phase in order to eliminate capillary pull-down forces caused by evaporating liquids. Organic molecules employed in previous studies include alkyltrichlorosilanes and perfluoroalkyl trichlorosilane such as octadecyl trichlorosilane (OTS) and perfluorodecyl trichlorosilane (FDTS), among others (Ashurst et al. 2000; Srinivasan et al. 1998a). It has been demonstrated that molecular coatings of these materials effectively eliminate release stiction by reversing the shape of the water meniscus on the surface of hydrophilic microstructures (Abe et al. 1995). From water contact angle measurements, the contact angle increases from less than 30° on a hydrophilic silicon oxide surface to more than 110° on a silica surface coated with an OTS monolayer (Ashurst et al. 2001a).

Several other engineering solutions to release stiction have been developed which do not alter the structure surfaces and instead involve additional processing steps during the release stage. These methods include the avoidance of liquid-vapor interfaces through the use of supercritical drying (Mulhern et al. 1993; Resnick and Clews 2001), freeze sublimation (Petersen 1982; Guckel et al. 1990), polymer support ashing (Mastrangelo 1997; Orpana and Korhonen 1991; Mastrangelo and Saloka 1993), and vapor-phase hydrofluoric acid (HF) etching (Kozlowski et al. 1995; Lee et al. 1996; Anguita and Briones 1998).

The supercritical drying process, developed by Mulhern et al. (1993) using methods for preparing biological microscopy samples, begins with released microstructures which have been kept submerged in liquid since their sacrificial layer etch. The microstructure samples are placed within a high pressure vessel filled with an organic solvent (hexane, methanol, isopropanol) which is completely displaced by liquid carbon dioxide (CO_2). Following displacement, the

highly pressurized CO_2 is heated isochorically to the supercritical state. Venting the supercritical fluid at an elevated temperature effectively dries the microstructures while avoiding the liquid-vapor interface and associated detrimental capillary forces. Fig. 2.1 shows a generic pressure-temperature (P-T) diagram that depicts the pathway of the supercritical drying process. Freeze sublimation is another P-T process, illustrated in Fig. 2.2, which allows for the drying of micromachines by avoiding the liquid-vapor interface. In this process, the organic solvent submerging a microdevice is displaced by another solvent which is then frozen to the solid phase. Vapor above the solid-phase is pumped off by a vacuum pump. In time, the entire solid-phase will sublimate and be pumped off leaving only the dried micromachine sample (Guckel et al. 1990; Legtenberg 1996).

Polymer ashing is another wet-release process that uses a physical change in order to avoid capillary destruction of microstructures. In this procedure, structures are first partially released by a short timed etch. A polymer film is then deposited into the released areas, creating a film of polymer support posts that will hold the structures in place as the remainder of the sacrificial layer is etched away. Following the sacrificial layer removal, the polymer support devices can be removed from the liquid and dried by evaporation. Finally, by means of oxygen plasma, the polymer supports are burned off leaving behind fully released and freestanding microstructures (Mastrangelo 1997; Orpana and Korhonen 1991).

Some release methods, rather than using a special drying technique to avoid detrimental effects of the liquid-vapor interface, simply avoid the use of liquid etching procedures. Vapor HF etching is a process that completely avoids the issue of displacing solvents. In this
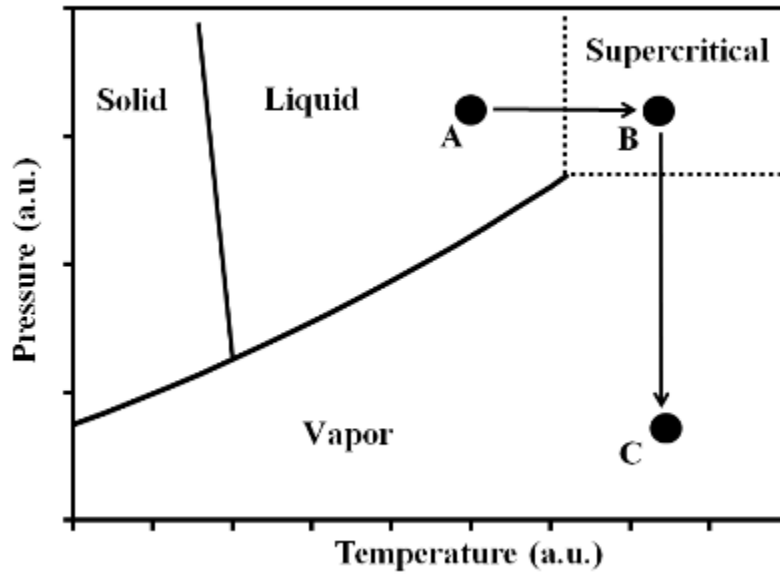
Figure 2.1. P-T diagram illustrating the pathway for supercritical drying in order to avoid the

liquid-vapor interface. Pressurized fluid (A) is heated into the supercritical regime (B).

Isothermal depressurization then allows for the removal of the fluid

and drying of the enclosed sample (C).
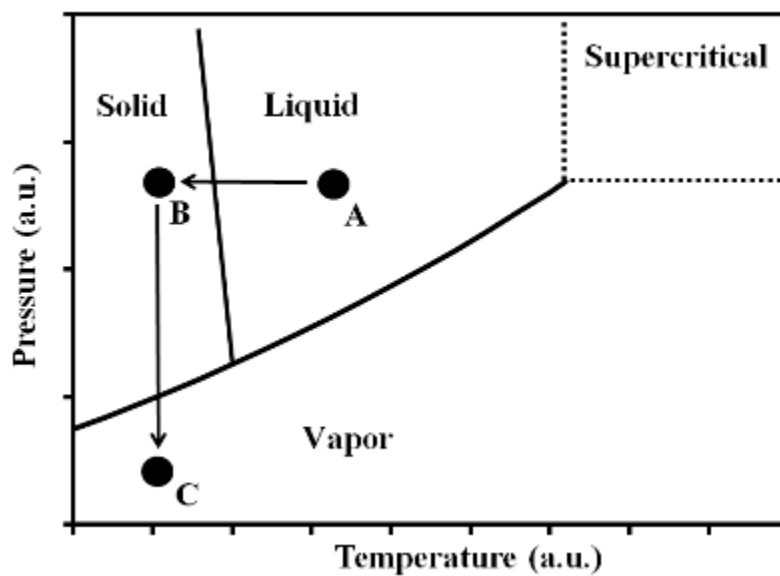
Figure 2.2. P-T diagram illustrating the freeze sublimation process. Pressurized liquid (A) is frozen into a solid (B) which is then sublimated into a gas (C).

procedure, the sacrificial layer etch is carried out by an isotropic gaseous etchant. Generally, samples are placed above an HF/water solution rather than being submerged into the liquid. The vapors given off by the solution perform the sacrificial layer etch, leaving behind freestanding structures (Mastrangelo and Saloka 1993; Offenberg et al. 1994; Kozlowski et al. 1995; Lee et al. 1996; Anguita and Briones 1998). However, since the etchant vapors are performing the etch in this procedure, much more time is required to fully remove the sacrificial layers.

While all of these engineering solutions have either reduced or effectively eliminated release stiction as an issue in the MEMS industry, these methods do have varying degrees of success. The non-trivial implementation of these techniques is subject to human error and often requires very specialized equipment. In addition, procedures which do not chemically alter the surface of micromachines do not prevent the occurrence of stiction during device operation. Chemical surface alterations such as SAMs, on the other hand, have been shown to eliminate release stiction as well as reduce in-use stiction. However, SAM formation also has its limitations as will be discussed in the next section.

2.2 Previous studies to alleviate in-use stiction

Unlike release stiction, which only occurs during the release step of microstructure processing, in-use stiction can occur at any time. Therefore, viable solutions to alleviate in-use stiction must have long-term anti-stiction effects. Initial attempts to reduce microstructure sticking focused primarily on the reduction of contact surface area between adjacent surfaces by increasing the surface roughness of polysilicon microstructures and substrates (Fan et al. 1989; Alley et al. 1993; Houston et al. 1995; Yee et al. 1996). However, due to achieving only a moderate factor of 20 times reduction in adhesion by surface roughening (Yee et al. 1996),

recent efforts have shifted to focus on methods that chemically alter polysilicon surfaces (Maboudian and Carraro 2004).

2.2.1   Self-assembled monolayer coatings

The majority of chemical treatment studies for modifying the surfaces of microstructures have involved the formation of self-assembled monolayers (SAMs). SAMs are formed when a molecule attaches to the surface with other adsorbed molecules which are oriented to create a single molecule deep thin film. One of the most widely studied molecules for SAM formation is octadecyl trichlorosilane (OTS) which orients its polar head group toward the substrate while the non-polar tail group points away from the surface. The tail groups orient themselves to create a film of closely packed alkane chains with methyl termination which gives the film a very hydrophobic nature. SAM coatings, such as OTS, deposited from solution onto micromachines have been demonstrated to achieve the following constructive characteristics when properly integrated into the sacrificial layer removal process (Srinivasan et al. 1997; Srinivasan et al. 1998a; Deng et al. 1995a; Srinivasan et al. 1998b; Houston et al. 1996; Maboudian et al. 2000; Cabuz et al. 2000):

1. Elimination of release stiction by effectively reversing the shape of the water meniscus that forms underneath microstructures during liquid evaporation.

2. Reduction of in-use stiction, quantified by apparent work of adhesion, up to four orders of magnitude with respect to unprocessed, released structures.

3. Reduction of the coefficients of friction in microengines.

Several classes of organic monolayer films have previously been explored, including alkyl- and perfluoroalkyl trichlorosilanes (R-$SiCl_3$) (Srinivasan et al. 1998a; Maboudian et al. 2000),

dichlorosilanes (Ashurst et al. 2001a; Kim et al. 2001), and alkene-based monolayers (Ashurst et al. 2000). Among these organic molecules, octadecyl trichlorosilane ($CH_3(CH_2)_{17}SiCl_3$) is the most widely studied organic monolayer film.

The formation of OTS (or other chlorosilane) films on silicon oxide surfaces begins with the hydrolyzing of the precursor, in which a trichlorosilane molecules reacts with three molecules of water producing three molecules of hydrochloric acid (HCl) and a trisilanol.

$$R\text{-}SiCl_3 + 3H_2O \rightarrow 3HCl + R\text{-}Si(OH)_3$$
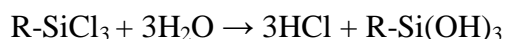
The water molecules for this reaction come from ambient humidity, due to the hygroscopic nature of the solvent in which the reaction takes place (generally hexane). Therefore, the reaction is highly sensitive to ambient humidity, resulting in poor monolayer formation. For example, if the water content is too low (less than ca. 40% relative humidity) not enough of the chlorosilane molecules will be hydrolyzed. If the humidity is too high (greater than ca. 70%) bulk polymerization of the precursor may be observed. Following hydrolysis, the trisilanol molecules orient themselves on the extremely hydrophilic silicon oxide surface where the hydroxyl groups condense, releasing water and forming Si-O-Si bonds (Sung et al. 2000). Although the exact mechanism for the formation of chlorosilane monolayers is debatable (Carraro et al. 1998; Schwartz 2001), a simplified conceptual model of an OTS monolayer on silicon oxide is presented in Fig. 2.3 (Ashurst 2003).

Alley et al. (1992) first considered the use of organic SAMs for alleviating adhesion and stiction in microfabricated cantilever beam arrays. The results were promising, although no quantitative measurements could be made. Deng et al. (1995a, b) performed further studies involving alkyltrichlorosilane-based SAM films which demonstrated a clear improvement in the release and wear properties of polysilicon wobble micromotors. Houston et al. (1996) further
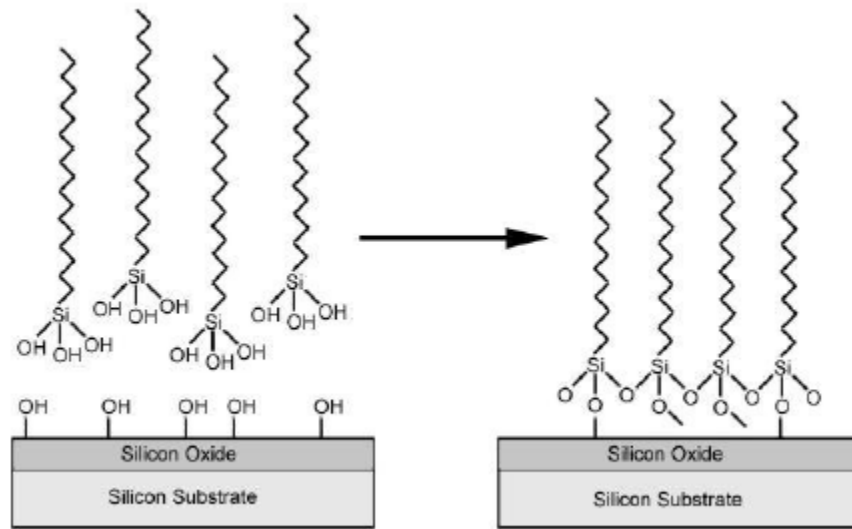
Figure 2.3. Simplified diagram for the formation of a self-assembled OTS

monolayer on silicon oxide (Ashurst 2003).

examined the effect of OTS coatings on microstructures on release and in-use stiction. It was found that release stiction was effectively eliminated while the work of adhesion, a quantitative value for in-use stiction, was reduced by three orders of magnitude when compared to conventional oxidation release procedures.

In addition to OTS, there have been studies performed with many other precursor molecules in order to produce oriented, hydrophobic monolayers onto silicon surfaces. Such studies have illustrated that perfluorinated alkyltrichlorosilanes produce the most effective results (Banga et al. 1995). For example, monolayer coatings formed from 1H,1H,2H,2H-perfluorodecyl trichlorosilane (FDTS) have critical surface tensions as low as 6 mJ/m^2 compared to 22 mJ/m^2 for OTS coatings (Brzoska et al. 1994). SAM coatings formed from FDTS have, in fact, resulted in lower apparent work of adhesion values compared to OTS and natural silicon oxide layers (Srinivasan et al. 1998a). However, FDTS monolayers tend to form large particulates on the surface due to bulk polymerization of the precursor more often than OTS monolayers. Table 2.1 presents interfacial property comparisons between various silicon surface treatments. A third precursor which has been extensively studied for use as SAM coatings on MEMS is dimethyl dichlorosilane ((CH_3)$_2$SiCl$_2$, DDMS). DDMS monolayers are highly comparable to OTS monolayers in terms of film properties and their effectiveness to reduce in-use stiction of microstructures. Although reduced polymerization with DDMS coatings has been shown compared to OTS monolayers, DDMS produces slightly higher coefficient of friction and apparent work of adhesion values (Ashurst et al. 2001a; Kim et al. 2001).

29

2.2.2   Limitations of self-assembled monolayer formation

Even though organic SAM coatings have shown great potential to reduce adhesion in microsystems, there are several limitations hindering the commercialization of SAM-forming processes. In particular, chlorosilane chemistry imposes limitations on SAM formation. SAM precursor molecules must first be hydrolyzed before they can be bound to a silicon surface, which produces the equivalent of one HCl molecule for each Si-Cl bond that is hydrolyzed. Metal (or metal compounds) that may be present on devices for use as electrical contacts or switches may be threatened by the presence of these HCl molecules (Henck 1997).   Charge trapping is also a concern, as silicon surfaces must first be oxidized using hydrogen peroxide (H_2O_2) or exposure to oxygen plasma. This oxide is an electrically insulating layer which may lead to unfavorable performance or device failure (Cabuz et al. 2000).

Another limitation arises due to the sensitivity of precursor polymerization to ambient moisture and water concentration (Maboudian et al. 2000; Bunker et al. 2000). Water required for the hydrolysis is supplied from the ambient air and, therefore, the humidity must be controlled in order to have sufficient water for polymerization. Too little water can lead to an incomplete monolayer while too much water can lead to the formation of large agglomerates which may lead to unpredictable device performance. Once bulk agglomerations have formed, there is no satisfactory method for removing the large particles. Therefore, the SAM formation process must be done right under controlled environmental conditions. The sensitivity of precursor polymerization and the coating process to ambient humidity also means that fresh precursor solutions must be made and maintained before each coating process, requiring large amounts of chemicals (Rozlosnik et al. 2003; Wang and Lieberman 2003). These issues with the

chemistry of SAM formation lead to the issue of being able to accurately reproduce monolayers on a large number of samples.

The inability to scale up wet SAM formation processes is another major bottleneck. Current processes allow for only a few microdevices on the order of 1 cm^2 to be coated. In order to process a full silicon wafer of devices, an excessive amount of organic material is required. In addition, user chemical handling is required to ensure that wafers are not dried until the process is complete. SAM anti-stiction coatings are also suspect to durability issues. SAMs are not mechanically hard materials and have been shown to wear off under high contact pressure (Ashurst 2003). Due to these issues concerning self-assembled monolayer coatings, alternative anti-stiction coatings may be much more favorable as long as device performance is not diminished.

2.2.3   Other approaches to reduce stiction

Recent developments in the technology of producing chlorosilane-based self-assembled monolayers have addressed some of the SAM formation limitations by performing the coating process in the vapor phase. Vapor phase processing eliminates the use of organic solvents and greatly simplifies the user handling of samples and chemicals (Ashurst 2003). It has been demonstrated that monolayer films produced from tridecafluoro-1,1,2,2-tetrahydrooctyl trichlorosilane ($CF_3(CF_2)_5(CH_2)_2SiCl_3$, FOTS) in low-pressure chemical vapor deposition (CVD) reactors exhibit very low adhesion energies (Mayer et al. 2000; Zhuang et al. 2007; Knieling et al. 2007). The results demonstrate high contact angle and low adhesive force for all vapor-phase SAM coatings. Fluorinated chlorosilane precursors exhibit the best anti-stiction capabilities, however, the effect on the coefficient of static friction is less pronounced than with OTS

monolayers (Zhuang et al. 2007). Unfortunately, vapor-phase SAM formation requires that microstructures undergo a dry release process such as critical point drying or vapor HF etching before receiving the monolayer coating.

Other studies have examined two step processes incorporating multiple SAMs or SAMs coated with a second material. Bai and Cheng (2008a) coated silicon surfaces with the precursor 3-mercaptopropyl trimethoxysilane (MPTS) and oxidized the terminal –SH groups in order to produce –SO_3H groups with high chemisorptions ability. Lanthanum thin films were then deposited onto the MPTS-formed monolayer. The study showed that lanthanum thin films have lower adhesive force than untreated silicon surfaces and lower friction was attributed to the strong La-SO_3 bond.

2.3   Approaches to address friction and wear

It is widely known that friction, on the microscale, is highly dependent upon adhesion and adhesive forces (Bhushan 1990b). Therefore, many attempts to alleviate in-use stiction were also attempted to reduce friction in microstructures. For instance, studies performed using OTS and FDTS precursor molecules resulted in much improved coefficients of static friction compared to natural oxidized silicon surfaces (see Table. 2.1). These results suggest that drastically different friction-related properties can be achieved by chemically altering the surface of microstructures. Cléchet et al. (1994) also investigated the lubricating properties of alkyltrichlorosilane SAMs on oxidized Si(100) microstructures, finding that the coefficient of dynamic friction reduced from 0.6-0.7 for SiO_2 surfaces down to about 0.12 for OTS coatings. In terms of wear, OTS and other SAM coatings have proven to be a marked improvement over the wear properties of SiO_2 coated surfaces. Deng et al. (1995a, b) found that polysilicon wobble

Surface treatment	Water contact angle	Hexadecane contact angle	Work of adhesion (mJ/m^2)	Coefficient of static friction	Particulate formation rate
OTS	110°	38°	0.012	0.07	High
FDTS	115°	68°	0.005	0.10	Very high
SiO$_2$	0-30°	0-20°	20	1.1	--

Table 2.1. Physical property data for various silicon surface treatments (Ashurst et al. 2001a; Srinivasan et al. 1998a; Srvinivasan et al. 1997; Houston et al. 1996).

motors coating with OTS SAMs exhibited low wear and good durability by operating for nearly 80 million cycles over a nine month period. However, regardless of this success, the durability of SAM-coated microstructures and MEMS is still debatable. The need still exists for the development of anti-stiction and anti-friction coatings for MEMS and microdevices which are highly durable.

2.4   Tribology of nanoparticle-roughened surfaces

Interfacial forces that exist between two relatively smooth microstructures are responsible for causing adhesion and friction in MEMS (Maboudian and Howe 1997; Maboudian and Carraro 2004). These interfacial forces are highly dependent on the separation between surfaces, which makes force measurements extremely sensitive to surface contamination (DelRio et al. 2006). For instance, Frantz and Salmeron (1998) discovered a decrease in surface energy for mica sheets in contact due to contamination on the surface, which Ohnishi et al. (1999) later attributed to small nanoparticles left on the surface after the mica cleaving process.

DelRio et al. (2006) later discovered the presence of silicon carbide (SiC) nanoparticles (20-50 nm in diameter) on cantilever beam test structures that were a result of residual carbon for sacrificial layers migrating to the polysilicon surfaces. These contamination particulates were shown to strongly influence the interfacial adhesion of microfabricated structures by altering the average separation distance of the surface interface. The results of the study illustrated a decrease in adhesion energy from 8.0 to 2.1 $\mu J/m^2$ as the RMS roughness of the surfaces increased from 2.6 to 10.3 nm. The reduction in adhesion surface energy is attributed to asperity deformation forces, which Komvopouos (1996) describe as repulsive forces resulting from a surface contacting the highest asperities of a deformable medium.

Alternatively, Patton et al. (2008) have investigated the use of nanoparticle liquids (NPLs) as lubrication for MEMS switch contacts. NPLs are hybrid materials comprised of inorganic nanosized metallic cores surround by a low-viscosity organic corona, which exhibit liquid-like properties (Itoh et al. 2004; Bourlinos et al. 2005; Li et al. 2005). Studies were performed using 15-25 nm in diameter gold nanoparticles, with about a 2-nm corona of ionic liquid surrounding the particles, which were spin coated onto gold electrodes. The gold NPLs demonstrated a controlled nanoscale surface roughness that not only enhanced thermal and electrical conductivity of the contacts, but also have a self-healing capability in order to prevent wear of devices. However, these NPLs could have detrimental effects on mechanical components due to their liquid-like properties which may exhibit strong capillary forces.

Previous studies on how nano-sized particulates can reduce interfacial forces by increasing surface roughness have opened the door for new fundamental research on the use of nanoparticles as polysilicon surface modifications. However, the particulates examined by DelRio et al. (2006) were not intentionally deposited onto the surface of polysilicon cantilever beams. The SiC nanoparticles resulted from a side reaction during the microfabrication process. Generally, nanoparticles used for applications are deposited onto materials by means of drop casting (Collier et al. 1998; Sigman et al. 2004). Drops of dispersed nanoparticles within a solvent are placed on a surface and allowed to evaporate, leaving a film of dry nanoparticles. Unfortunately, the dewetting process of evaporating a solvent gives rise to capillary forces and high surface tensions at the liquid/vapor interfaces (Lin et al. 2001; Korgel and Fitzmaurice 1998; Ohara and Gelbart 1998; Motte et al. 1997; Giersig and Mulvaney 1993) which not only affect the deposition of particles but will also cause the collapse of microstructures on a device. Therefore, in order to intentionally deposit nanoparticles onto the surface of MEMS and

microfabricated structures, procedures must be used or developed which are compatible with current microfabrication technologies.

2.5 Gas-expanded liquid nanoparticle deposition

Several research groups, in recent years, have demonstrated the use of gas-expanded liquids as a new, alternative class of solvent. Gas-expanded liquids (GXLs) are mixtures of compressible gases (CO_2, ethane) dissolved within an organic solvent (Jessop and Subramaniam 2007). As CO_2 (or another compressible gas) dissolves into an organic liquid, the liquid volume expands; hence the term *gas-expanded liquid*. Certain organic liquids, such as methanol, hexane, and most other traditional solvents, dissolve large quantities of CO_2 and expand greatly. Fig. 2.4 illustrates the volume expansion of n-hexane by CO_2, showing that the volume effectively doubles as the CO_2 pressure is increased from 100 to about 700 psi. This expansion consequently causes significant changes in virtually every physical property of the organic solvent, including liquid density, solubility, and viscosity.

Previous studies have demonstrated that organic nanoparticle dispersions expanded volumetrically by CO_2 pressurization allow for the size-selective fractionation (McLeod et al. 2005a; Anand et al. 2005; Anand et al. 2008) and targeted thin film deposition (McLeod et al. 2005b; Liu et al. 2006; Kim et al. 2006) of gold and silver nanoparticles. In order for nanoparticles to remain stabilized within dispersions, they are generally coated with long ligand tails which interact with the organic solvent. CO_2 is often a very poor solvent for the solvation such ligand-coated particles. Therefore, as a CO_2 is dissolved within the liquid solvent, the solvent-ligand interactions decrease and particles begin to precipitate once a threshold solvent strength is reached (Anand et al. 2005; McLeod et al. 2005a, b; Kitchens et al. 2009). Fig. 2.5
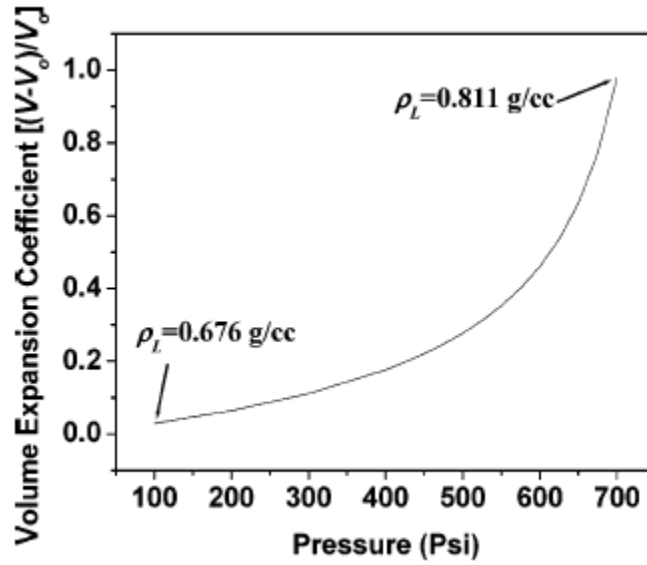
Figure 2.4. Volume expansion coefficient of liquid n-hexane with increasing gaseous

CO_2 pressure (Anand et al. 2005).
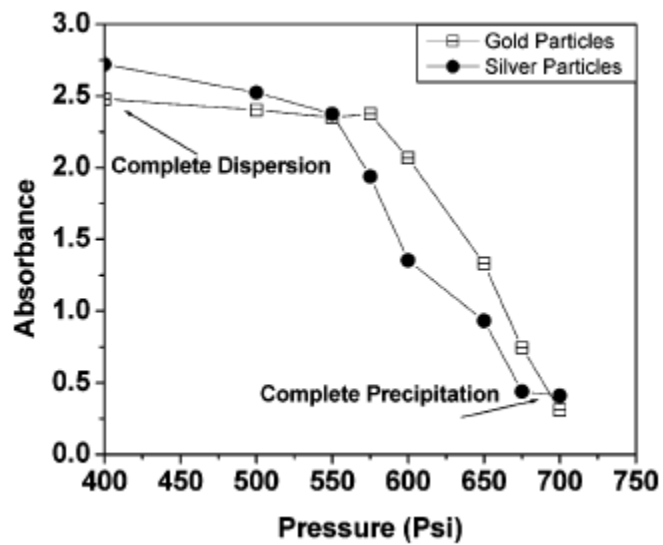
Figure 2.5. UV-visible absorbance of dodecanethiol-stabilized gold and

silver nanoparticles dispersed in liquid hexane/CO2 mixtures

with system pressure (Anand et al. 2005).

shows the decline of UV-visible absorbance of gold and silver nanoparticles being precipitated from a hexane/CO_2 gas-expanded liquid. This precipitation process is commonly referred to as gas-antisolvent (GAS) precipitation (Jessop and Subramaniam 2007).

Once nanoparticles have been deposited onto a surface by means of a gas-expanded liquid, the nanoparticle thin film is typically dried by means of supercritical drying. The liquid CO_2/solvent mixture is heated to the supercritical regime (much like in Fig. 2.1) and then depressurized isothermally to avoid crossing the liquid-vapor interface that is experienced during solvent evaporation. It has been demonstrated that depositing nanoparticles by GXL deposition followed by supercritical drying allows for wider-area nanoparticle films (McLeod et al. 2005a, b; Liu et al. 2006; Hurst et al. 2007; Kitchens et al. 2009). Fig. 2.6 presents transmission electron micrographs of decanethiol-stabilized gold nanoparticles (AuNPs), with an average diameter of 4.0 ± 1.2 nm, deposition by (a) solvent evaporation and (b) CO_2-expanded hexane/supercritical CO_2 drying. The particles deposited by GXL exhibit a wide-area film of closely packed nanoparticles, yielding a surface coverage of greater than 60%. By contrast, the nanoparticles deposited by evaporation exhibit a surface coverage of less than 25%. The difference in surface coverage, despite the use of identical particle concentrations, is attributed to the liquid/air interface experienced during evaporation which leads to the development of highly concentrated areas of particles in random areas of the sample along with areas sparse of particles. Particles deposited via gas-expanded liquids, however, are free to deposit in a much more ordered manner, leading to fewer film defects caused by interfacial surface tensions. This technology would allow for MEMS surfaces to be intentionally coated with particles using microfabrication-compatible processes without detrimentally affecting the microstructures.
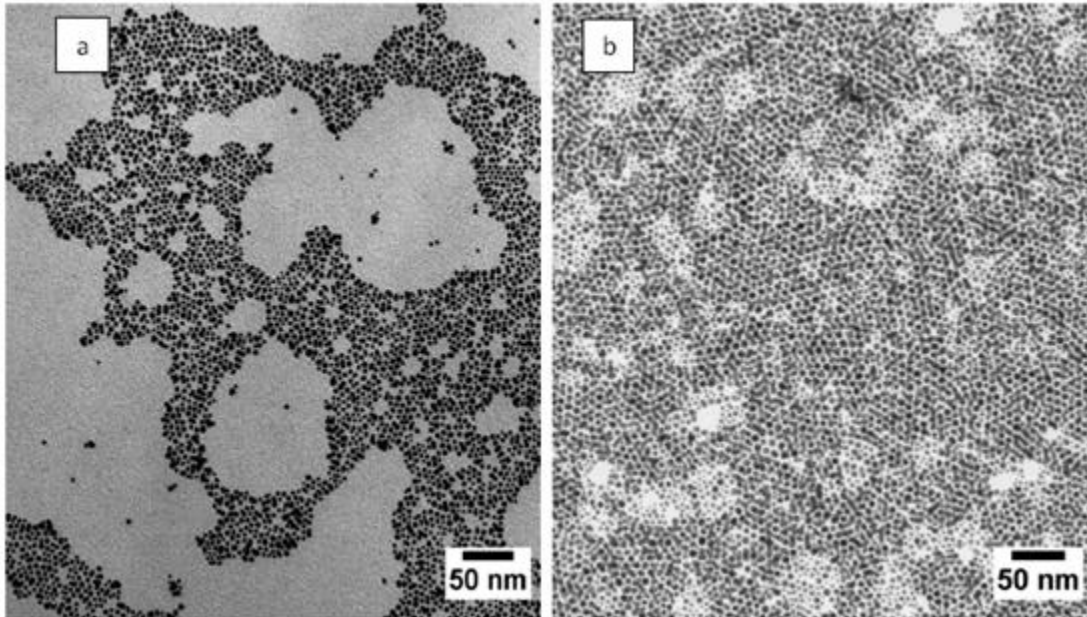
Figure 2.6. TEM photographs of gold nanoparticles deposited on carbon-coated

TEM grids via (a) solvent evaporation and (b) CO_2-expanded liquid/

supercritical drying (Hurst et al., 2007).

2.6 Nanoparticle attachment to self-assembled monolayers

Due to the unique optical, electronic, catalytic, and magnetic properties of metallic nanoparticles, considerable recent attention has been devoted to assemble and immobilize such particles onto solid surfaces (Yonezawa and Toshima 2001; Yamanoi et al. 2004). Specifically, such strategies would allow for the immobilization of nanoparticles for electronic applications in the semiconductor industry. Over the last decade, several techniques have been published for immobilizing metal-based nanoparticles on single-crystalline silicon surfaces, typically through interactions between particles and self-assembled monolayers.

Several recent papers have examined the immobilization of various metallic films on 3-mercaptopropyl trimethoxysilane (MPTS) self-assembled monolayers (Goss et al. 1991; Bhat et al. 2003; Xu et al. 2003; Wang et al. 2004; Lee and Xia 2008; Ali et al. 2008; Khatri et al. 2008). Vekarelski et al. (2007) investigating the attachment of silica nanoparticles to MPTS monolayers on gold surfaces. The "mercapto" (sulfur-containing) end of the molecules readily adsorb and self-assemble on a gold surface while the silanated ends react with the SiO_2 nanoparticles like most silane SAMs react to polished SiO_2 wafers. This examination also led Vakarelski et al. (2007) to examine the reverse effect: immobilizing gold nanoparticles to MPTS monolayers deposited on silicon. The study found that 50-nm gold nanoparticles readily adsorbed to the monolayer-covered silicon surface, and that particles began to agglomerate and cluster on the surface as the nanoparticle solution concentration increased.

A number of MPTS monolayer studies have also been performed by Bai and Cheng (2006, 2008a, 2008b). These studies have primarily examined and characterized the tribological properties of MPTS monolayers on single-crystal Si(111) surfaces. In these studies, the investigators dip-coated polished silicon samples into an MPTS/benzene solution for various

periods of time. They found that with increasing deposition times up to roughly 20 minutes the roughness of the sample (analyzed by AFM) increased rapidly. Deposition times of 90 minutes or longer experienced no real change in surface roughness, with roughness analysis measurements of about 0.5 nm compared to 0.144 nm for a clean, polished Si(111) surface (Bai and Cheng 2008b). Although Bai and Cheng (2006) did not attempt to immobilize nanoparticles onto these MPTS coatings, they did discover that the friction coefficient of the surface was drastically reduced with SAM deposition time.

Amino-terminated molecular films have also been widely studied for the immobilization of nanoparticles (Sugimura and Nakagiri 1997; Li et al. 2001). Aminosilanes such as aminopropyl trimethoxysilane (APTMS) and aminophenyl trimethoxysilane (APhTS) have shown promise for binding free amines to various nanoparticles and molecules to promote adhesion (Zhang and Srinivasan 2004; Zhang and Srinivasan 2005; Trouillon et al. 2007; Zhang and Srinivasan 2008).

Majewski and Fuchs (2007) and Wuister and Meijerink (2003), rather than coating surfaces with SAMs for the immobilization of nanoparticles, coated the nanoparticles themselves with monolayers. Wuister and Meijerink (2003) synthesized cadmium sulfide (CdS) quantum dots (2-6 nm diameter) capped with MPTS molecules. The free silanized ends of the capping molecules would allow for these nanoparticles to be encapsulated within a silicon shell. Majewski and Fuchs (2007), on the other hand, capped SiO_2 nanoparticles with MPTS to create hydrophobic SiO_2 nanoparticles. Theoretically, these hydrophobic particles could later be deposited onto metallic surfaces that have an affinity for the free thiol groups.

Bhat et al. (2003) made important discoveries relating to gradients within SAM coatings and their effect on the immobilization of gold nanoparticles. The study involved the vapor-phase

deposition of aminopropyl triethoxysilane (APTES). A gradient of APTES molecules was exhibited with increasing distance from the organic precursor source. This APTES concentration gradient allowed for a gradient of nanoparticle surface number density on the surface. This nanoparticle number density gradient has the potential to serve a number of applications, including the texturing of silicon surfaces for improved microstructure reliability.

2.7   Related research objectives

The previous works presented in this chapter have opened a door for integrating these techniques into MEMS industry-compatible surface modification processes. Based on these studies, the following related research objectives are proposed:

- Integrate the gas-expanded liquid nanoparticle film deposition process for MEMS and microstructures. Due to the liquid/vapor interface of an evaporating liquid, nanoparticles cannot be evaporated onto microstructure surfaces without detrimentally affecting the structures themselves. Therefore, the use of a GXL process to deposit nanoparticles and dry the microstructures may help avoid this interface and allowing for a nanoparticle-based surface modification that is compatible with the MEMS industry.

- Investigate the tribological effects of nanoparticle-based surface modifications on adhesion, friction and wear of microstructures. The tribology of nanoparticles on MEMS and microstructures is still a fundamentally new concept. Therefore, extensive research must be performed to determine if nanoparticle-based modifications are feasible for the MEMS industry. Such investigations will include the effect of various nanoparticle concentrations and the effect of particle number density on microstructure surfaces.

- Examine the effect of immobilizing nanoparticles onto MEMS and microstructures by means of self-assembled monolayers. SAMs have already been shown to drastically reduce adhesion and friction in microstructures with very minimal increases in surface roughness. By using these monolayers to immobilize nanoparticles on the surface, adhesion and friction may be further reduced or even eliminated.

- Examine the effect of superhydrophobic coatings on MEMS components. Couple durable, nanoparticle-roughened surfaces with low energy, fluorinated compounds to create extremely low surface energy surfaces to prevent adhesion and reduce interfacial phenomena in MEMS.

- Begin early stages of examining superhydrophobic surface coatings that couple nanoparticle-roughened surfaces with low energy thin films. Study the effect of surface roughness and asperity coverage on superhydrophobic nature of the coatings, as well as the durability of coatings.

CHAPTER 3

EXPERIMENTAL AND ANALYTICAL METHODS

In this chapter, general descriptions of experimental methods and analytical measurement techniques are presented and discussed. The experimental methods discussed include the synthesis and precipitation of gold nanoparticles, silicon substrate cleaning and preparation, and tribological testing. Analytical tools described in this section include film characterizations methods, microscopy techniques, and a test for durability utilizing water erosion.

3.1 Gold nanoparticle synthesis

Dodecanethiol-stabilized gold nanoparticles are synthesized by a two-phase liquid arrested precipitation process similar to that of Sigman et al. (2004). A 36-ml aqueous solution containing 0.38 g hydrogen tetrachloroaurate was combined with a solution of 2.7 g of the phase transfer catalyst tetraoctylammonium bromide in 24.5 ml toluene. After 1 h mixing, the aqueous phase was removed and discarded, leaving an organic phase containing gold ions. The organic solution was then combined with a 30-ml aqueous solution containing 0.5 g $NaBH_4$ which reduced the ions ground state gold atoms. The mixture was then mixed for 8-10 h to allow for particle formation and growth before the aqueous phase was discarded. 240 µl of 1-dodecanethiol was then added to the organic solution and mixed for 4 h in order to cap and stabilize the gold nanoparticles. The nanoparticle dispersion was then centrifuged with equal

parts ethanol at 4500 rpm for 5 min to rinse the particles of excess thiol and reducing agent molecules. After repeating the centrifugation step several times, the nanoparticles were dispersed and stored in n-hexane. This particle synthesis route produces polydisperse gold nanoparticles with an average diameter of about 5 nm. All chemicals were purchased from Alfa Aesar (Ward Hill, MA).

3.2   Gas-expanded liquid particle precipitation and supercritical drying

Within a large beaker of hexane, one test device chip consisting of tribological test microstructures (or one clean single-crystalline silicon wafer), was carefully placed upside-down on top of a 1.6-mm thick, 9.5 mm I.D. stainless steel washer inside of a 10-mm deep, 14.3-mm diameter glass vial. Samples were placed upside-down to avoid the deposition of large particle agglomerations that can no longer remain dispersed and fall onto the sample surface due to gravity, as shown in Fig. 3.1. This phenomenon will be discussed further in a subsequent section. The complete glass sample vial setup is illustrated in Fig. 3.2. This glass vial setup was then removed from the hexane-filled beaker, and hexane was carefully removed to a level just above the sample surface without allowing air to contact the sample. 25 μl of concentrated AuNP dispersion (in hexane) was then added to the vial and carefully mixed. The sample vial was then placed inside a 30-ml stainless steel high-pressure vessel, equipped with a quartz viewing window, a resistive temperature detector (RTD), heating rope, and pressure gauge. To prevent the rapid evaporation of the organic dispersion, approximately 400 μl of pure hexane was added alongside the sample vial to saturate the vessel headspace with organic vapor prior to sealing the vessel faceplate using Teflon o-rings. The complete experimental apparatus is illustrated in Fig. 3.3.
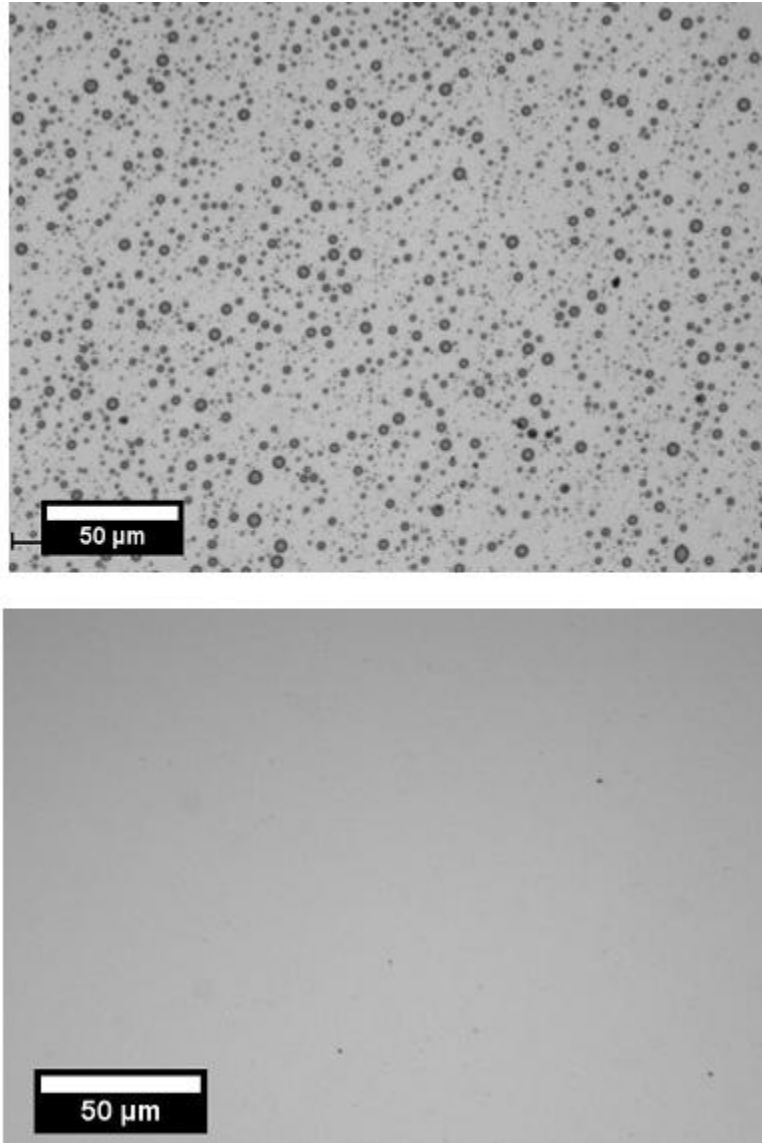
Figure 3.1. Optical microscope photographs illustrating deposition of
large, oily particle agglomerations; (a) 20X photograph of AuNPs
deposited on Si(100) with sample surface facing upwards; (b) 20X
photograph of AuNPs deposited on Si(100) with sample
surface upside-down.
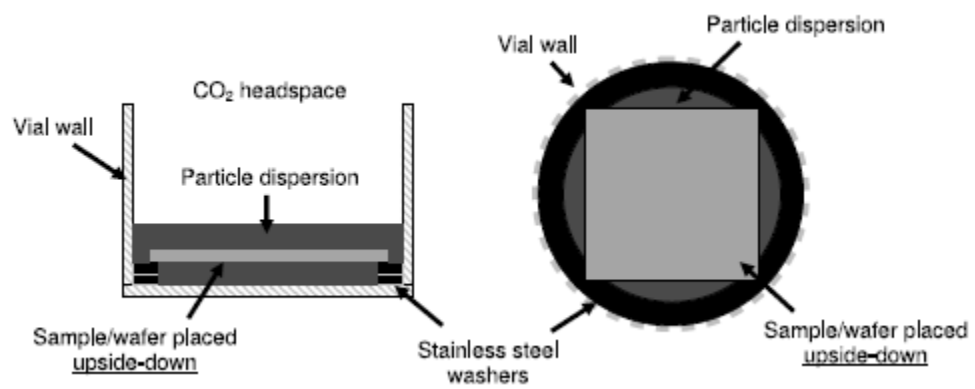
Figure 3.2. Side and top views of the glass sample vial used for GXL particle deposition.
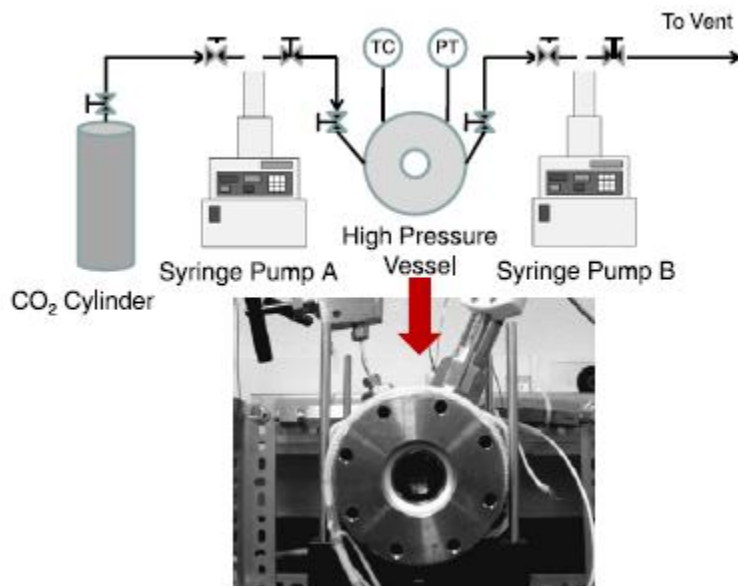
Figure 3.3. Illustration of the GXL particle deposition experimental setup including a photographic image of the stainless steel high-pressure vessel.

Once the high pressure vessel was sealed, the chamber was pressurized with CO_2 to approximately 23 bar at room temperature (22 °C), in equilibrium with a 500-ml Teledyne ISCO (Lincoln, NE) piston syringe pump. The chamber was then slowly pressurized, by setting the pump flow rate between 0.2 and 0.6 ml/min, up to the vapor pressure of the gas (ca. 58 bar at 22 °C). During pressurization, CO_2 dissolved into the organic phase, effectively expanding the volume of the liquid mixture and reducing the strength of the organic solvent. This reduction in solvent strength reduces the steric stabilization of the nanoparticles. Once the solvent strength was diminished below the threshold for stabilization, the particles began to precipitate out of solution. Dodecanethiol-stabilized gold nanoparticles in the size range of 3 to 7 nm typically precipitate within the pressure range of 34.5 to 55.2 bar (McLeod et al. 2005b).

Pressurization continued until the entire vessel chamber was filled with liquid CO_2, dissolving the organic solvent. The liquid mixture was heated isochorically to 40 °C to achieve a supercritical state. The chamber was then flushed with several volumes of pure supercritical CO_2 (at 40°C and ca. 90 bar) at a rate of approximately 0.5 ml/min to ensure the removal of the organic solvent. Following the purge of pure supercritical CO_2, the chamber was slowly depressurized (at 40 °C) by venting to the atmosphere (through a water bubbling system), and the dry, nanoparticle-coated sample was recovered.

Achieving the supercritical state is essential for the drying of the particle films and device chips. It provides a pathway from the condensed liquid phase to the vapor phase without crossing over the liquid-vapor interface boundary. By avoiding an interface, dewetting effects and capillary forces that can detrimentally affect both the quality of the particle film and microstructures are eliminated. Fig. 3.4 illustrates the pathway of the nanoparticle deposition process and drying on P-T diagrams. Fig. 3.4(a) represents the liquid-vapor (L-V) transition of

CO_2 (calculated using Peng-Robinson equation of state), including the pure CO_2 critical point and the binary mixture critical point of CO_2 and hexane. In the figure, the operating critical point for the CO_2/hexane binary mixture (0.991 CO_2 mole fraction) was estimated by performing a best-fit analysis to available experimental data (Liu et al. 2003).

In this work, the mole fraction of hexane in the system was about 0.01 (0.99 mol% CO_2). The labeled triangles represent the process conditions beginning at the initial condition A at 22 °C and atmospheric pressure. State B represents the endpoint of the isothermal pressurization up to ca. 58 bar. Heating to 40 °C increases the pressure to ca. 90 bar, state C, which is in the supercritical regime for a 0.009 mol% hexane binary mixture. Flushing of the system with several vessel volumes of pure supercritical CO_2 (at 40 °C and 90 bar) removes the excess solvent and returns the critical point to that of pure CO_2 as shown in Fig. 3.4(b). From state C, isothermal depressurization is now needed to safely reach state D (40 °C, atmospheric pressure) without crossing the liquid-vapor phase boundary, effectively preventing dewetting and capillary effects.

3.3   Silicon substrate and tribology chip preparation

Prior to the deposition of any films on silicon-based substrates or the testing of films on tribology chips, the samples first required cleaning and preparation techniques. 6-in Si(100) wafers (University Wafer, Boston, MA), diced into 1 x 1 cm squares, were used as platforms for film characterization. These silicon wafers are initially coated with a rough native SiO_2 layer. In order to prepare a smooth, uniform SiO_2 layer, the silicon substrates were first cleaned by immersion in HF (49%, Fisher Scientific) for 10 min which etches away native SiO_2 from the surfaces leaving behind hydrogen-terminated silicon. The samples were then copiously rinsed
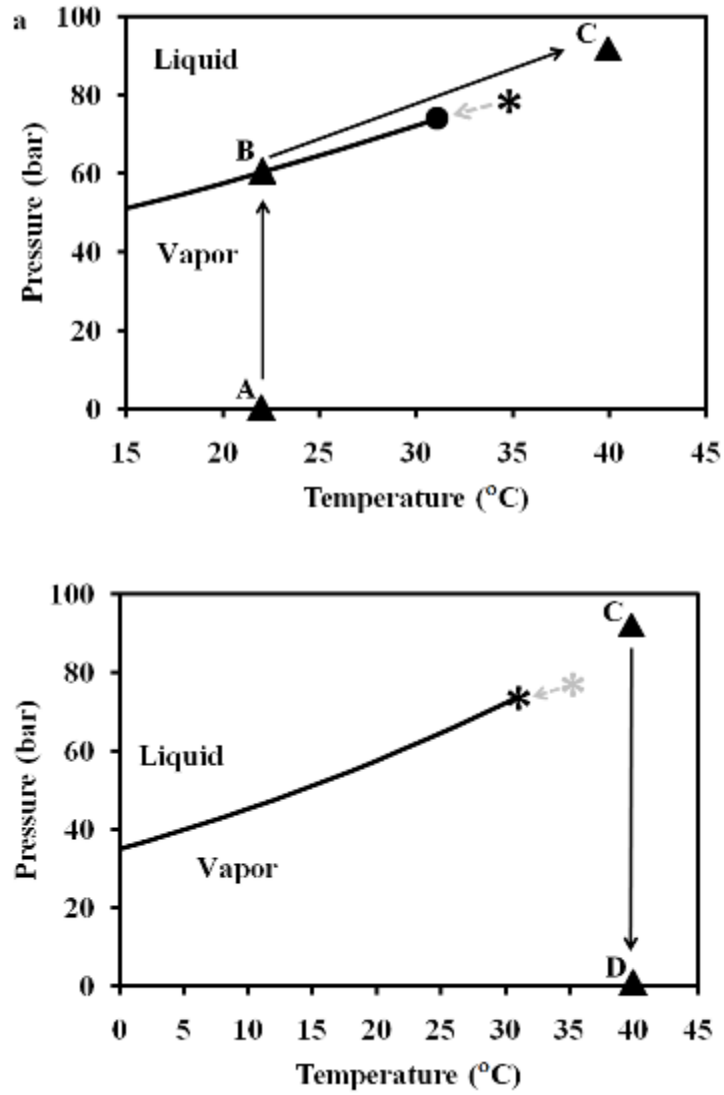
Figure 3.4. Liquid-vapor phase boundary for CO_2 showing the pure CO_2 critical point (●) and process operating critical point for a CO_2/hexane binary mixture (✻) estimated using available literature (Liu et al. 2003).

with DI water and dried under a stream of nitrogen. Substrates were then subjected to O_2-plasma at 25 W and 260 mTorr (O_2) partial pressure for 5 min which allowed for a uniform, thin layer of SiO_2 to form on the surface. The two steps were then repeated to ensure the formation of a very uniform and smooth SiO_2 layer. This preparation method also serves to remove any residual organics from the silicon surfaces. Following this cleaning step, the samples were washed with DI water and dried under a stream of nitrogen gas.

In the case of silicon or polysilicon microstructures and tribology chips, the pre-fabricated devices required a releasing procedure which would remove sacrificial layers and release the test structures. First, the sacrificial layers were etched in a 1:1 (v/v) HF (49% wt%)/HCl (36 wt%) solution for varying times depending the fabrication process and the sacrificial layer thickness. The chips were then rinsed by a serious of DI water rinses, without being exposed to ambient air, until the residual HF was effectively removed and the pH became neutral. Next, the chips were transferred to a 1:2:12 (v/v/v) NH_4OH (30 wt%)/H_2O_2 (30 wt%)/H_2O "descumming" solution heated to 70 °C. This solution cleaned the device chips and facilitated the formation of a very thin, uniform SiO_2 layer. After being submerged in the "descumming" solution for about 15 minutes, the chips were carefully transferred to 30 wt% H_2O_2 heated to 70 °C and then rinsed with DI water until the pH once again became neutral. The chips were then rinsed with electronic grade isopropanol and *n*-hexane, and then stored in vials of *n*-hexane until they could be supercritically dried for analysis.

3.4   Tribology chip actuation and testing

Tribology chips are fabricated microstructure chips that contain devices to measure various tribological properties such as work of adhesion, coefficients of friction, stiffness, and

resonance frequency. In this work, two different tribology chips were used to analyze the effectiveness of nanoparticle-based surface modifications and coatings. Polysilicon tribology chips fabricated at Sandia National Laboratories (Albuquerque, NM) were utilized to measure apparent work of adhesion via in-plane cantilever beams. Tribology chips were also fabricated in-house with silicon-on-insulator (SOI) wafers which produce very smooth Si(100) in-plane surfaces. These tribology chips included in-plane cantilever beams, friction testers and mass resonance frequency testers. The following subsections will describe the tribological devices used in this work and how they are actuated to quantify film properties.

3.4.1   In-plane cantilever beams

Release and in-use stiction is typically characterized and evaluated by a commonly used cantilever beam array (CBA) technique (Mastrangelo 1997; Mastrangelo and Hsu 1992; de Boer and Michalske 1999; Jensen et al. 2001; Ashurst et al. 2001b). Cantilever beams are very mechanically simple structures which are easily fabricated by surface micromachining methods. Fig. 3.5 presents a cantilever beam array fabricated at Sandia National Laboratories using their standard surface micromachining process called SUMMiT V^{TM} (de Boer et al. 1998). This particular CBA consists of 18-μm wide and 2.5-μm thick cantilever beams with one anchored side and one free-standing side. The beams range in length from 150 to 900 μm (50 μm increments) and rest about 2 μm above the underlying substrate.

The CBA presented in Fig. 3.5 is actuated electrostatically by placing tungsten probe tips to the ground and actuation pads. By applying a voltage to the actuation pad, the beams in the array begin to deflect towards the substrate. Each beam initially makes contact with the substrate at the tip and, with increasing applied voltage, will make increased contact based on the overall
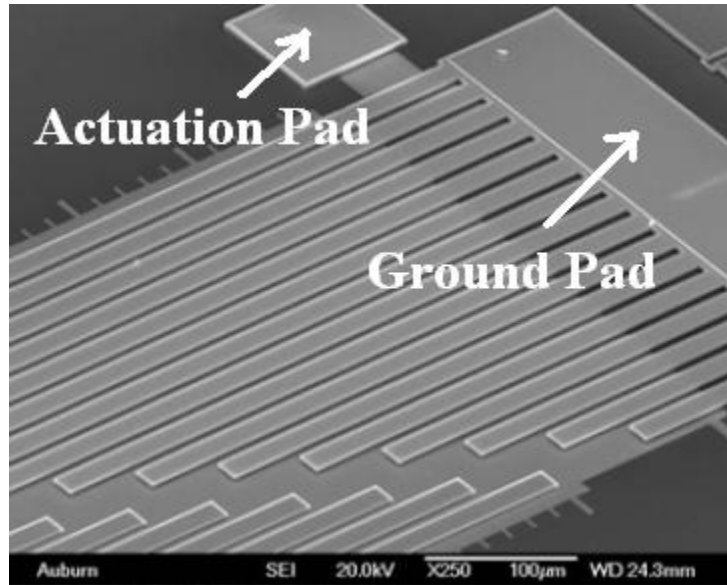
Figure 3.5. Polysilicon in-plane cantilever beam array fabricated by

Sandia National Laboratories.

beam length. This means that for a given electrostatic load longer cantilever beams will exhibit higher real contact areas with the underlying substrate than will shorter beams. In this work, these polysilicon CBAs were actuated by increasing the electrostatic load from 0 to 120 V in 10 V increments, followed by an unloading in 10 V increments back to the 0 V (unloaded) state. Following this actuation, it could be determined which cantilever beams were permanently adhered to the substrate.

CBAs were also fabricated in-house on SOI wafers which, due to the very smooth Si(100) in-plane surfaces, exhibit much greater adhesion. Fig. 3.6 presents a CBA comprised of 1000-μm long cantilever beams with nominal widths and thickness of 30 μm and 2 μm, respectively. In this case, the cantilever beams in the SOI CBAs were actuated manually by carefully pressing down on individual beams with a very fine tungsten probe tip.

Following actuation, long working distance interferometry was performed using a modified EM Optomechanical 622A interferometer in order to quantify the adhesion of cantilever beams. Interferometry procedures allow for the conversion of pixel intensity versus pixel position into vertical beam position versus horizontal beam position data with an accuracy of about 10 nm (Hariharan et al. 1987; de Boer and Michalske 1999). Fig. 3.7 presents an interferogram of a CBA illustrating how various beam shapes can be observed based on the interference fringe pattern. From such images, experimental beam profile data can be extracted as shown in Fig. 3.8. From this experimental data, the apparent work of adhesion between the substrate and the adhered cantilever beams can be quantified using a new method discussed in Chapter 4.
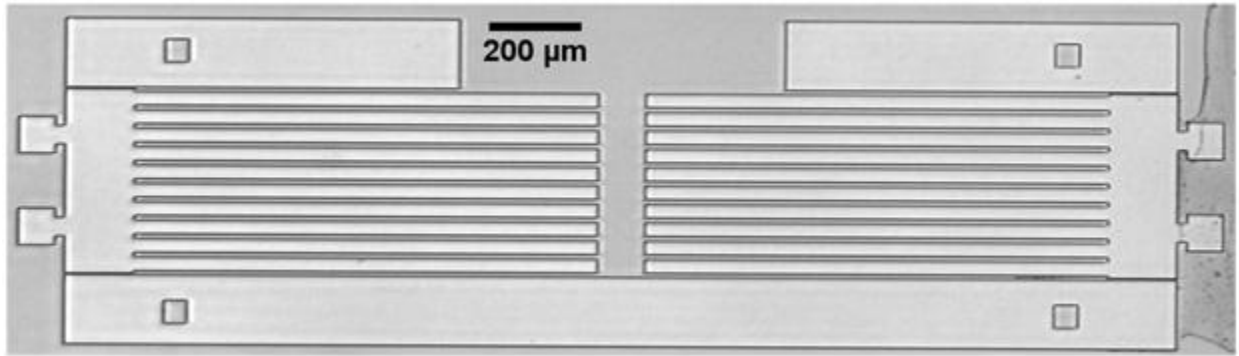
Figure 3.6. 1000 μm long CBA fabricated on an SOI wafer with

very low in-plane inherent roughness.
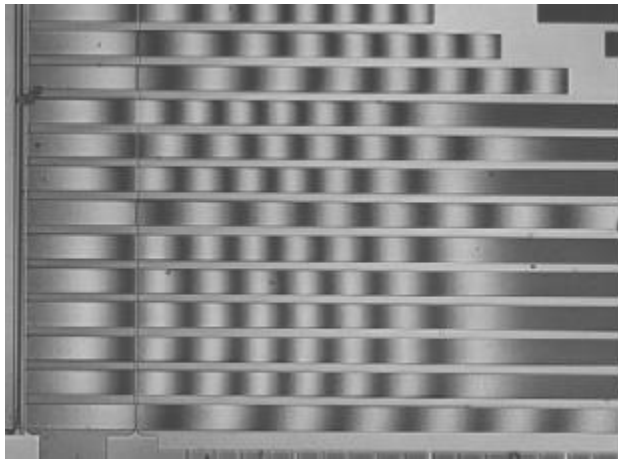
Figure 3.7. Interferogram illustrating various interference fringe patterns.
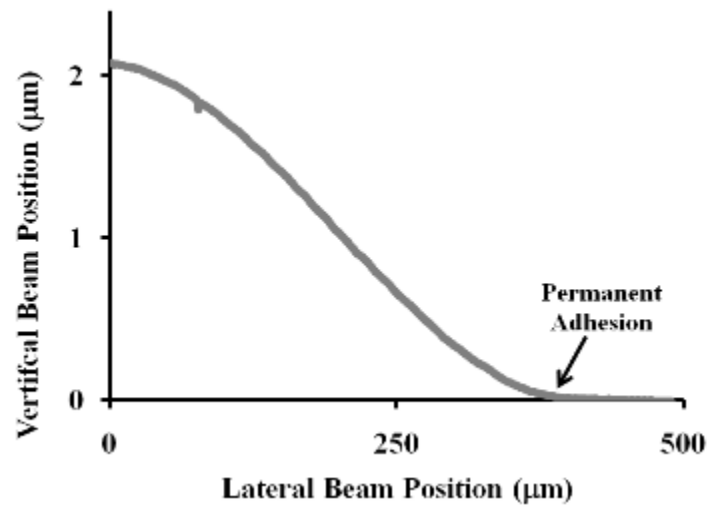
Figure 3.8. Example of experimental beam profile data collected via interferometry.

3.4.2 Friction testers and mass resonators

The SOI tribology chips also consisted of devices used to measure static coefficients of friction (μ_s) and resonance frequency (f_R). Fig. 3.9 presents a side-wall friction and adhesion tester. When the larger of the two comb drives is actuated, a normal force is applied against the surface of a small tab (see inset). The second comb drive then applies a tangential frictional force by rubbing the two components. The known applied normal force (N) and the frictional force (F), between the two contacting surfaces, are quantified interferometrically combine to give the coefficient of static friction following:

$$\mu_S = \frac{F}{N} \tag{3.2}$$

The frictional force is determined using a stick-slip technique that occurs when the force caused by the tangential comb drive can overcome the friction and adhesion caused by the normal load.

Fig. 3.10 presents a mass resonator which is used to quantify additional mass that has been added to the device chips. In terms of this work, these devices were used to quantify the coverage or number density of nanoparticle coatings. The resonators are actuated by applying a voltage to each comb drive. The middle beam of the device begins to resonate and the resonance frequency is measured. Based on changes in the mass frequency, the total effective mass (M_{eff}) is calculated following:

$$f_R = \frac{1}{2\pi} \sqrt{\frac{k_x}{M_{eff}}} \tag{3.3}$$

where k_x is the material spring constant.
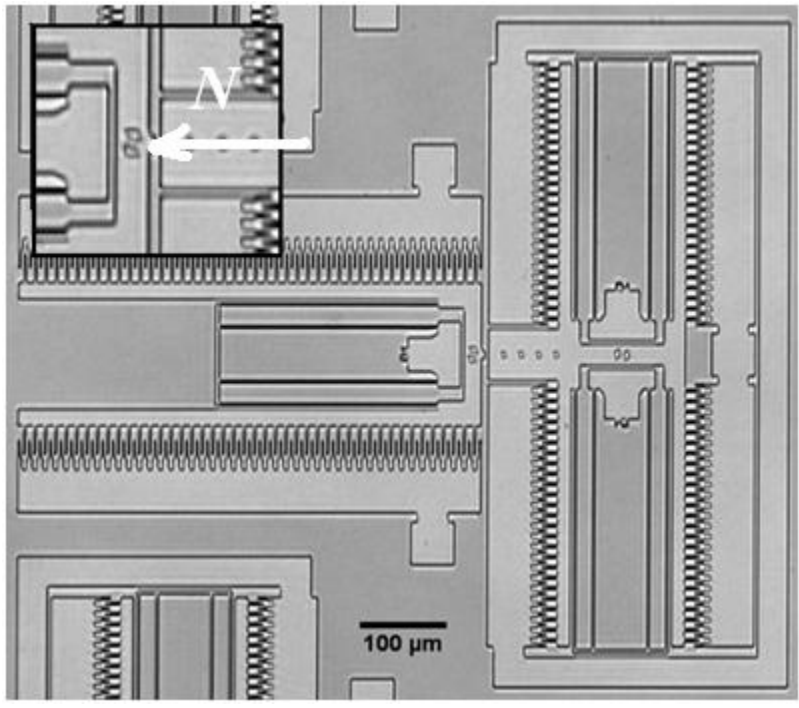
Figure 3.9. Image of a side-wall static friction tester. Inset depicts a normal force (*N*)

acting on a moveable structure.
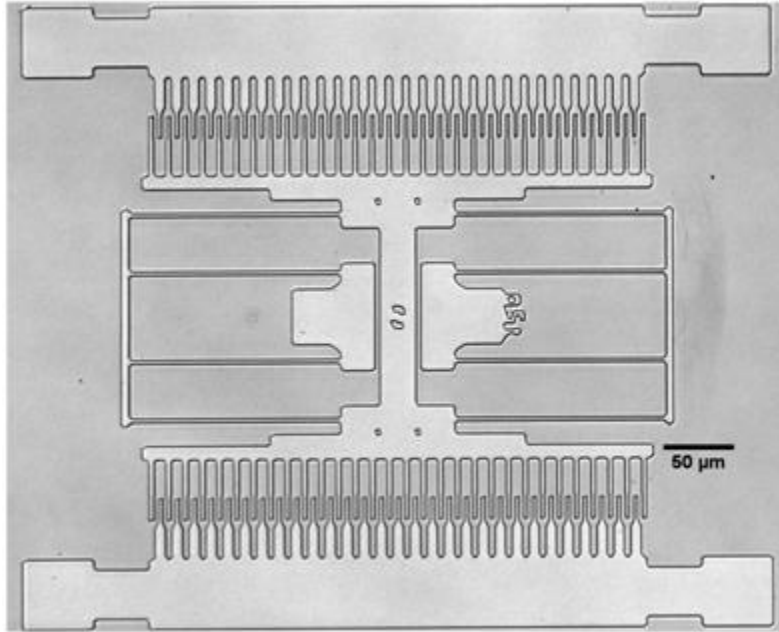
Figure 3.10. Image of a mass resonator device.

3.5 Contact angle analysis

The hydrophobic nature of deposited films on silicon substrates was analyzed using a Rame-Hart Instrument Co. standard goniometer (model 200-00-115). Fig. 3.11 presents a photograph of the goniometer setup. The setup consists of a CCD digital camera, a backlight source, a moveable sample stage, and a liquid injection syringe calibrated to deliver controlled liquid drop sizes to the sample surfaces. The contact angle is the angle at which a liquid/vapor interface (typically the water/air interface) meets a solid surface. The contact mechanism arises from the thermodynamic equilibrium between the three phases present: the droplet liquid phase (L), the solid substrate phase (S), and the ambient vapor phase (V). Fig. 3.12 illustrates how the contact angle arises from the interfacial energies existing between all three phases present (Kwok et al. 1997). Following the Young Equation, given by (Eqn. 3.4), the contact angle (θ_C) can be calculated from the surface energies present at the solid-vapor interface (γ_{SV}), the solid-liquid interface (γ_{SL}), and the liquid-vapor interface (γ_{LV}) (Zisman 1964):

$$\gamma_{LV} \cos \theta_C = \gamma_{SV} - \gamma_{SL}. \tag{3.4}$$

DROPimage software developed by Rame-Hart images liquid droplets on the substrate surfaces (in ambient conditions) and profiles the droplet to measure the angles of contact. Fig. 3.13 presents a screen shot depicting a water droplet on a SAM-coated substrate yielding a mean contact angle of 105.5°. Hydrophilic surfaces which have high surface energies will result in water contact angles < 20°. SiO_2 surfaces are very hydrophilic and will often result in contact angles that are unreadable because the water droplet completely wets the surface. Surfaces with lower surface energy and exhibit hydrophobic nature will yield contact angles of about 90°.

Figure 3.11. Photograph of a Rame-Hart standard goniometer for contact angle analysis.
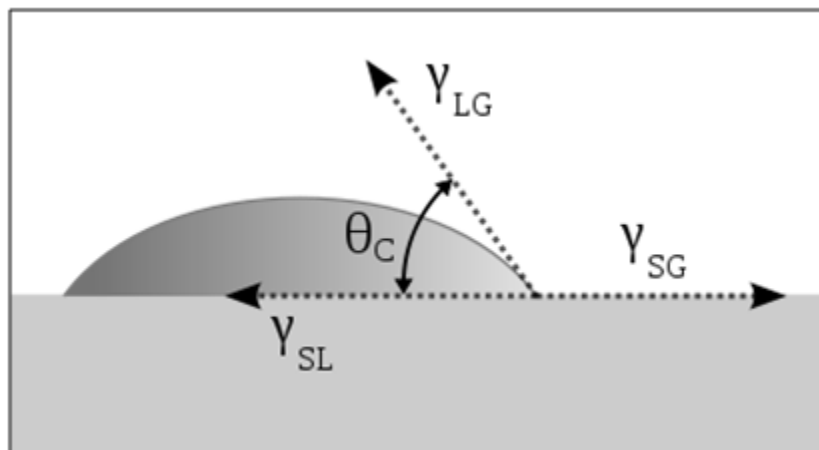
Figure 3.12. Definition of the contact angle given by vectors representing the

interfacial energies between the solid, liquid, and vapor phases.
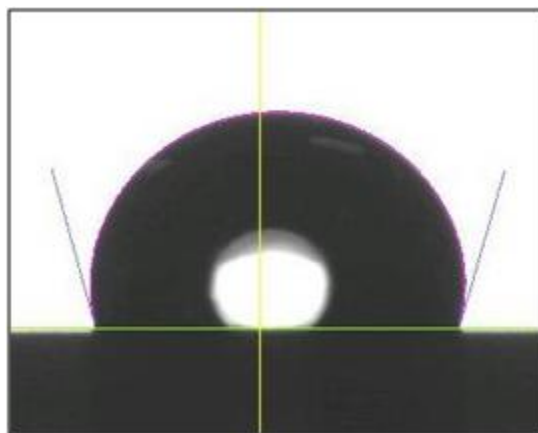
Figure 3.13. Screenshot from DROPimage software depicting the

measurement of contact angles.

3.6 Ellipsometry

A Rudolph Research ellipsometer equipped with a 1 mW (max) HeNe laser and Auto EL III software was utilized to measure the thickness of SiO_2 and organic thin films. Electromagnetic radiation emitted from the laser light source impinges the reflective sample surface and reflected radiation passes to an analyzer and detector, as illustrated in Fig. 3.14. From the reflected radiation, the ellipsometer measures the reflection amplitude ratio (ψ) and the phase shift (Δ) (Ohlidal and Franta 2000). The ellipsometry software then models these two parameters, using the refractive index (n) of the film, to determine the film thickness by an iterative procedure. In this work, the refractive index of SiO_2 and organic SAM films are both equal to 1.463. Therefore, to accurately measure the thickness of deposited SAMs on SiO_2 coated substrates, reference SiO_2 thicknesses must also be measured to correct the SAM thickness measurement data. The Auto EL III software can measure film thicknesses between ranging from 10 Å to 3.0 μm with an accuracy of ±3 Å. The repeatability of the system is within 1%. In addition, if the approximate film thickness or refractive index is known, the software can iteratively calculate both optical properties as long as the initial guess is within reasonable range.

3.7 Fourier transform infrared spectroscopy

Infrared spectroscopy studies the interaction of infrared light with a surface. Fourier transform infrared spectroscopy (FTIR) splits the beam of light, measuring the optical path difference between a direct beam and a beam reflected from the sample. The resulting data produces a spectrum typically in the wavenumber range between 400 and 4000 cm^{-1}. Attenuated total reflectance (ATR) is a specialized FTIR technique which is typically used to obtain the spectra of solid, liquid and thin film samples. ATR utilizes a crystal made from an infrared
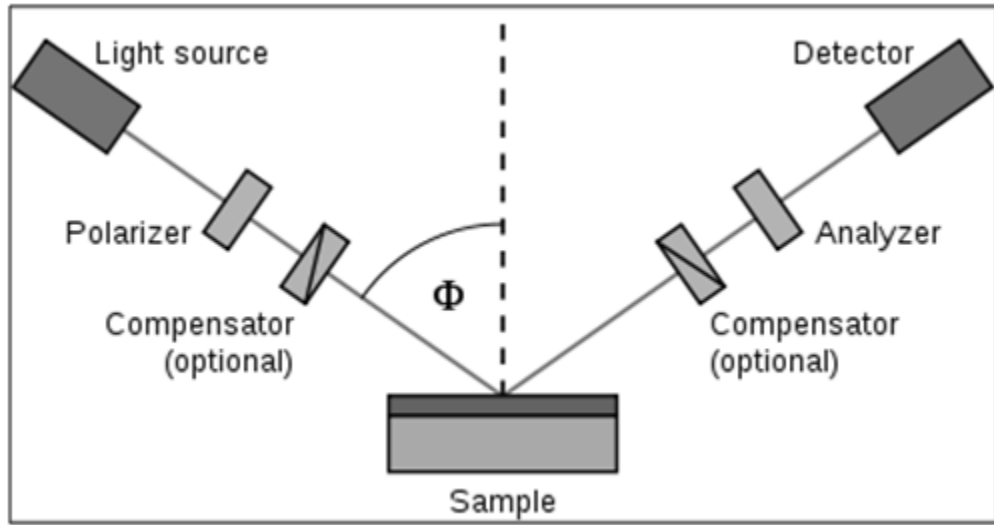
Figure 3.14. Illustration of a light source impinging a sample

surface and reflecting to the ellipsometer detector.

transparent material, such as zinc selenide (ZnSe), with a high refractive index. When the infrared beam is lined up with the proper angle of incidence, the beam passes into the crystal and then bounces between the highly refractive crystal surfaces before exiting the other side towards the detector. Fig. 3.15 illustrates the total internal reflection of an infrared beam through an ATR crystal. A solid or liquid sample can be placed on one (or both) of the ATR crystal surfaces, as shown in Fig. 3.15. As the infrared beam penetrates the crystal surfaces, an evanescent wave of radiation is created, which penetrates a short distance beyond the crystal surface. This evanescent wave then contacts and interacts with the sample. Infrared radiation is absorbed by the sample and the infrared spectrum is detected when two split infrared beams are compared.

The interactions detected by ATR-FTIR correspond to various resonant frequencies which match the vibrational frequencies of specific bonds. Such vibrations between atoms include symmetrical and asymmetrical stretching, rocking, and wagging. Each type of vibration can be detected at varying wavenumbers. For instance, C-H stretching modes can be detected in the 2800-3400 cm^{-1} region while C-H bending peaks are found closer to 1000 cm^{-1}. Fig. 3.16 presents a chart of wavenumbers illustrating where particular bond energies absorb infrared radiation. Based on this information, it is possible to analyze samples to determine what atoms or molecules are present, if reactions have taken place, or determine if any additional changes in chemistry have occurred.

3.8 Microscopy

Various microscopy methods were utilized in this work to analyze nanoparticles and nanoparticle films on various substrates. Along with basic optical microscopy at magnifications
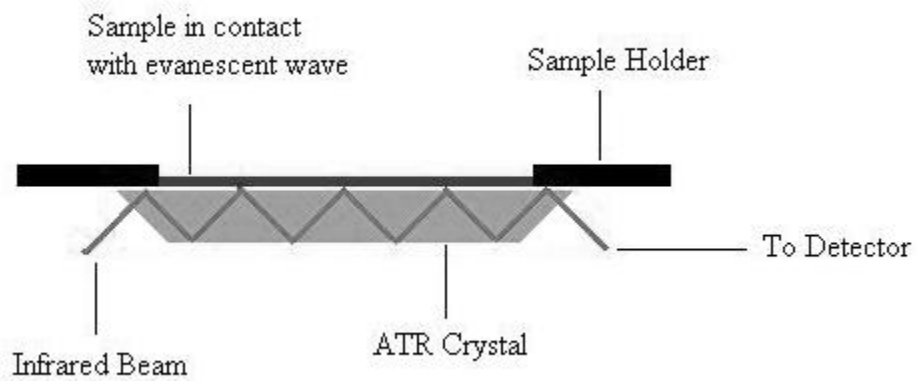
Fig. 3.15. Schematic of an infrared beam penetrating an ATR crystal, undergoing total internal

reflection, and exiting the crystal towards the detector.
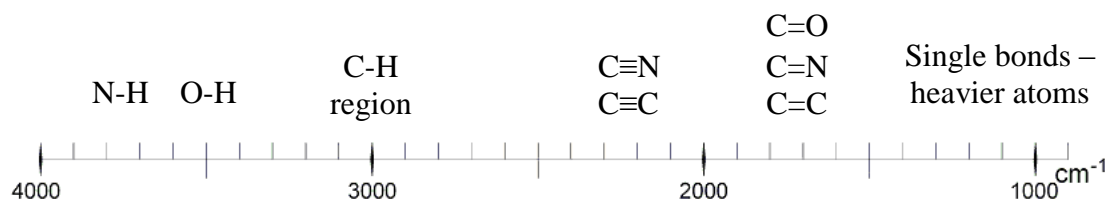
Fig. 3.16. Chart giving approximate wavenumber regions for various types of bonds.

of 10X and 20X, such techniques as transmission electron microscopy (TEM), scanning electron microscopy (SEM) and atomic force microscopy (AFM) were also utilized. The following subsections briefly discuss these advanced microscopy techniques and how high resolution imaging is achieved.

3.8.1   Transmission electron microscopy

The transmission electron microscope (TEM) is related to the common compound light microscope, with the exception that it takes advantage of shorter wavelength illumination emitted by an electron beam (Watt 1997). Images are produced by transmitting an electron beam through a very thin sample. As the beam interacts with the sample, depending on the properties and the chemical make-up, electrons will adsorb onto the sample surface while electrons surrounding the sample pass straight through. This interaction between the electron beam and the thin, solid sample creates a transmitted beam which contains information about the electron density and the phase of the object. This information is utilized to create an image of the sample which is typically recorded by taking a photograph of the imaging surface. Fig. 3.17 presents a schematic drawing of a transmission electron microscope.

Following imaging, the collected photograph negatives are digitally scanned and analyzed via imaging software. Setting the scale of the images and sizing of particles or other samples in the scanned TEM images is done using ImageJ software following a procedure developed by Kitchens (2004). The scale of scanned images is set using Eqn. (3.5),

$$\delta = \frac{M\delta_S}{3.936 \times 10^{-8}} \qquad (3.5)$$

where δ is the scale resolution (pixels/nm) for image analysis, δ_S is the scan resolution (pixels), and M is the magnification of the image. Fig. 3.18 presents a scanned TEM negative film of
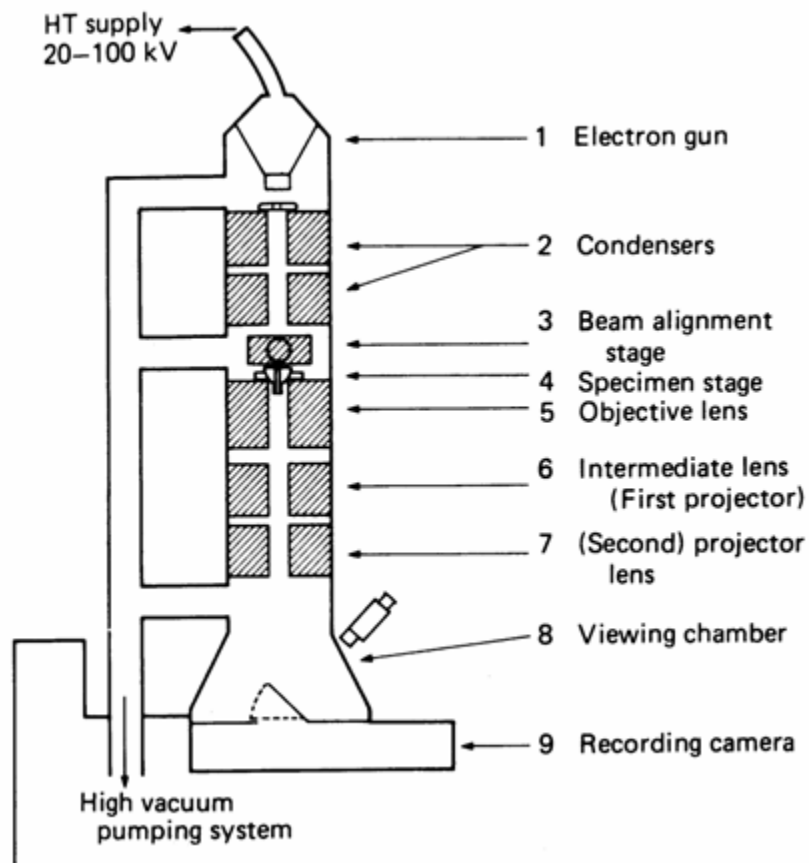
Figure 3.17. Schematic diagram of a transmission electron microscope (Watt 1997).
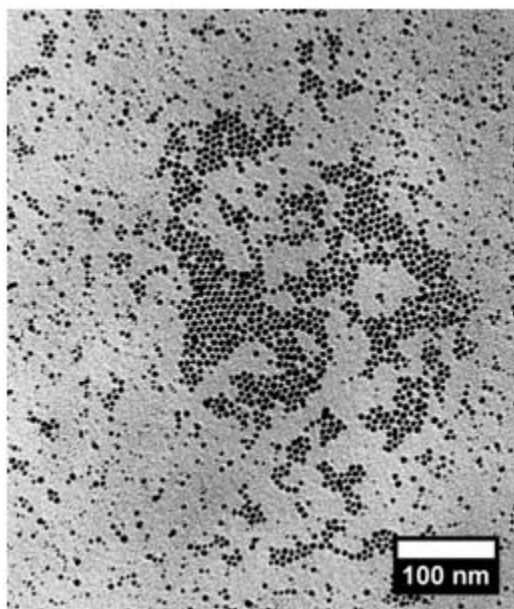
Figure 3.18. TEM image at 100,000X of Pd nanoparticles.

palladium (Pd) nanoparticles deposited onto the thin TEM sample holder imaged at a magnification of 100,000X. The scale resolution, using Eqn. (3.5), for a 100,000X TEM image scanned at a resolution of 720 pixels is 2.834 pixels/nm. Setting this scale in the software makes it possible to accurately size samples in the image, such as spherical nanoparticles shown in Fig. 3.18.

3.8.2   Scanning electron microscopy

Scanning electron microscopes (SEM) impinge a sample surface with a high-energy electron beam which scans across the surface is a raster-type pattern. The impinging electron beam, after penetrating the sample surface, produced secondary electrons and back-scattered electrons containing information about the chemical make-up and topography of the sample to a detector. These signals result from the atomic interactions that occur at the sample surface. SEMs are capable of producing images up to 500,000X magnification with a resolution revealing details of less than 1 nm. Fig. 3.19 presents a schematic diagram of a typical scanning electron microscope. The small, scanning electron beam allows for three-dimensional imaging as shown in Fig. 3.20, which presents an SEM image of a single-walled carbon nanotube (SWNT) forest (Hata et al 2004). For the purpose of image analysis using Image J, a relation for the image resolution (pixels/μm) yields a linear relationship with the magnification of the SEM instrument following:

$$\delta = 0.0106M \tag{3.6}$$

where δ is the scale resolution (pixels/μm) and M is the image magnification.
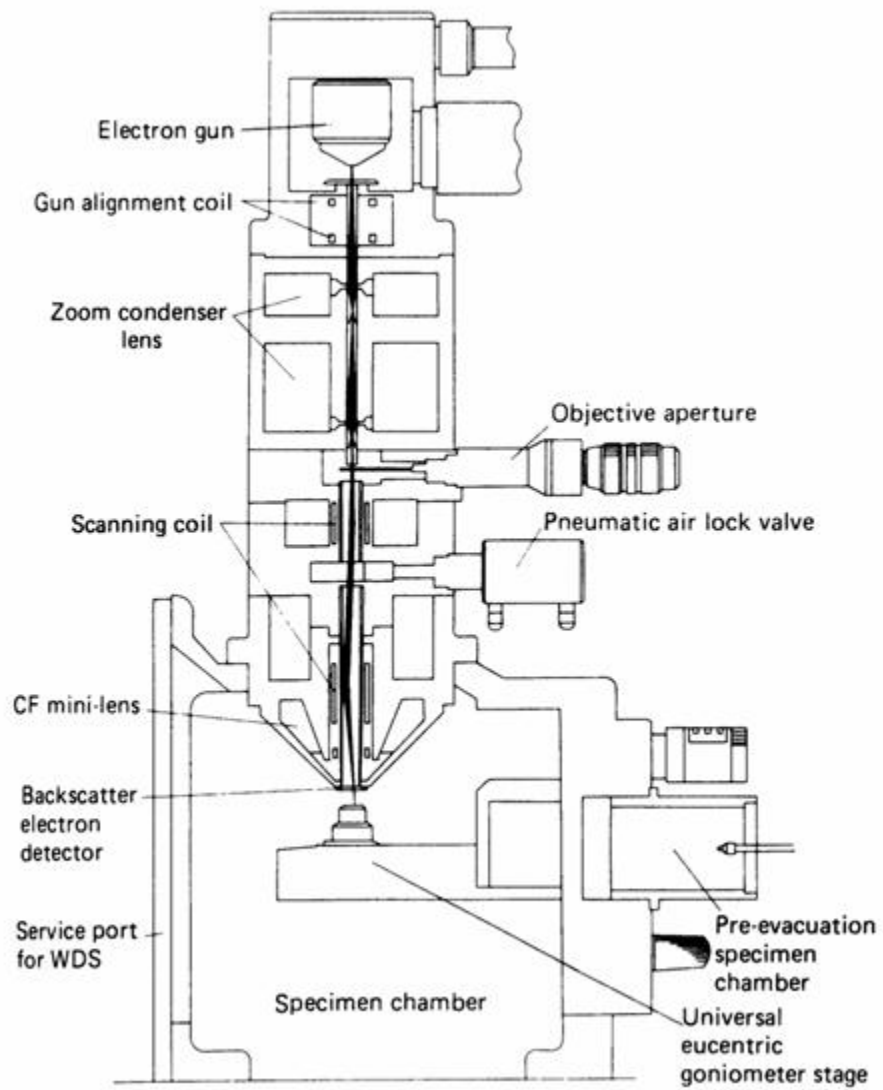
Figure 3.19. Schematic illustration of a scanning electron microscope (Watt 1997).
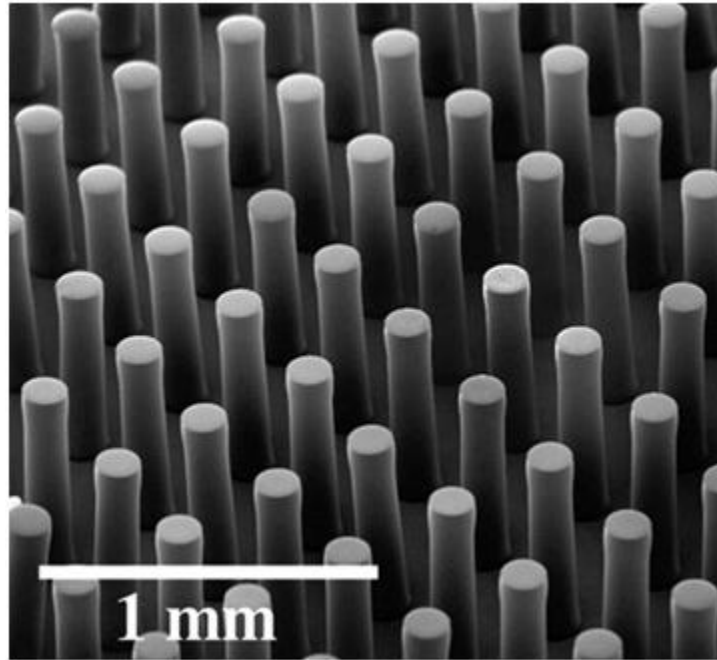
Figure 3.20. SEM image of a carbon SWNT forest (Hata et al 2004).

3.8.3   Atomic force microscopy

Atomic force microscopy (AFM) is a type of scanning probe microscopy (SPM) which allows for extremely high-resolution imaging of surfaces. The AFM can image surface features at the nanoscale by information gathered while scanning the surface with a mechanical probe. The AFM utilizes a cantilever with a small probe tip at its end which is used to scan the surface of a specimen. When the tip is brought into proximity of a sample surface, forces between the tip and the sample lead to a deflection of the cantilever. The deflection is measured by a laser reflected from the cantilever tip to a photodiode detector. A feedback mechanism is employed to adjust the tip-to-sample distance while scanning in order to maintain a constant force between the tip and sample in order to avoid collisions between the probe and surface topography which may exist. A simple schematic diagram of this feedback scanning process is illustrated by Fig. 3.21. AFM imaging holds the advantage over SEM imaging of topographically mapping a surface at a high resolution comparable to TEM imaging, without requiring an ultra-high vacuum environment.

3.9   Water erosion durability testing

Typical techniques for quantifying the durability of thin films utilize probes which scratch the surface while measuring the force required remove the film from the substrate material. However, such measurements either require specialized equipment or time and money to outsource samples to a third party. In order to quantify the durability of thin films in this work, a unique water erosion technique was employed which correlates directly with scanning indenter probe wear data. The water erosion testing was performed by dropping water at a rate of approximately 2 drops per second onto a 45° inclined surface from a height of 18 in. At this
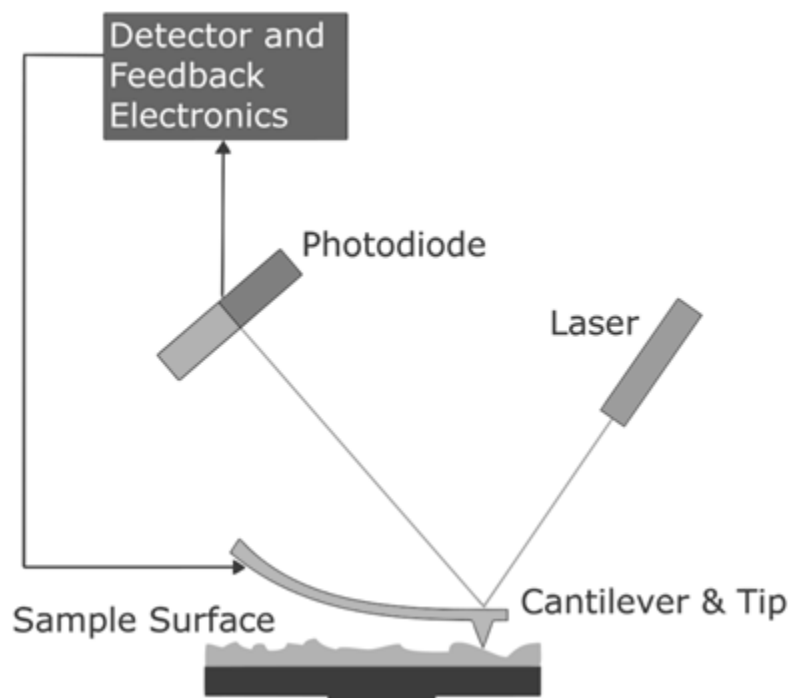
Figure 3.21. Schematic diagram of AFM scanning feedback process.

height, the velocity of each droplet when it hits the surface, following Eqn. (3.7) where g is gravitational acceleration, is 3.0 m/s.

$$v_y = \sqrt{2gh} \qquad (3.7)$$

The force of impact of the droplets on the surface was not important to the correlation, but was simply estimated as 490 μN per drop following:

$$F_g = mg \qquad (3.8)$$

where m is the droplet mass (5.0 x 10^{-5} kg for a 50 μl drop).

Water droplets were impinged on the film-covered substrates for periods of several hours, after which the contact angles of the films were measured. If the contact angle of a particular film remained unchanged, the water erosion testing was continued for several more hours. However, if the film experienced a significant decrease in contact angle after H number of hours of water erosion, the film was said to have a water erosion time of H which corresponds to some total force experienced by the surface which significantly degraded the film.

A correlation between film durability and water erosion time (H) was developed utilizing scanning indenter probe wear data provided by Hysitron (Minneapolis, MN). Several silicon substrates coating with various superhydrophobic coating recipes were analyzed by scratching the films under known normal forces. The scratched areas were also imaged via AFM to determine the normal force required to completely remove the coating from the substrate. This normal force can be equated to the force being exerted between the substrate and film in order to keep the film intact. Fig. 3.22 presents an AFM image of a film subjected to scanning wear forces between 20 and 25 μN. The figure illustrates that when a force of about 22.5 μN was used to scratch the surface, the film was completely worn away from the substrate. The normal forces obtained during the scanning wear tests were directly compared with water erosion test
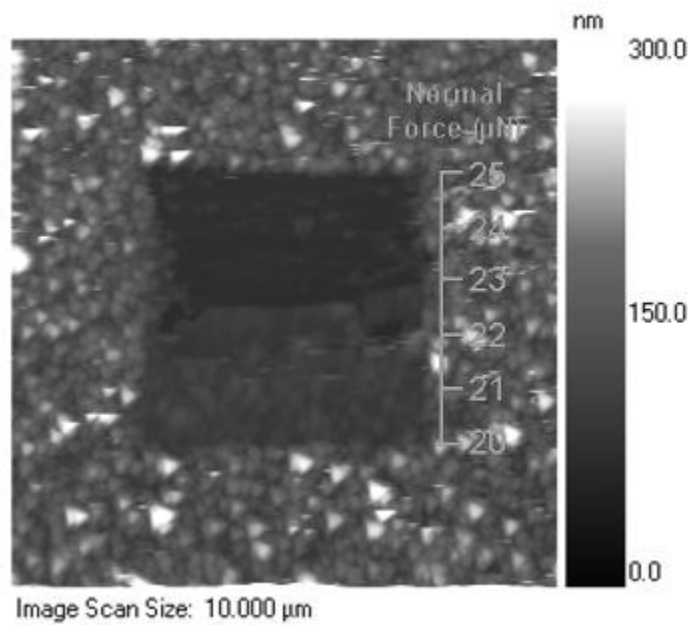
Figure 3.22. Hysitron AFM image depicting film durability up to 22.5 µN normal force.

results on the same superhydrophobic coatings. Table 3.1 presents scanning wear data and water erosion times for a number of superhydrophobic coating recipes.

It was hypothesized that if the water drop rate and size was assumed to be constant, the sum of the forces impinged on a surface by the droplets over a given period of time would be linear regardless of the film properties. Therefore, it was expected to see a trend between the force required to remove films from a substrate (Hysitron data) and the water erosion time required to reduce the contact angle. Fig. 3.23 plots the Hysitron wear data and water erosion times for each recipe given in Table 3.1. The figure illustrates that there is an obvious trend between water erosion time and the scanning wear data – the normal force required to scratch off the coating. In order to further examine the relationship, Fig. 3.24 plots the scanning wear directly as a function of water erosion time. The figure shows that there is a direct relationship between water erosion time and scanning wear force. The R-squared fit of the trend line is 88%, which is accurate enough to confirm that the trend exists.

A newer water erosion apparatus has also been developed which utilizes a Waterpik® WP-100 Ultra Water Flosser which has been retrofit with a 20-L water carboy, as shown in Fig. 3.25. The water flossing unit can provide a water pressure between 5 and 90 psi. At the lowest pressure setting of 5 psi, the water jet velocity out of the 0.1016 cm diameter nozzle is 3.4 m/s. The force of the water jet leaving the nozzle, estimated as

$$F_y = \rho A v_y^2 \tag{3.9}$$

where F_y is the water jet force, ρ is the density of water, A is the nozzle area (8.11×10^{-7} m^2), and v_y is the velocity in the y-direction (aimed straight down at the surface). Based on a volumetric flow rate measured experimentally, the water jet force is on the order of 9400 μN – nearly 20 times more than the force implied by water droplets. The hypothesis for this new apparatus is

Coating name	Average Hysitron scanning wear (μN)	Water erosion time (h)
Recipe A	2	0.25
Recipe B	4.5	0.5
Recipe C	6	0.5
Recipe D	6	3.3
Recipe E	10	10
Recipe F	10	22.5
Recipe G	15	42
Recipe H	18.5	80
Recipe I	22.5	100

Table 3.1. Scanning wear data and water erosion time for various coatings.
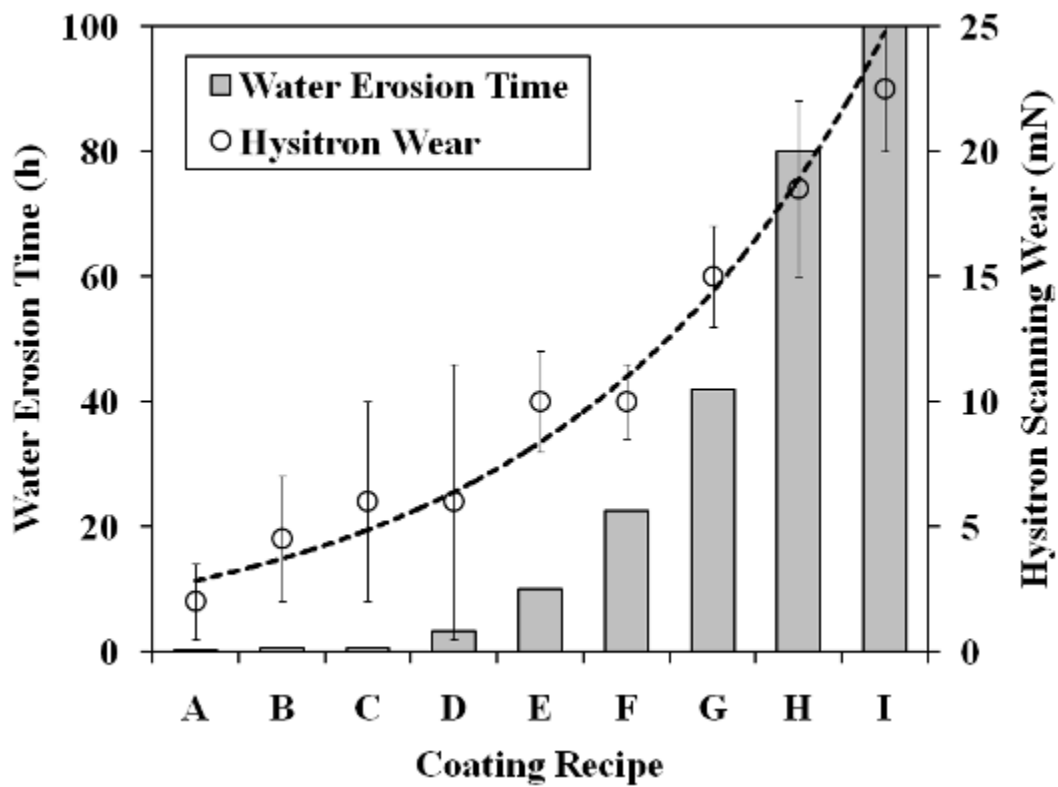
Figure 3.23. Water erosion time and Hysitron wear data for various

superhydrophobic film recipes.
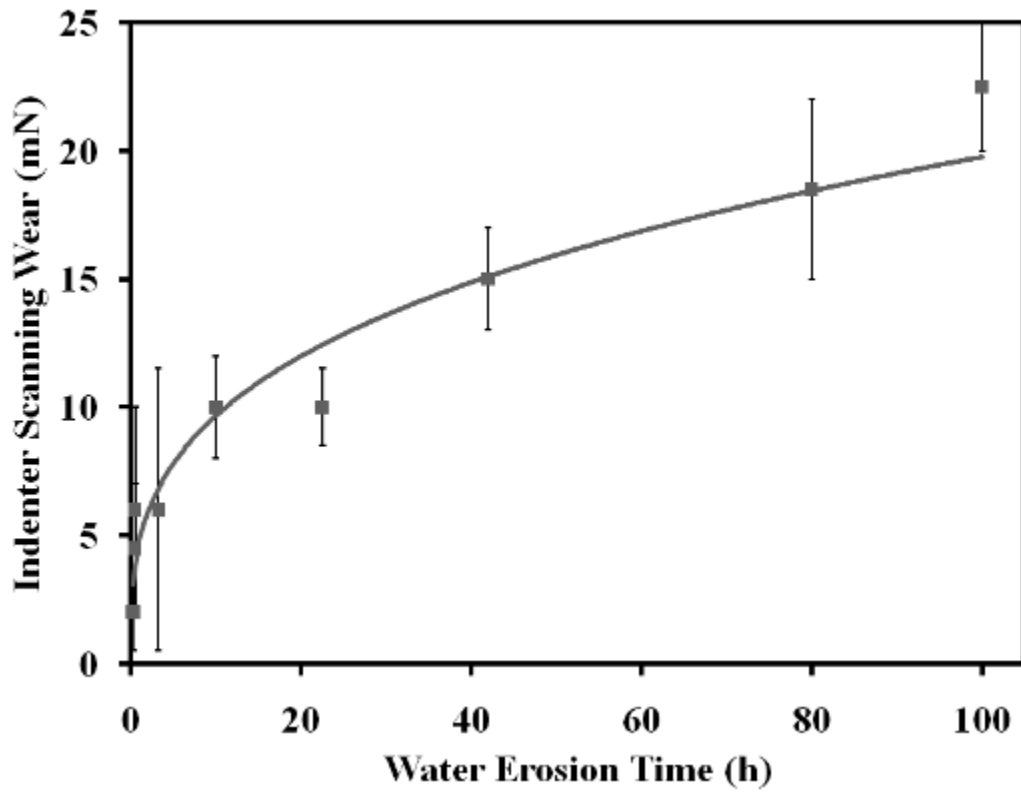
Figure 3.24. Trend between water erosion time and scanning wear force.

Figure 3.25. Photograph of the new Waterpik® water erosion apparatus.

that similar film durability data can be collected in less time – minutes as compared to hours of water erosion. Fig. 3.26 shows the water erosion time (with standard deviations) utilizing this new apparatus for four randomly selected superhydrophobic coatings. The exact recipes used to produce the four coatings are unknown, however, Coating D is required multiple days of water erosion using the drop-wise apparatus. The results in Fig. 3.26 indicate that repeatable water erosion times can be achieved using this new apparatus and the time required is significantly reduced from 80+ h down to less than 20 min.

3.10 Surface coverage image analysis

In several upcoming chapters, it was desired to determine how much of a surface is covered by nanoparticles deposited using the GXL particle deposition process. This was accomplished by determining the fractional surface coverage – or the fraction of substrate surface area coated by a nanoparticle film – utilizing simple techniques in ImageJ image analysis software available for free download on the internet from the National Institutes of Health. In this work, version 1.40g was used.

First, a grayscale image (such as a digital SEM micrograph) is opened in the software. The scale of the image is set following Eqn. (3.6) by selecting Analyze → Set Scale. This will tell the software how many microns are represented by each pixel in the image. Next, following any necessary cropping of the image, thresholding is performed by selecting Image → Adjust → Threshold. The threshold is then adjusted so that the nanoparticle films are colored red while the free space remains in grayscale, as shown in Fig. 3.27. There is some user error associated with this process and the level of thresholding will vary from person to person. Following the threshold the Apply button is selected which produces a black and white image as shown in Fig.
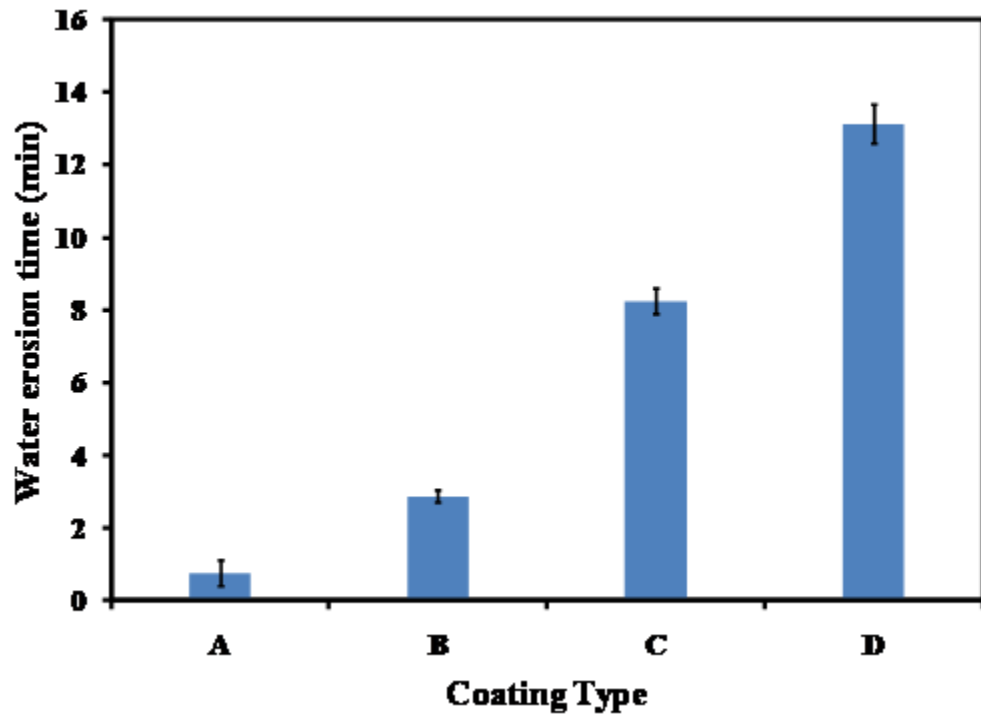
Figure 3.26. Water erosion time (with standard deviations) for four randomly selected superhydrophobic coatings using the new Waterpik® apparatus.
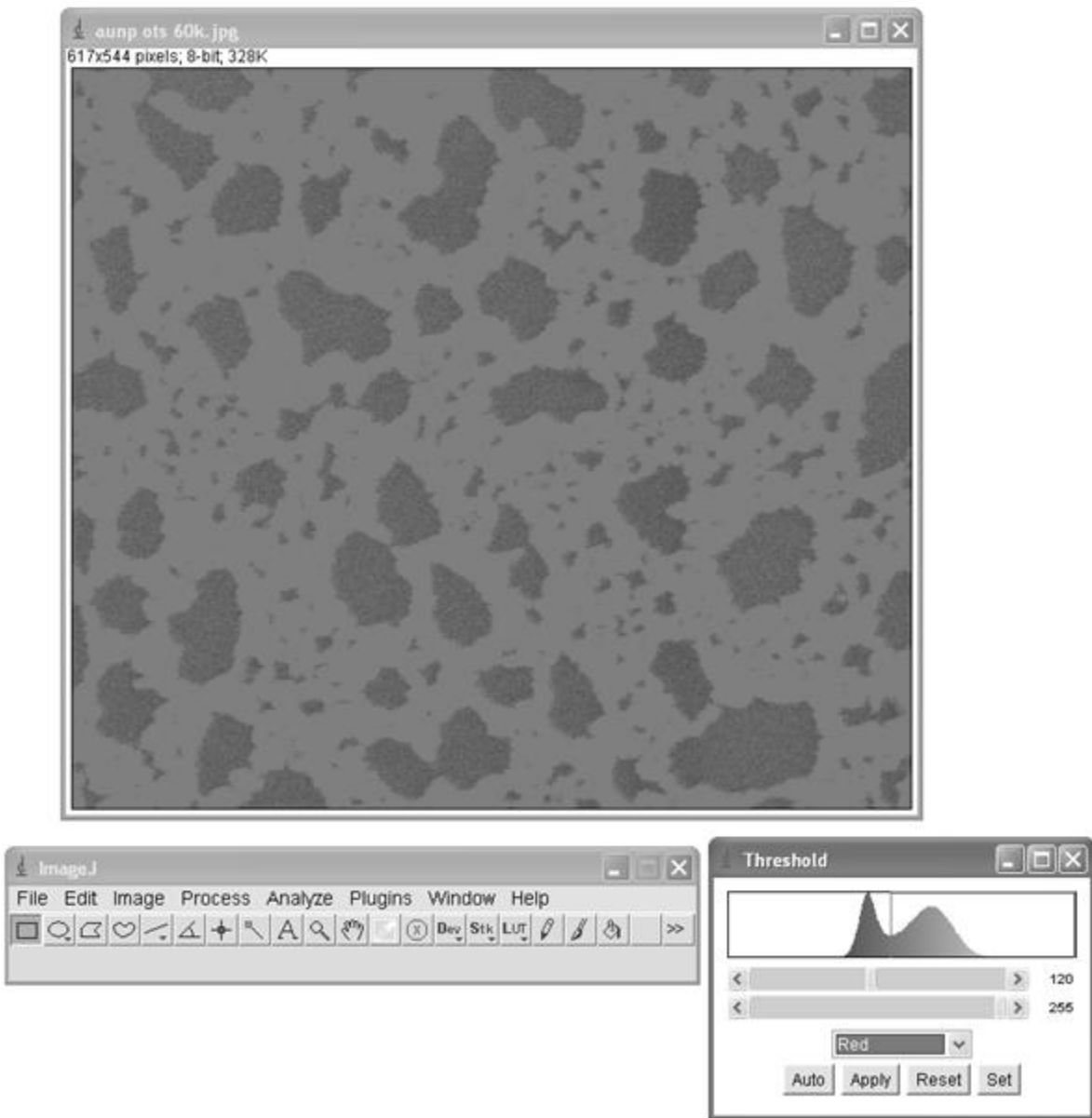
Figure 3.27. Depicting of adjusting the threshold of a digital SEM image in ImageJ.

3.28. In the image, the black represents the nanoparticle film while the white regions represent free space.

When an image such as Fig. 3.28 is produced, the desired measurements are selected by Analyze → Set Measurements. Within the box that appears, Area Fraction is selected for measurement. Finally, Analyze → Measure is selected which then measures the percentage of the threshold image which is black (nanoparticle coated) and presents the results. In the case of Fig. 3.28, the resulting area fraction is 64.3%. In subsequent chapters that utilize this technique, the fractional surface coverage would be presented as 0.64.
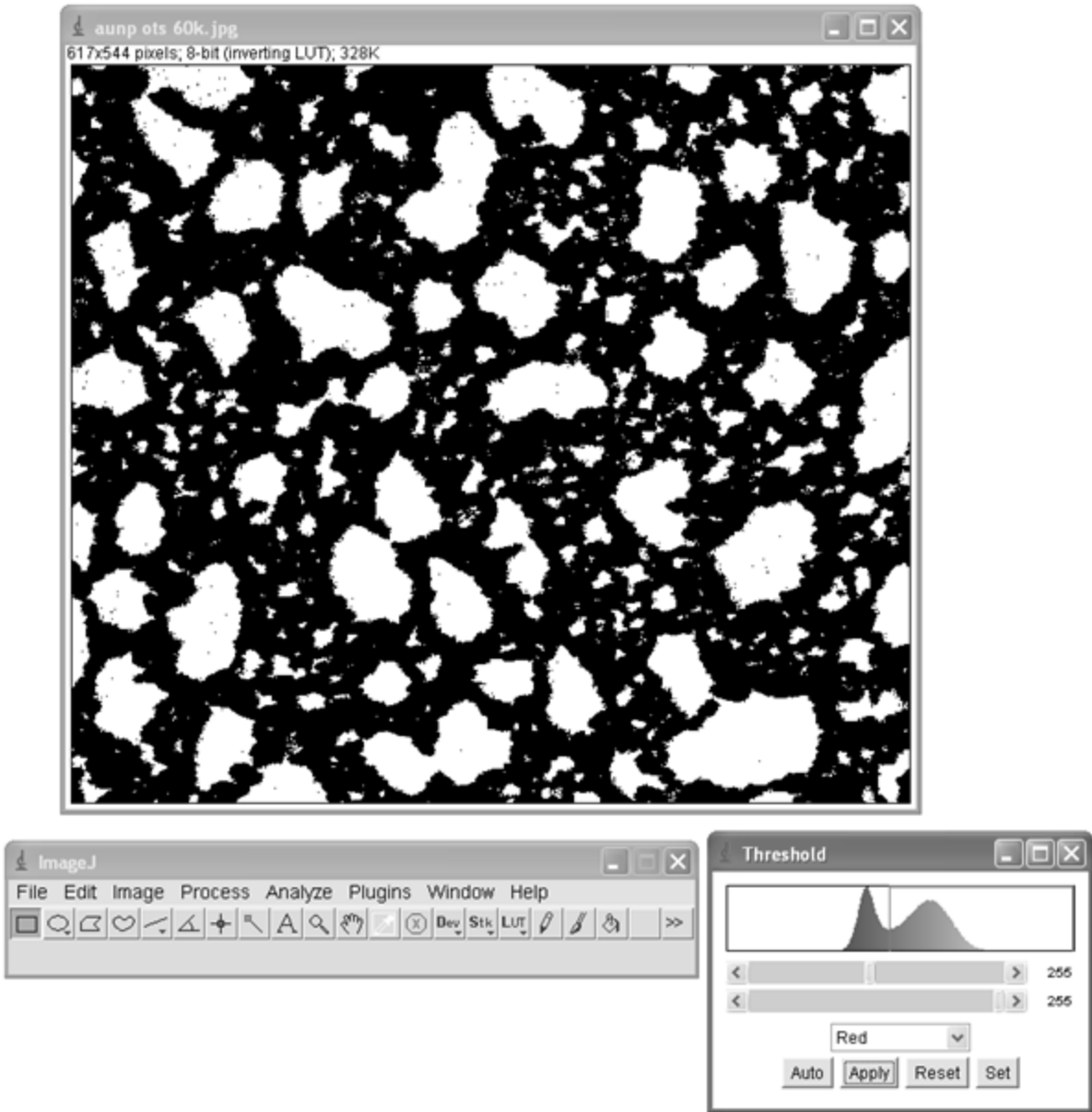
Figure 3.28. Black and white image of a nanoparticle film following thresholding in ImageJ.

CHAPTER 4

QUANTIFYING WORK OF ADHESION DIRECTLY

FROM EXPERIMENTAL DATA

4.1 Introduction

To quantify stiction and adhesion that exists between two microstructures, methods have been developed which determine the apparent adhesive surface energy causing adhesion, or work of adhesion (Mastrangelo 1997; Mastrangelo and Hsu 1992; de Boer and Michalske 1999, Knapp and de Boer 2002). The methods typically determine an "apparent" work of adhesion value as the mechanical analysis neglects adhesion caused by capillary collapse and does not take into account reduction in real contact surface area associated with surface roughness. Mastrangelo (1997) presented an equation for quantifying the apparent work of adhesion of adhered cantilevers not subjected to external loads. This calculation method is very useful and accurate for determining the surface energy of typical S-shaped, adhered cantilever beams. Unfortunately, many arc-shaped cantilever beams are permanently adhered to the substrate in varying degrees, indicating that $0 < m < 1.5$, and m is not a readily determinable quantity from experimental data due to factors preventing accurate interferometry near the tip region, such as tip diffraction, focusing issues, and anomalous contacts at the boundaries. Therefore, in order to accurately quantify the adhesion of cantilever beams to the substrate regardless of beam shape (i.e., regardless of m), a new calculation method for the work of adhesion was desired which is

92

not dependent on any presumed boundary conditions. In this chapter, a new calculation method that directly uses experimental height profile data measured by interferometry is presented.

4.2   Mastrangelo's work of adhesion

Mastrangelo (1997) developed a theoretical method for measuring the surface energy of micromachined cantilever beams by balancing mechanical forces. This measurement technique considers the equilibrium between the elastic energy in a deformed cantilever beam (U_E) and the interfacial surface energy promoting adhesion (U_S), yielding the total mechanical energy balance

$$U_T = U_E + U_S = \frac{Ewt^3}{24} \int_0^S \left(\frac{d^2u}{dx^2}\right)^2 dx - \gamma_S w(L-s) \tag{4.1}$$

where E is the Young's modular of the beam material, w and t are the beam width and thickness, respectively, L is beam length, s is the crack length and $u(x)$ is the deflection of the beam between $0 \leq x \leq s$. The crack length, s, is defined as the distance between the beam anchor point ($x = 0$) and the point at which the beam comes into complete contact with the substrate at $x = s$. Fig. 4.1 illustrates two cantilever beams which are adhered in both an "S" shape and "arc" shape. S-shaped beams, as illustrated in Fig. 4.1, have a crack length $s < L$ while arc-shaped beams have crack lengths equal to L with an angle θ existing between the beam and substrate surface (for S-shaped cantilever beams, $\theta = 0$).

The beam deflection, $u(x)$, is the solution to

$$EI\frac{d^4u}{dx^4} = 0, \quad I = \frac{wt^3}{12}, \tag{4.2}$$

when no external forces (electrostatic, capillary, or manual deflection) are acting on the beam. Eqn. (4.2) is solved under two specific sets of boundary conditions based on whether an adhered

beam is S- or arc-shaped. The deflection for S-shaped cantilever beams is solved subject to the boundary conditions

$$\frac{du}{dx}\bigg|_0 = \frac{du}{dx}\bigg|_S = 0,\, u(0) = 0,\, u(s) = h, \tag{4.3}$$

which completely ignores the effects of finite compliance at the step-up posts (Meng et al. 1993; Mullen et al. 1991). The boundary conditions for arc-shaped beams are

$$\frac{du}{dx}\bigg|_0 = 0,\, \frac{du}{dx}\bigg|_S = \theta = \frac{hm}{s},\, u(0) = 0,\, u(s) = h, \tag{4.4}$$

where m is a non-dimensional number that describes the shape of a deflected beam based on the shear tip angle θ.

Solving Eqn. (4.2) using the two sets of boundary conditions yield two equations for the beam deflection:

$$u = h\eta^2(3 - 2\eta),\quad \eta = \frac{x}{s} \tag{4.5}$$

for S-shaped cantilever beams, and

$$u = h\eta^2((m - 2)\eta + (3 - m)),\, \eta = \frac{x}{s} \tag{4.6}$$

for arc-shaped cantilever beams. Notice that when $m = 0$, Eqn. (4.6) reduces to Eqn. (4.5). Mastrangelo and Hsu (1992) determined that the stored beam energy is

$$U_E = \frac{6EIh^2}{s^3}\left(1 - m + \frac{1}{3}m^2\right) \tag{4.7}$$

for $0 \leq m \leq 3/2$, where $m = 0$ corresponds to a shear tip angle $\theta = 0$ and $m = 3/2$ corresponds to the maximum shear tip angle at which a beam can remain adhered. For beams with shear tip angles

$$\theta \geq \frac{3h}{2s},$$

the adhesive surface energy is not adequate to cause stiction and the beam will release from the substrate. Incorporating Eqn. (4.7) into Eqn. (4.1) and minimizing the total energy by differentiation with respect to s, the work of adhesion is determined as

$$\gamma_S = \frac{3Et^3h^2}{2s^4}\left(1 - m + \frac{1}{3}m^2\right), \quad 0 \leq m \leq \frac{3}{2}. \tag{4.8}$$

However, the value of m is not readily determined for beams that exist between $m = 0$ and $m = 3/2$. Therefore, the use of Eqn. (4.8) is generally restricted for cantilever beams which are adhered in the typical S-shaped profile or arc-shaped beams which are on the verge of being released from the substrate. Any unloaded cantilever beams adhered at the tip with $0 < m < 3/2$ require a new quantification method. The work in this chapter expands on Mastrangelo's quantification method by directly utilizing interferometrically collected experimental data to solve the integral in Eqn. (4.1) and quantify the apparent work of adhesion.

4.3 Mathematical development

The mathematical development begins similarly to Mastrangelo (1997) in that we consider the total system energy approach as in Eqn. (4.1). The equilibrium between the elastic bending energy and the interfacial adhesion energy is found by setting $dU_T/ds = 0$ to obtain a relationship between γ_s and s, given by Eqn. (4.9):

$$\gamma_s = \frac{Et^3}{24}\frac{d}{ds}\int_0^s \left(\frac{d^2u}{dx^2}\right)^2 dx. \tag{4.9}$$

Since the shape of a cantilever beam is dependent on the value of s, the beam deflection function u is a function of both lateral position x and crack length s. In order to evaluate the derivative of

95
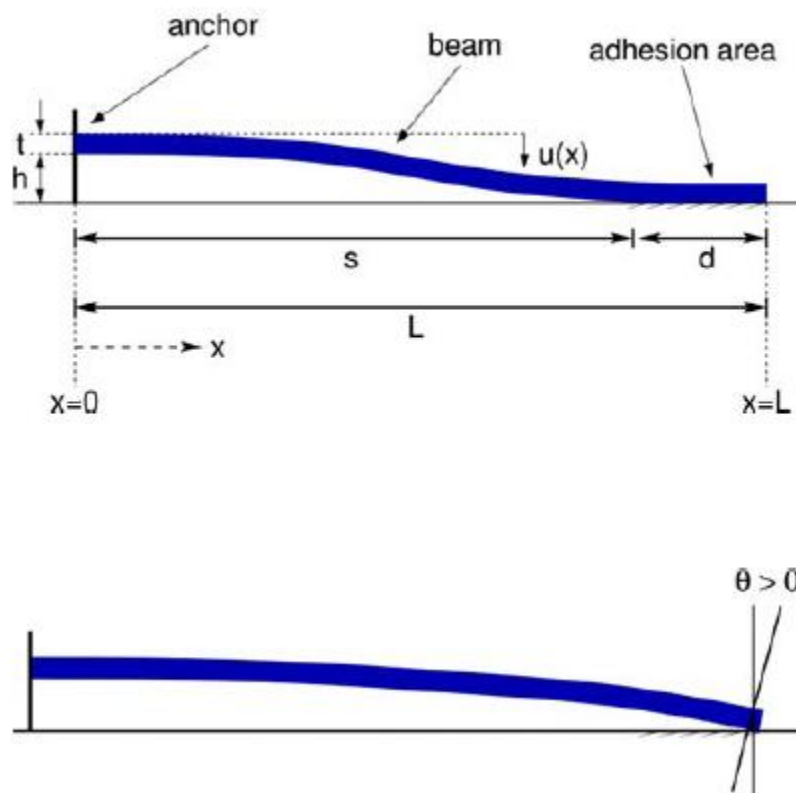
Figure 4.1. Illustrations of cantilever beams in both S- and arc-shapes.

the integral in Eqn. (4.9) for an arbitrary and well behaved function $u(x,s)$, the Leibniz Integral Rule must be used which states (Khuri 2003):

$$\frac{d}{ds}\int_{a(s)}^{b(s)} u(x,s)dx = \int_{a(s)}^{b(s)} \frac{\partial}{\partial s}u(x,s)dx + \frac{db(s)}{ds}u(x,s)\Big|_{b(s)} - \frac{da(s)}{ds}u(x,s)\Big|_{a(s)}$$ (4.10)

Using Eqn. (4.10) to evaluate the integral in Eqn. (4.9) yields

$$\gamma_s = \frac{Et^3}{24}\left[\int_0^s \frac{\partial}{\partial s}\left(\frac{d^2u}{dx^2}\right)^2 dx + \left(\frac{d^2u}{dx^2}\right)^2\Big|\right]_s.$$ (4.11)

It is desired to solve Eqn. (4.11) using a function $u(x,s)$ determined directly from experimental data. The height profile data collected using interferometry includes lateral beam position x with vertical beam position $h(x)$. Since the beam deflection function $u(x) = h_0 - h(x)$, where h_0 is the nominal beam height, it is convenient to note that

$$\left(\frac{d^2u}{dx^2}\right)^2 = \left(\frac{d^2h}{dx^2}\right)^2$$ (4.12)

allowing the square of the second derivative of the height function to be used directly in Eqn. (4.11). Based on typical solutions to cantilever beam mechanics, we postulated that the height function should be normalized to the crack length, s. The easiest way to do this is to rescale the x-dimension by s and consider the height, h, as a function of η where

$$\eta = \frac{x}{s}, \quad 0 \le \eta \le 1$$ (4.13)

and is consistent with earlier developments. From this normalized data, a 3rd-order polynomial fit on $h(\eta)$ was performed yielding a function of the form

$$h(\eta) = a_3\eta^3 + a_2\eta^2 + a_1\eta + a_0,$$ (4.14)

97

which always satisfies Eqn. (4.2) and does not pre-suppose specific boundary conditions because the polynomial fitting process automatically accounts for them. Manipulating Eqn. (4.14) to obtain the desired terms in Eqn. (4.11) yield

$$\gamma_s = \frac{3Et^3}{2s^4}\left(a_3^2 + a_2 a_3 + \frac{1}{3}a_2^2\right)$$
(4.15)

which can directly be used to determine the apparent work of adhesion or surface energy for any adhered cantilever beam, regardless of its shape, as long as the coefficients a_3 and a_2 can be determined from appropriately scaled experimental data.

To reduce the time required to obtain experimental height data for a cantilever beam and perform the operations described above, a computational script was developed using the MEMScript platform. The script allows for the rapid determination of crack length and apparent work of adhesion following the above method. In our case, the script also commanded the integral hardware to collect the interferometric data. However, one can also use empirical $h(x)$ data collected by other means. The script, which is found in its entirety in Appendix B, was written to perform the following operations in order:

- Five interferograms of the selected cantilever beam are collected at $\pi/4$ phase increments. A five-point Hariharan phase shift calculation (Hariharan et al. 1987) is performed using the interferograms to collect lateral x and vertical $h(x)$ data.

- The script iteratively fits a profile to the experimental data by selecting values of s between 0 and the beam length, l. The data averaged error is calculated during each iteration and the value of s that minimizes this error is determined and used for subsequent steps.

- The lateral position data is rescaled from 0 to 1 by dividing x by s, giving the η-coordinate data and the corresponding $h(\eta)$ data. Values of η above 1 are not included in

the rescaled data. The data is fit to a 3rd order polynomial as a function of the η coordinate.

- The apparent work of adhesion is calculated using coefficients from the polynomial, as well as material property and geometric information (i.e. E, t) about the cantilever beam input by the user before running the script by way of Eqn. (4.15).

4.4 Method validation

To ensure that Eqn. (4.15) can accurately predict the apparent work of adhesion of an adhered cantilever beam by determining the coefficients a_3 and a_2 directly from experimental data, the method was validated using three distinct types of cantilever beam data. Two data sets were calculated (synthetic) both with and without random noise, while a third set of data was collected from measurements (empirical). The apparent work of adhesion values determined by both Eqn. (4.8) and Eqn. (4.15) for each set of data were compared to determine the validity of the method described in this chapter.

4.4.1 Validation based on calculated height profiles

Synthetic data for arc-shaped and S-shaped cantilever beams were produced following:

$$h(x) = h_0 - h_0\left(\frac{x}{s}\right)^2\left[(m-2)\left(\frac{x}{s}\right) + 3 - m\right] + n, \quad 0 \le x \le s$$
$$h(x) = 0 + n, \quad s < x \le L$$

(4.16)

where n is random noise generated between -0.025 and 0.025 μm. The initial beam height, h_0, was equal to 2 μm. The first synthetic data sets generated using Eqn. (4.16) were generated without noise (i.e., $n = 0$). Fig. 4.2 presents the generated artificial data for two arc-shaped beams ($m = 1.5$ and 0.8) and an S-shaped beam ($m = 0$), all of length 300 μm. The crack length

and apparent work of adhesion for each of the beams were determined using our new scripted calculation method as well as the established analytical method where s is determined by a best-fit model to the experimental data and the adhesion is quantified by Eqn. (4.8). Since no random noise was generated within the data, it was expected that the work of adhesion results by each method would be equivalent for each respective set of data. For the synthetic beams, the values of E and t were 160 GPa and 2.5 μm, respectively.

The first data set analyzed was generated for a beam of length 300 μm and crack length 250 μm ($m = 0$). Analyzing the data using Eqn. (4.8) yielded a surface adhesion energy of 3.84 mJ/m^2. The new method, after accurately determining the crack length by an automated iterative method, calculated an adhesion energy of 3.84 mJ/m^2. Two arc-shaped beams were also generated with $m = 1.5$ and $m = 0.8$, respectively. After performing the 3rd-order fit to determine the coefficients, both Eq. (4.15) and Eqn. (4.8) yielded the same work of adhesion values: 0.463 and 0.765 mJ/m^2, respectively, for the two arc-shaped beams. These results indicate that when noise-free cantilever beam data exists, the new method described in this chapter is mathematically identical to the method described by Mastrangelo (1997). However, the new method allows for the determination of the apparent work of adhesion for any cantilever beam when m is an unknown value. This is an important point since m is often not well known.

In order to test the new method differently, a hypothetical array of beams was synthesized pre-supposing an apparent work of adhesion of 0.965 mJ/m^2 which would yield an "S-shape" crack length of 353 μm. Height data for ten beams were synthesized beginning with a length of 150 μm and incrementing beam length by 50 μm per beam. Cantilever beams with an overall length of longer than 353 μm would exhibit S-shaped profiles when adhered to the substrate. Shorter beams would either exhibit an arc shape or be free standing (un-adhered)
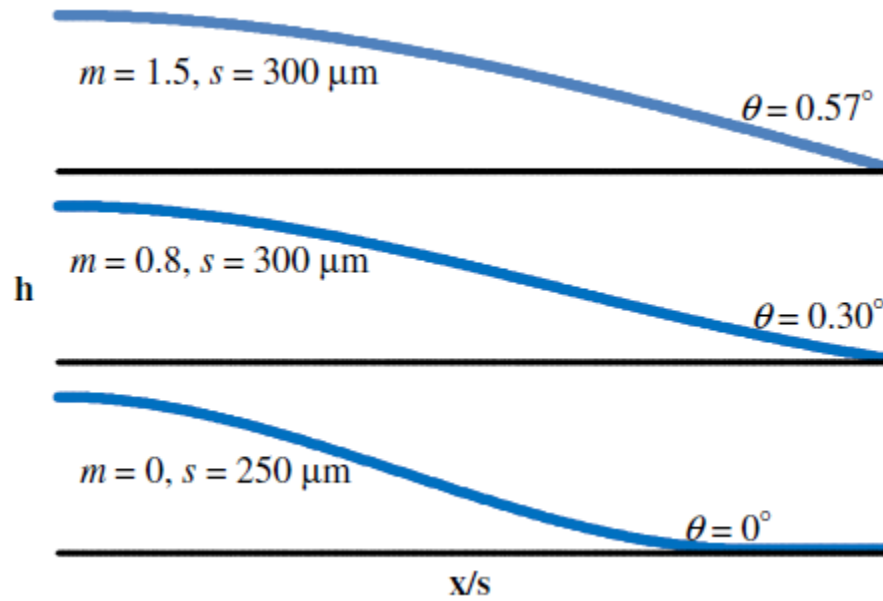
Figure 4.2. Artificial data sets generated (without noise) for 300-μm long cantilever beams. The first two beams are arc-shaped with $m = 1.5$ and 0.8, respectively. The third beam is S-shaped ($m = 0$) with $s = 250$ μm.

based on a limiting arc length, l^*. This limiting length is the beam length at which the adhesion energy is not strong enough to permanently affix the beam, and is estimated using Eqn. (4.8) when $m = 1.5$, or

$$l* = \left(\frac{3Et^3h^2}{8\gamma_s} \right)^{1/4}$$

In this case, l^* is equal to 249.7 µm, indicating that any beam shorter than this length would not be adhered to the surface.

Table 4.1 presents the beam lengths and m values, determined by Eqn. (4.8), used to generate the artificial cantilever beam array. Due to the limiting beam length, the 150-µm and 200-µm long beams would not be adhered by an adhesion energy of 0.965 mJ/m². Beam numbers 3, 4 and 5 ($l^* < L < s$) exhibit arc shapes with shape factors that vary over the range $0 < m < 1.5$. Beams 6 through 10 ($L > s$) all exhibit S-shaped profiles. Fig. 4.3 illustrates the profiles of beams 2 (free-standing), 3 through 5 (arc), and 6 ("S"), along with their associated m values and shear tip angles following $\theta = mh/s$ (Mastrangelo 1997). Table 4.1 also presents the estimated crack length (determined iteratively), the coefficients a_3 and a_2 determined by the 3rd-order fit, and the apparent work of adhesion values using the newly developed method. The results reveal an average crack length (determined iteratively) of 353.8 ± 1.1 µm and an average work of adhesion of 0.962 ± 0.020 mJ/m². These average values are in agreement with the "fixed" values of 353 µm and 0.965 mJ/m² used to generate the data sets. The slight difference is attributed to the noise incorporated when generating the data, which falls in a much greater range than expected when analyzing actual cantilever beam data obtained by interferometry.

Beam no.	Beam length, L (μm)	Shape factor, m	a_3	a_2	Determined crack length, s (μm)	Determined work of adhesion, γ_s (mJ/m^2)
1	150	n/a	n/a	n/a	n/a	n/a
2	200	n/a	n/a	n/a	n/a	n/a
3	250	1.44	1.10	-3.10	250	0.963
4	300	0.60	2.79	-4.79	300	0.957
5	350	0.04	3.89	-5.87	350	0.945
6	400	0	4.03	-6.00	355	0.958
7	450	0	4.06	-6.07	355	0.974
8	500	0	3.94	-5.90	353	0.939
9	550	0	4.06	-6.10	353	0.995
10	600	0	4.09	-6.11	353	0.988

Table 4.1. Values used to generate an artificial array of cantilever beams based on uniform

surface adhesion energy of 0.965 mJ/m^2 and the crack length and adhesion energy determined

from generated data (with random noise).
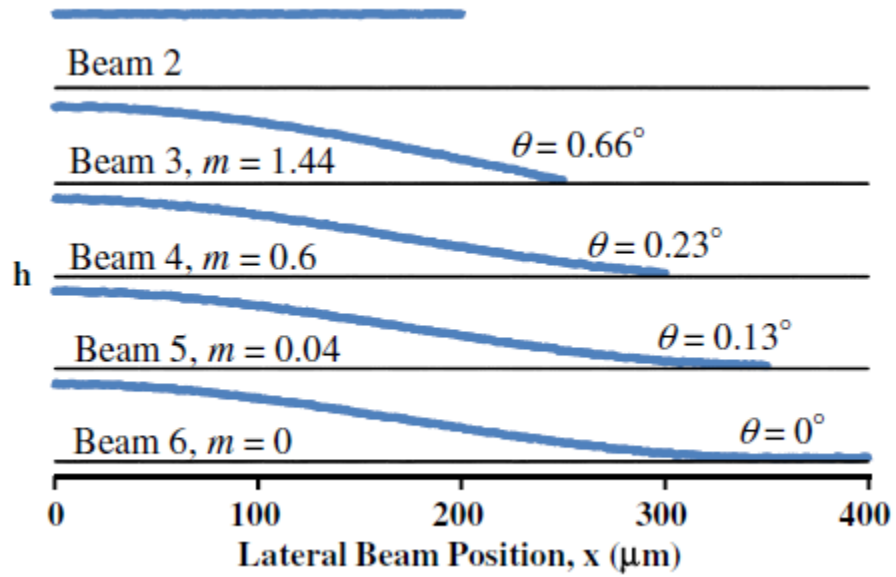
Figure 4.3. Profiles of beam numbers 2 through 6 (from Table 4.1), illustrating a free-standing

beam, various arc-shaped beams with varying *m* values, and an S-shaped beam.

4.4.2   Validation based on experimentally measured beam data

The new method for quantifying the apparent work of adhesion described in this work was also examined using experimental data collected from real cantilever beams. Briefly, the beam data was collected using an EM OPTOPro 622A long working distance profilometer with monochromatic green (λ = 532 nm) light. Table 4.2 presents the beam length and determined crack length for the selected beams, as well as the calculated work of adhesion using both Eqn. (4.15) and Eqn. (4.8). The percent difference between the work of adhesion values are also tabulated. The results indicate that work of adhesion values determined by the new method are in excellent agreement with values determined using Eqn. (4.8). The percent difference between the two methods, for all beams tested, was no greater than about 1%.

In each case, the adhesion energy value determined by fitting the data and using Eqn. (4.15) was slightly higher than the value calculated by Eqn. (4.8). Fig. 4.4 presents the experimental data collected for beam no. 13 (see Table 4.2) and the corresponding fit to the data using Eqn. (4.8). In the inset of Fig. 4.4, the two small dips labeled as "shadows" are real, detected artifacts resulting from layer-by-layer fabrication process. Fig. 4.4 illustrates that even though the crack lengths and nominal heights (h_0) are equal, Eqn. (4.5) does not entirely describe the shape of the adhered beam. A generic 3rd-order polynomial fit to the beam data typically represented the cantilever beam shape more accurately. The polynomial fit is not illustrated in Fig. 4.4 because the polynomial fit and experimental data are indistinguishable. Fig. 4.5 plots the difference, $\Delta h(\eta)$, between the experimental height and calculated height for beam no. 13, using both Eqns. (4.5) and (4.14), following

$$\Delta h(\eta) = h_{\text{exp}}(\eta) - h_{fit}(\eta)$$

(4.10)

105

Beam number	Beam length, L (μm)	Crack length, s (μm)	γ_s using Eqn. (4.15) (mJ/m^2)	γ_s using Eqn. (4.8) (mJ/m^2)	Percent difference
7	450	347.1	0.954	0.952	0.21 %
8	500	402.7	0.523	0.521	0.38 %
9	550	360.4	0.814	0.811	0.37 %
10	600	487.2	0.223	0.221	0.90 %
11	650	367.5	0.756	0.753	0.40 %
12	700	376.4	0.680	0.677	0.44 %
13	750	373.3	0.648	0.641	1.09 %
14	800	377.5	0.628	0.622	0.96 %

Table 4.2. Beam length, crack length, and work of adhesion values determined

for experimental data from real, adhered cantilever beams.
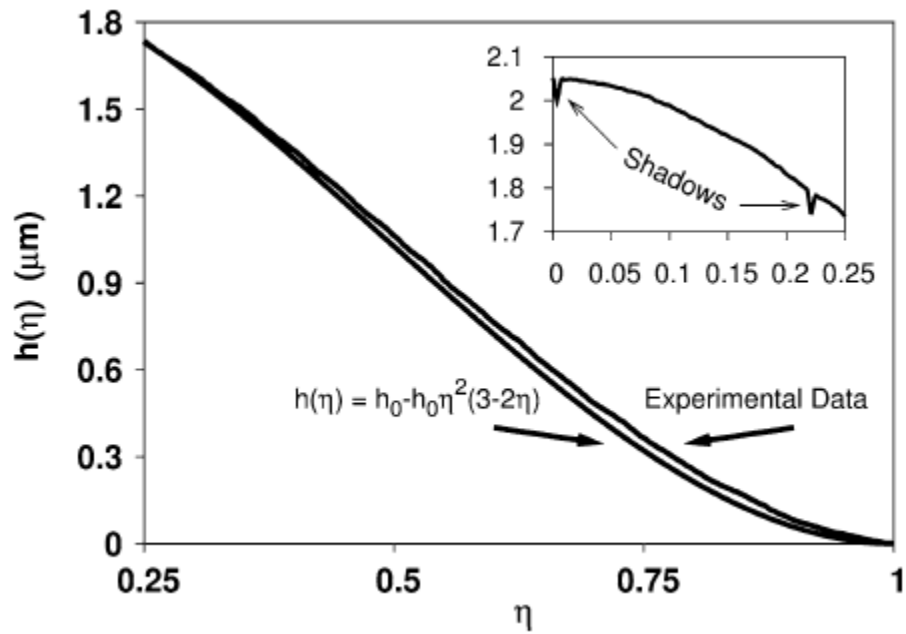
Figure 4.4. Fit of Eqn. (4.5) to empirical data for beam no. 13 following normalization of

data to $\eta = 1$.   The inset illustrates two shadows which result from microfabrication.

where $h_{exp}(\eta)$ and $h_{fit}(\eta)$ are the experimental and calculated height values, respectively, at a particular value of η. Fig. 4.5 illustrates that the difference between the experimental data and calculated data using Eqn. (4.14) is closer to zero, while the difference to the data calculated using Eqn. (4.5) strays further from zero between η values of 0.25 and 1. This was the case for all beams presented in Table 4.2. This finding suggests that, for the set of cantilever beams examined in this study, the current method provides further improvement in estimating the apparent work of adhesion due to improved representation of the beam shape. In other words, the new method presented in this work more accurately utilizes the beam shape and, therefore, may more accurately estimate the apparent work of adhesion.

4.5 Conclusions

In this chapter, a new method for quantifying the adhesion of microstructured cantilever beams directly from experimental data collected via interferometry has been developed and validated. This method allows for the estimation of apparent work of adhesion for all adhered cantilever beams, including arc-shaped beams where $0 < m < 1.5$, as long as no outside forces or loads are present. Previous techniques have not allowed for an accurate estimation between m values of 0 and 1.5.

The new adhesion quantification method accurately replicates the calculated work of adhesion values determined using Eqn. (4.8) for artificially generated data sets. When analyzing synthetic beam data (free of experimental noise), the new technique using Eqn. (4.15) is mathematically equivalent to the method developed by Mastrangelo (1997). The method also successfully describes the shape of adhered cantilever beams and more accurately determines the
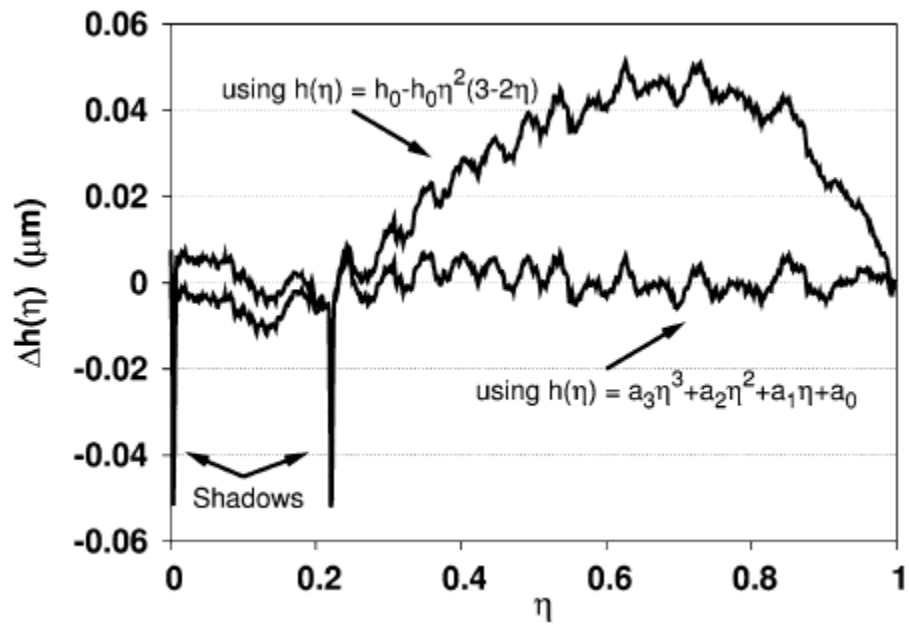
Figure 4.5. Difference between experimental height and calculated height, using

Mastrangelo and 3rd-order polynomial fits, to the experimental data shown in

Fig. 4.4. The two shadows result from the microfabrication process.

apparent work of adhesion from experimental data collected via interferometry than previous methods.

CHAPTER 5

GXL PARTICLE DEPOSITION ONTO MEMS –
A PROOF OF CONCEPT

5.1 Introduction

As previously discussed, stabilized nanoparticles cannot be drop cast and evaporated from dispersion onto MEMS or fabricated microstructures due to the strong interfacial forces that exist. Therefore, a nanoparticle deposition technique is required which is compatible with current MEMS fabrication methods. This chapter investigates the use of a gas-expanded liquid/supercritical drying process for the deposition of gold nanoparticles onto microstructures, which is discussed in more detail in Chapter 3. Preliminary results and significant findings about the use of the GXL particle deposition method for MEMS are presented here.

5.2 Nanoparticle agglomeration

As discussed in Chapter 3, early experiments were performed with silicon and microdevice samples placed facing upward within the glass sample vial. During these early runs, several large and oily particulates were deposited on the substrate surfaces, as seen in Fig. 3.1(a). Fig. 5.1 also demonstrates this phenomenon on a micro-gear device. This figure illustrates regions where very few of these larger particulates are deposited. These particulate-free regions were, at the time of nanoparticle deposition, covered by microstructures which had been later

moved. Notably, the large particulate-free region in Fig. 5.1 was originally home to a larger micro-gear that was removed in order to view the substrate surface beneath the gear. This indicates that the particulates only deposited on the top surfaces of the device, by means of gravity.

Fig. 3.1(b) demonstrates that when the samples are placed upside-down within the deposition chamber, these large particulates are not experienced. This indicates that the particulates are large agglomerations of particles that agglomerate due to the long deposition time. At some point, these agglomerations become too large to remain thermodynamically stabilized in the dispersion and crash out due to gravitational forces. This can be avoided, as shown by Fig. 3.1(b), by placing samples upside-down within the chamber and forcing only smaller nanoparticles to deposit onto the substrate surfaces due to only surface-to-surface attractive forces. This attraction-based deposition is discussed in more detail in the next subsection.

5.3 Thermodynamics of nanoparticle deposition

Due to the miniscule size of the nanoparticles, attractive van der Waals forces dominate gravitational forces, causing particles on the brink of precipitation to attract to any surface submerged in the dispersion. Fig. 5.2 compares estimated values for non-retarded (instantaneous dipole-dipole interaction) van der Waals attractive force to a flat silicon surface to the gravitational force experienced by a 5-nm diameter gold nanoparticle. The attractive forces were estimated using Eqn. (5.1):

$$F_{vdw} = \frac{AR}{6D^2} \tag{5.1}$$
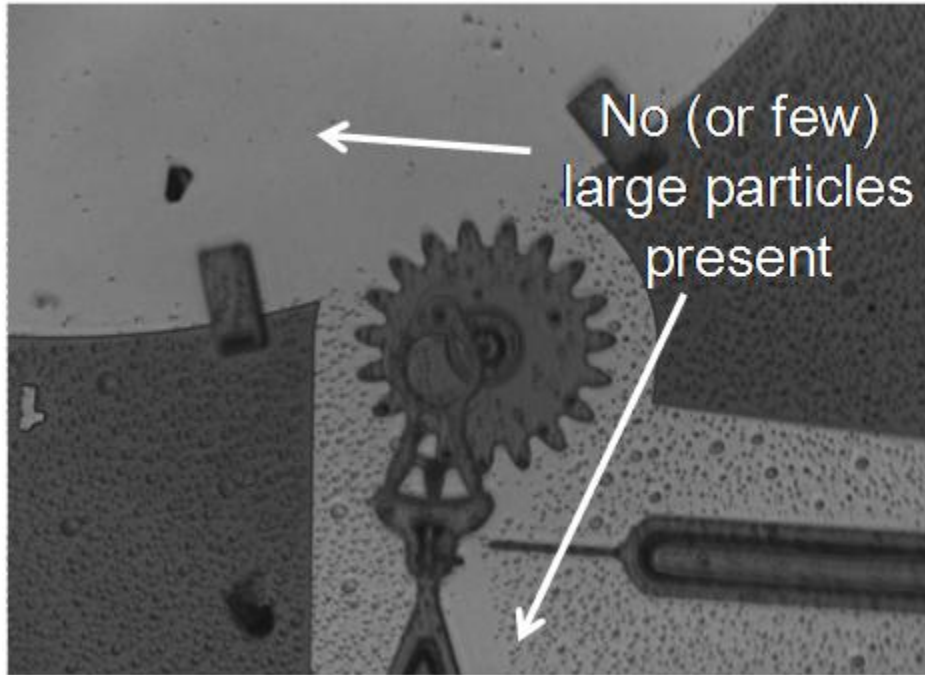
Figure 5.1. 20X optical photograph of large particle agglomerations on a polysilicon

micro-gear device. The areas where agglomerations are sparse (denoted by arrows)

were originally covered by microstructures.

where R is the spherical particle radius, D is the particle-to-surface separation distance, and A is an overall Hamaker constant for the system (Israelachvili 1992). The overall Hamaker constant was approximated by Eqn. (5.2) (Israelachvili 1992):

$$A \approx \left(A_{11}^{1/2} - A_{33}^{1/2}\right)\left(A_{22}^{1/2} - A_{33}^{1/2}\right) \tag{5.2}$$

where A_{11}, A_{22}, and A_{33} are the individual Hamaker constants for gold, silicon and the hexane medium, respectively. The Hamaker constants for gold, silicon, and hexane are 31.0×10^{-20} J (Bargeman and Vader 1972), 6.50×10^{-20} J (Bachmann et al. 2006), and 4.00×10^{-20} J (Israelachvili 1992), respectively. Observing the results, Fig. 5.2 illustrates that for separation distances smaller than 1 μm (half the typical microstructure-to-substrate gap height) the attractive force is at least three orders of magnitude greater than the gravitational force exerted on a single nanoparticle. This suggests that nanoparticles should attract towards the nearest surface (even vertically) rather than falling out of solution due to gravity.

However, since the nanoparticles are made of a different material than the surface, the attraction between particles is also of importance. The non-retarded van der Waals force between two spherical particles in solution is given by Eqn. (5.3):

$$F = \frac{A}{12D^2}\left(\frac{R_1 R_2}{R_1 + R_2}\right) \tag{5.3}$$

where R_1 and R_2 are two differing particle radii (Israelachvili 1992). Assuming the radius of every particle is approximately equivalent, Eqn. (5.3) reduces to:

$$F = \frac{AR}{12D^2} \tag{5.4}$$

Although the ratio of Eqn. (5.1) to Eqn. (5.4) is 2, the difference in these two forces resides in the overall Hamaker constants. For nanoparticles made of the same material, the Hamaker constant A in Eqn. (5.4) is very different from that of Eqn. (5.1) for particles of one material to a surface
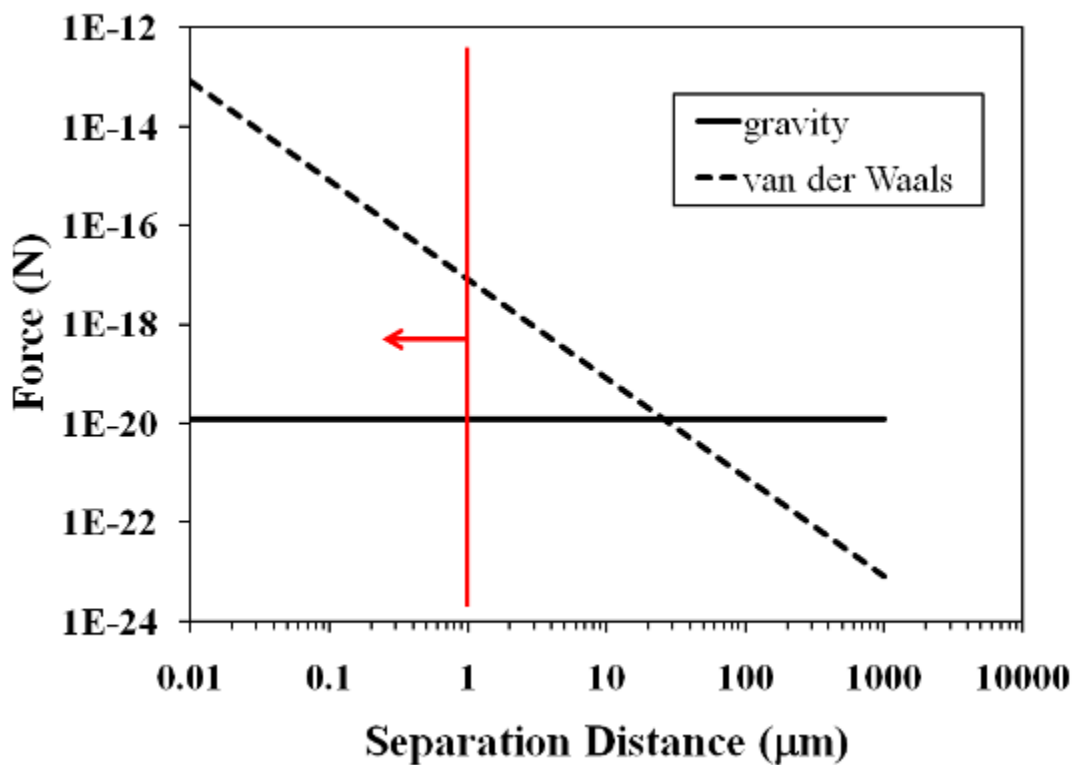
Figure 5.2. Comparison of non-retarded van der Waals attractive and gravitational forces

of a 5-nm gold nanoparticle to a large, flat silicon surface with varying

separation distance. Region of interest lies to the left of 1 μm.

of another material. The overall Hamaker constant for the three-component system used to estimate the van der Waals attractive force in Fig. 5.2 was approximately 1.96 x 10^{-20} J. However, for a two-component system (only gold nanoparticles in hexane), the overall Hamaker constant is approximately 1.27 x 10^{-19} J which is one order of magnitude higher. Therefore, the interaction between two gold particles of equal diameters is stronger than that of a gold particle of the same size to a large, flat silicon surface. Although this slightly stronger attractive force will not prevent the attraction of nanoparticles to the silicon substrate surfaces, it does affect how particles are deposited and oriented on the surface.

Fig. 5.3 presents an AFM scan of 5-nm gold nanoparticles that were deposited onto a clean, smooth Si(100) surface using the gas-expanded liquid deposition process. This image illustrates that the nanoparticles oriented into large islands up to approximately 15 µm wide. Further analysis of the scan, shown by the line analysis plot in Fig. 5.3, illustrates that these nanoparticle islands were roughly 15 nm (or three 5-nm nanoparticles) in height. This gold nanoparticle island formation further proves that although the particles were attracted to the silicon surface, a greater particle-to-particle attraction exists. This phenomenon is actually very reminiscent to Volmer-Weber film growth which occurs when a metallic species (such as gold) forms islands rather than monolayers when deposited onto ceramic or semiconductor substrates (Ohring 2002). The driving force behind this island growth mechanism is the desire to minimize surface free energy. In this case, the surface tension of the nanoparticle film exceeds the surface tension of the silicon substrate, or $\gamma_{sv} < \gamma_{fs} + \gamma_{fv}$ where γ_{sv}, γ_{fs} and γ_{fv} are the surface tensions between the substrate-atmosphere, film-substrate and film-atmosphere, respectively. The mechanism by which the nanoparticle islands are formed may be explained what is known as *Ostwald ripening*. At the atomic level, the tendency is for atoms to escape from regions where

116

the chemical potential is large to an area with decreased chemical potential (Ohring 2002). Due to the extremely small size of the gold nanoparticles, their behavior more closely resembles that of atomic gold (as opposed to bulk gold), and therefore may experience a similar ripening phenomenon where the mass transport of particles takes place on the surface to areas where free energy is minimized following:

$$\gamma = \frac{\mu_i r_i}{2\Omega} \tag{5.5}$$

where r_i is the radius of a particular island, μ_i is the chemical potential, and Ω is the atomic volume (Ohring 2002).

5.4   Effect of nanoparticles on adhesion

As a proof of concept, 5-nm gold nanoparticles were deposited by gas-expanded liquid deposition onto polysilicon microcantilever beam arrays (CBAs). Fig. 5.4 presents two SEM photographs of (a) a native SiO_2-coated cantilever beam dried with supercritical CO_2 and (b) a gold nanoparticle-coated cantilever beam processed by GXL. Fig. 5.5 is an SEM photograph of a cantilever beam underside coated with gold nanoparticles. The images serve to illustrate that nanoparticles are uniformly deposited over the entire surface of the polysilicon beam and substrate. The images also indicate that the visible particles are larger than 5 nm, suggesting that like the Si(100) shown in Fig. 5.3 the particles created islands or larger nanoparticulates. In fact, image analysis of the particulates indicated an average diameter of nearly 25 nm. These larger particulates should be advantageous for reducing microstructure adhesion by creating a rougher surface and reducing the real surface area available for contact. The typical root-mean-square (RMS) roughness of a clean Si(100) surface is on the order of 0.2 nm. The RMS roughness of

117
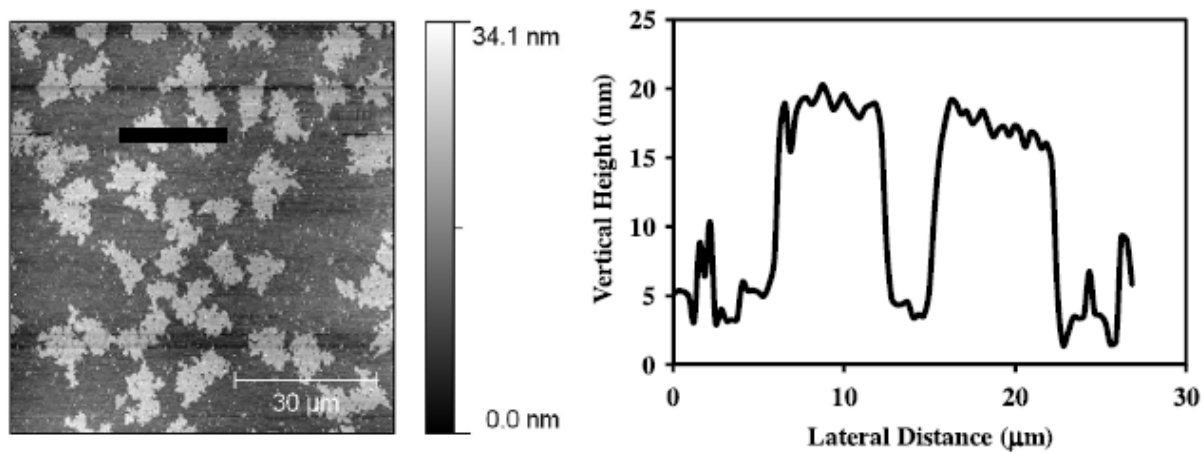
Figure 5.3. 80 x 80 μm AFM scan of gold nanoparticle islands formed from the GXL deposition of 5-nm particles onto Si (100). The black bar represents the line scan analysis presented at right indicating average island height of approximately 15 nm.
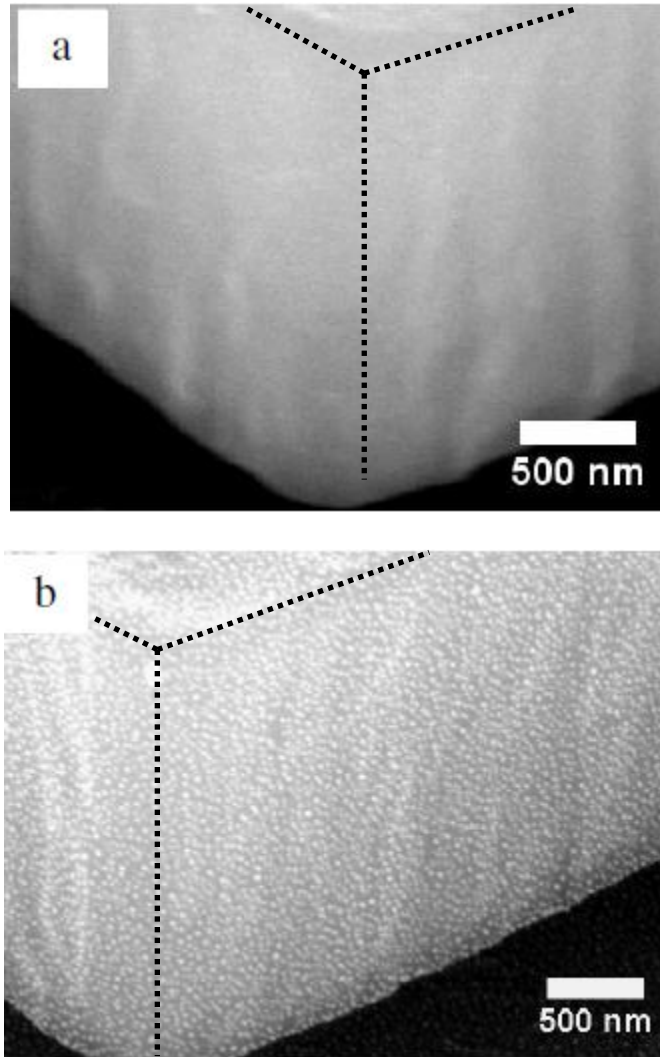
Figure 5.4. SEM photographs of (a) native oxide-coated cantilever beam and (b) gold nanoparticle-coated cantilever beam. Top and two-side surfaces of the beams are visible and indicated by the dashed lines.
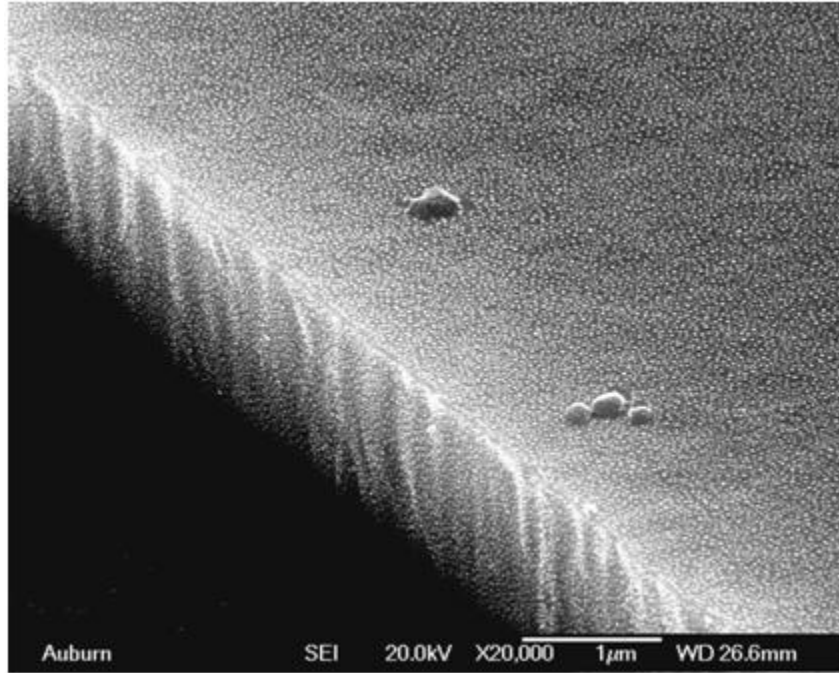
Figure 5.5. SEM photograph of cantilever beam underside coated with

gold nanoparticles.

the AFM scan in Fig. 5.3 was increased to approximately 6 nm after gold nanoparticle deposition. The typical RMS roughness of polysilicon surfaces is 5 to 7 nm, with pits and valleys as deep as 10 nm. The 10-20 nm particulates formed during nanoparticle deposition should, therefore, theoretically be large enough to overcome these deep features and further increase the surface roughness.

Several polysilicon device chips were actuated and measured following the procedures discussed in Chapters 3 and 4 in order to determine the effect of GXL deposited gold nanoparticles on adhesion (Hurst et al. 2009b). Fig. 5.6 presents interferograms of a native oxide-coated cantilever beam control array. Fig. 5.6(a) represents the array in the initially free standing, unloaded state. The free standing position is evidenced by the lack of interference fringes, as described in Chapter 3. In contrast, one beam in this array is not free standing (second beam from the bottom). This particular array, as well as many other control arrays, were electrostatically loaded and then relaxed. Fig. 5.6(b) illustrates the cantilever beam array following actuation. After the beams were unloaded, they exhibited adhesion to the substrate and are no longer free standing as indicated by the interference fringes. All of the cantilever beams within these control samples were unable to overcome the inherent surface forces following actuation, becoming permanently adhered to the substrate. Fig. 5.7 presents the experimental beam profiles for the 500-μm long cantilever beam from Fig. 5.6 at varying applied voltages. In Fig. 5.7(a), the actuation voltage is increased from 0 to 120 V. Profiles of the experimental data collected at 0, 30, 60, 90, and 120 V are shown to illustrate the deflection of the beam with increased voltage. Fig. 5.7(b) presents the beam profiles while the voltage was decreased from 120 V back to the unloaded state of 0 V. The profiles illustrate that the beam was permanently adhered to the substrate and, at the unloaded state, is said to have an "S"-shape.
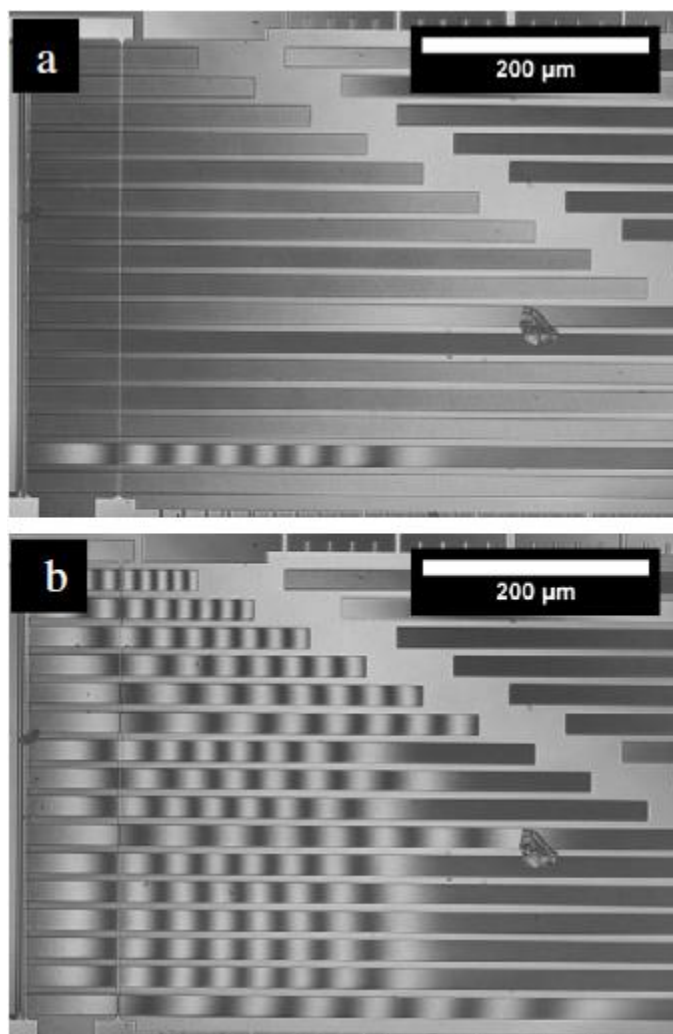
Figure 5.6. Interferograms of a native oxide-coated cantilever beam array (a) initially free

standing prior to actuation and (b) permanently adhered to the

substrate following actuation.
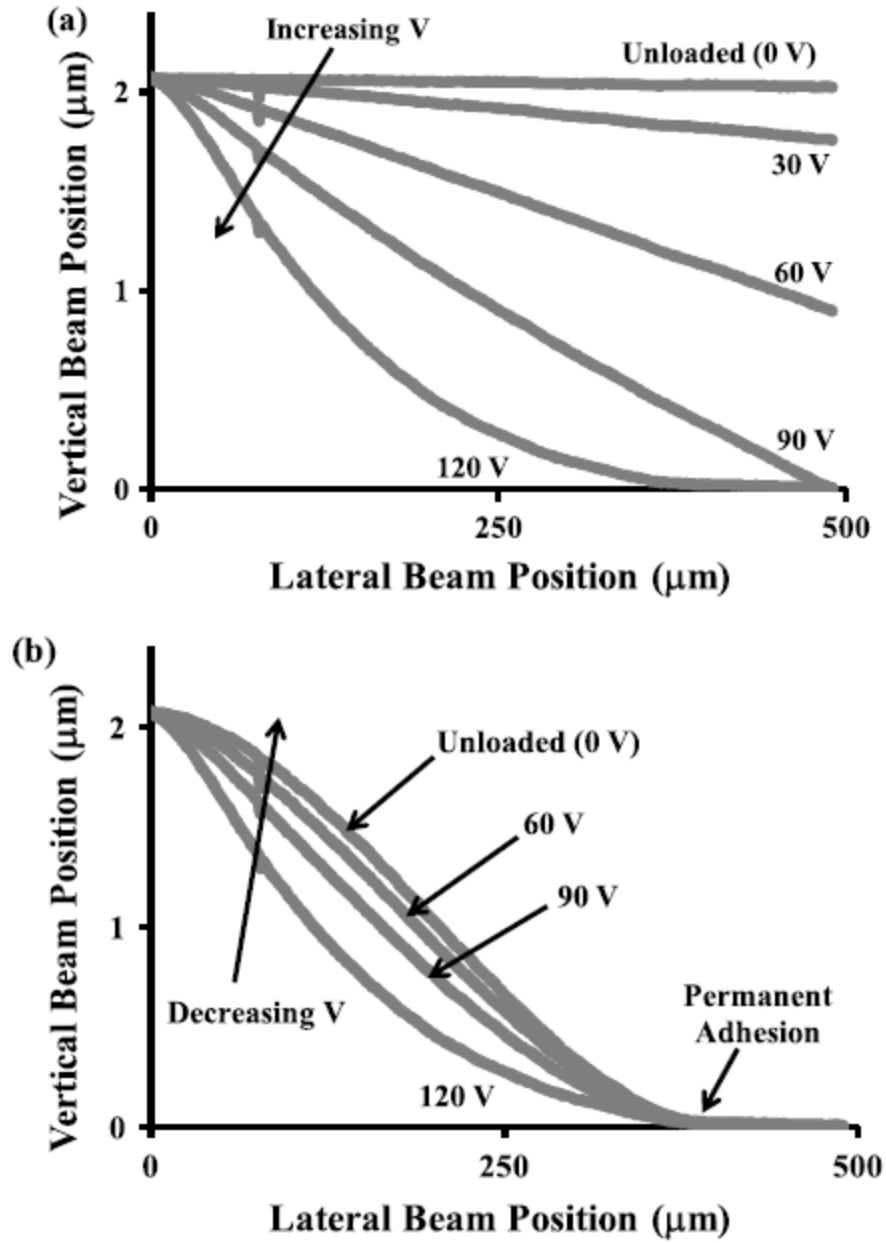
Figure 5.7. Profiles of a selected cantilever beam from Figure 5.10 (a) with increasing

electrostatic loading and (b) decreasing electrostatic loading.

Beam thickness is not to scale.

The apparent work of adhesion of these control cantilever beam arrays was quantified using the method discussed in Chapter 4. Extremely clean polysilicon cantilever beams, with a very uniform layer of native silicon oxide, typically exhibit an apparent work of adhesion of ca. 20 mJ/m^2 (Ashurst et al. 2000; Ashurst et al. 2001a). The native oxide-coated arrays examined in this study exhibited an apparent work of adhesion of 700 ± 100 μJ/m^2. This adhesion energy is still relatively high, but is likely lower than the expected value due to surface contamination and inhomogeneities characteristic of native oxide layers. For these control arrays, the adhesion energy was still great enough to permanently adhere the beams to the substrate.

Cantilever beam arrays coated with AuNPs deposited by gas-expanded CO_2 were also actuated and analyzed following the same actuation procedure. Fig. 5.8 presents an array of AuNP-coated cantilever beams (a) initially free standing before actuation, (b) electrostatically loaded with a voltage of 120 V and (c) following actuation at an unloaded state. Once again, the lack of interference fringes in Fig. 5.8(a) illustrates free standing beams, while the appearance of fringes in the electrostatically loaded case confirms the bending and contact of beams to the substrate following the same procedure as the native oxide-coated array in Fig. 5.7. However, for the AuNP-coated beams, as the electrostatic load was relaxed, a majority of the beams returned to their original free standing positions as illustrated by Fig. 5.8(c). The final unloaded states of the cantilever beams in Fig. 5.8(c) are noticeably different than those in Fig. 5.6(b), indicating a reduction in apparent work of adhesion.
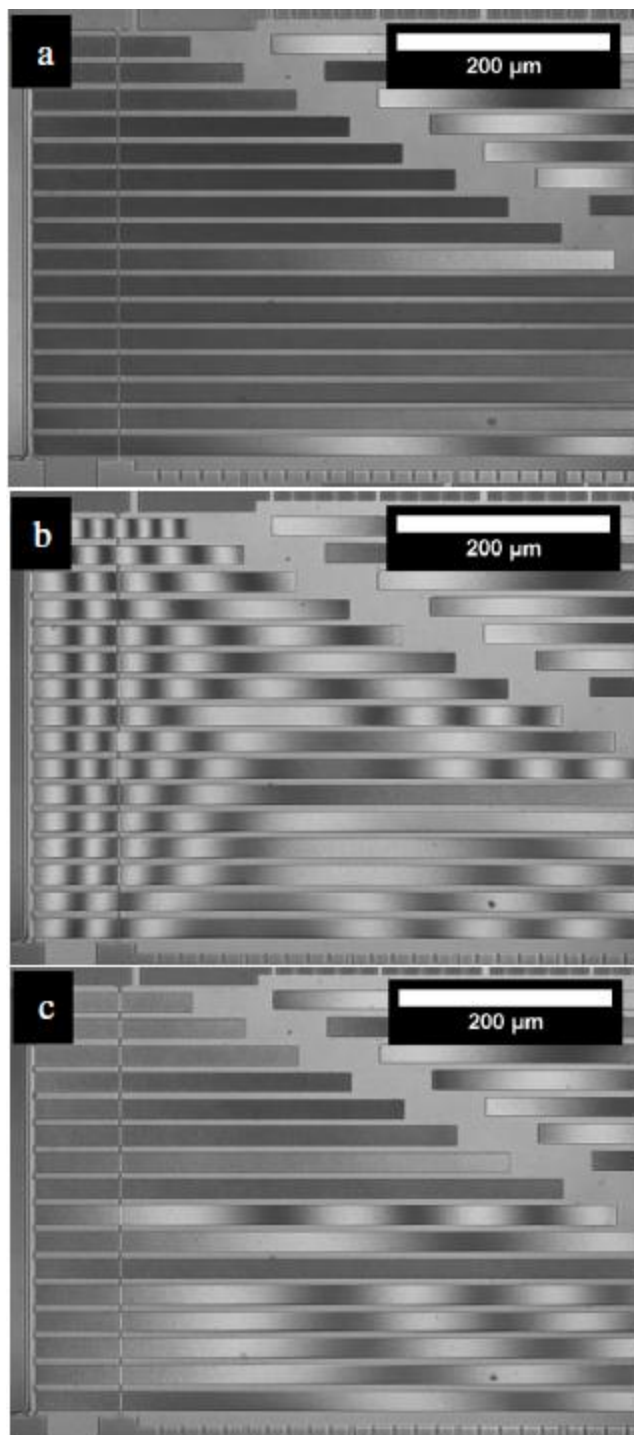
Figure 5.8. Interferograms of an AuNP-coated cantilever beam array (a) initially free standing before electrostatic actuation, (b) electrostatically loaded at 120 V and (c) unloaded following actuation.

125

Several cantilever beam arrays coated with AuNPs were examined in this study. Following actuation, not a single beam located within any AuNP-coated array exhibited the S-shaped adhesion seen in Figs. 5.6(b) and 5.7(b). All of the beams in these arrays either returned to their original free standing position or adhered to the substrate near the beam tip after actuation. The fact that AuNP-coated beams were not observed to adhere in the typical S-shape and on occasion adhered in an arc-shape suggests that (1) adhesion is reduced by the presence of AuNPs deposited by gas-expanded liquids and (2) adhesion at the tip may result from some other phenomenon. Fig. 5.9 presents an SEM image of an AuNP-coated substrate where a cantilever beam was adhered at the tip. The image indicates that in the region of contact and adhesion, areas exist where no particles were found after removal of the beam. This observation suggests that particles can be moved from areas of the polysilicon surface leaving particle-free regions where adhesion can occur due to recovery of native oxide contact areas.

Although some adhesion was experienced with AuNP-coated CBAs in the form of arc-shaped beams, the estimated apparent work of adhesion was drastically reduced when compared to native oxide-coated beams. In fact, all of the beams less than or equal to 500 μm in length became free standing, while all beams longer than 500 μm were adhered in an arc-shape. Based on Eqn. (4.15), the shortest adhered beams will exhibit the highest adhesion energies due to the s^4 dependence on crack (or un-adhered) length. Therefore, the shortest beam that remained adhered (700 μm) yields an upper limit apparent work of adhesion of approximately 10 μJ/m^2. Even this estimated value is a great improvement over polysilicon cantilever beams coated with a natural silicon oxide layer. Table 5.1 compares apparent work of adhesion values for silicon oxide layers, organic monolayer coatings (Ashurst et al. 2000) and AuNP coatings on polysilicon beams. Beams coated with AuNPs exhibit a much lower apparent work of adhesion than
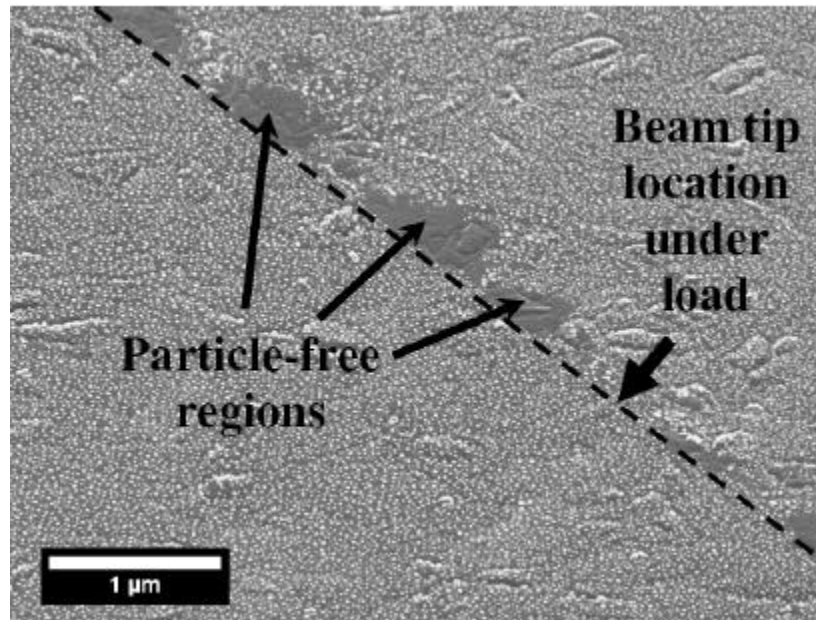
Figure 5.9. SEM image of a region of tip-adhesion of AuNP-coated

CBAs illustrating particle-free regions.

Coating	Apparent work of adhesion ($\mu J/m^2$)
Very smooth SiO_2	ca. 20,000
SiO_2 (this study)	ca. 700
OTS	12
FDTS	10
AuNP (this study)	< 10

Table 5.1. Comparison of apparent work of adhesion values.

achieved in previous examinations, including results obtained using hydrophobic SAMs such as octadecyl trichlorosilane (OTS) and perfluorodecyl trichlorosilane (FDTS).

5.5   Conclusions

In this chapter, gold nanoparticles were successfully deposited onto polysilicon cantilever beams using CO_2-expanded hexane and supercritical drying. This resulted in reduced microstructure adhesion presumably due to additional roughening of the surfaces and commensurate reduction of the real area of contact. In contrast to traditional methods of surface roughening, the deposition of hydrophobic ligand-capped nanoparticles would provide opportunities for control over the chemical nature of contact as well as the topographical benefits of reduced contact area. The gas-expanded liquid particle deposition technique is conformal and compatible with current microfabrication techniques as opposed to simple evaporation or drop casting of nanoparticles.

Polysilicon cantilever beams coated with AuNPs exhibited decreased apparent work of adhesion of less than 10 $\mu J/m^2$ – approaching two orders of magnitude lower than beams coated with native oxide layers. This new surface modification technique of depositing nanoparticles via GXLs successfully increases the surface roughness of microstructures fabricated from silicon-based materials and, in turn, decreases the real contact surface area between microstructures and the underlying substrate. By providing hydrophobic asperities onto the hydrophilic silicon surfaces, inherent attractive surface forces are reduced, allowing for the mechanical restoration forces of bending microstructures to overcome the attraction and avoid permanent adhesion. The subsequent chapters will further examine how nanoparticles deposit onto surfaces during the GXL process, the effect of varying nanoparticle concentration (and by

extension surface roughness and real contact surface area) on adhesion, as well as methods for

producing more robust and durable AuNP coatings that cannot be affected by simple mechanical

contact.

CHAPTER 6

NANOPARTICLE DEPOSITION ON SUBSTRATES OF

VARYING SURFACE ENERGY

6.1 Introduction

The deposition of stabilized nanoparticles via gas-expanded liquids onto silicon-based surfaces for microtribology control is a fundamentally new concept and, therefore, little is known about how nanoparticles deposit onto the surfaces. The opportunity exists to deposit various self-assembled monolayers in liquid phase onto MEMS and tribology chips prior to nanoparticle deposition in order to further reduce microstructure adhesion by providing both a low energy surface and a rough nanoparticle coating. Before the deposition of nanoparticle films on SAM-coated silicon becomes a viable option for anti-stiction coatings, the behavior of GXL-deposited nanoparticles on such surfaces must be characterized. In this chapter, dodecanethiol-stabilized gold nanoparticles are deposited by CO_2-expanded liquids onto monolayers of octadecyl trichlorosilane (OTS), perfluorodecyl trichlorosilane (FDTS), mercaptopropyl trimethoxysilane (MPTS), and aminophenyl trimethoxysilane (APhTS). The wetting behavior of the SAM films is examined by determining the critical surface tensions of the surfaces. The behavior of nanoparticle coatings is then examined as a function of surface energy as well as film hydrophobicity and oleophobicity.

6.2   Experimental details

Si (100) substrates were first prepared following the cleaning process described in Chapter 3. Self-assembled monolayer coatings were then deposited via a variety of methods. OTS monolayers were deposited by immersing substrates into a 1 mM solution in hexane. Prior to substrate immersion, the 1 mM solution was allowed to react for 45 min. Substrates were then immersed for 45 min before being copiously rinsed in hexane and dried with nitrogen. FDTS monolayers were formed by a similar method using a 1 mM solution in hexane. MPTS monolayers were formed by immersing the substrates into a solution containing 400 µl MPTS and 400 µl DI water in 20 ml electronic grade isopropanol heated to 70 °C for 30 min (Vakareslski et al. 2007; Goss et al. 1991). The samples were then rinsed in isopropanol, hexane and DI water consecutively to remove any excess physiosorbed organic molecules. APhTS monolayers were formed following a procedure outlined by Zhang and Srinivasan (2004). Samples were first rinsed consecutively in isopropanol, a 1:1 (v/v) mixture of isopropanol and toluene, and pure toluene. Then the samples were immersed in a 3 mM APhTS solution in toluene for 30 min. Following monolayer deposition, the samples were rinsed in toluene, immersed in toluene for 30 min, and rinsed in isopropanol. Following monolayer deposition, rinsing and drying under nitrogen, all coated substrates were heated at 120 °C for 1 h to anneal coatings. Contact angles of water were then measured to confirm monolayer deposition. The contact angle of water on OTS, FDTS, MPTS, and APhTS coated substrates were 108.7°, 115.5°, 73.1°, and 67.9°, respectively. All of these values are in agreement with values that can be found in literature. Dodecanethiol-capped AuNPs were finally deposited in equal concentrations on SiO_2 and SAMs on Si (100) following the GXL particle deposition procedure described in Chapter 3.

6.3 Critical surface tension of SAMs

The critical surface tension of a surface, developed from experiments by Zisman (1964), is a way to relate the surface energy of a solid to the minimum liquid surface tension required for complete spreading (or wetting) on the surface. Utilizing a Zisman plot, the contact angles are plotted against known surface tensions of various liquids. In this work, six liquids with known surface tensions were used to create Zisman plots for OTS, FDTS, MPTS, and APhTS monolayer films. The six liquids and their respective surface tensions (dyne/cm) at 25 °C are found in Table 6.1. The measured contact angle (θ) of a particular liquid droplet on a surface is directly proportional to the known surface tension of the liquid (γ_L) following Eqn. (6.1):

$$\cos\theta = c_1\gamma_L + c_2 \tag{6.1}$$

where c_1 and c_2 are linear coefficients. When a Zisman plot is created, plotting the cosine of the contact angles for a variety of liquid surface tensions, the critical surface tension (γ_C) for complete liquid spreading can be extrapolated at the point where $\cos\theta = 1$.

To further illustrate how a Zisman plot for a particular solid surface produces the critical surface tension, Fig. 6.1 presents the Zisman plot for an OTS monolayer film using the surface tension of the six liquids given in Table 6.1. The plot illustrates the linear trend that exists between the contact angle and surface tension. The linear trend line in Fig. 6.1 trends to the experimental data with an R^2 value of 98% and yields the equation:

$$\cos\theta = 1.5921 - 0.0272\gamma_L. \tag{6.2}$$

Extrapolation of Eqn. (6.2) at $\cos\theta = 1$ yields a critical surface tension, γ_C, of 21.8 dyne/cm. The reported literature value for a close-packed OTS monolayer on silicon is 20.2 ± 1 dyne/cm (Tillman et al. 1988). The disparity in the two numbers can be attributed to parameters such as liquid purity, temperature and ambient humidity (Brzoska et al. 1992).

Chemical name	Liquid surface tension at 25 °C (dyne/cm)
Methanol	22.5
Chloroform	26.7
Hexadecane	27.5
Dimethyl sulfoxide	43.5
Ethylene glycol	47.3
Water	72.1

Table 6.1. Liquid surface tensions of chemicals used for critical

surface tension measurements (Kulkarni et al 2005).
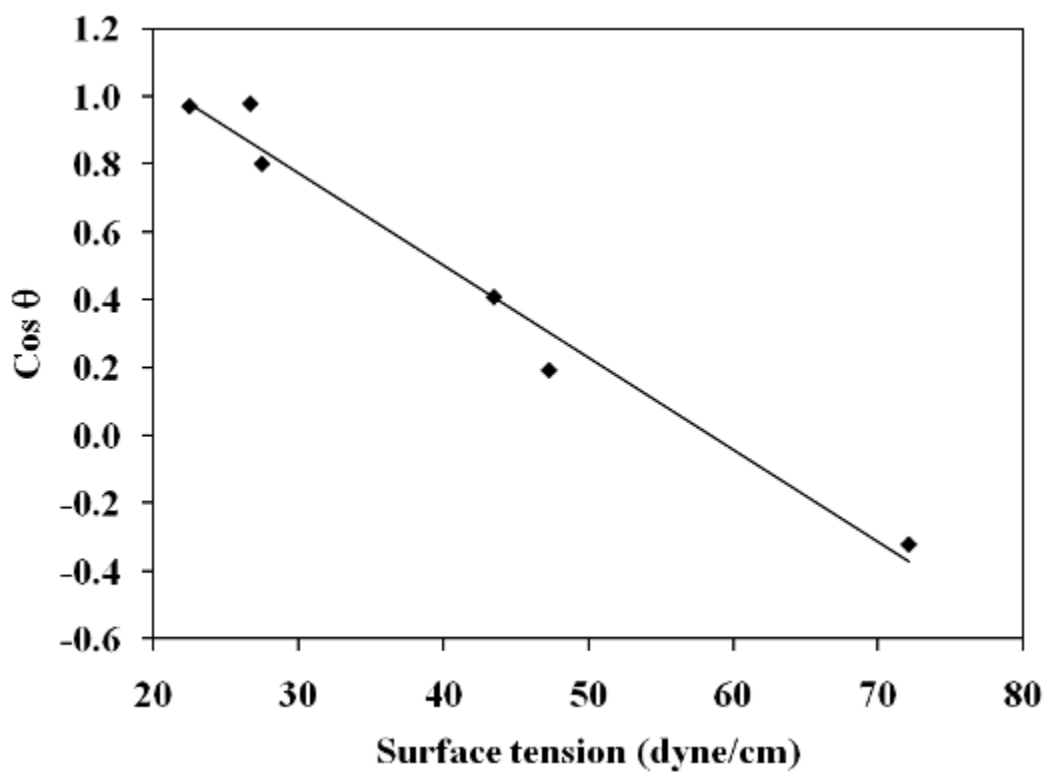
Figure 6.1. Zisman plot for an OTS monolayer on Si (100) illustrating the linear trend between

contact angle and liquid surface tension.

Fig. 6.2 presents the combined Zisman plots for FDTS, MPTS and APhTS coatings on Si (100). Table 6.2 gives the critical surface tensions determined from the plots for all five surface coatings, in addition to the c_1 and c_2 coefficients for the linear trends which can be inserted into Eqn. (6.1) for extrapolation. The critical surface tension values indicate that the FDTS monolayer, with a critical surface tension of 3.6 dyne/cm, likely cannot be completely wetted by any liquid. Meanwhile, MPTS monolayers can only be wetted by liquids with surface tensions of 25.2 dyne/cm or less, such as oily substances like methanol. The critical surface tension of very smooth and clean SiO_2 is very difficult to determine experimentally due to its extremely hydrophilic and oleophilic nature. Therefore, the accepted literature value of 140 dyne/cm (Janssen et al. 2006) is used during this study. The critical surface tensions in Table 6.2 will be further used to examine the behavior of deposited gold nanoparticles on SAM coated substrates.

6.4 Characterization of AuNPs on SAMs

Due to the gold nanoparticles being stabilized by "oily" dodecanethiol ligand tails during gas-expanded liquid deposition, the hydrophobicity and oleophobicity of surfaces to be coated with nanoparticles becomes increasingly important. To illustrate the impact that surface oleophobicity has on the deposition of gold nanoparticles, Figs. 6.3, 6.4 and 6.5 present optical microscope photographs of equal concentrations of dodecanethiol-capped nanoparticles deposited onto SiO_2, OTS and FDTS, respectively. For the most part, Fig. 6.3 represents an optically clean surface after particle deposition. However, agglomerations of particles are visible on the OTS coated substrate in Fig. 6.4. This effect is even more evident on the FDTS coated substrate in Fig. 6.5. The explanation for this particle agglomeration lies within the oleophobicity
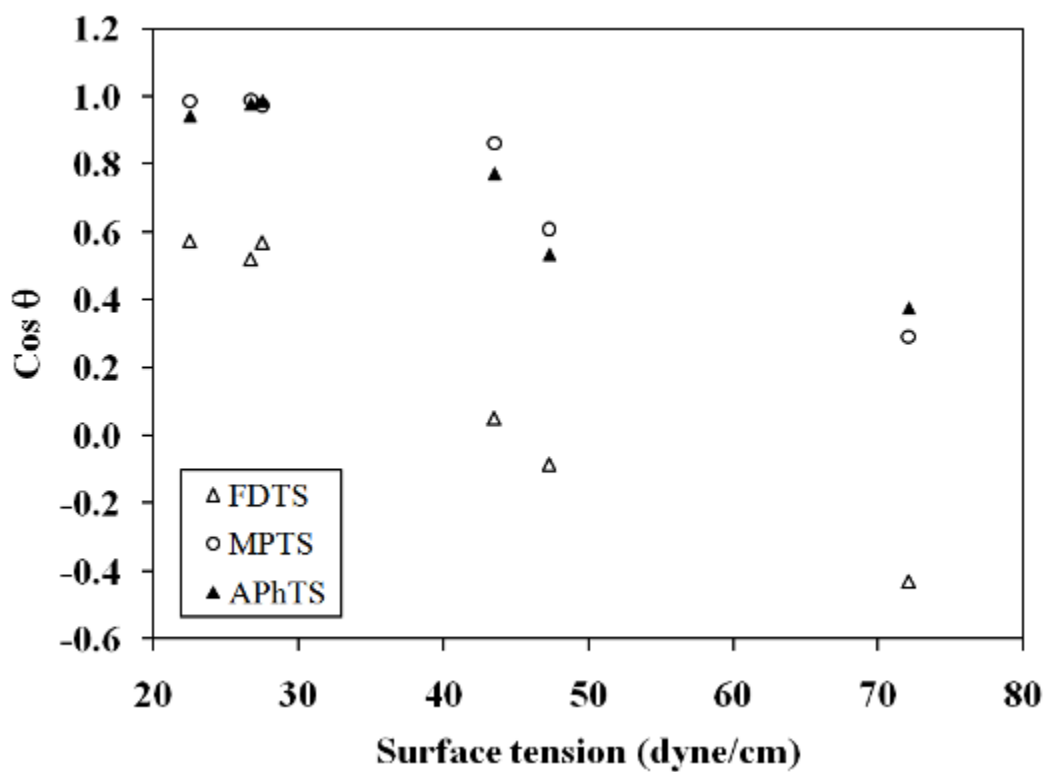
Figure 6.2. Combined Zisman plots for FDTS, MPTS and APhTS coatings on Si (100)

substrates.

Coating	Critical surface tension (dyne/cm)	c_1 coefficient	c_2 coefficient
SiO_2	140	N/A	N/A
OTS	21.8	-0.0272	1.5921
FDTS	3.6	-0.0220	1.0797
MPTS	25.2	-0.0147	1.3700
APhTS	22.0	-0.0133	1.2996

Table 6.2. Critical surface tensions and Zisman plot linear coefficients.
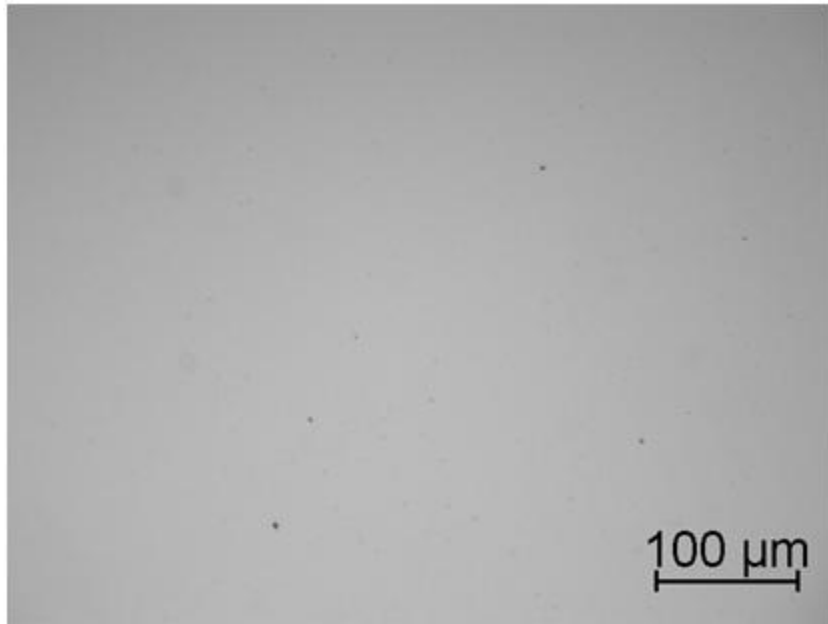
Figure 6.3. Optical photographs of AuNPs on native SiO_2 at 20X.
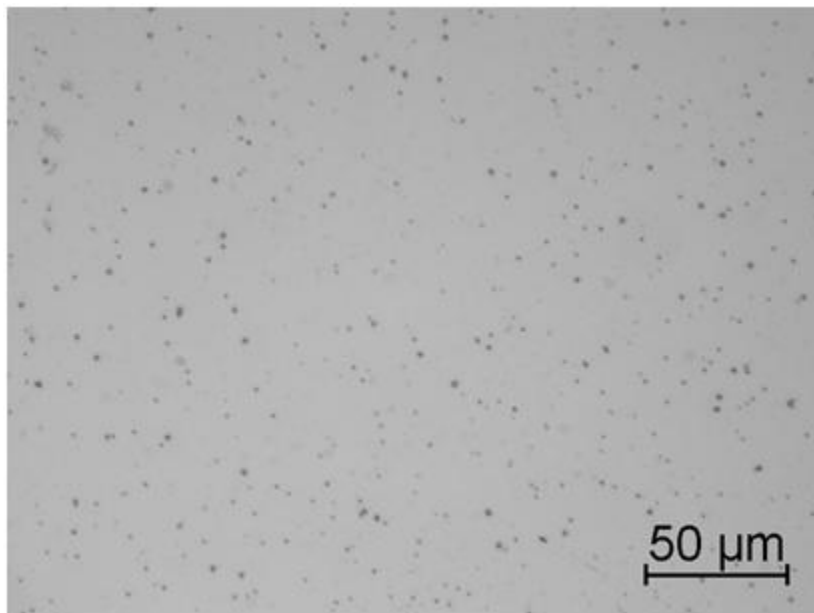
Figure 6.4. Optical photograph of AuNPs on OTS-coated silicon at 40X.
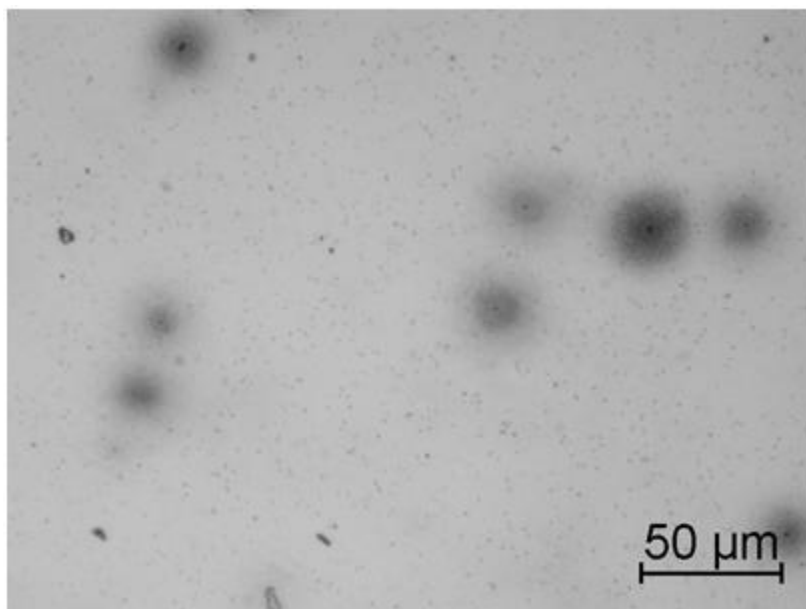
Figure 6.5. Optical photograph of AuNPs on FDTS-coated silicon at 40X.

of the three surfaces. SiO_2 is an oleophilic surface on which "oily" dodecanethiol-capped particles can freely deposit. OTS however is slightly oleophobic, with a hexadecane contact angle of 36.8°. Therefore, there is repulsion between the OTS monolayer and the oily particles attempting to deposit on the surface. Rather than deposit into a uniform nanoparticle film, the particles prefer to form aggregates on the surface. The repulsion by the surface and the desire of the particles to aggregate are increased on the FDTS monolayer, which exhibits greater oleophobicity. On the other hand, MPTS and APhTS are oleophilic and would, therefore, allow for nanoparticles to deposit in a cleaner fashion similar to SiO_2. This will be further illustrated in Chapter 8.

In order to more closely examine the deposition characteristics of "oily" gold nanoparticles on the various SAM coatings, samples were examined via both SEM and AFM. Figs. 6.6, 6.7, 6.8, 6.9, and 6.10 present SEM micrographs taken at 35000X magnification of AuNP films on SiO_2, OTS, FDTS, MPTS, and APhTS, respectively. At first glance, it is easily determined that the agglomeration occurs on the OTS and FDTS surfaces in Figs. 6.7 and 6.8. A higher percentage of the substrate surfaces coated with MPTS and APhTS appear to be covered by nanoparticles, as illustrated by Figs. 6.9 and 6.10. Initial glance of the nanoparticles deposited on SiO_2 in Fig. 6.6 gives indication that the particles prefer to agglomerate on the oleophilic surface rather than readily form ordered monolayers. However, since this would contradict the hypothesis that oleophobic nature is important for particle film formation, further investigation was performed by zooming out on the AuNP-coated SiO_2 substrate. Fig. 6.11 provides a 15000X magnification SEM image of the same sample imaged in Fig. 6.6. This SEM image depicts "holes" in two different layers of nanoparticles. The darker, more visible holes
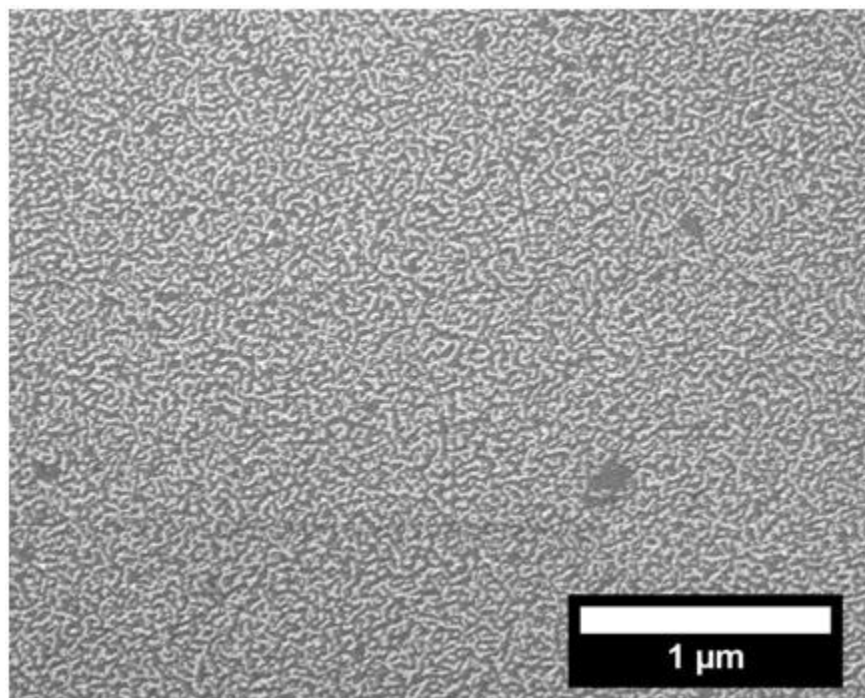
Figure 6.6. SEM micrograph (35000X) of AuNPs on SiO_2.
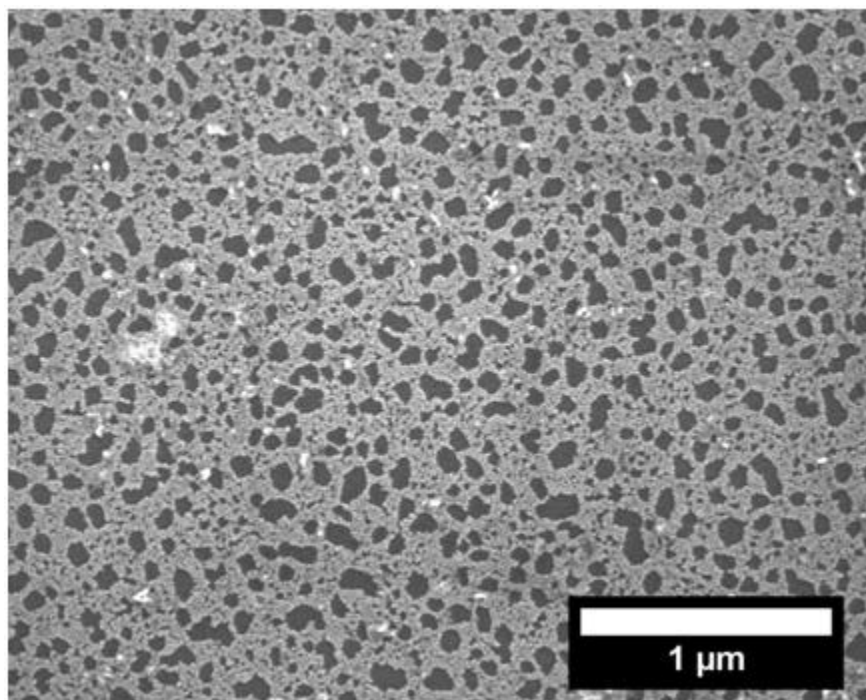
Figure 6.7. SEM micrograph (35000X) of AuNPs on OTS.
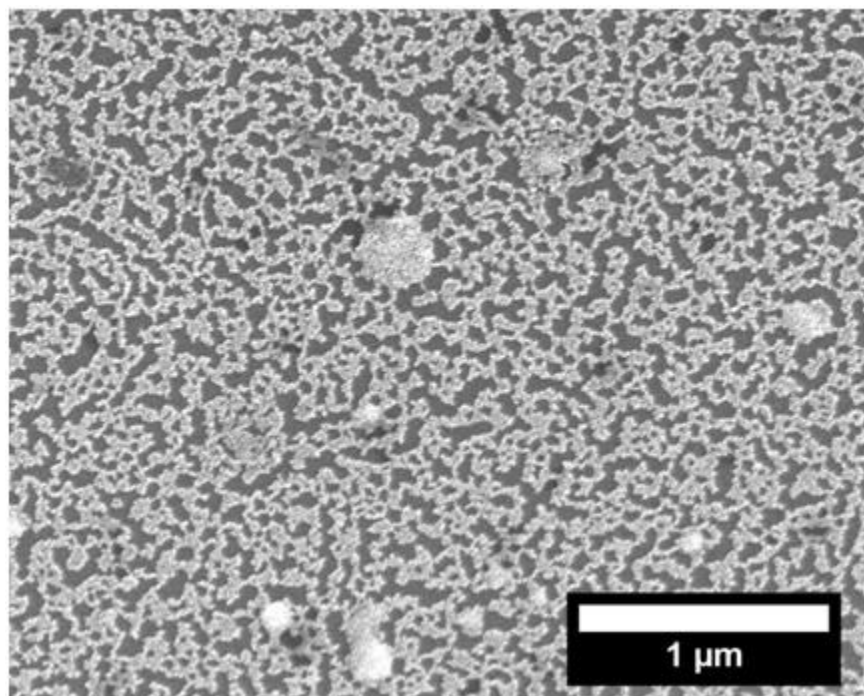
Figure 6.8. SEM micrograph (35000X) of AuNPs on FDTS.
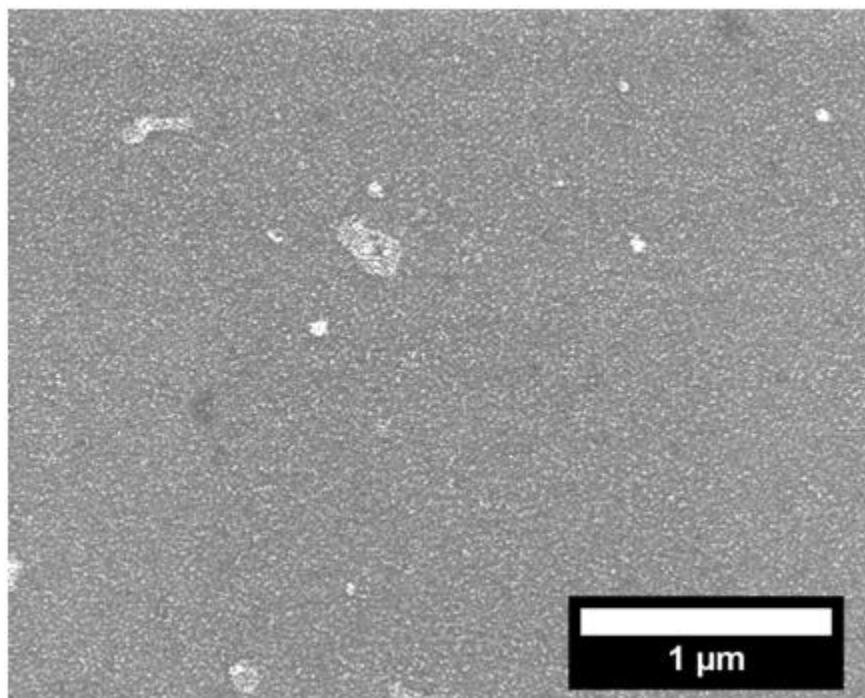
Figure 6.9. SEM micrograph (35000X) of AuNPs on MPTS.
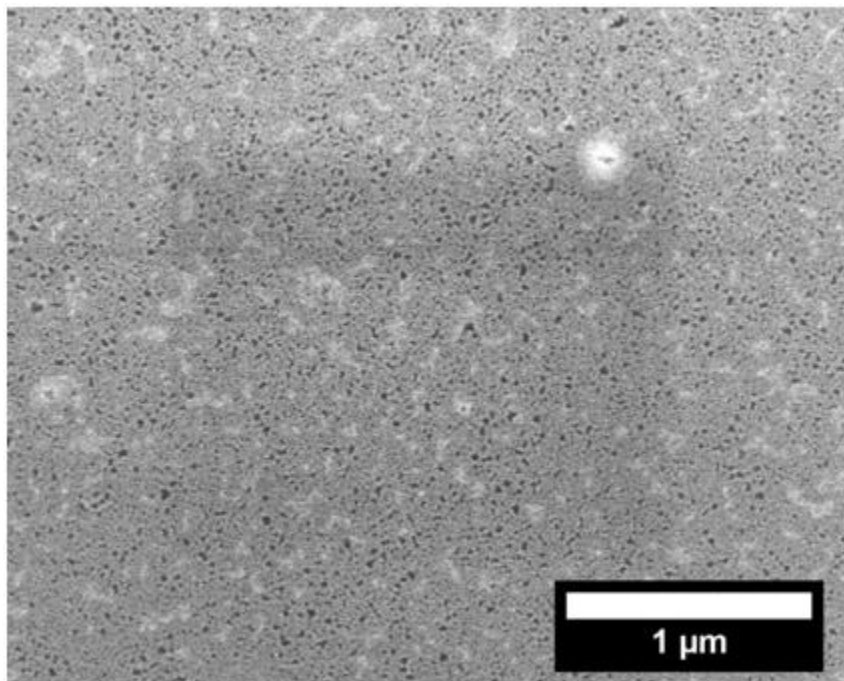
Figure 6.10. SEM micrograph (35000X) of AuNPs on APhTS.
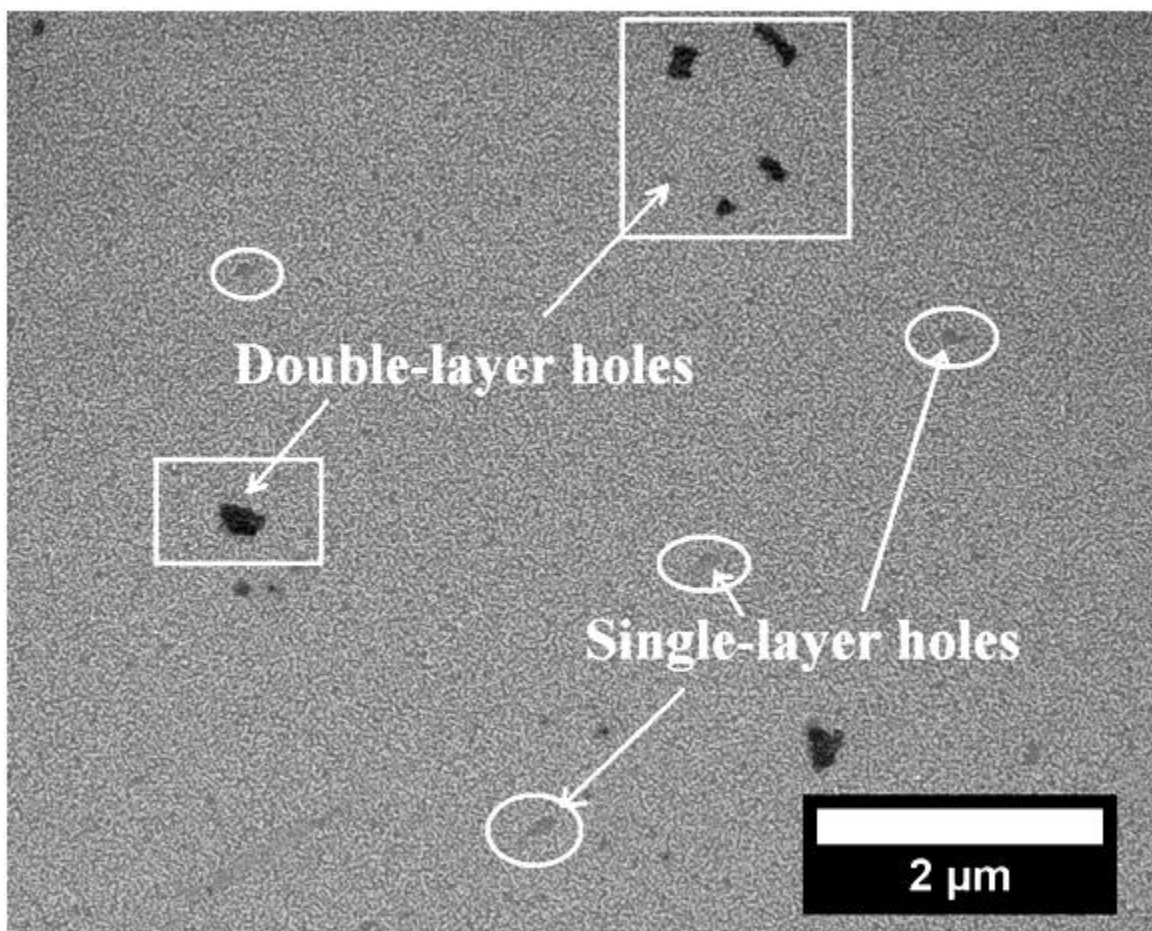
Figure 6.11. SEM micrograph (15000X) of AuNPs on SiO_2 illustrating "holes"

in two individual layers.

represent areas where the SiO₂ substrate is exposed while the lighter holes exist in an upper AuNP layer where a primary AuNP layer already exists.

Based on this information, the surface coverage fraction – the fraction of the surface area covered by the nanoparticle film – was estimated for the five separate samples using simple thresholding techniques in ImageJ software. The surface coverage fractions of AuNPs on SiO_2, OTS, FDTS, MPTS, and APhTS, respectively, were 0.96, 0.67, 0.59, 0.87, and 0.91. The fractional surface coverage was plotted as a function of hexadecane contact angle to examine the trend between substrate surface energy and particle coverage, as shown in Fig. 6.12. Hexadecane, an oily hydrocarbon consisting of a sixteen-carbon chain, was assumed to interact similarly to the surface as the exposed twelve-carbon chain of dodecanethiol capping ligands. As shown in the graph, the experimental data presents a distinct second-order polynomial trend. This data confirms that the oleophobic nature of the substrate is critical for the deposition of dodecanethiol-stabilized AuNP films. However, the fractional surface coverage cannot be easily compared to the substrate critical surface tension due to the values of OTS, MPTS and APhTS all being within about a 3 dyne/cm range. Therefore, oleophobic and hydrophobic nature is the only true way to compare the results. The data in Fig. 6.12 illustrates that as the contact angle of hexadecane on a particular surface approaches zero, the wettability of dodecanethiol-capped nanoparticles increases allowing for a higher projected particle surface coverage. Fig. 6.13 charts the projected surface coverage of AuNP coatings on the various surfaces along with the respective contact angles of water and hexadecane. The figure illustrates that the surface coverage decreases as both oleophobicity (from hexadecane contact angle) and hydrophobicity (from water contact angle) increase. This trend can be further explained by the mode of film growth exhibited by the particles on the various surfaces.
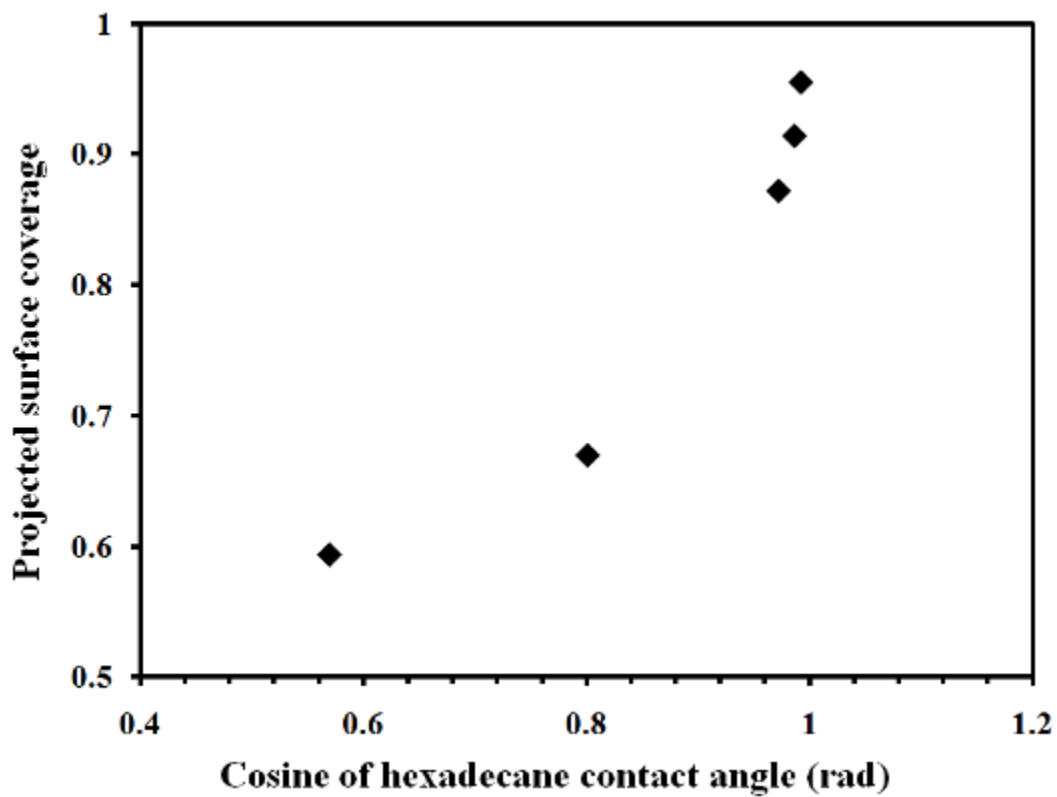
Figure 6.12. Fractional surface coverage of AuNPs plotted against the cosine of the contact

angle of hexadecane (cos θ).
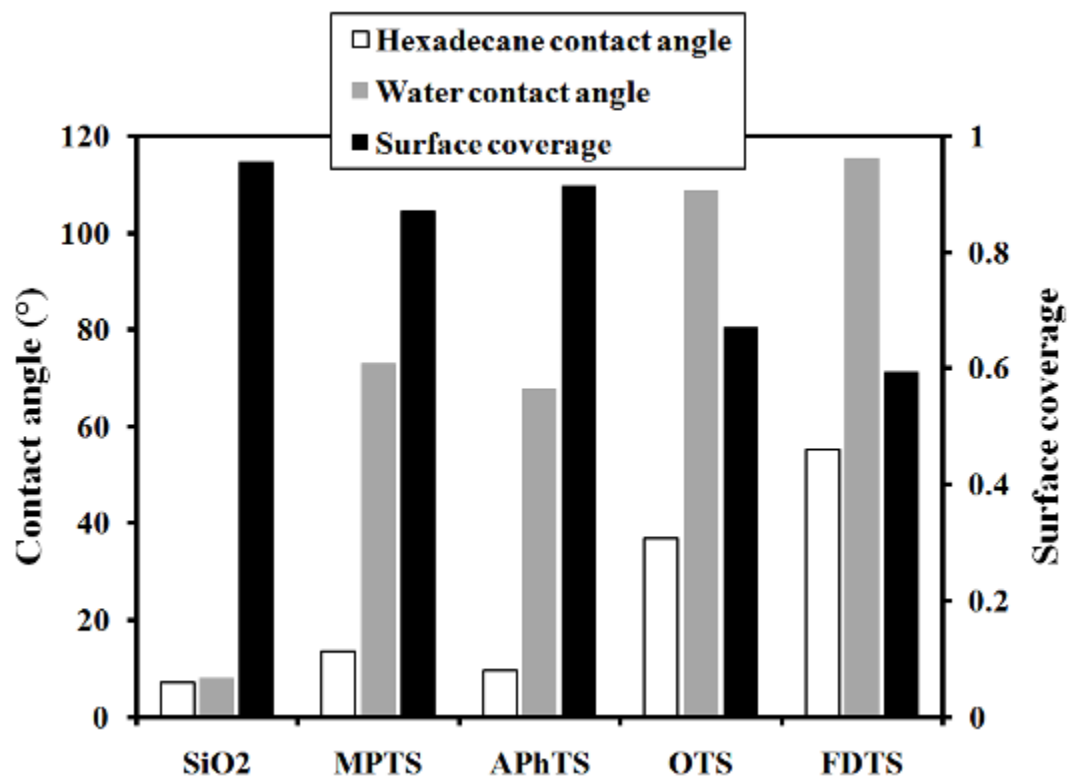
Figure 6.13. Water and hexadecane contact angles of SAM coatings and fractional surface coverage of AuNP films on SAMs.

Fig. 6.14 presents 3 x 3 μm AFM scans of AuNP films on (a) SiO$_2$, (b) OTS and (c) FDTS. A line scan of each AFM scan is shown to illustrate the height profile of the AuNP films on each respective surface. The line scans illustrate the height of nanoparticle films which can provide information about the mode of particle film growth. The peak height of AuNPs on SiO$_2$ represents a height of about 5 nm which is the approximate diameter of the nanoparticle population – illustrating that the nanoparticles are being deposited in monolayers following the Frank-van der Merwe (layer-by-layer) mode of film growth (Ohring 2002). This type of film growth occurs when the surface energy of the surface is greater than the surface energy of the film, i.e. $\gamma_s > \gamma_f$. This is intuitive, as the surface energy of SiO$_2$ is known to be extremely high. When low surface energy monolayers are deposited onto SiO$_2$ surfaces, a different mode of film growth is experienced. The line scan of AuNPs on OTS, shown in Fig. 6.14(b), illustrates some monolayer growth (~ 5 nm in height) as well as multiple layer islands of about 10 and 15 nm in height. The profile of AuNPs on FDTS exhibits even higher islands of up to 80 nm in height. This result suggests that as the surface energy is decreased, the mode of film growth shifts from layer-by-layer to a layer-plus-island (Stranski-Krastanov) mode, which occurs when the surface energy of the surface is less than that of the film ($\gamma_s < \gamma_f$).

To further explain the switch from layer-by-layer film growth to the growth of large islands, the critical surface tension of dodecanethiol films on a gold (111 orientation) substrate was estimated using experimental data from literature. Table 6.3 presents the contact angles of various liquids on a dodecanethiol monolayer as determined by Bain and Whitesides (1989), along with the liquid surface tensions. Creating a Zisman plot of the data yields a critical surface tension for dodecanethiol of 15.3 dyne/cm. This indicates that the surface energy of a gold film
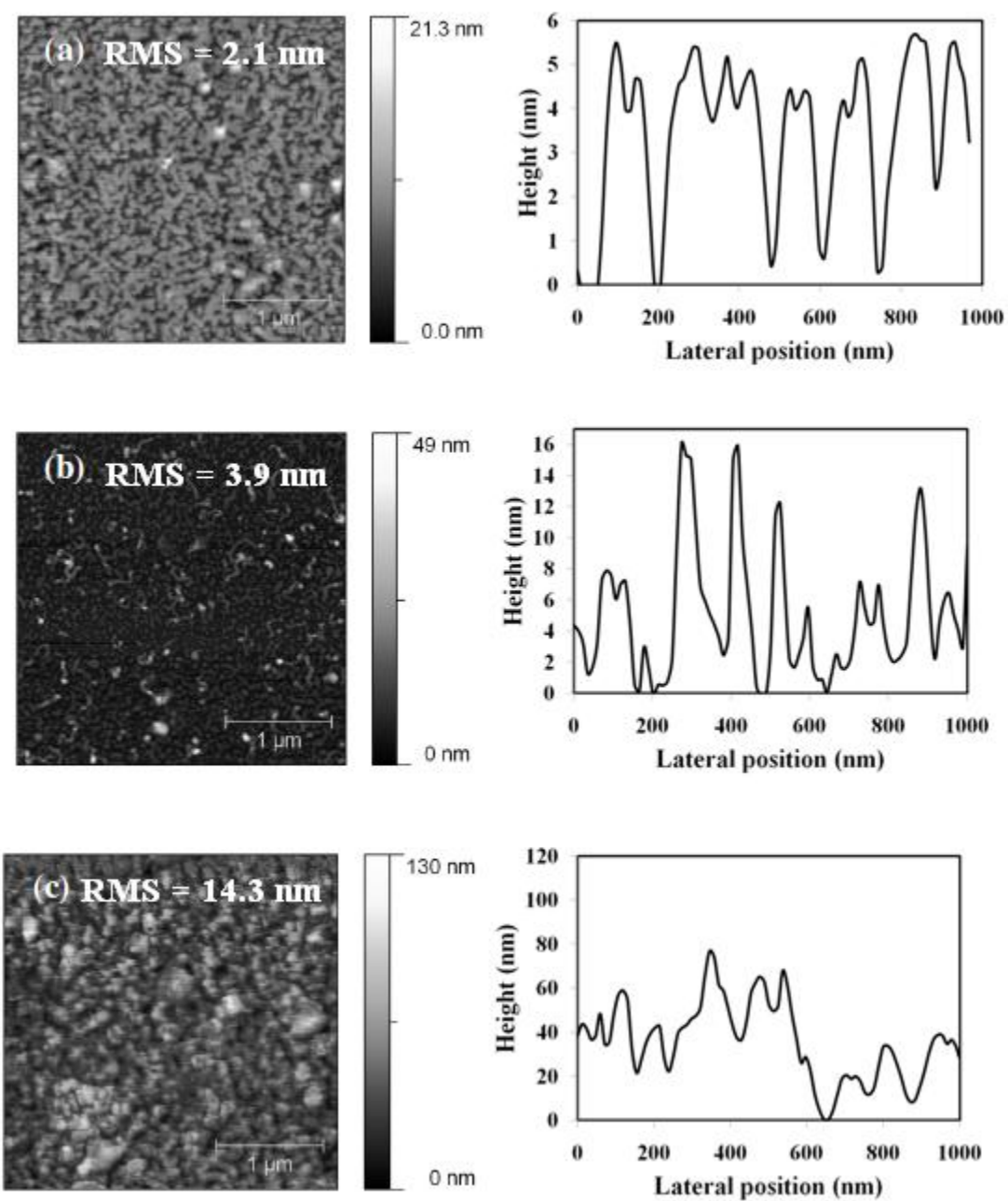
Figure 6.14. AFM scans and line scan profiles of AuNP films on (a) SiO$_2$,

(b) OTS and (c) FDTS.

Liquid	Surface tension (dyne/cm)	Contact angle (°)
Decane	23.8	36
Hexadecane	27.2	47
Bicyclohexyl	32.4	56
Bromonapthalene	44.4	68
Water	72.1	112

Table 6.3. Surface tension and contact angle of liquids used for

Zisman plot of a dodecanethiol monolayer.

made from dodecanethiol-capped particles is greater than the surface energy of an FDTS-coated substrate but less than the surface energy of all the other surfaces examined in this work. To easily view this phenomenon, Fig. 6.15 charts the RMS roughness of the resulting AuNP film on each of the five surfaces studied in order of decreasing critical surface tension (or surface energy). RMS roughness is a reasonable quantitative measurement for island formation as large islands result in a drastic increase in roughness, as previously shown by Fig. 6.14. The chart in Fig. 6.15 illustrates that the RMS roughness of films deposited onto surfaces with a critical surface tension of greater than 15.3 dyne/cm (designated by the vertical dashed line) have relatively similar values between 2 and 4 nm. However, the film deposited onto FDTS which has a critical surface tension of only 3.6 dyne/cm, has an RMS roughness of 14.3 nm due to the large nanoparticle islands that were formed. This confirms that a shift occurs at the surface tension of the capping ligand from layer-by-layer to layer-plus-island film growth.

6.5   Conclusions

Investigating how nanoparticle films deposit on surfaces of different surface energies is key for the ability to engineer nanoparticle films for various applications. This chapter provides a brief, yet very fundamental, investigation of how dodecanethiol-capped AuNPs deposit on oxide- and SAM-coated silicon surfaces. The initial hypothesis was that the surface coverage (projected by SEM image analysis) of AuNP films would trend directly with the Zisman critical surface tension of the coated surfaces. However, this proved to be false as the critical surface tension of SAM-coated silicon does not vary by more than about 3 dyne/cm. Therefore, the surface coverage was compared to the hydrophobicity and oleophobicity (as determined from water and

155
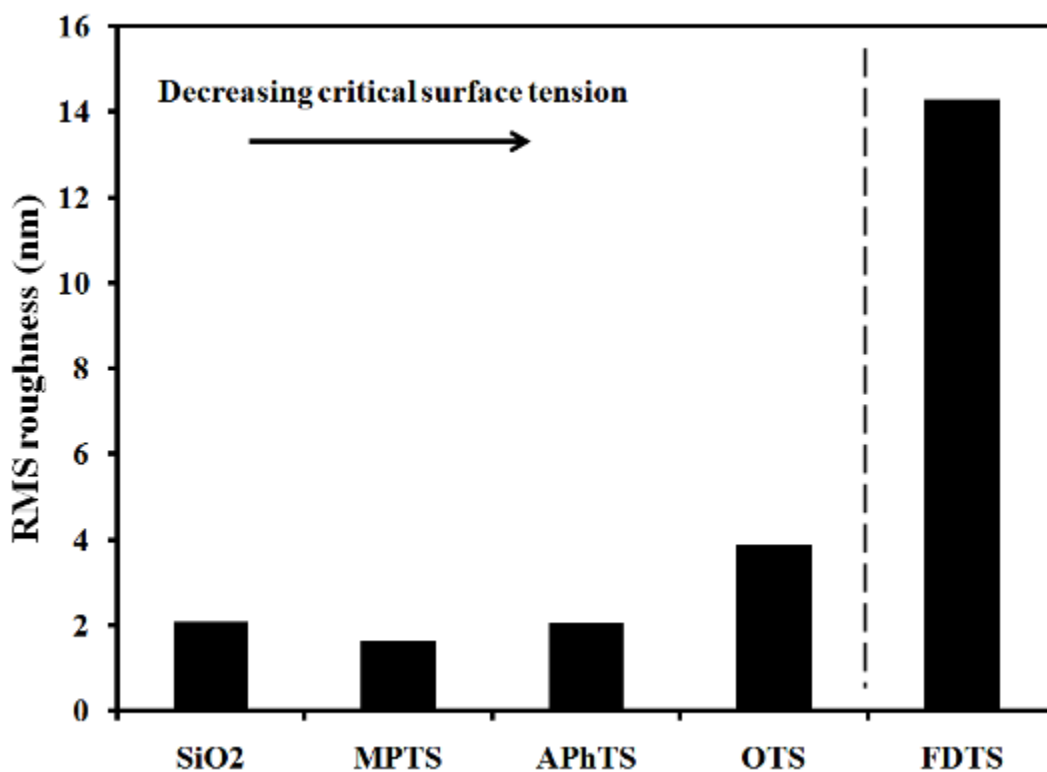
Figure 6.15. Chart of RMS roughness of AuNP films on examined surfaces in order of
decreasing critical surface tension. The dashed line represents the dividing boundary in surface
tension of 15.3 dyne/cm (dodecanethiol).

hexadecane contact angles) of the surfaces. Interestingly, yet intuitively, the surface coverage of the "oily" hydrocarbon-capped particles trended with the hexadecane contact angle. The interaction of the long hydrocarbon chains of dodecanethiol and hexadecane were assumed to be very similar, indicating that the oleophobic nature of the surface is very important for the morphology of the resulting nanoparticle film. It is important to note, however, that this investigation is very system-specific; i.e., the nanoparticle film morphology is also dependent on the choice of stabilizing/capping ligand and the interfacial interactions.

Of unique importance is the apparent effect of surface energy on the mode of nanoparticle film growth. AFM scan analysis of AuNP films on different surfaces illustrates a shift from layer-by-layer growth on SiO_2 to layer-plus-island growth on surfaces of reduced surface energy. When the critical surface tension of the substrate was reduced below that of the film (based on the capping agent used to stabilize the nanoparticles in solution), there was a shift from a layer-by-layer mode of film growth to one of layer-plus-islands. This shift drastically increased the surface roughness of the resulting nanoparticle film as well as the average height of asperities.

The ability to control or predict the morphology of nanoparticle films on surfaces is very important for the application of such films. For example, nanoparticle-based films for MEMS tribology control (i.e., anti-adhesion) require some surface roughness in order to reduce the real contact area between contacting surfaces. However, the typical vertical gap between structures and surfaces (~ 1-2 μm) places a limitation on the surface roughness and the nominal height of asperities. Therefore, the surface energy of a substrate plays a very integral role in the deposition of nanoparticle thin films.

CHAPTER 7

TRIBOLOGICAL EFFECT OF NANOPARTICLE FILM ROUGHNESS

7.1 Introduction

In Chapter 5, gold nanoparticles were successfully deposited onto silicon cantilever beams using a gas-expanded liquid deposition and supercritical drying process. The nanoparticle coatings, which proved to be uniform and conformal, effectively reduced the adhesion between polysilicon cantilever beams and the substrate by multiple orders of magnitude. Based on the preliminary results, more experiments were required to determine how varying nanoparticle concentrations (and, in turn, surface coverage or surface number density) would affect tribological properties of MEMS devices.

This chapter presents a systematic study on the effect of varying the surface coverage of nanoparticles deposited onto Si (100) SOI tribology chips. As previously discussed, these new single crystalline devices are extremely smooth (ca. 0.2 nm). Therefore, it was hypothesized that even very low concentrations of very small nanoparticles should have a very grand effect on the device tribology by drastically increasing the surface roughness and reducing the real area of contact. For the systematic study, 4.5 nm diameter gold nanoparticles were used to examine the effect of particle surface coverage and surface roughness. The surface coverage of nanoparticles on tribology device chips were determined by measuring the difference in resonant frequencies of mass resonator devices as described in Chapter 3 and by SEM image analysis. The surface

158

roughness values of various particle concentrations on tribology chips were determined via AFM measurements. The overall hypothesis of this work was that some optimal surface coverage or surface roughness would exist in which a maximum decrease in adhesion energy would be achieved. This decrease in adhesion and surface energy would drastically decrease both micromechanical stiction and static coefficients of friction between contacting microstructures.

7.2   Estimation of roughness and nanoparticle surface coverage

Gold nanoparticles were synthesized as previously described in Chapter 3. The particles were deposited onto six individual SOI tribology chips following the gas-expanded liquid particle deposition technique. Figs. 7.1 through 7.6 present AFM scans and SEM images used to determine RMS roughness and surface coverage estimates for six AuNP coatings A-F. The figures are presented in order of increasing nanoparticle concentration in the original dispersions used for film deposition. Using Gwyddion software, the AFM scans were analyzed to produce RMS roughness values in order to quantify the surface roughness. The RMS values are given in Table 7.1. Fig. 7.7 charts the RMS roughness attained for each of the six coatings in increasing order of nanoparticle concentration. Unfortunately, the exact nanoparticle concentrations are difficult to attain. However, the plot shows that as the particle concentrations are increased the RMS roughness decreases before significantly increasing. This is an intuitive result, as depositing a small number of particles on a smooth surface would drastically increase the roughness. However, as more particles are deposited, monolayers will form causing a decrease in overall surface roughness. Depositing even more particles causes the formation of bulk gold islands as shown in Fig. 7.6, which drastically increases the roughness further. It is expected that
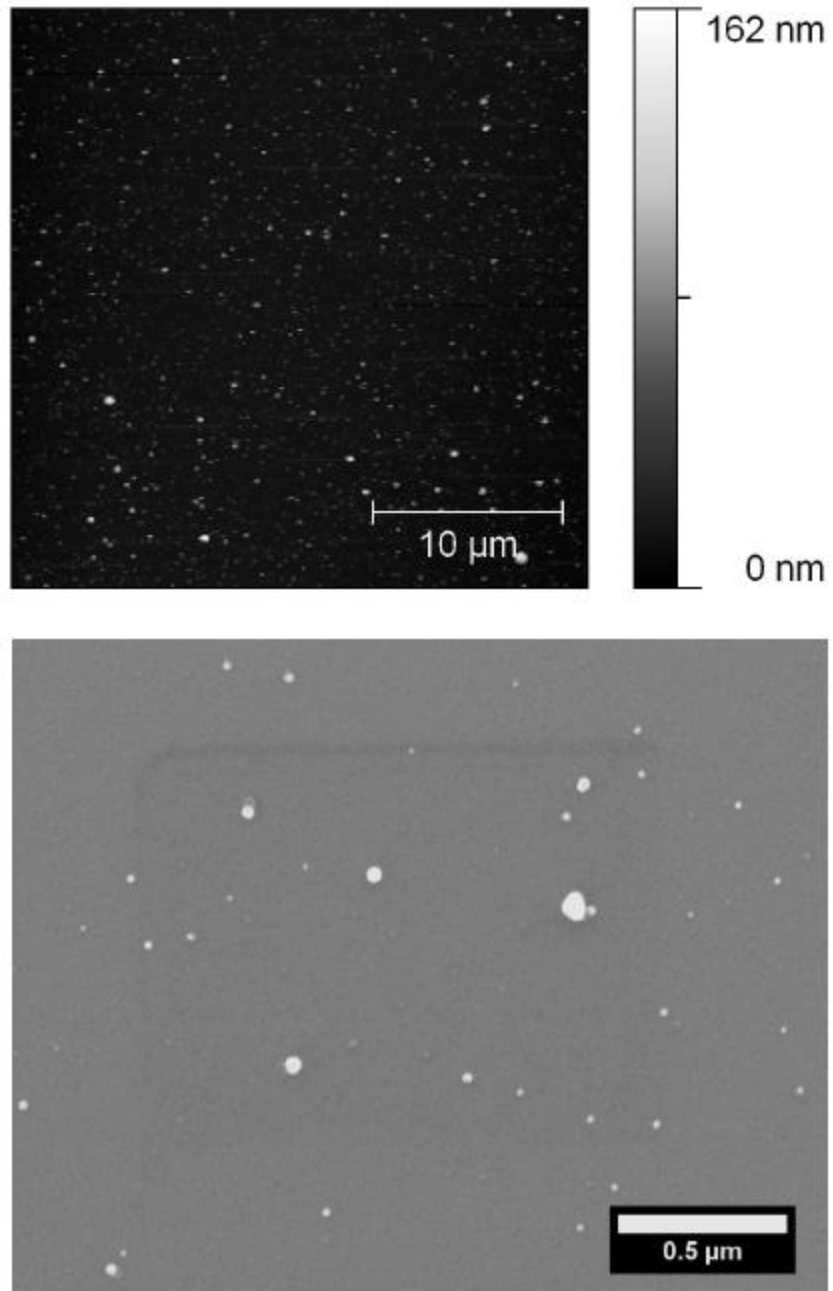
Figure 7.1. AFM scan and SEM micrograph of AuNP coating A with RMS roughness of 8.7 nm.
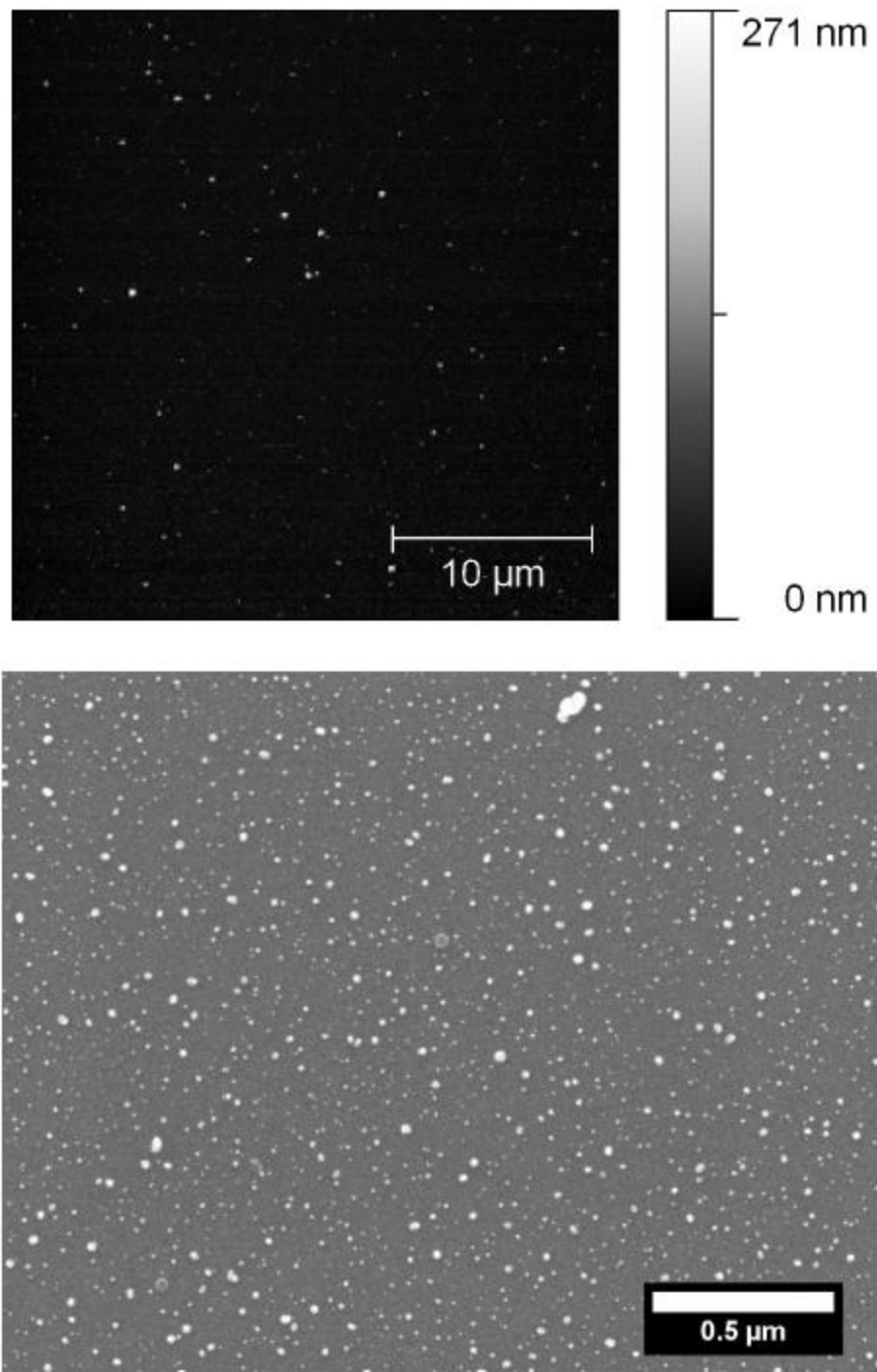
Figure 7.2. AFM scan and SEM micrograph of AuNP coating B with RMS roughness of 9.0 nm.
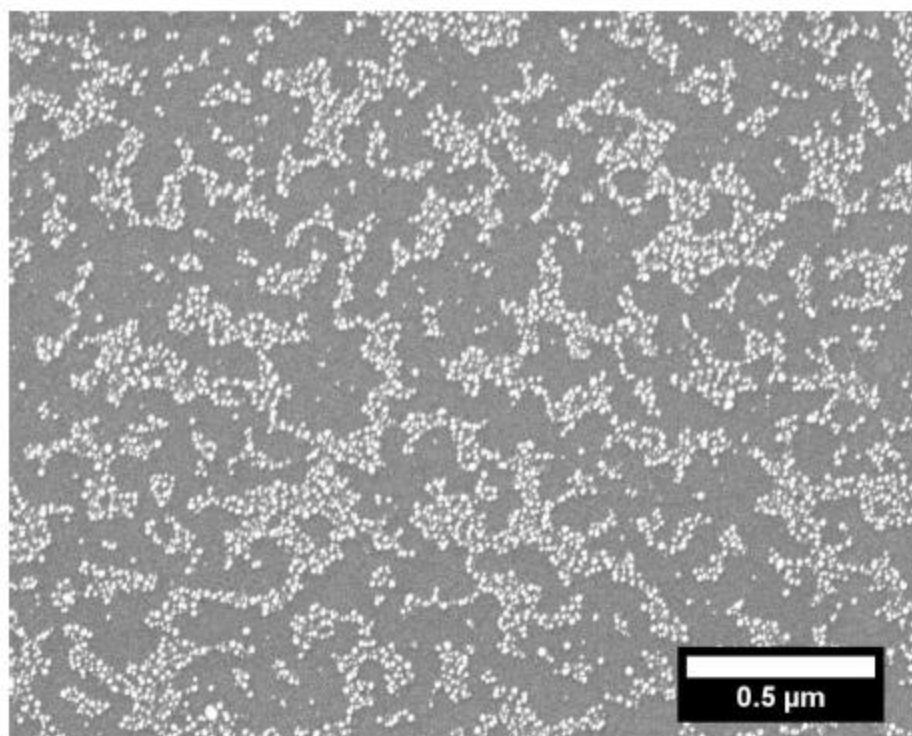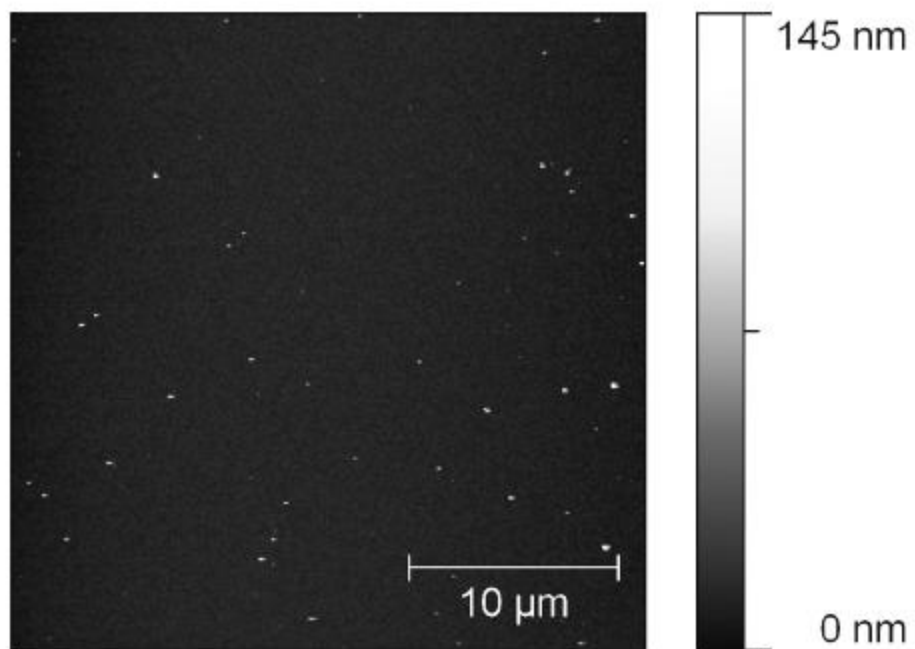
Figure 7.3. AFM scan and SEM micrograph of AuNP coating C with RMS roughness of 4.0 nm.
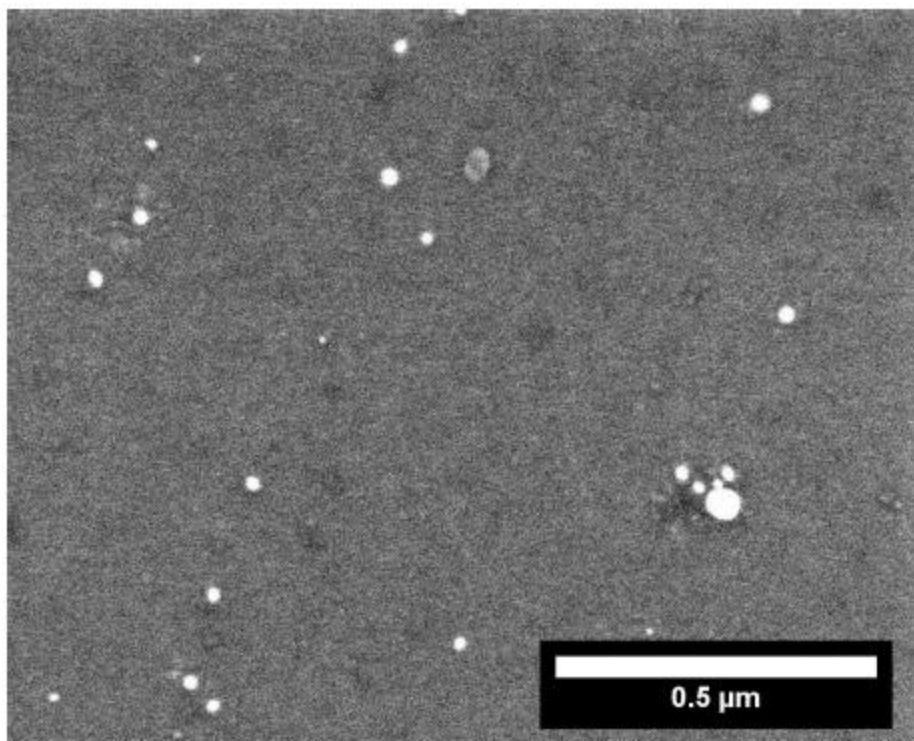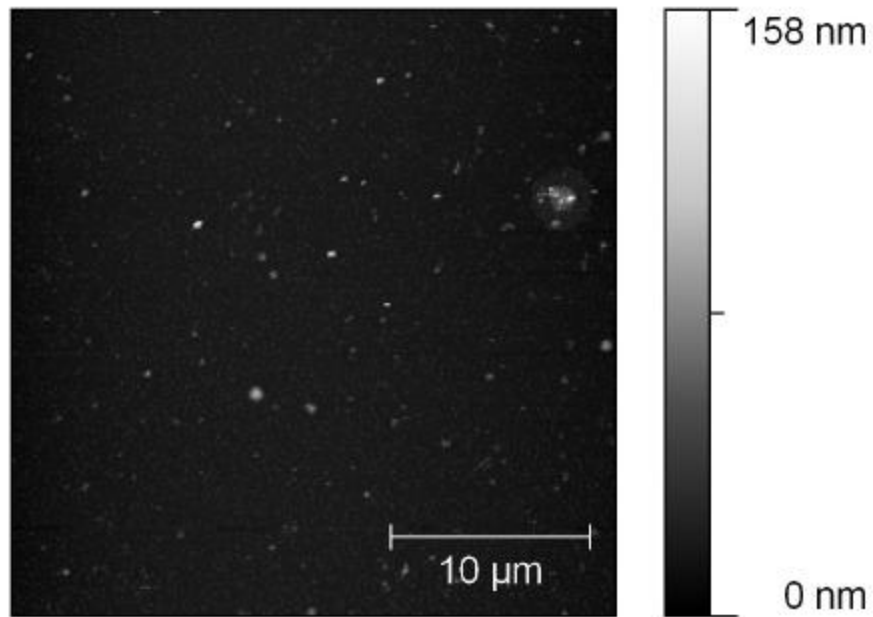
Figure 7.4. AFM scan and SEM micrograph of AuNP coating D with RMS roughness of 6.0 nm.
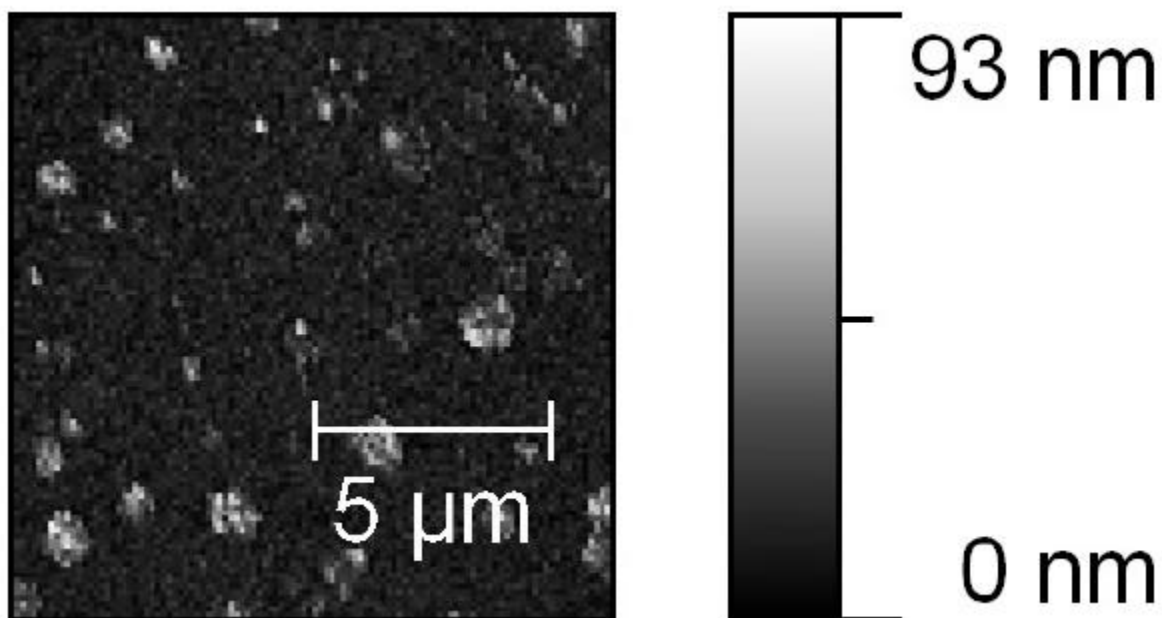
Figure 7.5. AFM scan of AuNP coating E with RMS roughness of 13 nm.

SEM micrograph is not available.
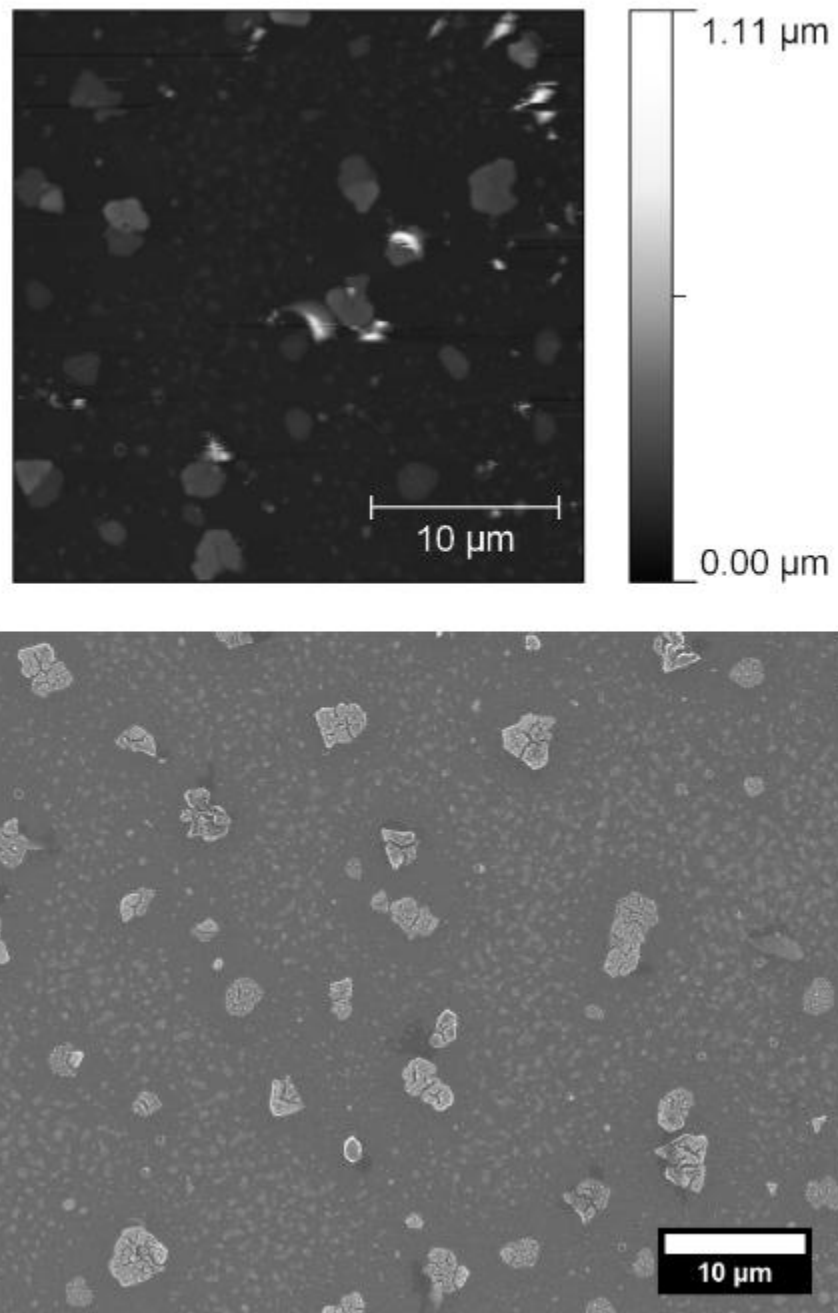
Figure 7.6. AFM scan and SEM micrograph of AuNP coating F with RMS roughness of 56 nm.
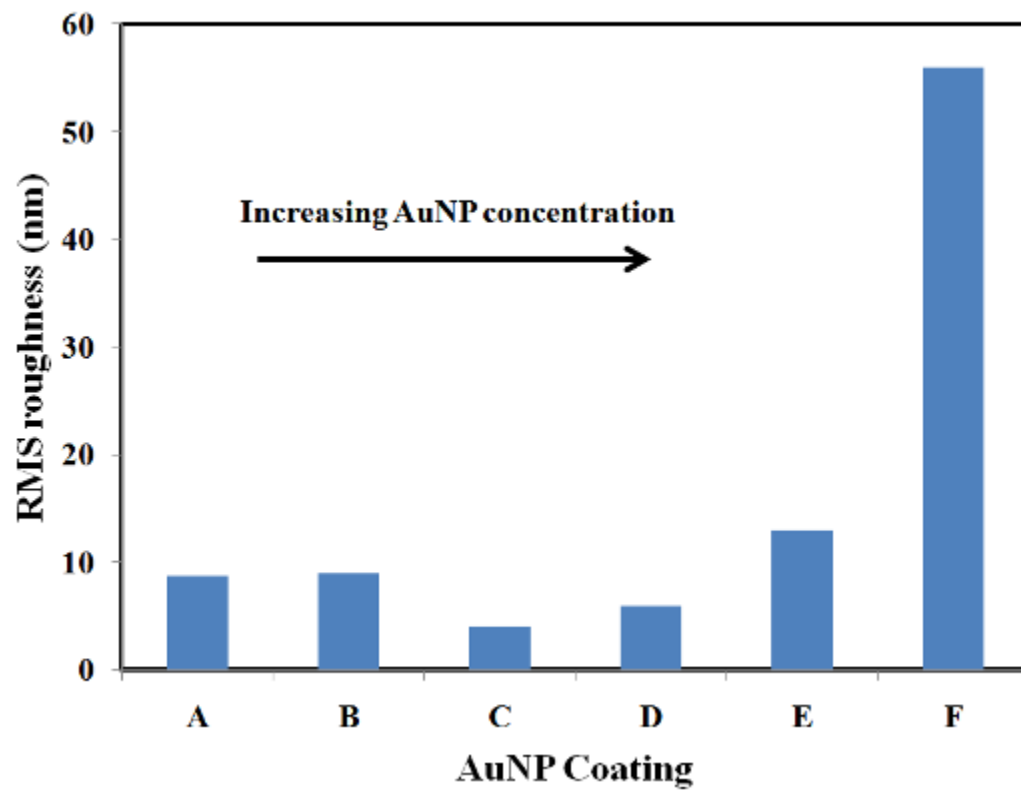
Figure 7.7. RMS roughness values for AuNP coatings in increasing concentrations.

Coating (increasing concentration)	RMS roughness (nm)	Projected surface area coverage from SEM	Real contact surface coverage from SEM	Resonant frequency of MR device (kHz)	Surface coverage from MR (± 4%)
A	8.7	1.2 ± 0.5%	1.2 ± 0.5%	8.31	16
B	9.0	15.4 ± 2.0%	4.2 ± 1.1%	8.24	47
C	4.0	30.5 ± 5.7%	23.2 ± 2.6 %	8.19	70
D	6.0	76.0 ± 6.3 %	1.1 ± 0.7 %	8.26	37
E	13.	n/a	n/a	8.21	61
F	56.	94.2 ± 4.8%	18.5 ± 7.0%	7.96	176

Table 7.1. RMS roughness and particle surface coverage values for the

various AuNP coatings. Sample E was not available for SEM imagining.

if even more particles were deposited onto the sample shown in Fig. 7.6, the islands will fill in more of the free space and actually reduce the RMS roughness.

The nanoparticle surface coverage was estimated two ways using SEM image analysis as described in Chapter 3. First, the surface coverage was determined as a "projected" surface area covered with any morphology of nanoparticle film. The projected surface area is described by Eq. (7.1):

$$A_P = \frac{A_f}{A_i} \times 100\% \tag{7.1}$$

where A_P is the projected surface area, A_i is the total area of the image analyzed, and A_f is the area of the image coated by AuNP film. These projected surface area coverages (presented in Table 7.1) trend with increased nanoparticle dispersion concentration, as expected. The highest nanoparticle concentration, used to create coating F, produced the highest projected surface area coverage of 94.2%. The SEM micrograph of coating F (Fig. 7.6) shows darker regions (typically near larger islands) which represent the ~6% of uncoated substrate area. In addition to the projected surface area coverage, the surface coverage of asperities − or highest features − was also estimated by image analysis. This method assumes that only the tallest asperities on rough contacting surfaces make contact. This is referred to as the "real" contact area. The "real" contact area (A_r) is the ratio of the surface area of the tallest asperities (A_a) to the total surface area (A_i), as shown in Eq. (7.2):

$$A_r = \frac{A_a}{A_i} \times 100\% \tag{7.2}$$

Fig. 7.8 represents a simple illustration of two rough surfaces coming into contact only at the points of "real contact." The real contact surface coverage values are also presented in Table 7.1. Fig. 7.9 charts both the projected surface coverage and real contact areas for five of the six
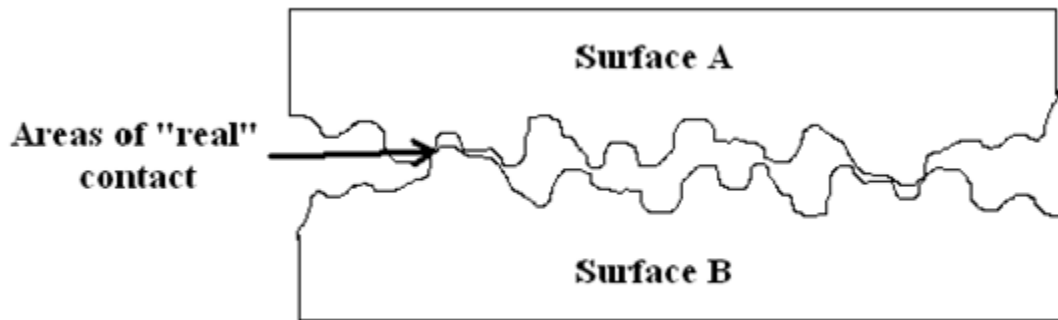
Figure 7.8. Illustration of two rough surfaces making contact at areas of "real" contact.
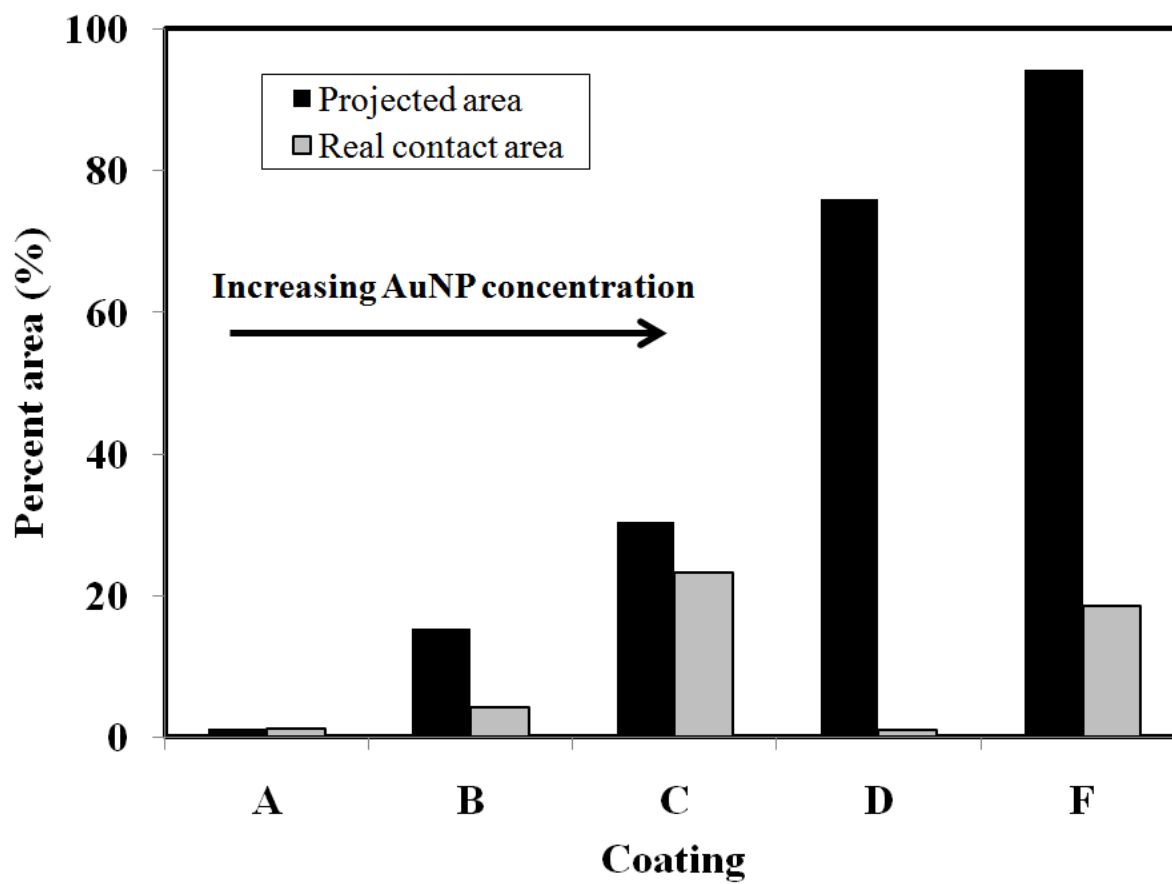
Figure 7.9. Projected surface coverage and real contact areas for individual AuNP coatings.

AuNP coatings. To better visualize the real contact area of the various AuNP coatings, Fig. 7.10 presents the black-and-white images created by the thresholding process using ImageJ. The black regions in the images represent the contact area provided by the highest features of each coating. Please note that the real contact area determined in this work by image analysis may still be slightly higher than the actual contact area due to the inability to take asperity shape and topography into account.

As previously noted, the projected surface coverage area increases with increasing nanoparticle concentration. The estimated real contact area, on the other hand, varies significantly. This is not counter-intuitive, however, as the trend can be explained by the formation of gold thin films. The formation of gold nanoparticle thin films on silicon has been shown to follow the Stranski-Krastanov ("layer-plus-island") mode of film growth (Zhou et al. 1999). The Stranski-Krastanov (SK) growth mode, illustrated by Fig. 7.11, is an intermediary mode in which particles initially form a monolayer before creating nucleation points at which large islands begin to form (Venables 2000; Ohring 2002). This mode of growth leads to the formation of large, triangular plates (Zhou et al. 1999; Yu et al. 2004) which appear to be forming in Fig. 7.6. Fig. 7.12 presents another SEM micrograph depicting the formation of these triangular plates a large concentration of gold nanoparticles. SK film growth explains the transition in estimated real contact area between AuNP coatings C (Fig. 7.3) and D (Fig. 7.4). In Fig. 7.3, the AuNPs are still attempting for form a complete monolayer whereas in Fig. 7.4 the monolayer has been formed and AuNPs have begun to nucleate to form larger asperities. These nucleation sites eventually turn into the triangular plates as in Fig. 7.6, which again increases the real contact area.
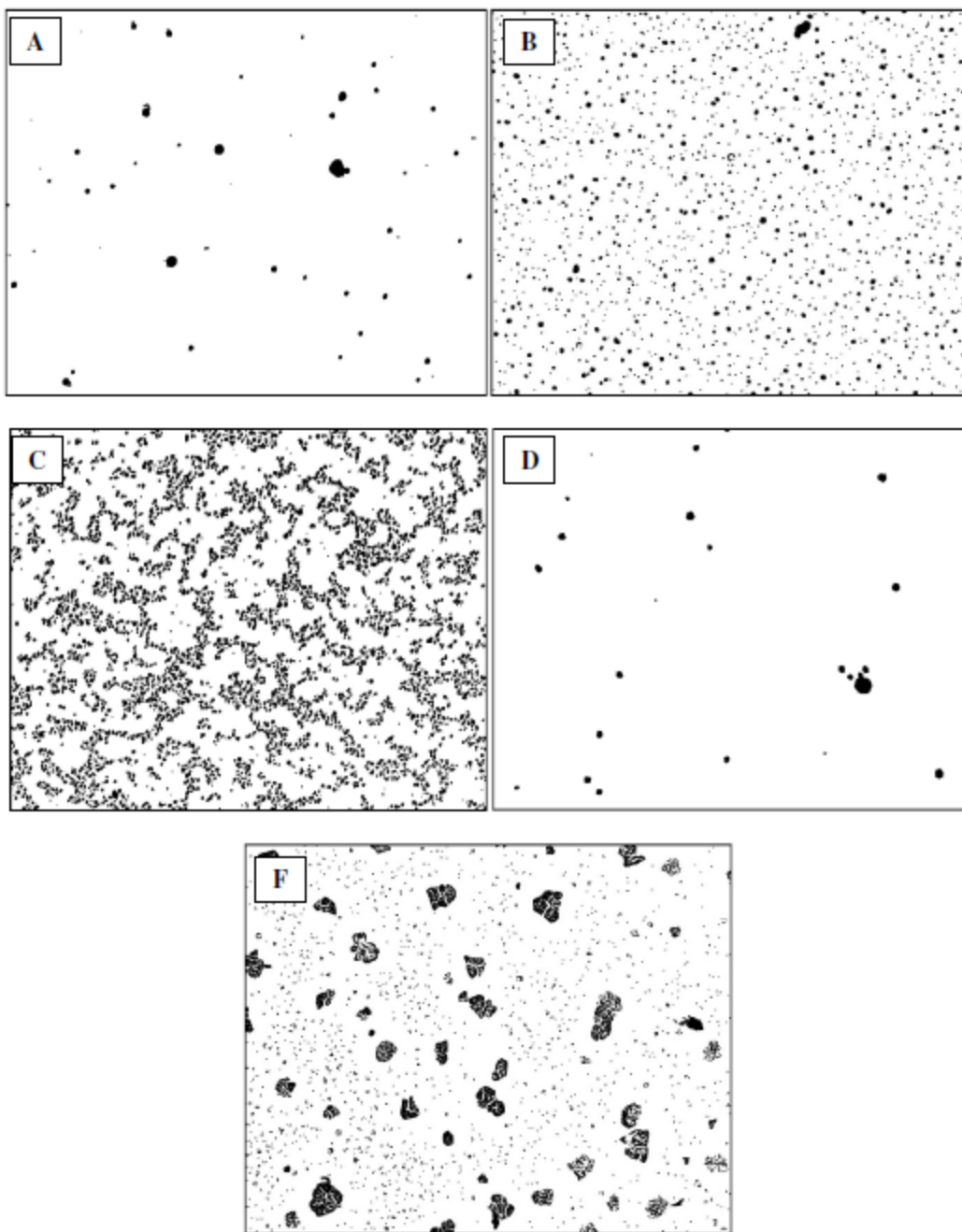
Figure 7.10. Thresholded SEM images illustrating the real contact area (black regions) of the various AuNP coatings. Coating indicated by the boxed letter.
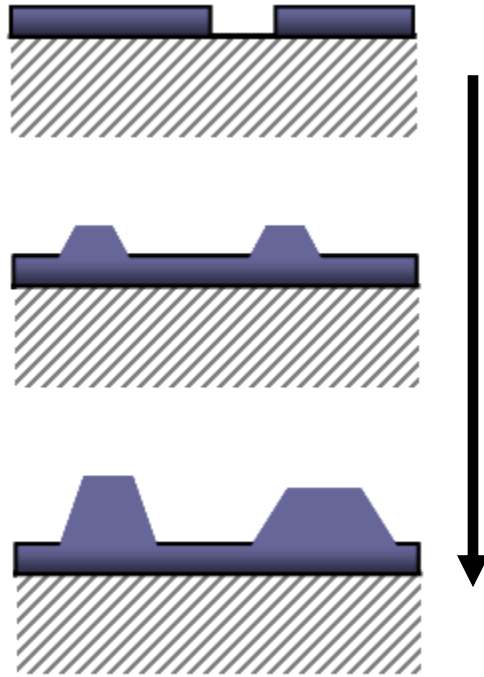
Figure 7.11. Illustration of Stranski-Krastanov film growth.
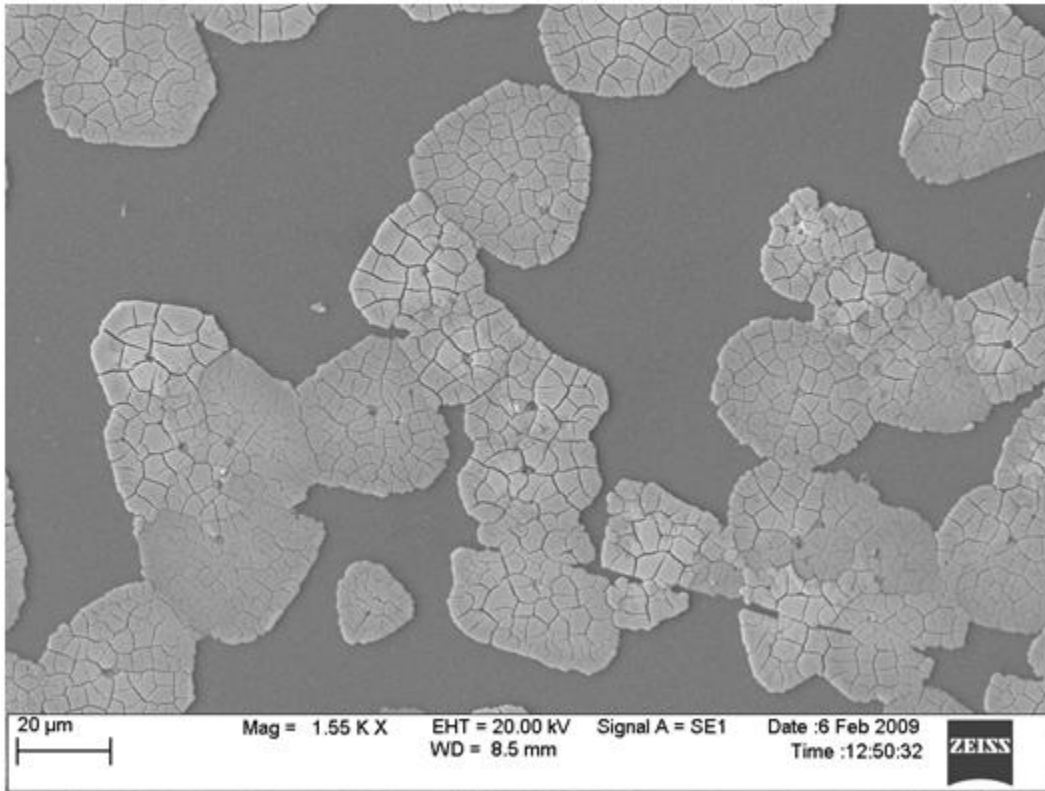
Figure 7.12. Triangular plates formed during the deposition of highly

concentrated AuNPs on silicon.

Table 7.1 also contains the surface coverage determined by coated mass resonator devices. The method and equations used for determining surface coverage based on changes in the resonating frequency are described in Chapter 3. The drawback towards this method is that it assumes the formation of up to a single monolayer. Based on the AFM scans and SEM micrographs of the AuNP coated samples, this was very rarely the case. This fact would explain why the coverage determined from the mass resonators was so much higher than from image analysis for Sample A – coated with the lowest nanoparticle concentration – as well as Sample F which was coated by the most particles. The coating in Sample A consists of small particulates of agglomerated AuNPs which have an average height of about 15 nm, as shown by the AFM line scan in Fig. 7.13(a). The mass resonator method of surface coverage calculation assumes that the mass of the particles on the device are no taller than 5 nm (one particle diameter), which was not the case – yielding an overestimated surface coverage. The same is true for the coating consisting of the most particles (F). The projected surface coverage from SEM image analysis was about 94%, which basically assumes monolayer coverage. Again, this is not the true case, as shown by the line scan in Fig. 7.13(b) which illustrates large gold islands of approximately 150 nm in height. The mass resonator technique estimated a surface coverage of greater than 100% due to the high mass of the large AuNP islands. Due to this limitation, the surface coverages determined from mass resonators were not included in the tribological analysis.

7.3 Effect of surface coverage and roughness on adhesion

The effect of the varying RMS roughness and surface coverage was examined on the adhesion and stiction of SOI cantilever beams. The hypothesis for these experiments, based on previous results and the theory behind "real" contact surface area, was that the apparent work of
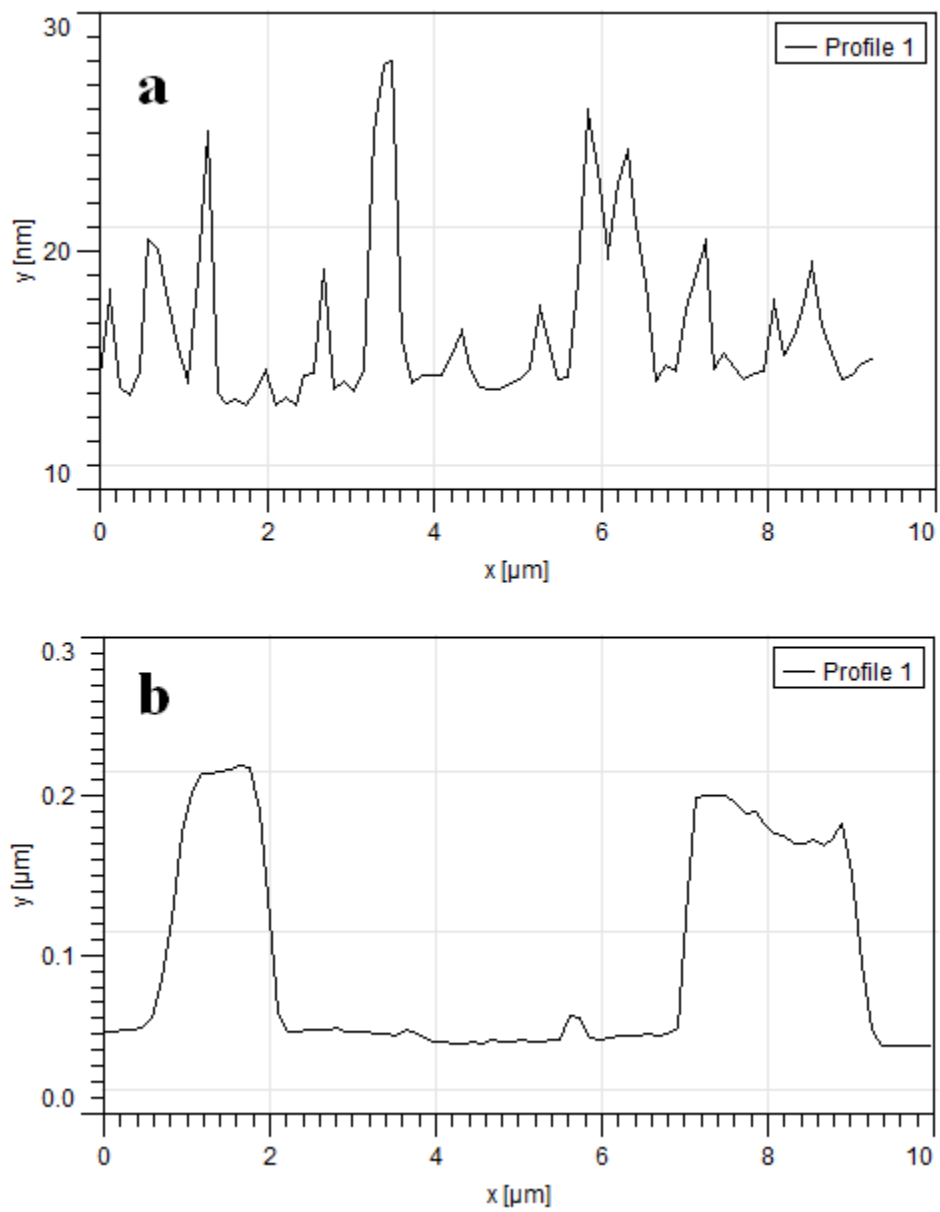
Figure 7.13. AFM line scan profiles of (a) AuNP coating A and (b) AuNP coating F.

adhesion (referred to as the adhesion energy) would drastically decrease with the introduction of low surface roughness. At some point, although the surface roughness continues to increase through the formation of nanoparticle islands, the real contact area would also increase – in turn causing the adhesion energy to increase. Adding additional surface roughness through the addition of more nanoparticles would then once again cause a decrease in adhesion energy as the film growth mechanism shifts from layer to island formation. This trend would be expected to repeat up to a point where the cantilever beams are no longer usable due to the formation of extremely large nanoparticle agglomerations.

Fig. 7.14 plots the average adhesion energies of cantilever beam arrays with the RMS roughness of the respective AuNP coatings. The plot shows a very steep decline in adhesion energy from the control (0.2 nm RMS) case with the introduction of a low concentration of nanoparticles (~ 4 nm RMS roughness). As the RMS roughness increases, the adhesion energy decreases before showing an increase when the RMS reaches beyond 10 nm. The highly concentrated AuNP-coated sample (56 nm RMS) exhibits drastically reduced adhesion energy of around 1 mJ/m^2 – lower than the adhesion energies associated with RMS roughness of 10-13 nm. The data points shown in Fig. 7.14 agree with the initial hypothesis of the study. The dashed line in Fig. 7.14 represents the hypothesized trend of the data, where an unknown local maximum exists between 13 and 56 nm RMS roughness. It may also be possible that multiple maxima and minima exist within this region. At any rate, the expected trend between adhesion energy and surface roughness occurred. However, it is important to note that the data points are specific for the system. In other words, the data presented in Fig. 7.14 are for dodecanethiol-capped gold nanoparticle films on smooth silicon oxide. The dodecanethiol-capped particles represent a specific system which has a specific surface energy. Results will vary when different ligand tails
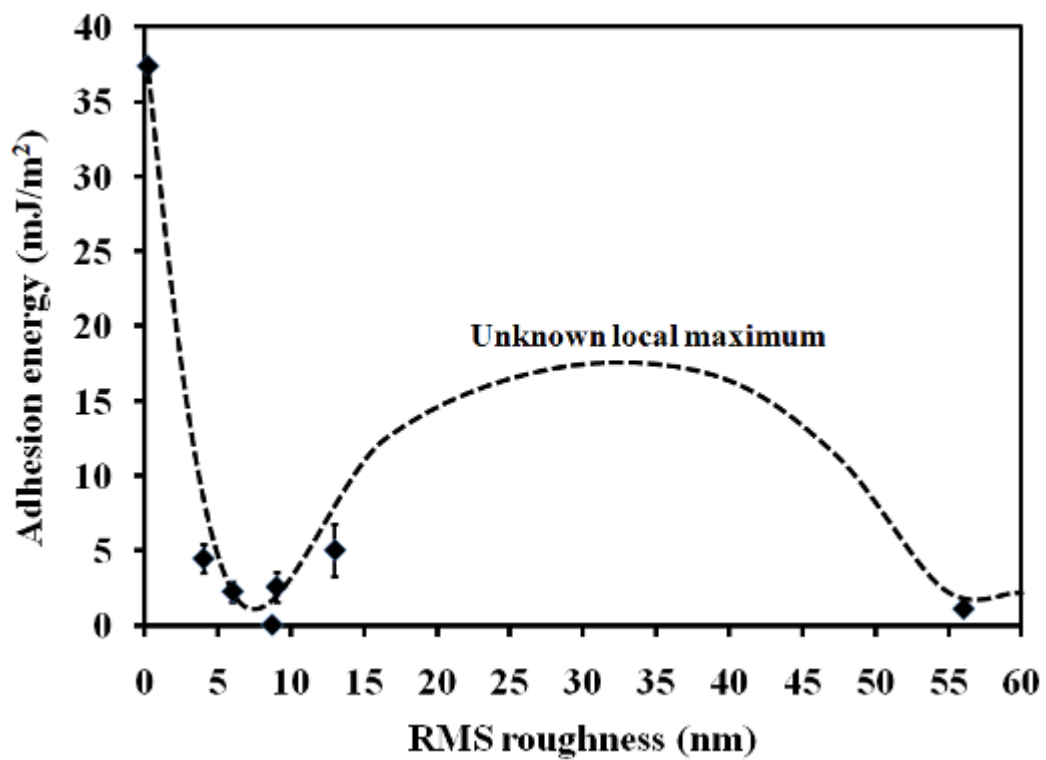
Figure 7.14. Trend of average cantilever beam adhesion energy with increasing

RMS roughness of gold nanoparticle coatings.

are used to stabilize the original nanoparticle dispersions. Nonetheless, the concluding results indicate that introducing a certain surface roughness can drastically reduce the adhesion between contacting microstructures.

In addition to RMS roughness, the adhesion energy was also compared to the estimated ratios of real contact surface area as determined by Eq. (7.2). Fig. 7.15 plots the adhesion energy as a function of real contact surface area (%). The control data point for smooth SiO_2 assumes that 100% of two surfaces are in contact. The results illustrate a very intuitive trend in that the adhesion energy decreases with decreased real contact surface area. Intuitively, it follows that if two surfaces could not make contact (0% real contact surface area), the two surfaces would have no desire to adhere to one another. The trends illustrated by Figs. 7.14 and 7.15 suggest that nanoparticle films can be engineered to have specific surface coverage, RMS roughness and adhesion energy.

7.4   Effect of surface coverage and roughness on friction

The effect of surface coverage and surface roughness of gold nanoparticle films on friction was also examined utilizing SOI friction testers as described in Chapter 3. Fig. 7.16 charts the experimentally determined coefficient of static friction for devices coated with native oxide (control) and AuNP thin films in order of increasing particle concentration. The coefficient of static friction, μ_s, for the control devices coated only by native silicon oxide films was 1.98 which is in good agreement with values found in literature (Cha and Kim 2001). The high value is attributed to the inclusion of severe adhesion which plays a large role in friction at micro- and nano-scales. Upon the introduction of surface roughness by a low concentration of AuNPs, the
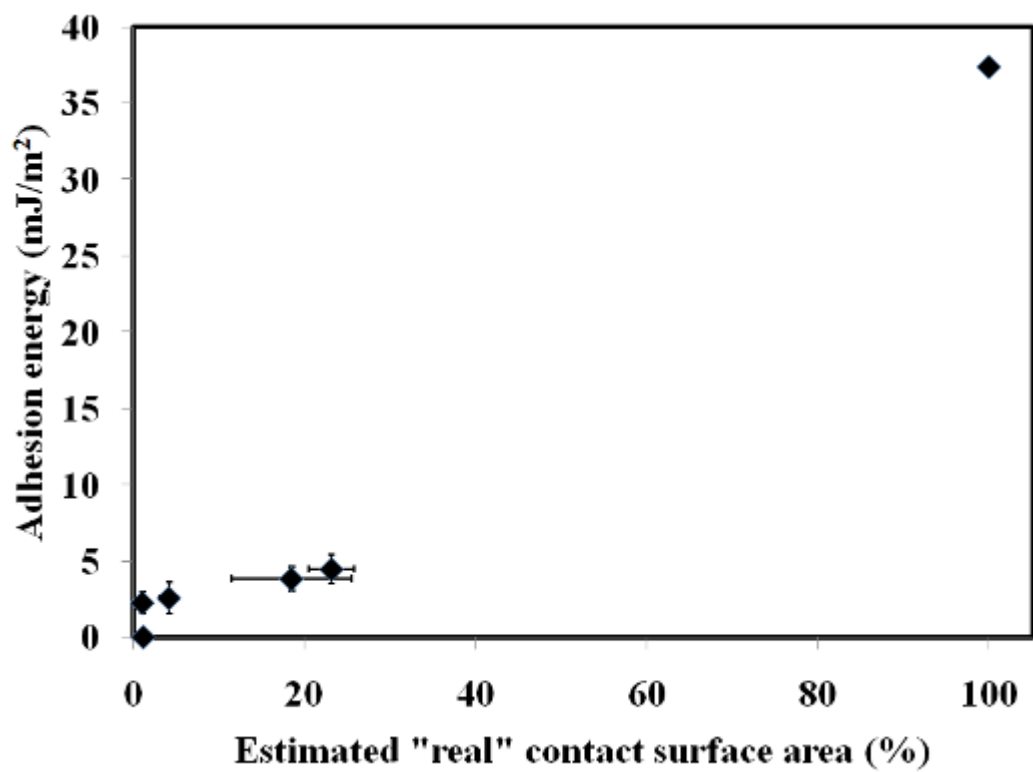
Figure 7.15. Adhesion energy as a function of estimated "real" contact surface area.
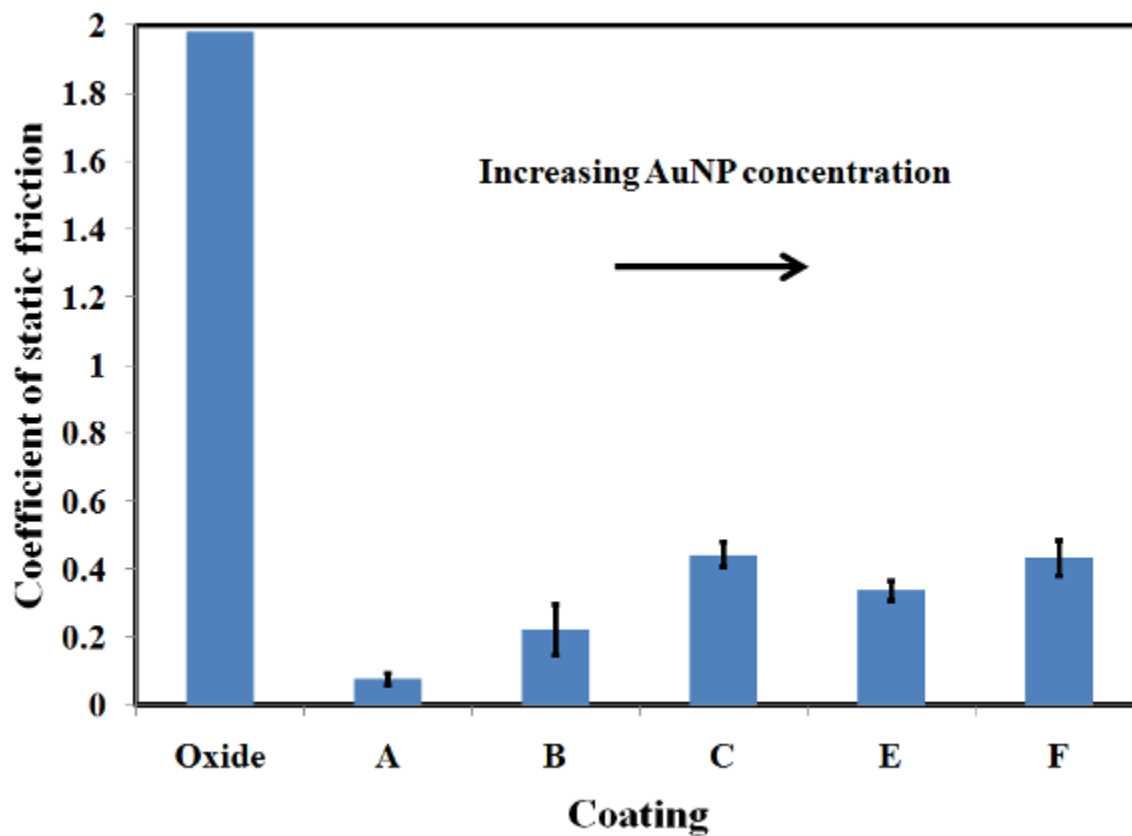
Figure 7.16. Coefficients of static friction determined experimentally for SOI friction testers coated with native oxide and increasing concentrations of AuNPs. Data for coating D is unavailable.

static friction decreases drastically to about 0.08. This prominent reduction is very likely attributed to the strong decrease in adhesion energy. As the concentration of particles deposited onto the surfaces increased, the static friction also increased slightly. This trend is similar to the trend of increasing RMS roughness on adhesion, exhibited in Fig. 7.14. The reason for the increased static friction of coatings utilizing a greater number of nanoparticles is likely due to the increased contact area and adhesion energy of the higher concentrated coatings. Table 7.2 compares the AuNP coatings to static friction coefficients determined for other popular surface treatments. The results indicate that AuNP films produced of very low concentrations of particles and exhibiting minimal contact area reduce the coefficient of static friction to levels comparable to surface modifications of OTS and FDTS monolayers (Patton et al. 2000).

Fig. 7.17 illustrates the effect of the estimated real contact area on the coefficient of static friction. The figure exhibits the same trend as the effect of real contact area on adhesion energy. As the estimated real contact area is decreased (from the assumed 100% for a native oxide surface) the coefficient of static friction also decreases. This further illustrates that static friction is highly influenced by stiction in MEMS. Fig. 7.18 plots the adhesion energy of the surfaces examined in this work with their respective coefficients of static friction. The figure exhibits a nearly perfect linear trend ($R^2 = 0.998$), which confirms the correlation between adhesion and friction.

7.5   Conclusions

In this study, the effects of surface roughness and nanoparticle surface coverage – both projected and real contact area – on microstructure adhesion and friction were examined. As expected, the adhesion of silicon cantilever beams sharply decreased when nanoparticles were

Surface modification	Coefficient of static friction (μ_s)	Adhesion energy (mJ/m^2)
Native SiO$_2$	1.98	37.4
OTS	0.07	0.01
FDTS	0.15	0.01
AuNP coating A	0.08	0.02
AuNP coating B	0.22	2.6
AuNP coating C	0.44	4.5
AuNP coating D	n/a	2.3
AuNP coating E	0.34	5.0
AuNP coating F	0.43	1.1

Table 7.2. Coefficients of static friction and adhesion energies for various surface modifications.
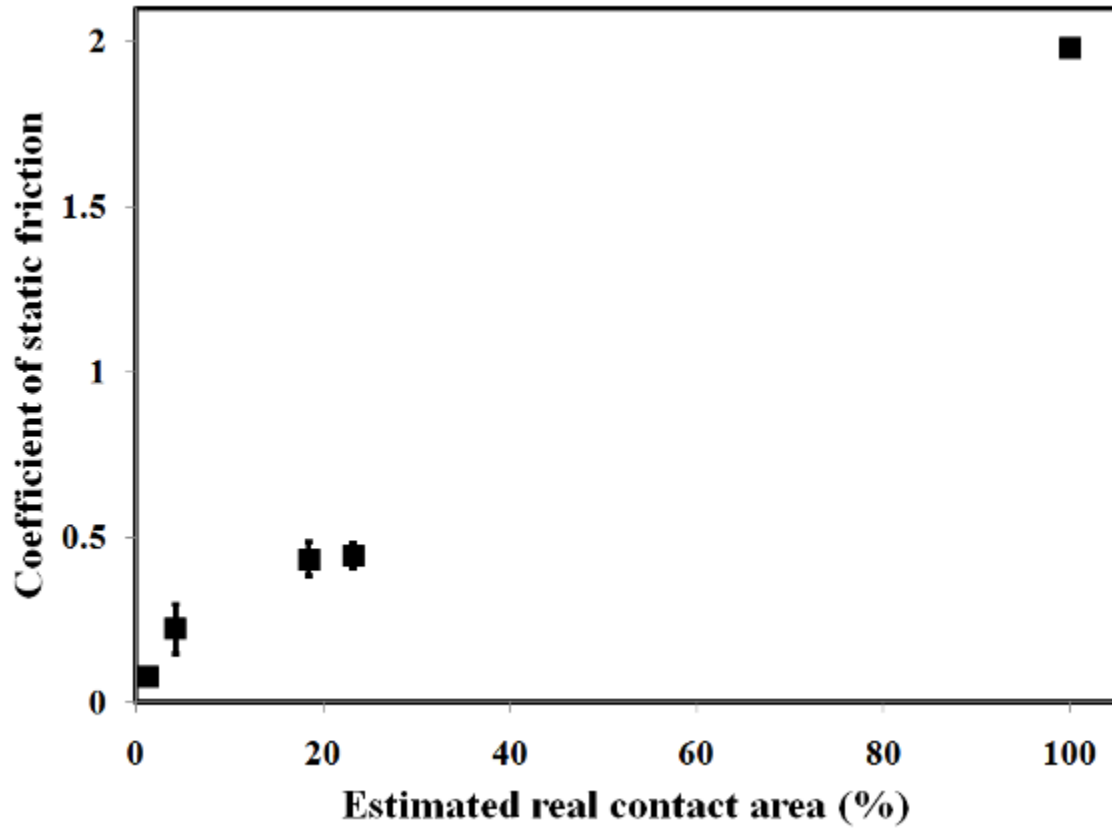
Figure 7.17. Effect of estimated real contact area on the coefficient of static friction.
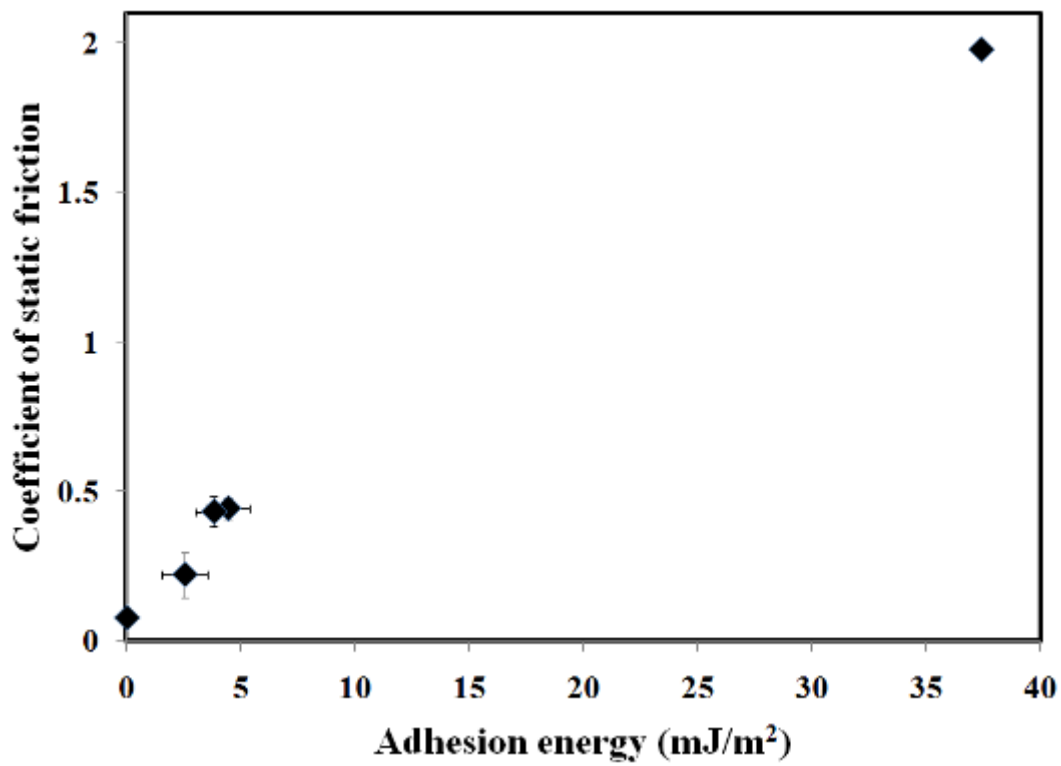
Fig. 7.18. Correlation between adhesion energy (stiction) and coefficient of static friction.

introduced to increase the surface roughness. However, as the roughness was further increased the adhesion also increased, to some unknown maximum, before decreasing again at a higher RMS roughness value. This trend was expected and was further explained by the effect of "real" contact surface area on adhesion. Decreasing the real contact area intuitively decreases the adhesion of two surfaces in contact. This result, when combined with the theory of Stranski-Krastanov film growth, explains why the adhesion increases and decreases over a range of RMS roughness values. From these results describing the effect of surface roughness and real contact area on adhesion, the conclusion can be made that AuNP films – and by extension most nanoparticle-based films – can be engineered to achieve a desired surface roughness, surface coverage, or adhesion energy.

In addition, the effect of nanoparticle surface coverage of the coefficient of static friction was also examined. The static friction between two surfaces in contact was also highly affected by the addition of AuNP thin films. The lowest coefficient of static friction determined in the current work was exhibited by AuNP coating A, which coincidentally had the lowest estimated real contact area of 1.2%. The effect of real contact area on static friction followed a similar trend to that of adhesion energy. In fact, when the respective adhesion energies and coefficients of static friction are plotted together the data represents a nearly perfect trend. This trend confirms the fact that friction is actually dominated by stiction at the microscale. Therefore, any attempts made which reduce stiction will also inherently reduce friction.

CHAPTER 8

MONOLAYER-IMMOBILIZED NANOPARTICLE FILMS FOR MICROTRIBOLOGY CONTROL

8.1 Introduction

The preliminary proof of concept experiments discussed in Chapter 5 revealed that nanoparticle coatings were indeed effective in reducing the apparent work of adhesion of polysilicon cantilever beams. However, once the beams made mechanical contact with the underlying substrate, nanoparticles were translated across the surfaces creating nanoparticle-free regions as shown in Fig. 5.13. These regions, consisting of high-energy native silicon oxide contacts, could once again be subject to high interfacial forces and cause strong or permanent adhesion. Therefore, more robust nanoparticle-based anti-stiction coatings are required which are more durable to the mechanical contact of contacting microstructures.

This chapter investigates the use of certain self-assembled monolayers to create more robust nanoparticle coatings by grafting, or permanently immobilizing, nanoparticles to the microstructured surfaces. In particular, 3-mercaptopropyl trimethoxysilane (MPTS) and *p*-aminophenyl trimethoxysilane (APhTS) are examined, which have the capability of attaching to silicon surfaces on one end of the molecule while attaching to gold, silver, and other metals on the opposing end. The effects of coupling these SAMs with nanoparticle coatings on adhesion and stiction are discussed in this chapter.

187

8.2   SAM/nanoparticle film preparation

Silicon substrates and tribology chips were first prepped following the cleaning and oxidation methods described in Chapter 3. Prior to monolayer formation, the silica surfaces were hydroxylated by immersing the samples in a 30:70 (v/v) mixture of H_2O_2 (30 wt%) and H_2SO_4 at 70 ºC for 30 min. This process is considered to leave behind approximately five reactive OH groups per nm^2 on the silicon oxide surface (Zhuravlev 1987; Laoharojanaphand et al. 1990); however, the exact number is debatable. The substrates were then copiously rinsed in DI water and dried under a nitrogen stream. When silicon-based microstructures and tribology chips were being coated, the drying step was not performed in order to avoid capillary collapse of the structures.

3-Mercaptopropyl trimethoxysilane (MPTS) monolayers were formed by immersing the substrates into a solution containing 400 µl MPTS and 400 µl DI water in 20 ml electronic grade isopropanol heated to 70 °C for 30 min (Vakareslski et al. 2007; Goss et al. 1991). The samples were then rinsed in isopropanol, hexane and DI water consecutively to remove any excess physiosorbed organic molecules. *p*-Aminophenyl trimethoxysilane (APhTS) monolayers were formed following a procedure outlined by Zhang and Srinivasan (2004). Samples were first rinsed consecutively in isopropanol, a 1:1 (v/v) mixture of isopropanol and toluene, and pure toluene. Then the samples were immersed in a 3 mM APhTS solution in toluene for 30 min. Following monolayer deposition, the samples were rinsed in toluene, immersed in toluene for 30 min, and rinsed in isopropanol. Si (100) substrates were coated along-side silicon tribology chips in order to prove SAM formation on the surfaces.

Following SAM formation, 5-nm gold nanoparticles dispersed in hexane were deposited by gas-expanded liquid deposition as described in Chapter 3. Fig. 8.1 presents simple schematic
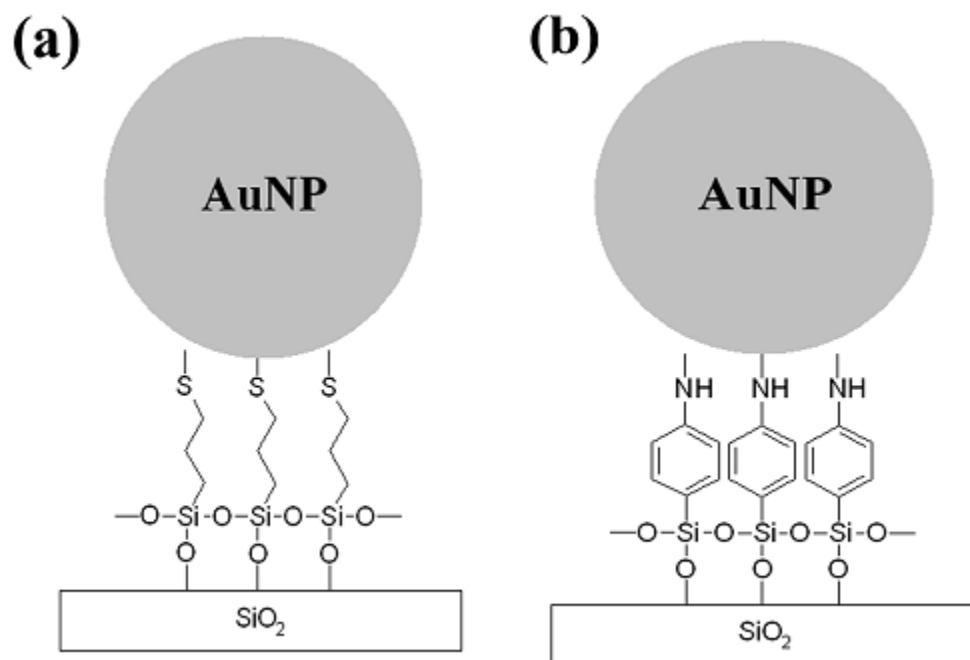
Figure 8.1. Schematic representation of a gold nanoparticle attached to (a) an MPTS

SAM coated silica surface and (b) an APhTS SAM coated silica surface.

diagrams of the attachment of a gold nanoparticle to MPTS and APhTS coated silica surfaces. Following nanoparticle deposition, silicon substrates were ultrasonicated in hexane for several minutes and rinsed with de-ionized water to wash away unbound nanoparticles and then dried under a stream of nitrogen. Tribology chips, however, were simply removed from the GXL apparatus and were not rinsed to ensure they remained dry. Dried samples were then heat treated at 115 °C for 1 h to anneal the SAM/nanoparticle composite films.

8.3   Characterization of SAM/NP films on Si substrates

Monolayer films were first deposited onto clean Si (100) substrates following the methods described above in order to characterize the deposition and examine the immobilization of gold nanoparticles. Ellipsometry measurements were first performed to compare the thickness of the organic monolayer/silicon oxide films to the thickness of reference silicon oxide. The average thickness of smooth, oxygen plasma-induced silicon oxide films was about 18.4 ± 0.6 Å. The average measured thickness of APhTS/SiO$_2$ and MPTS/SiO$_2$ films were 23.0 ± 1.3 and 29.9 ± 3.5 Å, respectively. Therefore, the thickness of the organic monolayer films of APhTS and MPTS were roughly 5 and 11 Å, respectively. These values are in good agreement with measurements in literature of 6 Å for APhTS (Ishizaki et al. 2007) and 9 Å for MPTS (Yakimova et al. 2007). Contact angle measurements of water on the monolayer films were also compared. The contact angles of water on APhTS and MPTS films, respectively, were 51.4 ± 1.9° and 69.8 ± 2.1°, which are also in good agreement with literature values (Sieval et al. 2001; Aswal et al. 2005).

FTIR was performed on APhTS and MPTS films to ensure the presence of primary (free) amines and thiols which are required for the immobilization of nanoparticles. First, a silicon

190

oxide seed layer was deposited onto a ZnSe FTIR crystal. The seed layer deposition was performed following the procedure of Anderson et al. (2008a). After a baseline FTIR scan of the silicon oxide seed layer was completed, APhTS was deposited onto the crystal following the same method as previously described. The FTIR scan in Fig. 8.2 represents the APhTS film with respect to the silicon oxide seed layer background. The large peak at 1100 cm^{-1} is characteristic of the formation of Si-O-Si bonds between the APhTS molecules and the silicon oxide seed layer. Another important peak at 1584 cm^{-1} illustrates the existence of primary amines which are free and available for attachment with nanoparticles. Negative peaks around 1650 cm^{-1} and 3100-3600 cm^{-1} indicate the removal of adsorbed water and the reaction of surface OH groups from the silicon oxide layer. Fig. 8.3 presents an FTIR scan of an MPTS film on a silica seed/ZnSe background. Again, the spectrum exhibits a large peak at 1100 cm^{-1} indicating the formation of Si-O-Si bonds. The peak at 825 cm^{-1} is also representative of Si in the system. The peaks between about 1200 and 1500 cm^{-1} are various modes of C-H indicating the presence of the hydrocarbon while the small but sharp peak at 2350 cm^{-1} represents available –SH groups (Brzezinski et al. 1995; Bellatreccia et al. 2009). However, adsorbed CO_2 from the ambient atmosphere can often interfere with the peak at 2350 cm^{-1} (Bellatreccia et al. 2009). To review, Table 8.1 lists the characteristic FTIR peak wavenumbers for APhTS and MPTS films.

The ability for monolayer films to immobilize gold nanoparticles was also examined on APhTS- and MPTS-coated Si (100) substrates. Gold nanoparticles were deposited via CO_2-expanded hexane onto silicon oxide, APhTS, and MPTS films. Following deposition and critical point drying, the particle-coated substrates were ultrasonicated in hexane for 10 min to remove as many particles as possible. The substrates were then examined by scanning electron microscopy (SEM). Fig. 8.4 presents SEM micrographs of gold nanoparticles that remained
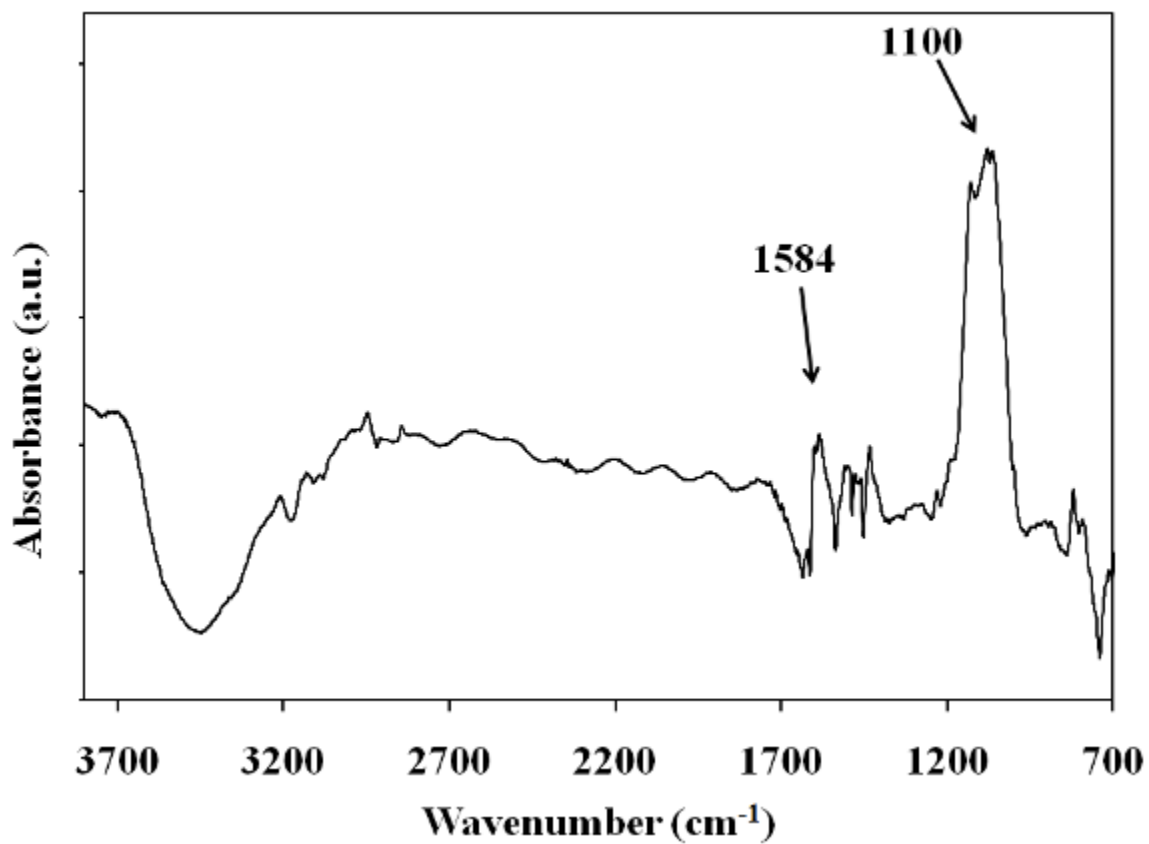
Figure 8.2. FTIR scan of APhTS monolayer film on silica seed layer
coated ZnSe crystal.
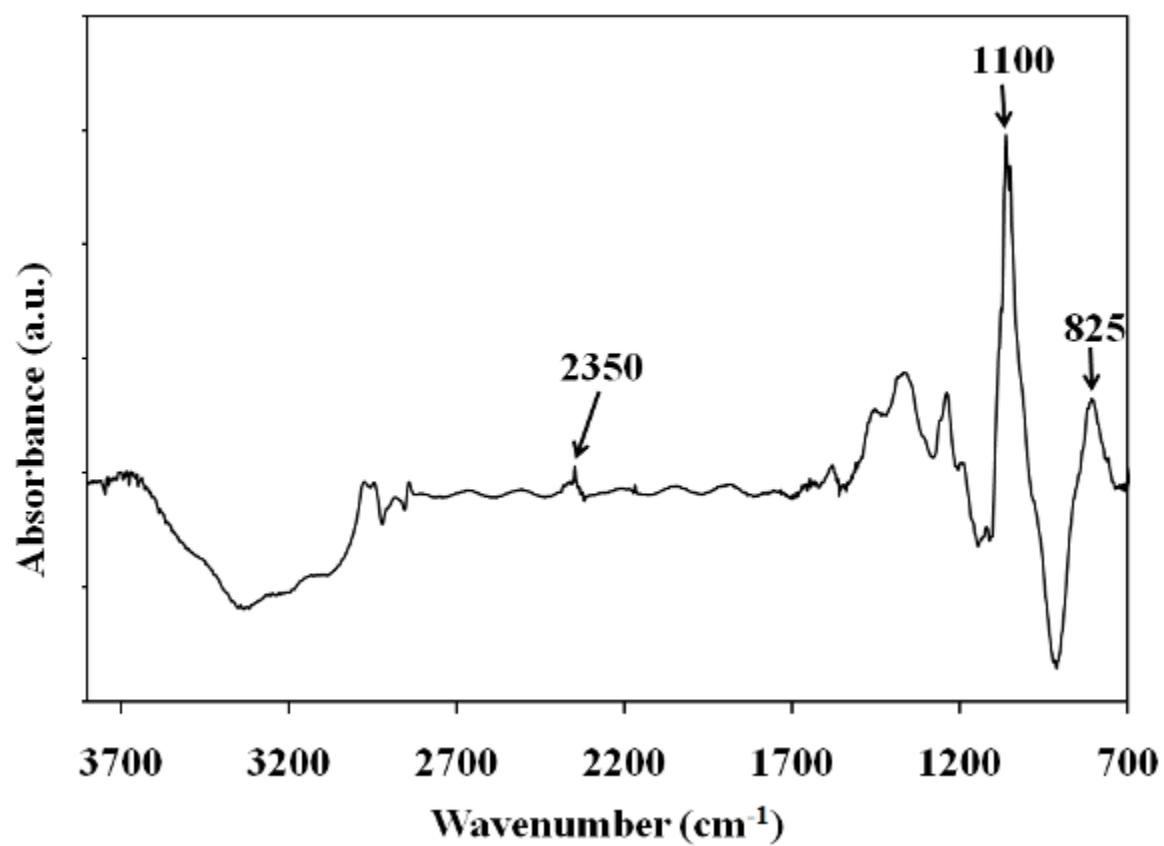
Figure 8.3. FTIR scan of MPTS monolayer on silica seed layer coated ZnSe crystal.

Wavenumber (cm^{-1})	Species, bond, or mode
825	Si-C
1100	Si-O-Si
1200 – 1500	CH deformation
1584	primary NH$_2$
1650	adsorbed H$_2$O
2350	SH vibration
2800 – 3000	CH stretching
3100 – 3600	OH stretching

Table 8.1. Characteristic FTIR wavenumbers of APhTS and MPTS films on silica.
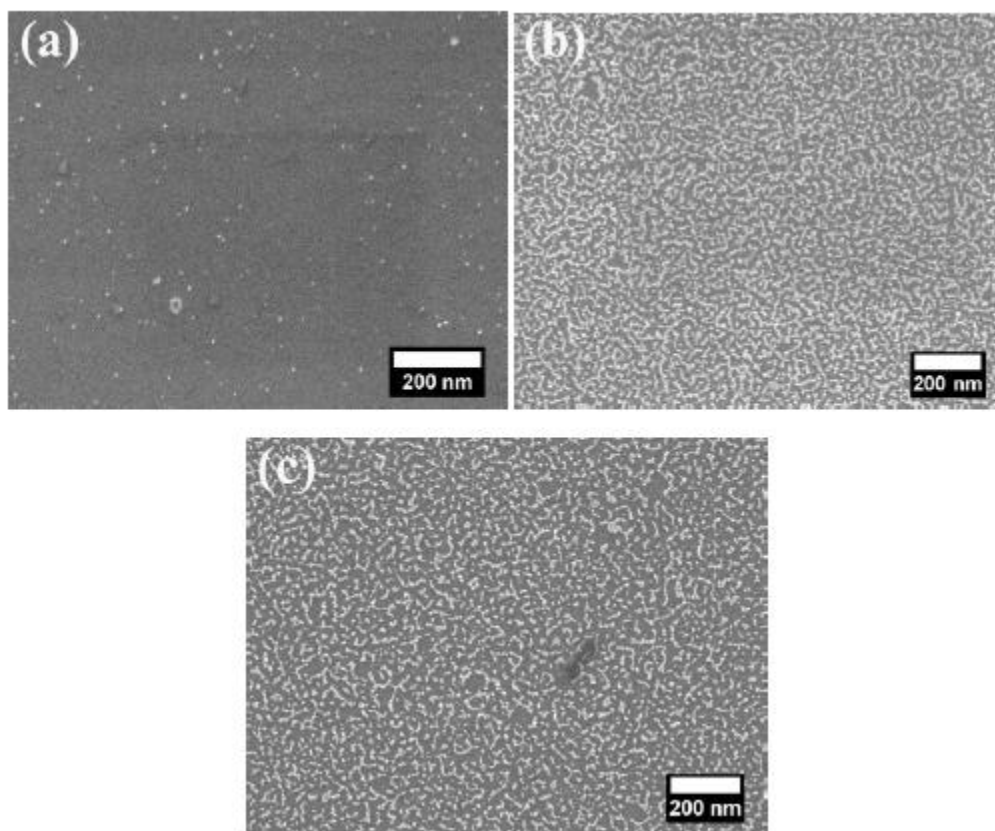
Figure 8.4. SEM micrographs of Au nanoparticles on (a) SiO$_2$, (b) APhTS, and (c) MPTS films

on Si (100) substrates after ultrasonication in hexane.

following ultrasonication on (a) SiO_2, (b) APhTS, and (c) MPTS. The micrographs illustrate that while some nanoparticles remain on the SiO_2 surface, most are washed away and resuspended into the hexane solvent. Meanwhile, the majority of particles remain on the APhTS- and MPTS-coated substrates indicating the immobilization of the nanoparticles.

SAM and nanoparticle coatings were also deposited onto polysilicon cantilever beams to initially study the effect the deposition processes have on device integrity. Fig. 8.5 presents optical photographs of cantilever beam arrays coated with (a) APhTS and (b) MPTS, followed by GXL nanoparticle deposition and supercritical drying. The images illustrate that in both cases a majority, if not all, of the beams were released and free-standing following the deposition procedures due to the lack of interference fringes. However, the APhTS/nanoparticle-coated array in Fig. 8.5a appeared to be much dirtier than the MPTS/nanoparticle-coated array in Fig. 8.5b. Using SEM to increase the magnification revealed several large "boulder" like features on the surface of the APhTS/nanoparticle-coated sample, as shown in Fig. 8.6. Such features were not exhibited on the APhTS-coated Si (100) substrate imaged in Fig. 8.4b, indicating that the inability to rinse or sonicate cantilever beams following deposition may leave behind agglomerated APhTS molecules or reaction byproducts.

It has also been widely shown in literature that CO_2 can absorb onto or react with primary amines (Aresta et al. 2000; Hampe and Rudkevich 2003; Chang et al. 2009; Culler et al. 1983; Battjes et al. 1991; Leal et al. 1995). Chang et al. (2009) illustrated that two nearby primary amines grafted onto silica can bind with a CO_2 molecule to form ammonium carbamate and, in the presence of water, further react to ammonium bicarbonate. FTIR studies were performed to further investigate this possible reaction and determine if the "boulders" in Fig. 8.6 were ammonium carbamate or bicarbonate. Fig. 8.7 presents FTIR spectra of an APhTS film on a
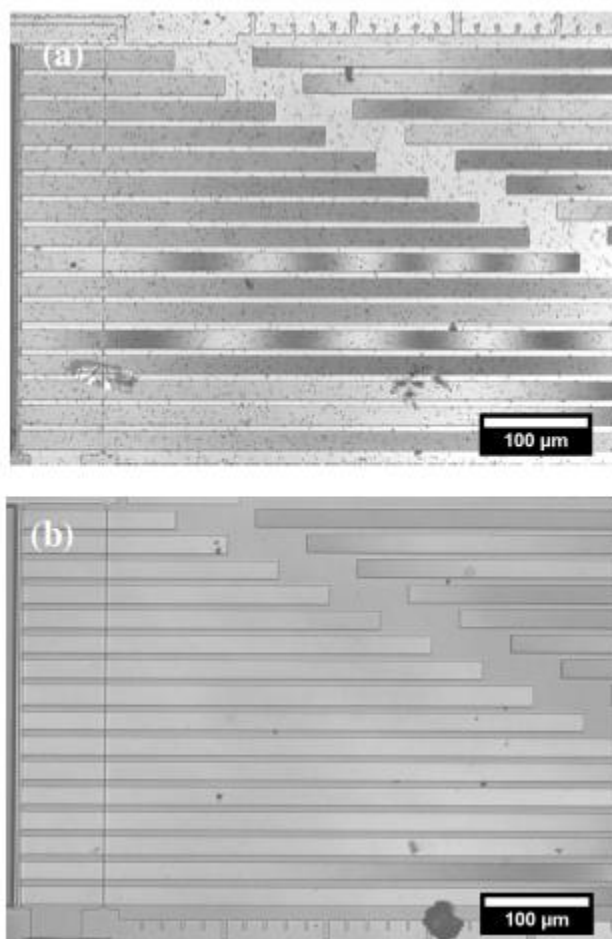
Figure 8.5. Optical photographs of polysilicon cantilever beam arrays coated with

(a) APhTS/AuNPs and (b) MPTS/AuNPs.
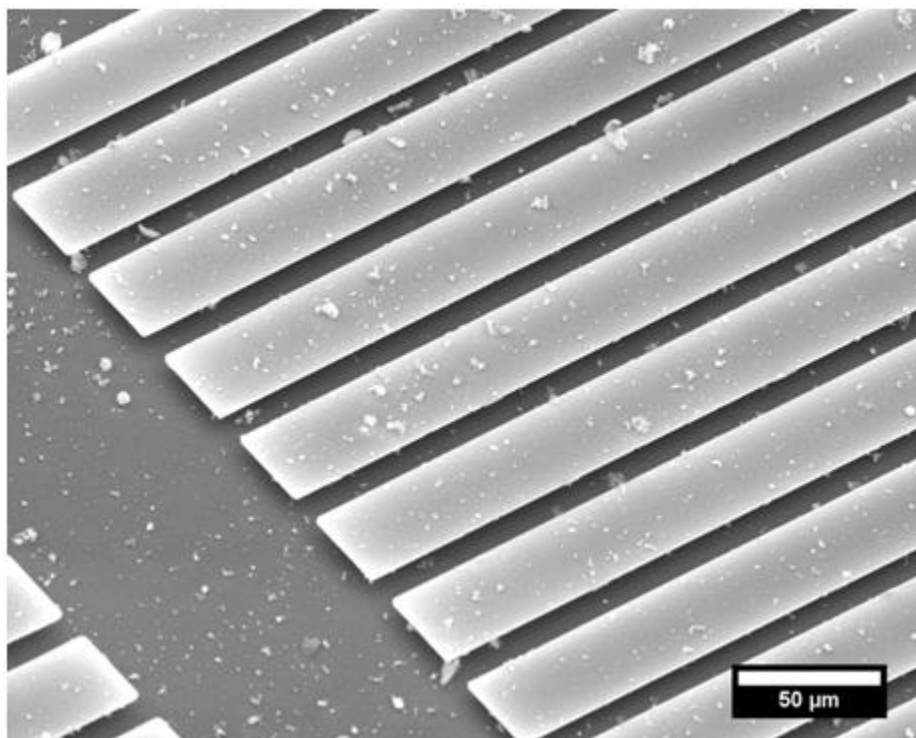
Figure 8.6. SEM image of boulder-like features on APhTS/NP composite films on Si (100) in-

plane cantilever beams.
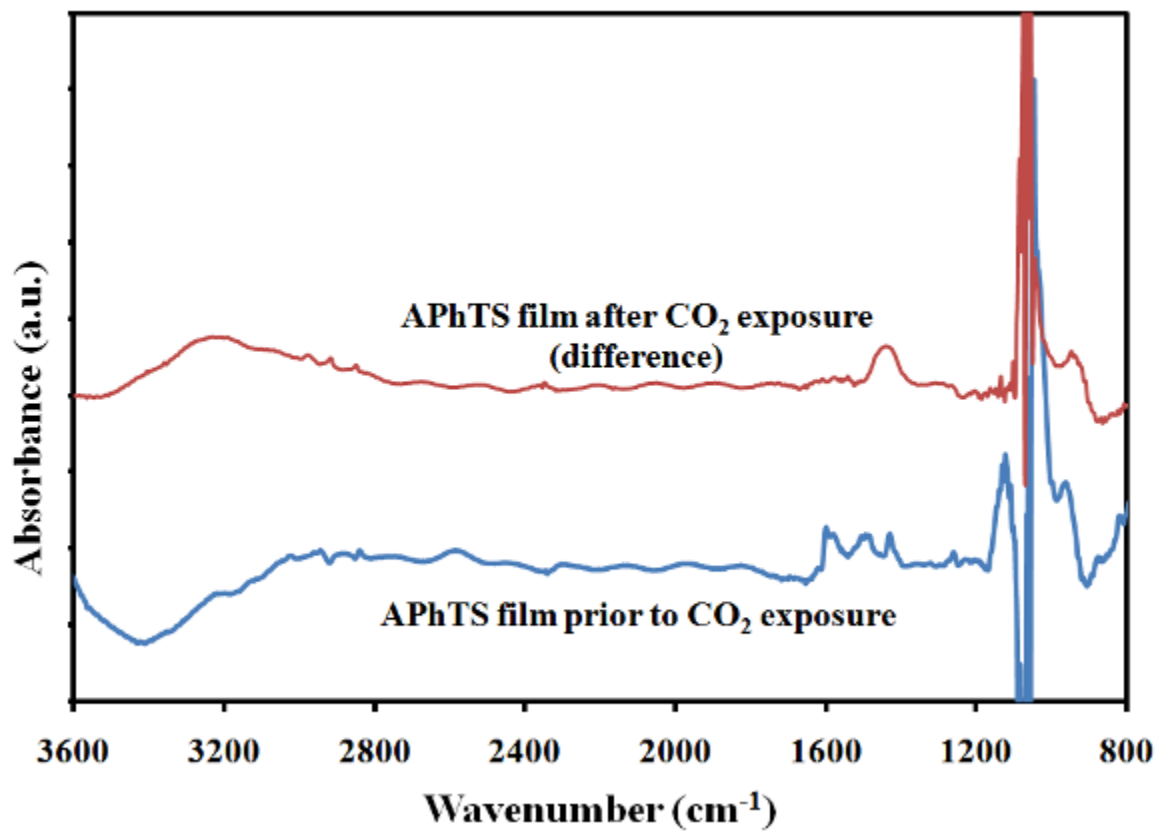
Figure 8.7. FTIR spectra of an APhTS film on silica before and after

exposure to CO_2 at ca. 8 bar.

silica seed layer both before and after exposure to CO_2 at a pressure of ca. 8 bar. The spectrum of APhTS prior to *ex situ* CO_2 exposure was used as a background so that the spectrum following exposure would signify only increases or decreases in species. The difference spectrum after exposure to CO_2 exhibits a broad peak between 1400 and 1500 cm^{-1}. While this peak could be attributed to some adsorbed moisture from the ambient atmosphere, it is also attributed to the C-O bending mode of carbamate (Leal et al. 1995). Zooming in to the region between 1300 and 1800 cm^{-1}, as shown in Fig. 8.8, very small peaks appear at 1580 and 1620 cm^{-1}. The appearance of these two weak peaks are attributed to the N-H bending mode of ammonium and the C=O stretching of carbonate (Leal et al. 1995).

8.4   Surface energy of SAM/NP composite films

Adhesion and hydrophobicity are both intrinsically related to the energy of a surface. Surfaces with high free surface energies will also exhibit increased adhesion energies and greater affinities to attract moisture and water. Therefore, examining the surface energy by means of contact angle analysis can also be a good indicator of how an anti-stiction coating will behave. The contact angle of water droplets on SiO_2, AuNP, MPTS/AuNP, and APhTS/AuNP films were measured to qualitatively compare the surface energies of the films. Fig. 8.9 presents photographs of water droplets on surfaces coated with (a) native silicon oxide, (b) non-immobilized gold nanoparticles on silicon oxide, (c) APhTS, (d) MPTS, (e) APhTS/AuNPs, and (f) MPTS/AuNPs. Table 8.2 presents the contact angles corresponding to the six surface modifications in Fig. 8.9. The images illustrate that the hydrophilic and rough nature of the nanoparticles alone are enough to significantly reduce the surface energy of silicon oxide, explaining why nanoparticle films were effective in reducing stiction as shown in Chapters 5 and
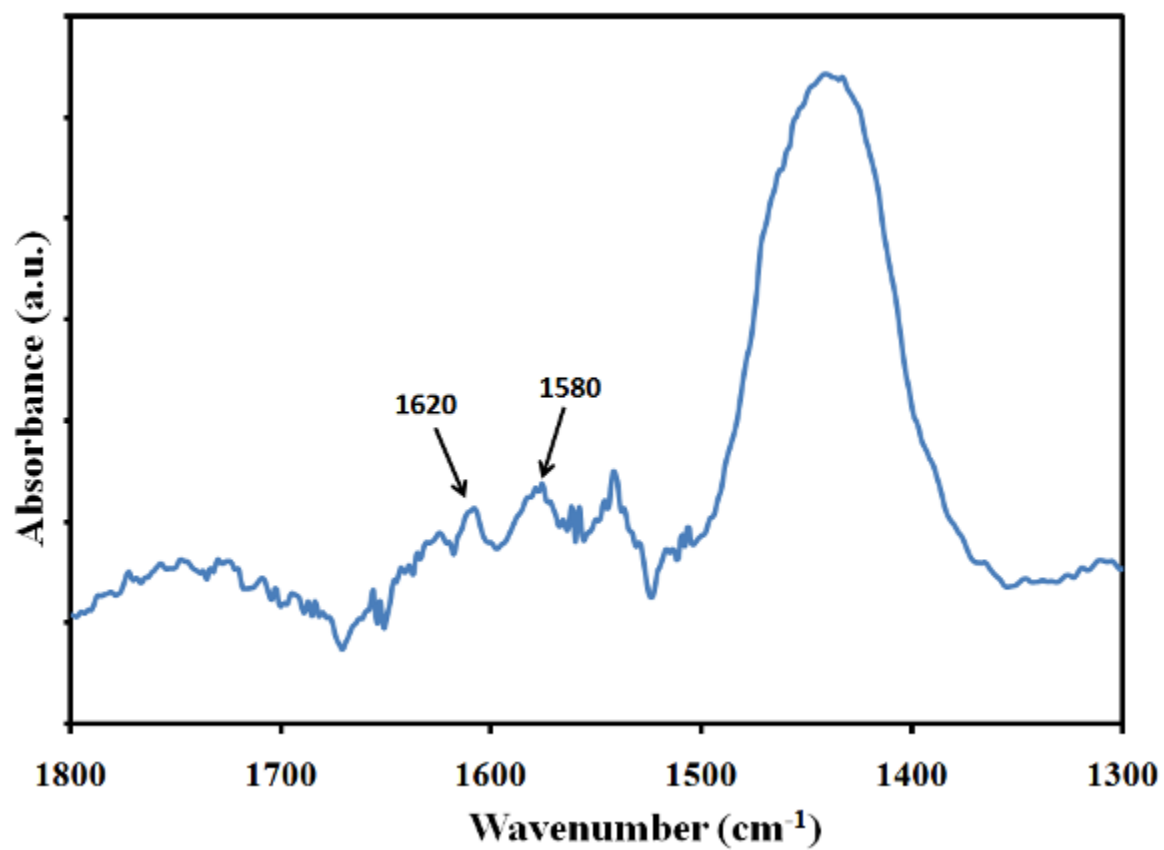
Figure 8.8. FTIR spectrum of APhTS film exposed to *ex situ* CO$_2$.

Surface modification	Contact angle
Native SiO_2	$< 20.0°$
AuNP	$71.6°$
APhTS	$51.4°$
MPTS	$69.8°$
APhTS/AuNP	$80.1°$
MPTS/AuNP	$91.4°$

Table 8.2. Contact angles of various surface modifications on silica.
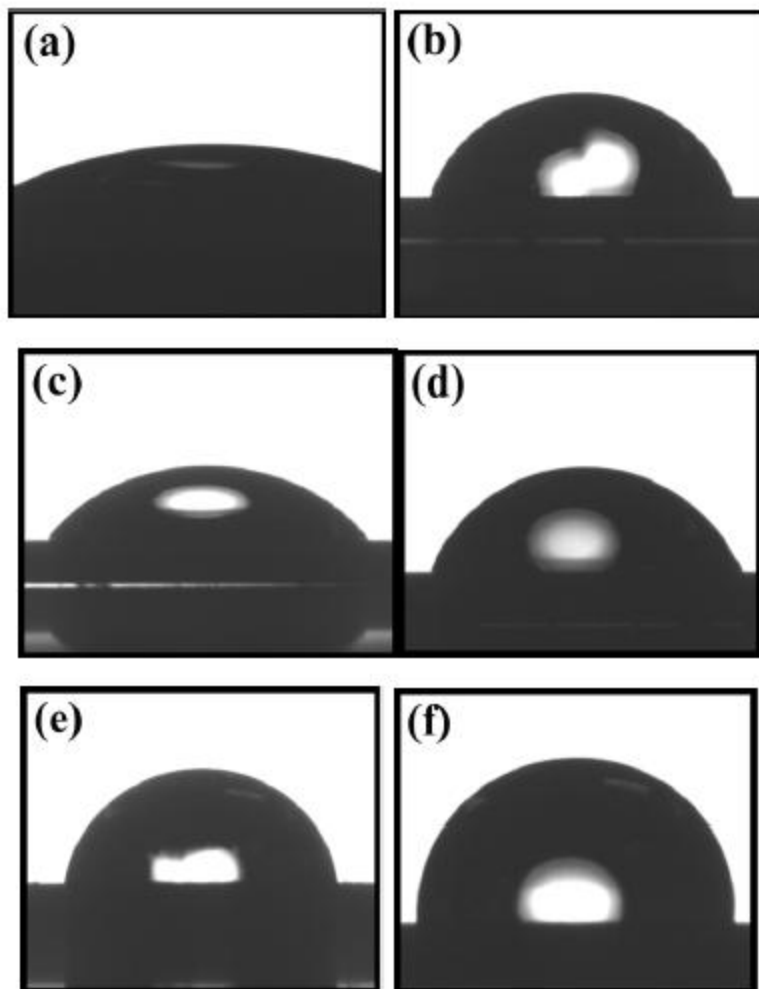
Figure 8.9. Photographs illustrating the contact of water droplets on (a) native SiO_2,

(b) unattached AuNPs on SiO_2, (c) APhTS, (d) MPTS,

(e) APhTS/AuNPs, and (f) MPTS/AuNPs.

7. The addition of the rough nanoparticle films onto SAMs also further reduces the surface energy. The contact angles of APhTS and MPTS films when coated with nanoparticles increase to 80.1° and 91.4°, which indicate increases of 56% and 31%, respectively. The phenomenon illustrated by the addition of hydrophobic features to an already hydrophobic surface was described by Wenzel (1936) and Cassie and Baxter (1944).

8.5   Durability of SAM/NP composite films

The durability of AuNP, SAM, and SAM/AuNP films were examined using the water erosion technique described in Chapter 3 and by examining the substrate via SEM imaging following mechanical contact. AuNP films have previously been shown to be easily translated and worn away during mechanical contact, which is undesirable for anti-stiction coatings for MEMS. Therefore, more robust and durable coatings are desired. Fig. 8.10 presents the change in contact angles of the various samples with increased water droplet erosion time up to 10 h. When only AuNPs were deposited onto Si (100) substrates, the contact angle decreased from about 72° to less than 20° after 1 h of water droplet erosion, indicating practically no film durability. This decrease in contact angle represents a reduction of 70%. APhTS and MPTS monolayers on Si (100) substrates experienced percent decreases in contact angle of 17% and 24%, respectively, after 1 h of water erosion. The erosion of SAM/AuNP composite films after 1 h were in the same range – 19% for APhTS/AuNP and 46% for MPTS/AuNP – indicating that the erosion of the composite coatings is limited by the rate of erosion of the monolayers from the silicon surface. This is not unexpected, however, as previous studies have shown decreased stability of siloxane films in aqueous environments (Barbier et al. 2006; Anderson and Ashurst 2009). Fig. 8.11 demonstrates how the water contact angle ratio, $1 - \theta/\theta_0$, changes for each

204
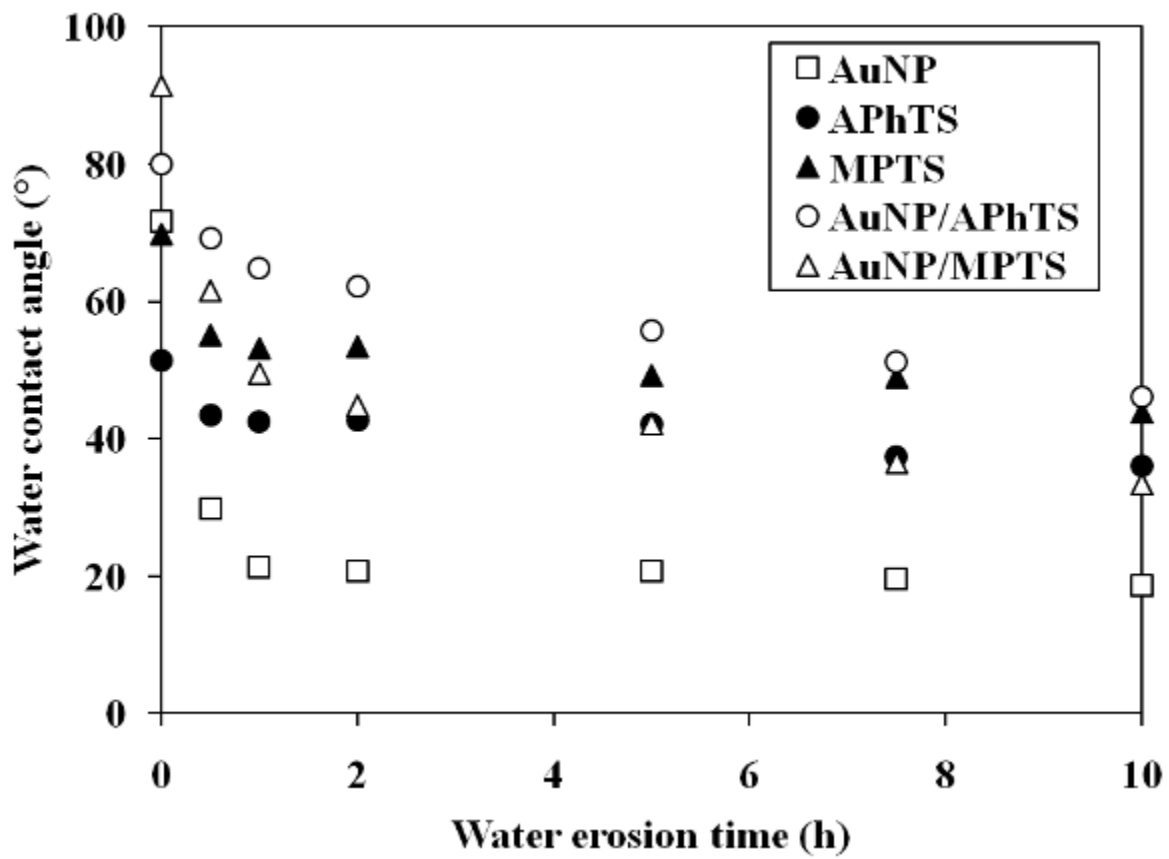
Figure. 8.10. Water contact angle for various surface modifications with increasing water erosion time.
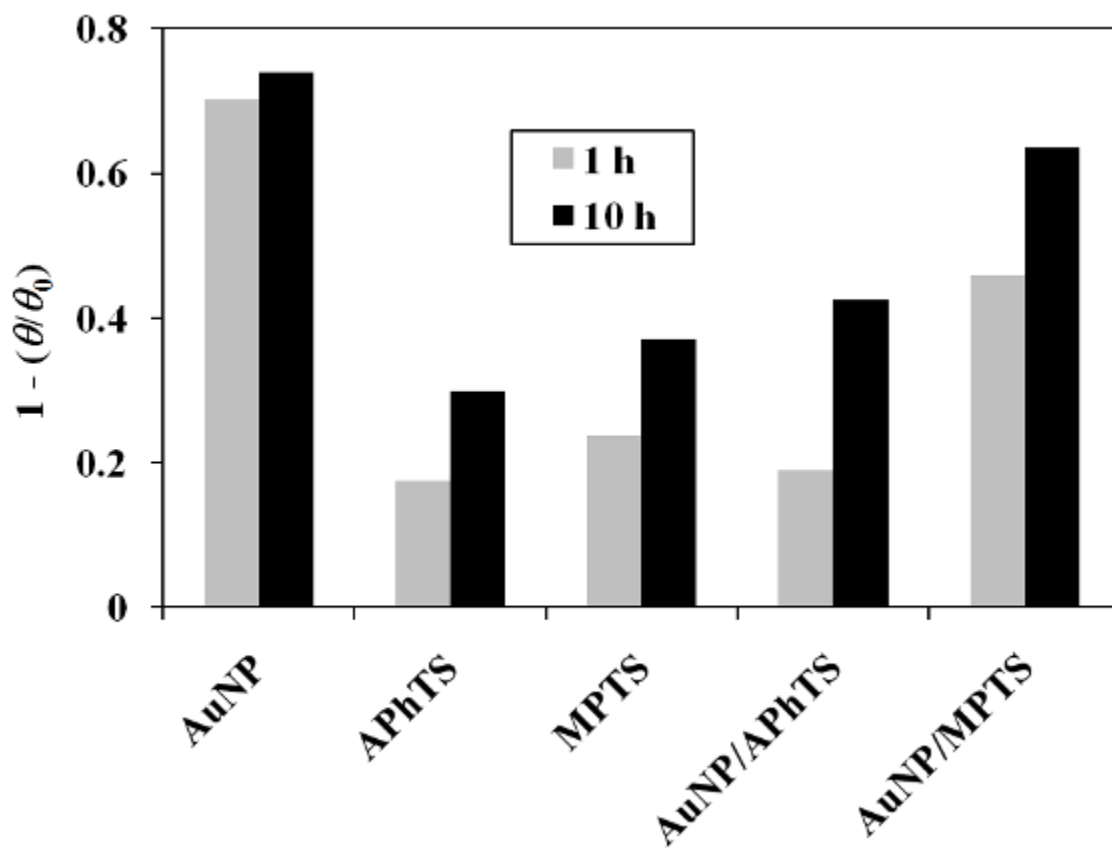
Figure 8.11. Change in water contact angle ratio following 1 and 10 h water erosion.

coating after 1 and 10 h of water erosion. This phenomenon is further illustrated by SEM in Fig. 8.12 which presents AuNP and MPTS/AuNP coatings on silicon before and after 1 h of water droplet erosion. Fig. 8.12(a) and (b) illustrate that a majority of the nanoparticles in the non-immobilized AuNP film are removed due to the impinging water droplets as the percent surface area covered by particles decreased from about 45% to 16.5%. In the case of MPTS/AuNP coatings in Fig. 8.12(c) and (d), the only discernable difference is the disappearance of the larger multi-layer AuNP islands after exposed to the water erosion test. The coverage area of nanoparticles on the surface remained constant at 52-54%. This indicates that the MPTS/AuNP composite coating is much more robust than non-immobilized nanoparticle films.

Fig. 8.13 presents SEM images of (a) a non-immobilized AuNP coating and (b) an MPTS/AuNP composite coating beneath a polysilicon cantilever beam following electrostatic actuation of 120 V. The areas between the dashed lines indicate the areas of sliding contact at the tip of the beam. Remarkably, there is no discernable difference in the coating in the area of contact compared to the rest of the substrate on the MPTS/AuNP coating, indicating that the composite coating was much more resilient to mechanical contact than nanoparticles alone, as previously illustrated. As shown in the figure, the mechanical contact of the in-plane surfaces was not enough to remove the weakly bound nanoparticles from the organic monolayer films, as opposed to non-immobilized nanoparticles which now show regions of nanoparticle translation. In addition, Fig. 8.14 presents an MPTS/AuNP film beneath a 500-μm Si (100) in-plane cantilever beam (illustrated by the black outline) following actuation and mechanical contact.

The differences in the evaluation of the coating durability in Figs. 8.12 and 8.13 can be explained by the amount of force experienced by the coatings during each durability test. In terms of the water erosion studies, the impact force of a 50 μl droplet of water impinging the
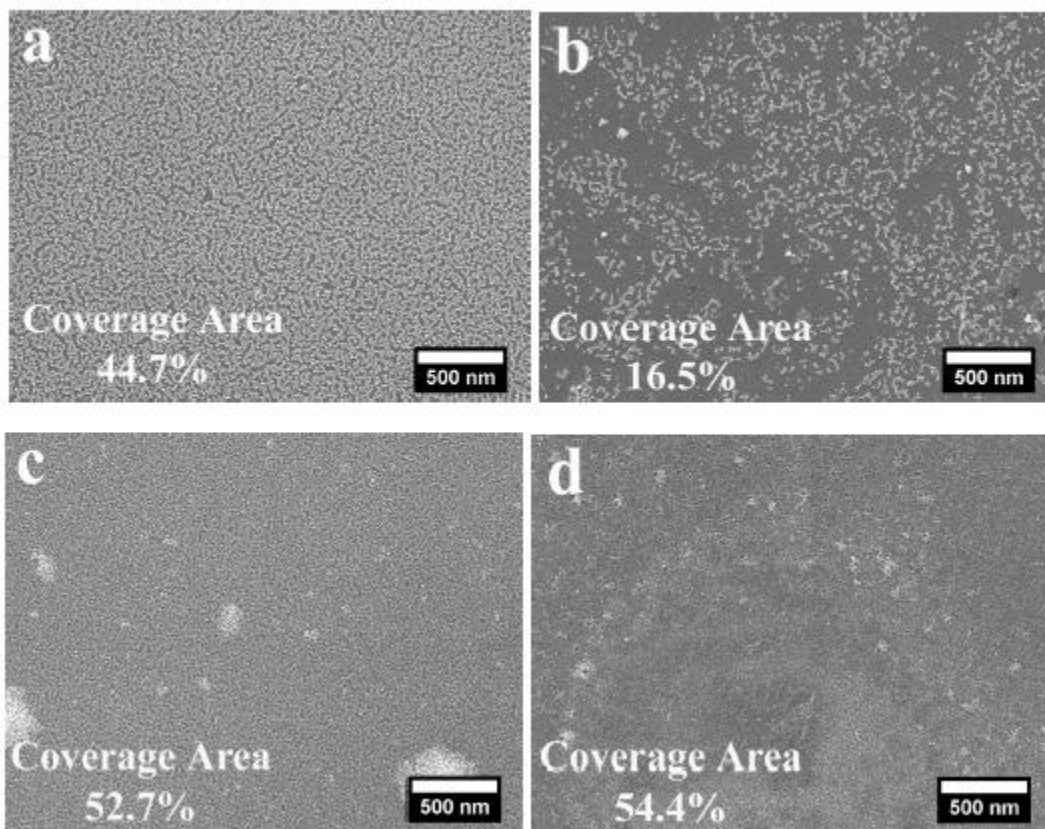
Figure 8.12. SEM images of Si (100) substrates coated with AuNPs only (a) before and (b) after

1 h water erosion and MPTS/AuNP composite films (c) before and (d) after 1 h water erosion.

Coverage area of nanoparticles on the surface was determined by image analysis.
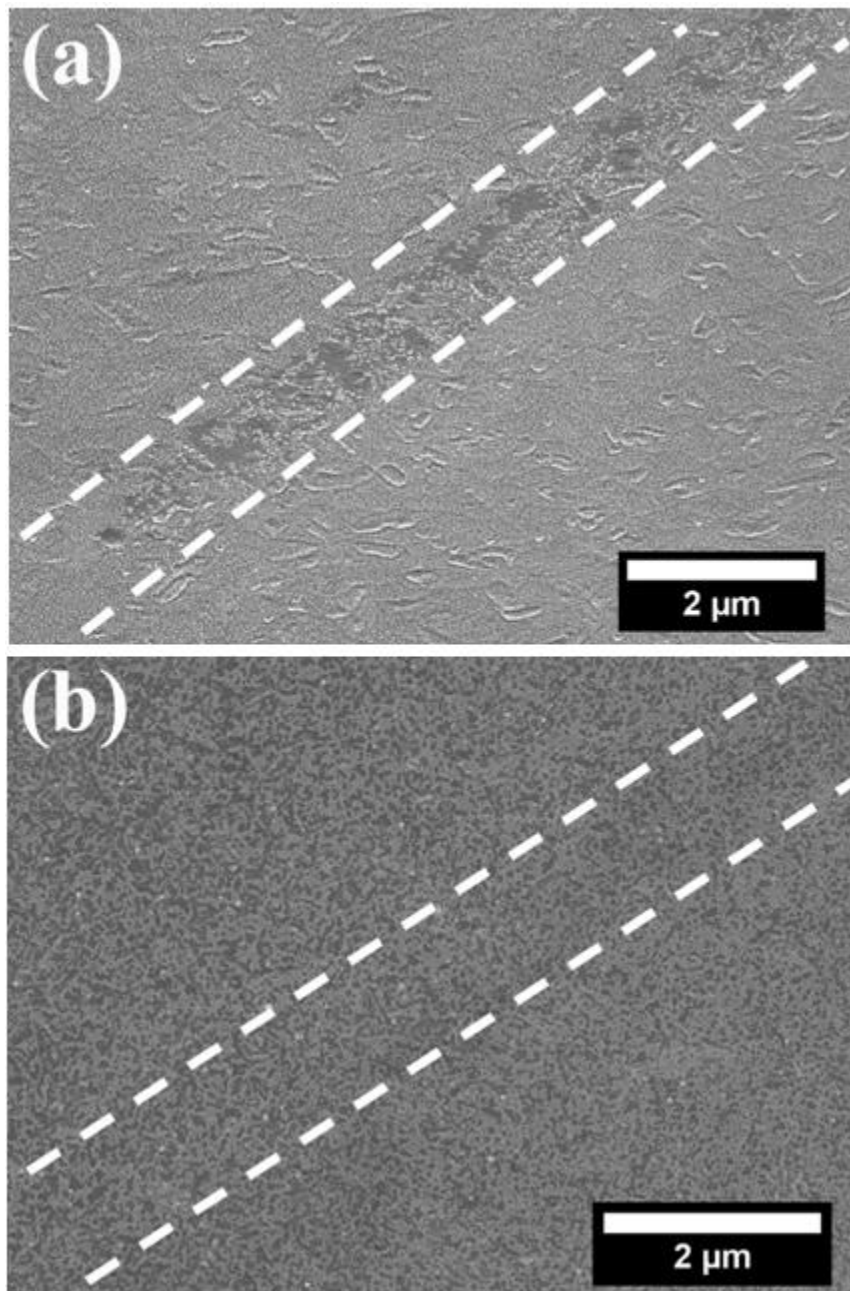
Figure 8.13. SEM images of (a) AuNP-coated polysilicon and (b) MPTS/AuNP coated polysilicon following cantilever beam actuation. The area between the dashed lines indicates the region of mechanical contact of the beam tip.
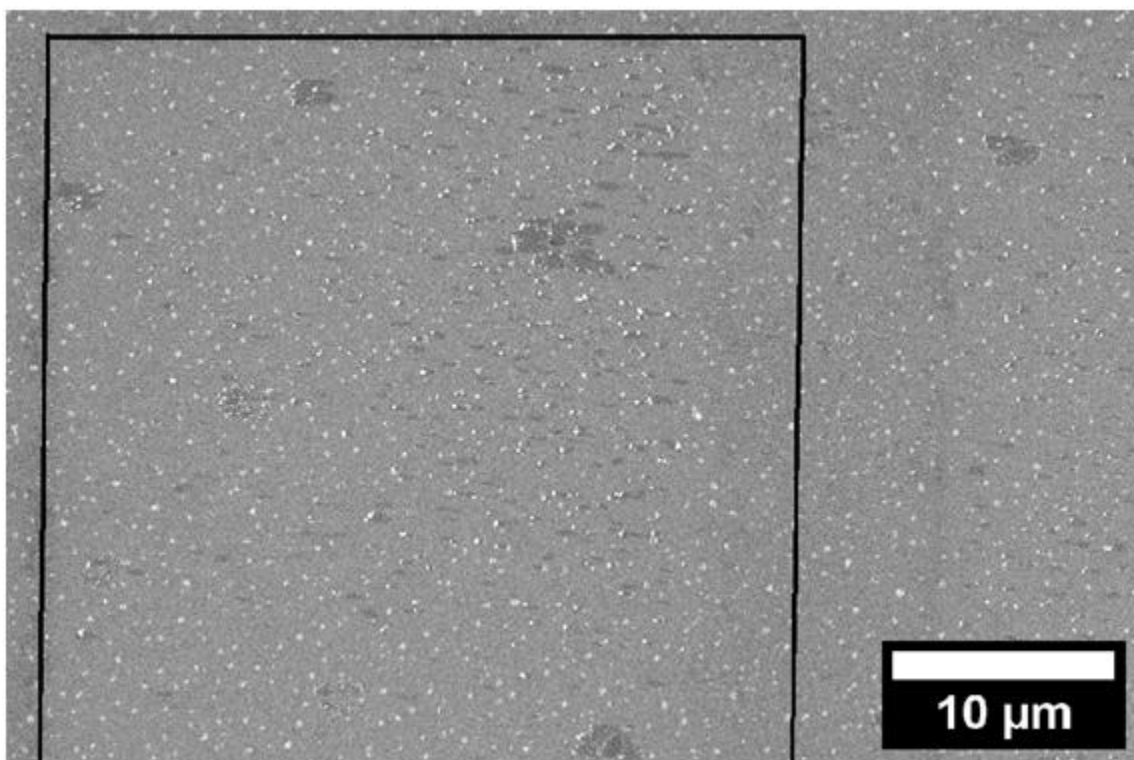
Figure 8.14. Region of Si (100) in-plane cantilever tip contact on MPTS/AuNP

composite film following actuation.

surface due to gravity is on the order of 500 μN. This was obviously enough force to wash away nearly all non-immobilized AuNPs and even some of the SAM/AuNP coatings as evidenced by Figs. 8.10 through 8.12. The mechanical contact force experienced between a deflected cantilever beam and the underlying substrate, however, is much smaller and is a direct result of two separate forces acting on the cantilever beam as shown in Fig. 8.15. In the figure, the applied electrostatic force (F_{el}) is a distributed load that occurs over a distance a and the restrictive force (F_r) is implied by the underlying substrate which keeps the beam tip deflection $u(x)$ to the maximum deflection u_{max} at $x = L$. This restrictive force is the force experienced by the coating when the beam and substrate come into mechanical contact.

The restrictive force can be calculated by superpositioning the individual beam tip deflections due to the individual forces as shown in Fig. 8.16. In Fig. 8.16, $u_1(F_{el})$ and $u_2(F_r)$ are the individual beam tip deflections due to the electrostatic and restrictive forces, respectively. The two individual deflections can be combined to describe the overall tip deflection, u, following

$$u = u_1\left(F_{el}\right) + u_2\left(F_r\right) \tag{8.1}$$

under the method of superpositioning (Gere and Timoshenko 1997). The tip deflections of the individual forces shown in Fig. 8.16(a) and (b) are well known solutions found in various texts. The deflection due to the electrostatic force is expressed by Eqn. (8.2):

$$u_1\left(F_{el}\right) = \frac{F_{el}a^2}{24EI}\left(4L - a\right) \tag{8.2}$$

where a is the length of the actuation pad distributing the load (80 μm), L is the beam length, E is the Young's modulus of the beam, and I is the moment of inertia where

$$I = \frac{wt^3}{12}.$$

211
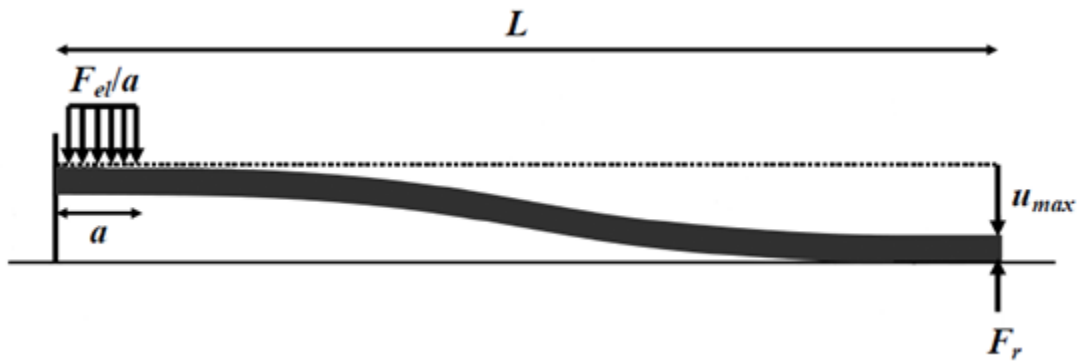
Figure 8.15. Cantilever beam subjected to an electrostatic force (F_{el}) and a restrictive force

caused by the underlying substrate (F_r).

(a)

a

$q = F_{el}/a$

$u_1(F_{el})$

(b)

$u_2(F_r)$

F_r
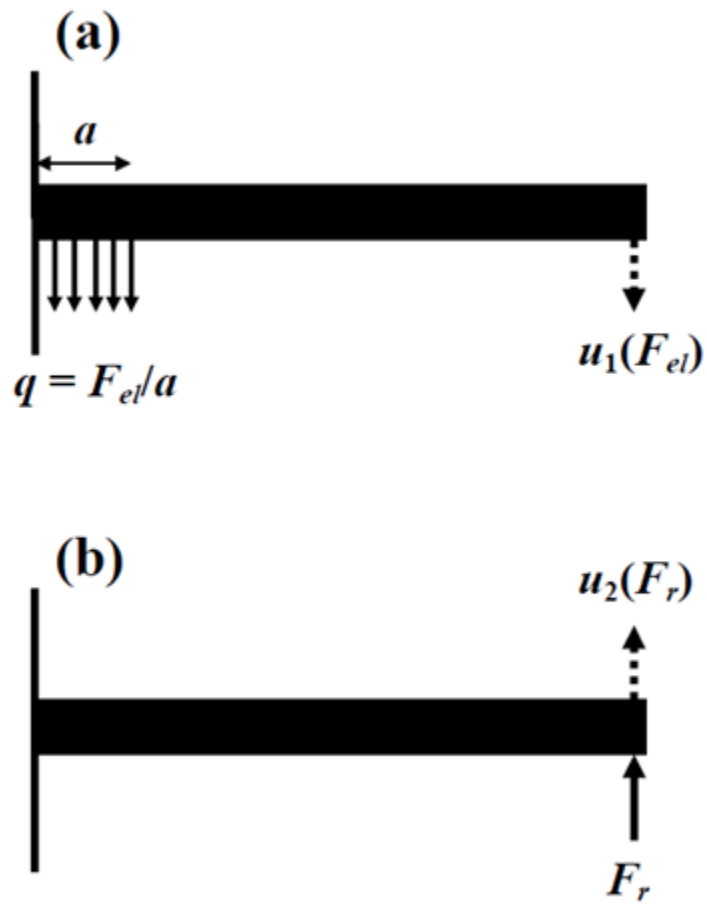
Figure 8.16. Diagrams illustrating the individual contributions of (a) the electrostatic actuation

force and (b) the restrictive contact force experienced by a cantilever beam.

The electrostatic force is a function of the voltage applied to actuate the beams, as shown in Eqn. (8.3):

$$F_{el} = \frac{1}{2} \frac{V^2 \varepsilon_0 \varepsilon_r wa}{g^2}$$ (8.3)

where V is the voltage, ε_0 is the permittivity of the free space (8.85 pF/m), ε_r is the relative permittivity of air, and g is the gap distance between the beam and the actuation pad/substrate which was determined by interferometry to be 2.09 μm. In this study, the maximum voltage applied was 120 V which yields an electrostatic force of 21.0 μN.

The tip deflection due to the point force associated with the restrictive force is given by Eqn. (8.4):

$$u_2(F_r) = -\frac{F_r L^3}{3EI}.$$ (8.4)

Notice that both deflections in Eqn. (8.2) and (8.4) are not only dependent on the forces but also on the overall beam length. This indicates that the restrictive force between the beam and substrate will change based on beam length.

When Eqn. (8.2) and (8.4) are substituted into Eqn. (8.1) and setting the deflection equal to the maximum value, the resulting tip deflection becomes:

$$u = u_{max} = g = \frac{F_{el} a^2}{24EI}(4L - a) - \frac{F_r L^3}{3EI}.$$ (8.5)

Solving Eqn. (8.5) for the restrictive force yields:

$$F_r = \frac{F_{el} a^2 (4L - a) - 24EIg}{8L^3}.$$ (8.6)

Following Eqn. (8.6), when a voltage of 120 V is applied, assuming a beam length of 500 μm, the restrictive force experienced between the beam tip and substrate is 0.07 μN which is four

214

orders of magnitude less than the force experienced by a coating due to a falling droplet of water. Therefore, the water erosion tests and beam actuation are expected to yield different results in terms of coating durability. From these experiments, it is evident that the SAM/AuNP coatings are much more resilient to the miniscule forces experienced during mechanical contact than non-immobilized AuNP coatings as shown in Chapter 5.

8.6 Effect of SAM/NP composite films on adhesion

The effect of SAM/AuNP composite coatings on stiction and adhesion of microstructures by actuating cantilever beams which have been coated. Both polysilicon and Si (100) in-plane cantilever beams were used to examine adhesion. The typical work of adhesion between polySi and Si (100) cantilever beams and the underlying substrates are about 0.700 and over 37 mJ/m^2, respectively. As previously discussed in Chapters 5 and 7, nanoparticles alone are enough to significantly reduce this adhesion by providing rough, low energy asperities. The addition of nanoparticles to self-assembled monolayers would couple the effects of film roughness with the very low surface energy of SAM films. Fig. 8.17 and 8.18 present interferograms of polySi and Si (100) in-plane CBAs which have been coated with MPTS/AuNP and APhTS/AuNP composite films, respectively. Fig. 8.19 depicts the vertical profile of a selected beam from Fig. 8.17(c) and (d) to prove that the beams are initially free standing and not adhered to the substrate.

Fig. 8.17(a) and (b) present a polySi CBA coated with an MPTS/AuNP composite film before and after electrostatic actuation. Fig. 8.17(c) through (f) present two MPTS/AuNP-coated Si (100) CBAs of lengths 500- and 1000-μm before and after manual actuation. None of the adhered polySi beams in Fig. 8.17(b) illustrate a characteristic crack length. The longest unadhered beam in this array was 700 μm in length. A 750-μm long beam, adhered only at the
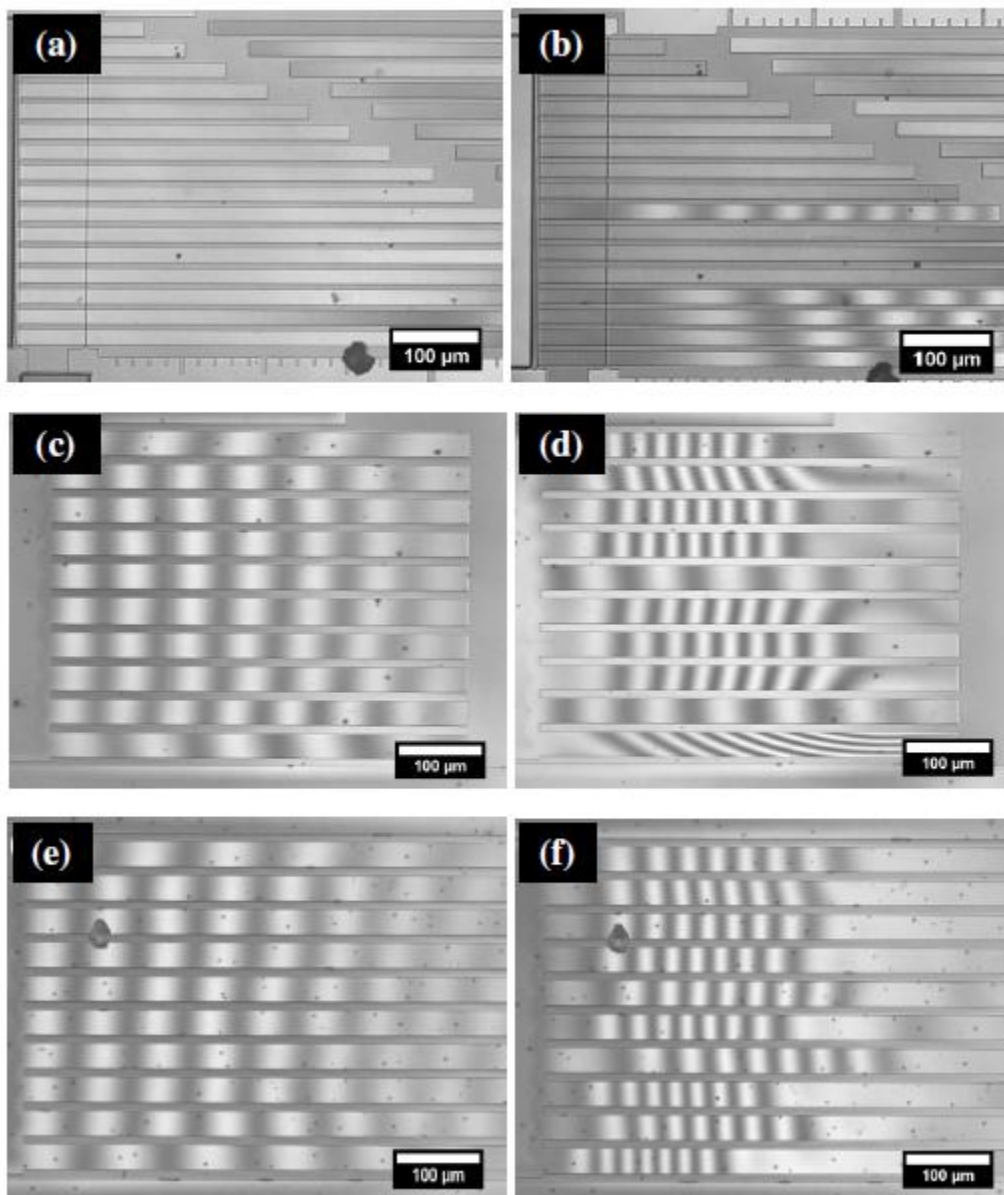
Figure 8.17. Interferometry images of MPTS/AuNP coated CBAs: (a) polySi before actuation, (b) polySi after actuation, (c) 500-µm Si (100) before actuation, (d) 500-µm Si (100) after actuation, (e) 1000-µm Si (100) before actuation, and (f) 1000-µm Si (100) after actuation.
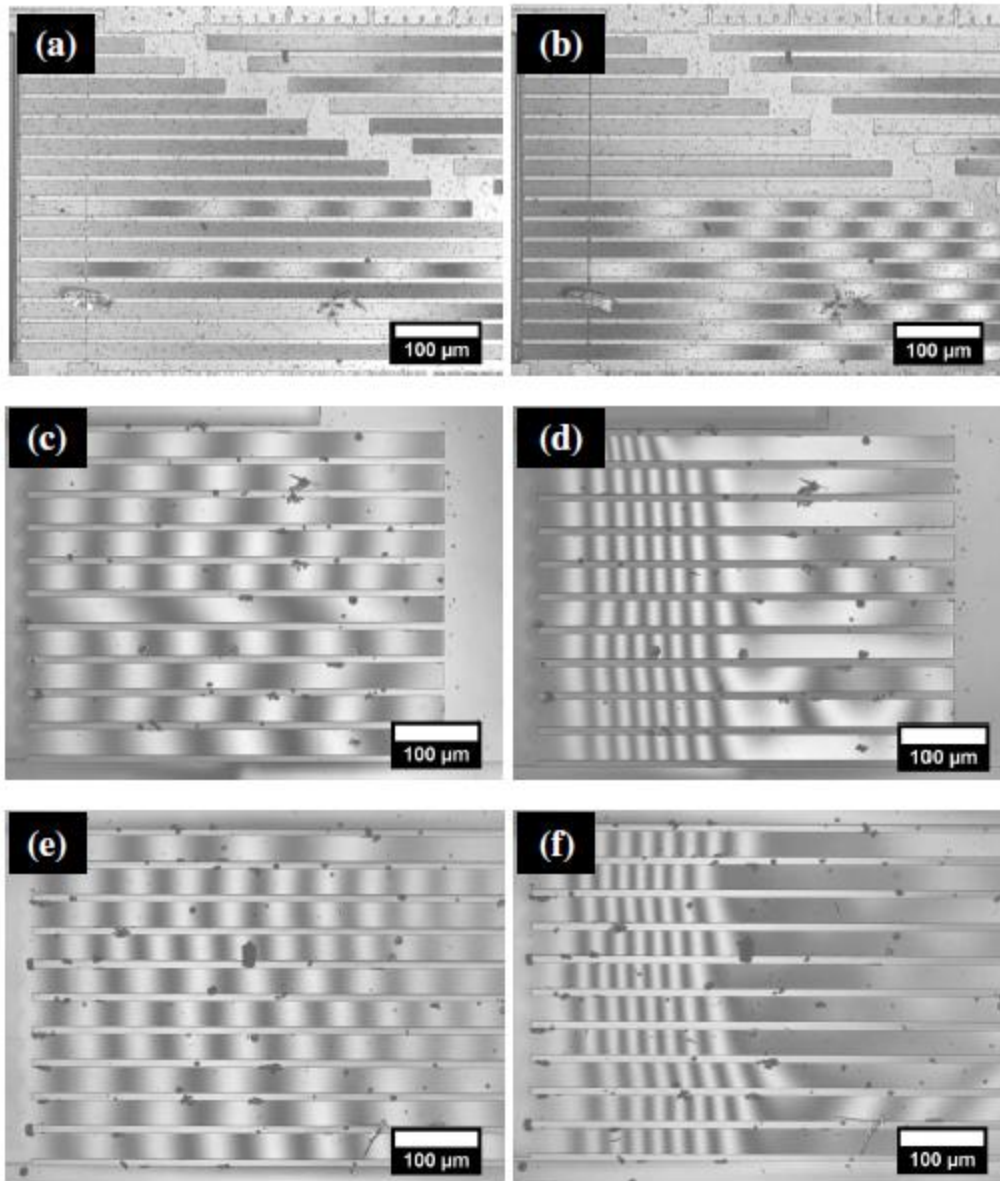
Figure 8.18. Interferometry images of APhTS/AuNP coated CBAs: (a) polySi before actuation, (b) polySi after actuation, (c) 500-µm Si (100) before actuation, (d) 500-µm Si (100) after actuation, (e) 1000-µm Si (100) before actuation, and (f) 1000-µm Si (100) after actuation.

217
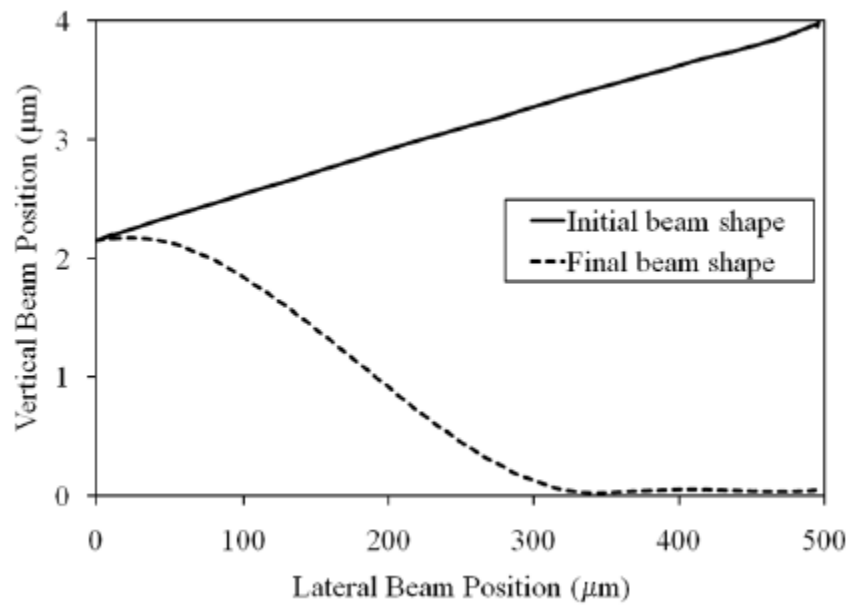
Figure 8.19. Vertical profile of a selected beam from Fig. 7.15(c) and (d)

showing the initial and final beam shape.

beam tip would yield a work of adhesion of less than 0.010 mJ/m^2. Therefore, it can be said that the expected adhesion energy for an MPTS/AuNP coated polySi array is less than this value. This value is two orders of magnitude lower than the typical 0.700 mJ/m^2 expected for an uncoated array.

The Si (100) CBAs coated with MPTS/AuNP presented in Fig. 8.17 yielded beams adhered to the substrate in the typical S-shape. The average crack length of all the adhered beams in Fig. 8.17(d) and (f), combined, was 383.9 ± 55.2 µm compared to about 94 µm for native oxide coated Si (100) in-plane beams. The average adhesion energy over all MPTS/AuNP coated Si (100) beams studied was 0.655 ± 0.329 mJ/m^2. This represents a substantial reduction in adhesion energy compared to native oxide coated Si (100) microdevices. For comparison, the crack length and adhesion energies of MPTS/AuNP composite films on polySi and Si (100) CBAs are presented in Table 8.3. There are two beams in Fig. 8.17(b) which do not indicate a characteristic crack length due to potential large particulates underneath the beam near the 384 µm region which prevented the beam from making contact and sticking. These beams were not included in the analysis.

Fig. 8.18(a) through (f) present interferograms of APhTS/AuNP coated CBAs before and after actuation. Fig. 8.18(a) and (b) show a polySi CBA coated with APhTS/AuNP before and after electrostatic actuation. In Fig. 8.18(b), the longest beam adhered at the beam tip is 550 µm in length. This detachment length, for a beam adhered only at the tip, results in an upper bound adhesion energy of about 0.040 mJ/m^2. This value is slightly higher than what was found for MPTS/AuNP coatings on polySi in-plane surfaces, but still two orders of magnitude lower than native oxide-coated CBAs.

Surface coating	Substrate	Average crack length (μm)	Average adhesion energy (mJ/m^2)	Percent decrease from native state
Native oxide	PolySi	350-400	0.700	N/A
	Si (100)	94	37.4	N/A
AuNP only	PolySi	700	0.010	98.6
	Si (100)	250	1.260	96.6
MPTS/AuNP	PolySi	750	0.010	98.6
	Si (100)	384	0.655	98.2
APhTS/AuNP	PolySi	550	0.040	94.3
	Si (100)	268	1.66	95.6

Table 8.3. Comparison of surface coatings on polySi and Si (100) in-plane

cantilever beams adhesion.

Fig. 8.18(c) through (f) are interferograms of APhTS/AuNP coated Si (100) in-plane CBAs before and after actuation. Again, two different lengths of beams were studied; 500 and 1000 μm. The average crack length for every beam examined was 267.5 ± 17.1 μm. This average crack length for APhTS/AuNP coated Si (100) beams was more than 100 μm shorter than that for the MPTS/AuNP coated counterparts, indicating a stronger work of adhesion. The average work of adhesion for APhTS/AuNP coated Si (100) beams was 1.66 ± 0.37 mJ/m^2 – more than 1 mJ/m^2 greater than the average adhesion energy for MPTS/AuNP composite coatings. The crack length and adhesion energies for the various coatings on various substrates are presented in Table 8.3. The percent decrease of adhesion energy was calculated based on the native oxide-coated states of 0.700 mJ/m^2 for polySi and 37.4 mJ/m^2 for Si (100).

8.8 Conclusions

In this chapter, gold nanoparticles were weakly immobilized on the surface of silicon and silicon-based microstructures by means of self-assembled monolayers with functional groups known to attract gold and other noble metals. Analysis showed that AuNPs deposited by the GXL deposition method onto MPTS or APhTS monolayers could not be redispersed into solution from SAM-coated silicon substrates, proving that particles could be immobilized. Further examination of SAM/AuNP composite films on silicon substrates showed that there increased film durability compared to AuNP films when subjected to falling droplets of water with a high impact force. Studies also suggested that the SAM/AuNP coatings were more robust towards mechanical contact made between cantilever beams and the underlying substrate than AuNPs alone.

In terms of adhesion energy, MPTS/AuNP composite films were equally as effective towards reducing the apparent work of adhesion of cantilever beam arrays as were AuNP coatings in previous studies. Both types of coatings reduced the adhesion energy of polySi and Si (100) in-plane surfaces by at least 97%. APhTS/AuNP composite films, on the other hand, were not as effective in reducing adhesion on either polySi or Si (100) surfaces. The adhesion energy on such surfaces was only reduced by about 94%. The inability to reduce adhesion on the level of MPTS/AuNP films could potentially be related to the large agglomerates left behind on the surface due to either APhTS polymerization or reaction of primary amines with CO_2.

The results from this study suggest that the use of SAMs such as MPTS or APhTS could provide a means for attached nanoparticles in order to create robust, rough surface modifications for permanent anti-adhesion properties. The only downside towards this method is the use of liquid-phase processing to deposit the monolayer films prior to GXL particle deposition and supercritical drying. The use of such processing may not be suitable for the large scale processing typically performed in the MEMS industry.

CHAPTER 9

ROUGH VAPOR PHASE DEPOSITED SILICA FILMS FOR

MICROTRIBOLOGY AND SUPERHYDROPHOBICITY

9.1   Introduction

In the previous chapter, gold nanoparticle films were immobilized on silicon surfaces and silicon-based microdevices by means of functionalized self-assembled monolayers. The studies found that SAMs with specific functional tail groups were very effective in immobilizing nanoparticles and allowing for the creation of robust AuNP thin films for microtribology control. However, there is still room to improve mechanically robust and durable nanoparticle coatings. In addition, the extensive use of solvents for the deposition of nanoparticle-immobilizing monolayers in the previous chapter is undesirable in industrial settings. Therefore, this chapter focuses on techniques for depositing rough, durable coatings from vapor phase techniques. The rough, vapor phase deposited (VPD) coatings have potential for both tribological properties as well as superhydrophobicity.

In this chapter, two methods are used to create coatings using vapor phase precursors. Chemical vapor deposition (CVD) is utilized to deposit silica and hydrophobic organic monolayers onto silicon surfaces for the purpose of creating anti-adhesive coatings for MEMS. The vapor-phase hydrolysis of silicon tetrachloride in order to form amorphous silica films has been demonstrated to occur at room temperature (Bannikova et al. 1969; Anderson and Ashurst

2008b), which would be desirable for industrial MEMS fabrication. The second method utilizes a novel vapor phase deposition (VPD) apparatus developed by Integrated Surface Technologies (Menlo Park, CA, USA). The VPD apparatus has been shown to produce rough and durable superhydrophobic thin films. The combination of surface roughness and low surface energy provides durable superhydrophobic coatings which have potential as water proof coatings for consumer electronics. Such surfaces, which typically link appropriately roughened surfaces with low surface energy materials such as fluorinated compounds (Lacroix et al. 2005), have the potential to greatly reduce the surface energy and effectively reduce detrimental interfacial phenomena. The VPD apparatus has the ability to produce aluminum oxide (Al_2O_3) nanoparticles from a gas phase reaction which can then be anchored and coated by the SiO_2 and hydrophobic layers. Superhydrophobic coatings have the potential revolutionize not only the MEMS industry, but the consumer electronics industry as well. The purpose of depositing silica over pre-deposited nanoparticle films is to entrap the particles and create rough, durable coatings as illustrated by Fig. 9.1.

9.2 CVD experimental setup and details

In order to create durable anti-stiction coatings for MEMS and tribology chips, gold nanoparticles (AuNPs) were first deposited onto SOI tribology chips and treated (cleaned) Si (100) substrates following the gas-expanded liquid deposition procedure described in Chapter 3. Following supercritical drying, the dodecanethiol ligand tails were burned off from the nanoparticle films by exposing the samples to a 30W oxygen plasma for 2 min. The AuNP-coated samples were then placed into the CVD chamber, illustrated by Fig. 9.2. The vapor delivery system vials shown in the figure contain liquid precursors of which vapor is drawn off
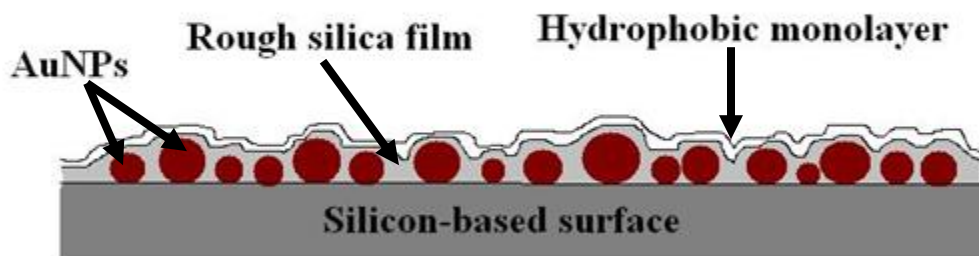
Figure 9.1. Schematic illustration of rough, durable AuNP-based coatings (not to scale).
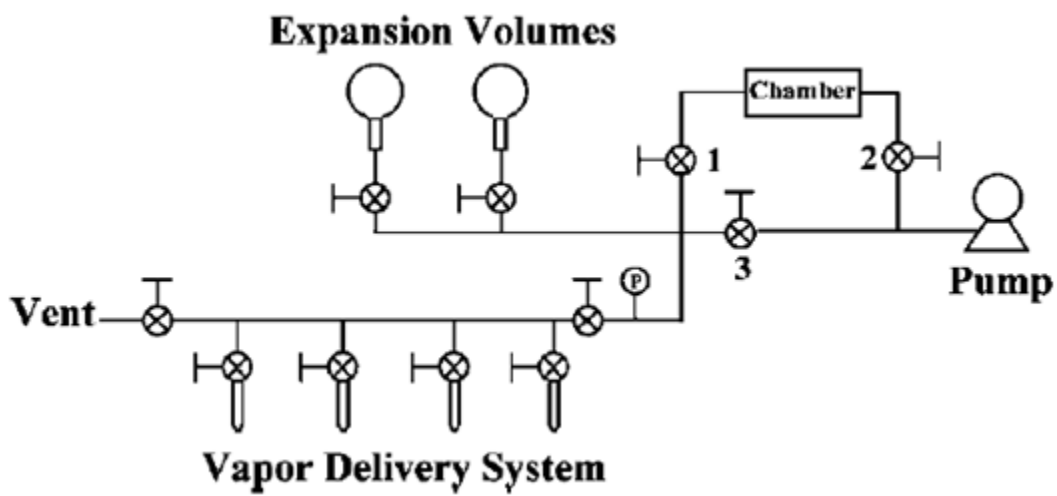
Figure 9.2. Illustration of the ultra low pressure CVD system utilized for

vapor phase coating deposition.

and carried to the reaction chamber for thin film deposition. The precursors in this study were water, tetrachlorosilane (SiCl$_4$), and perfluorooctyl trichlorosilane (FOTS).

The first reaction involves the deposition of a thin silica layer over the top of the GXL deposited AuNP films. The reaction utilizes small amounts of water and tetrachlorosilane which are respectively introduced to the two expansion volumes shown in Fig. 9.2 in sub-atmospheric conditions. After the system, including the reaction chamber containing the desired samples to be coated, is pumped down to a base pressure of about 4 mTorr, the expansion volumes are opened to allow for the precursors to react within the chamber for 10 min. The hydrolysis of SiCl$_4$ follows the reaction

$$SiCl_4(v) + 2H_2O(v) \rightarrow SiO_2(s) + 4HCl(v) \tag{9.1}$$
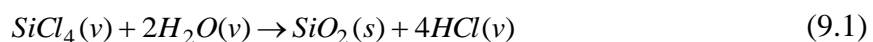
where two water vapor molecules react with a molecule of SiCl$_4$ to form one molecule of solid silicon oxide. Anderson and Ashurst (2008b) illustrated that the morphology of the resulting silica thin film from tetrachlorosilane hydrolysis can vary widely depending on the pressures of SiCl$_4$ and water precursors utilized for the reaction. In order to produce the most conformal and uniform silica coating possible, this study utilized 20 Torr of water vapor and 20 Torr of tetrachlorosilane. In theory, the increased roughness of the silica layer created by the underlying rough AuNP film should be enough to reduce the adhesion of microstructures. However, the rough silica film still maintains a very high surface energy. Therefore, the surface energy can be further reduced by the chemical vapor deposition of an organic SAM (i.e. FOTS). The deposition of FOTS follows a similar hydrolysis reaction at ultra low pressures, as shown in Fig. 9.3.

In this study, the morphology of AuNP/CVD silica films (with and without FOTS top layers) is examined by ellipsometry and AFM. The effect of the films is also examined on
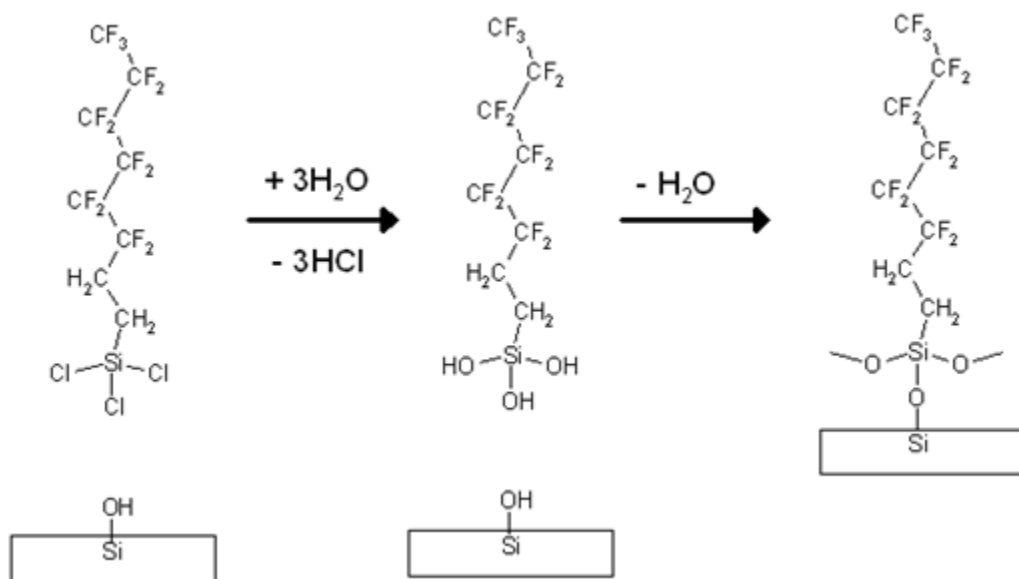
Figure 9.3. Schematic of the reaction of FOTS with water to form monolayers on SiO_2.

adhesion by depositing the films on SOI tribology chips consisting of cantilever beam arrays. The durability of AuNP/CVD films is also investigated by the water erosion method and by determining the coefficients of friction.

9.3 Characterization and durability of AuNP/CVD thin films

CVD SiO_2 and AuNP/CVD thin films were characterized by ellipsometry, AFM and contact angle goniometry to ensure film deposition. *In situ* ATR-FTIR spectroscopy was not readily available at the time to analyze interactions within the films. Freshly cleaned Si (100) substrates were uniformly oxidized by a 25W O_2 plasma to grow a smooth SiO_2 layer which was measured by ellipsometry to be 1.8 ± 0.1 nm thick. This was measured in order to keep track of any additional thickness added by the CVD process.

Following a quick 30W O_2 plasma for 2 min to remove any residuals from the surface, chips were subjected to water and $SiCl_4$ vapor as described in the previous section. After letting the precursors react for 10 min and pumping out the system for another 15 min, the samples were removed to analyze the resulting CVD SiO_2 film. The total SiO_2 thickness was 6.1 ± 0.1 nm as measured by ellipsometry, which indicates that an additional 4.3 ± 0.1 nm of SiO_2 was deposited. The contact angle of a static water droplet on the surface of the CVD deposited SiO_2 was $< 10°$, illustrating extreme hydrophilicity. Fig. 9.4 presents an AFM scan of the CVD deposited SiO_2 surface. Although the surface appears to be quite "bumpy" and rough, the RMS roughness of the surface is only 0.92 nm which is representative of a fairly smooth surface. A line scan taken from Fig. 9.4 is shown in Fig. 9.5. The line scan indicates that the majority of the peaks in the film are only 1.0 to 1.5 nm in height. This provides excellent evidence that any surface roughness created by GXL deposited nanoparticles prior to CVD SiO_2 deposition will be the
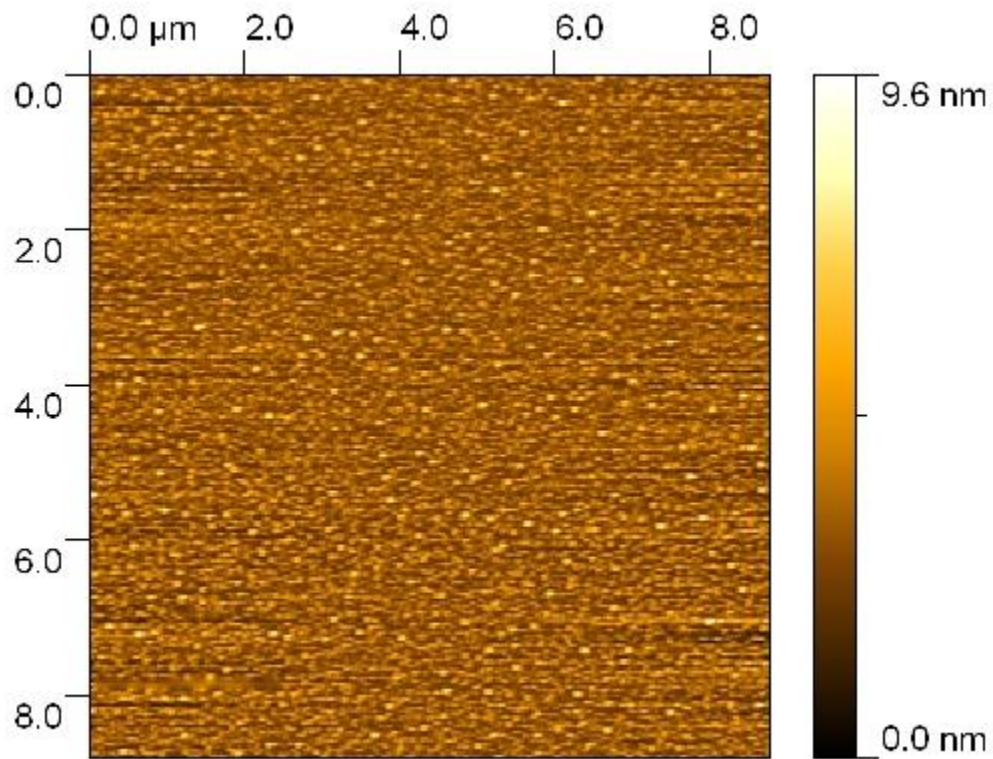
Figure 9.4. AFM scan of a CVD deposited SiO_2 layer on a smooth silicon substrate.
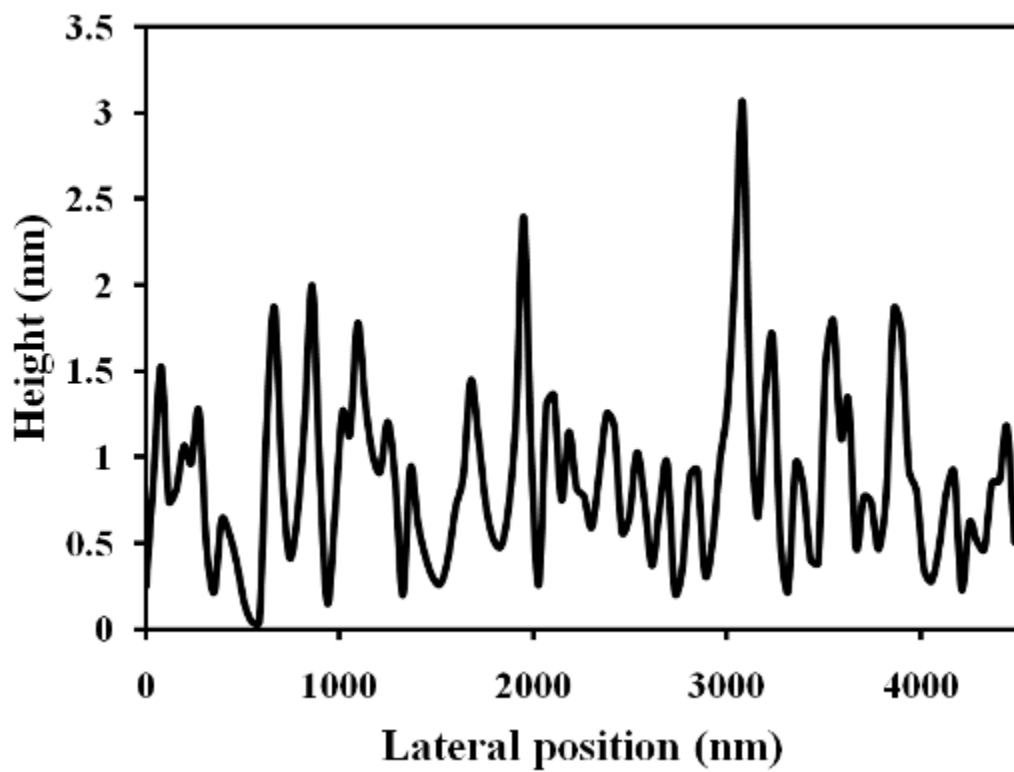
Figure 9.5. Line scan of CVD SiO_2 on smooth silicon.

contributing factor towards increasing surface roughness. In addition, the deposition of the CVD SiO_2 layer, due to its low inherent roughness, should not suppress the roughness given to the surface by any underlying nanoparticle films.

The same CVD process was performed on samples coated with AuNP thin films deposited by the GXL process. Prior to CVD SiO_2 deposition, the "oily" ligand tails were burned off by exposure to UV-ozone for 30 min. Fig. 9.6 presents an AFM scan of an AuNP thin film deposited onto a silicon substrate. The RMS roughness of the AuNP film in Fig. 9.6 is 4.68 nm, considerably more rough than the CVD SiO_2 layer in Fig. 9.4. In order to ensure that the CVD deposited SiO_2 layer will not add considerably to the overall surface roughness, the same procedure (reacting 20 Torr water vapor and 20 Torr $SiCl_4$) was performed on the AuNP thin film shown in Fig. 9.6. The AFM scan in Fig. 9.7 depicts the resulting AuNP/CVD SiO_2 film. The RMS roughness of the composite AuNP/CVD SiO_2 film is 5.40 nm which is only slightly higher than that of the original AuNP film. This is proof that the CVD SiO_2 layer does not contribute to the surface roughness. The static contact angle of water on the AuNP/CVD SiO_2 composite layer was 39.5°. This film still consisted of very hydrophilic silica, however, the surface roughness provided by the underlying AuNP film slightly decreased the overall surface energy resulting in an increased contact angle measurement.

In addition to studying SiO_2 covered AuNP films, self-assembled monolayers of FOTS were also deposited via CVD to further reduce the surface energy of the films. FOTS monolayers were deposited at ultra low pressures by letting approximately 200 mTorr FOTS and 400 mTorr water vapor react for 10 min. Fig. 9.8 presents an AFM scan of a FOTS monolayer deposited over the AuNP/CVD SiO_2 film from Fig. 9.7. The RMS roughness of the AuNP/CVD
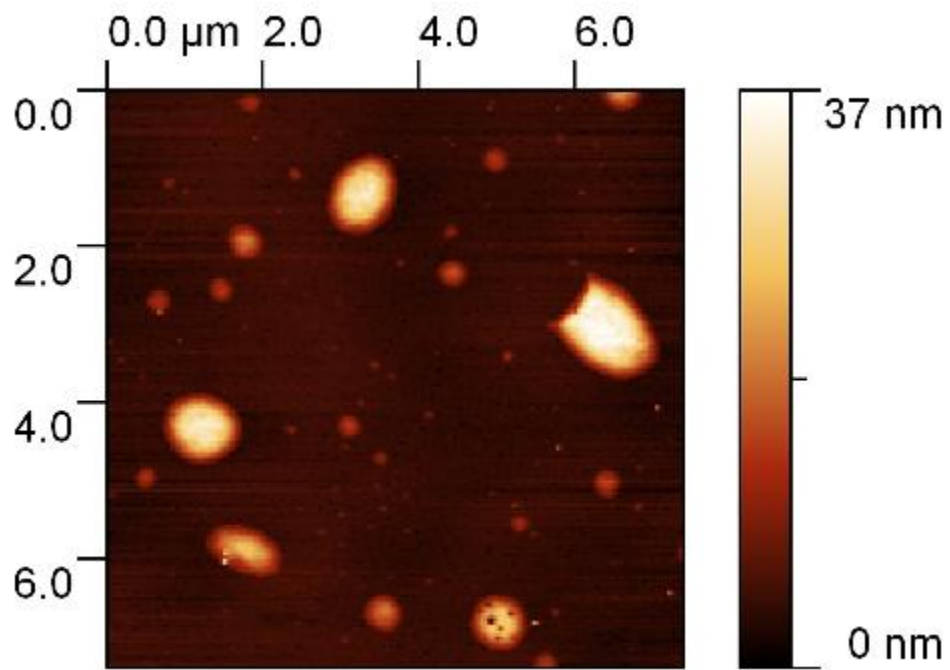
Figure 9.6. AFM scan of AuNP thin film on silicon.
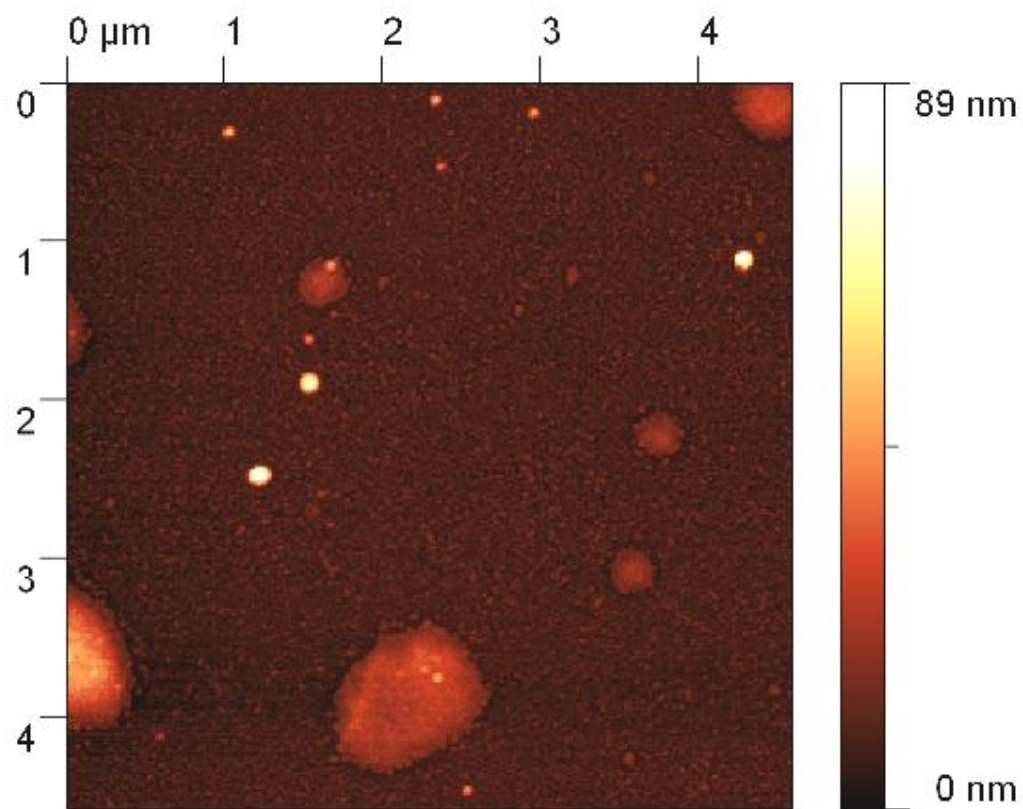
Figure 9.7. AFM scan of AuNP/CVD SiO$_2$ composite thin film.
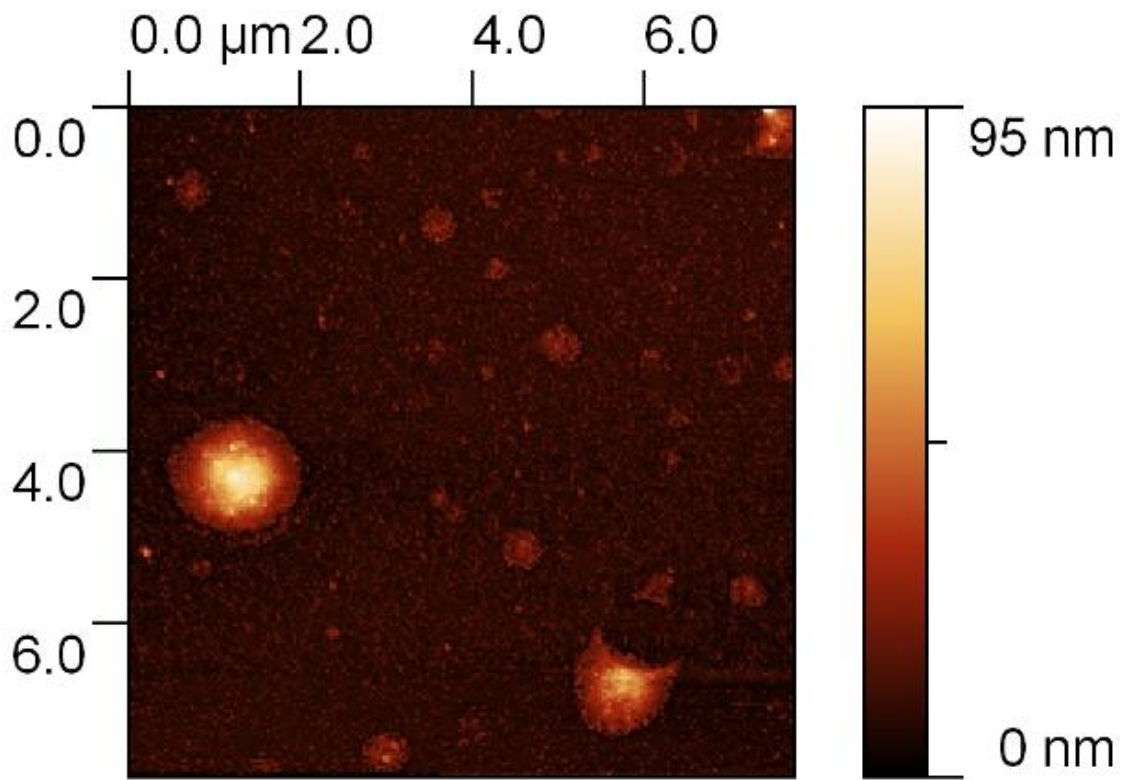
Figure 9.8. AFM scan of AuNP/CVD SiO$_2$/FOTS composite thin film.

SiO$_2$/FOTS composite film in Fig. 9.8 was 7.27 nm. This indicates just under a 2 nm increase in surface roughness by the addition of the FOTS layer. This increase is likely due to the formation of FOTS agglomerations on the silica surface which are known to occur. The contact angle of a static water droplet following FOTS deposition on an accompanying Si (100) substrate increased to 113°. The contact angle of a perfect monolayer of FOTS is typically around 108°, and therefore, any additional increase in contact angle from 108° is attributed to surface roughness. In this study, based on varying AuNP concentrations, the final contact angles ranged from 107° to as high as 120°.

The durability of AuNP/CVD/FOTS coatings was examined using the unique water erosion technique, as was previously performed on SAM-immobilized AuNP coatings. To gain perspective on the durability of these new composite coatings, the AuNP/CVD/FOTS coating was compared directly to non-immobilized AuNPs and MPTS/AuNP composite coatings under water droplet erosion for 10 h. Fig. 9.9 presents the water contact angle measurements for the three different coating types with increasing erosion time.   To recap, early AuNP coatings experienced rapid contact angle decreases indicating very rapid coating degradation. After 1 and 10 h of water erosion, the contact angle of water on AuNP coatings decreased by 58.4% and 73.9%, respectively. MPTS/AuNP coatings also exhibited fairly steep declines in contact angle, experiencing percent decreases of 32.7% and 63.5%, respectively, after 1 and 10 h of erosion. The new AuNP/CVD/FOTS composite coatings, however, exhibited only minute changes in contact angle, maintaining a water contact angle above 110° well after 10 h of water erosion. The percent decrease in contact angle over 10 h was only 4.4%, which is small enough that it could be based solely on measurement error. In fact, after 40+ h of water erosion, no significant
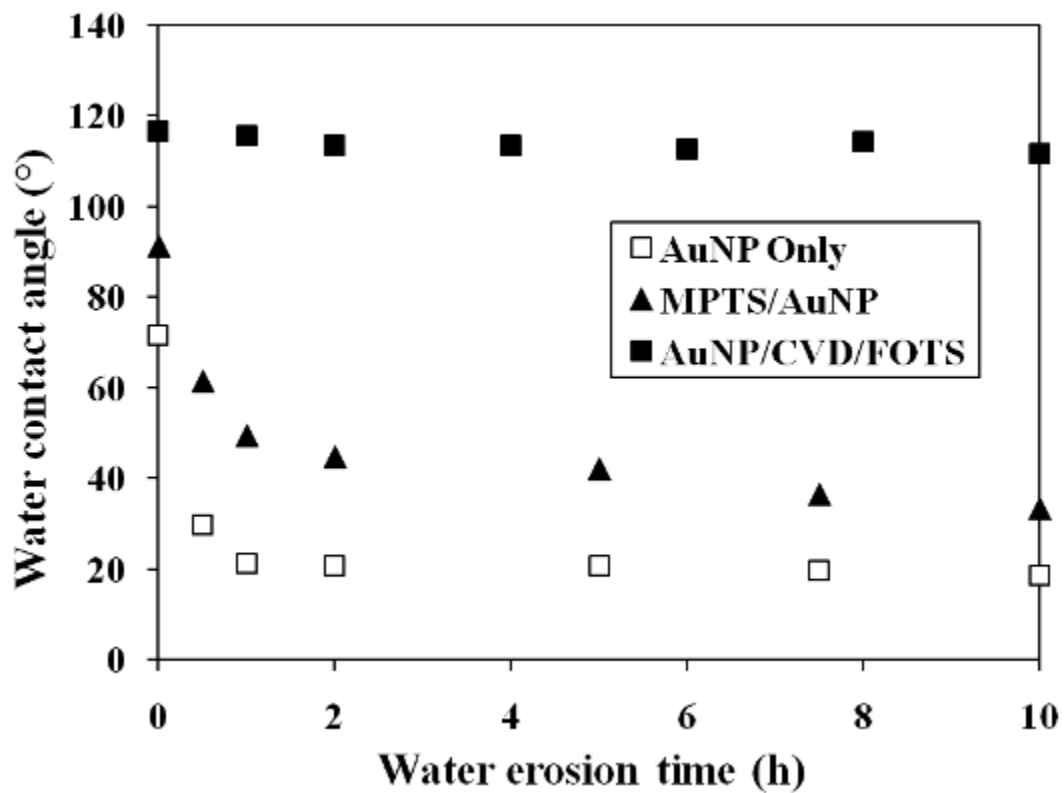
Figure 9.9. Average water contact angle with increasing water erosion time for AuNP,

MPTS/AuNP and AuNP/CVD/FOTS coatings.

change in contact angle was achieved, indicating that AuNP/CVD/FOTS coatings are extremely durable compared to other nanoparticle-based coatings examined in this work.

9.4 Tribological effect of AuNP/CVD thin films

The effect of rough AuNP/CVD SiO_2 and AuNP/CVD SiO_2/FOTS thin films on adhesion was investigated by depositing the films on SOI microtribology chips. Fig. 9.10 presents an AFM scan of a microtribology chip coated with AuNPs via the GXL deposition process with a surface roughness of 0.90 nm. Fig. 9.11 presents an AFM scan of the sample AuNP-coated chip after the deposition of a CVD SiO_2 layer. The RMS roughness increased only slightly to 1.76 nm. Following the deposition of silica, the tribology chip was exposed to UV-ozone for 1 h to ensure that no organic contaminants were on the surface. Arrays of cantilever beams were then actuated to quantify the adhesion.

Fig. 9.12 presents an interferogram of an array of 500-μm long cantilever beams coated with the AuNP/CVD SiO_2 thin film following actuation. The average crack length over multiple arrays of cantilever beams (including that shown in Fig. 9.12) was 315.5 ± 13.3 μm. This crack length is comparable to the average crack lengths achieved from MPTS/AuNP and APhTS/AuNP thin films investigated in Chapter 8. The apparent work of adhesion for this particular sample was reduced to 1.36 ± 0.14 mJ/m^2. This result was surprising because the AuNP/CVD SiO_2 films are still very hydrophilic. This indicates, surprisingly, that surface roughness – and likely the real contact area that results from adding surface roughness – can drastically reduce adhesion regardless of the composition of the contacting surfaces. The real contact surface area of the microtribology chip imaged in Fig. 9.12 is estimated to be

238
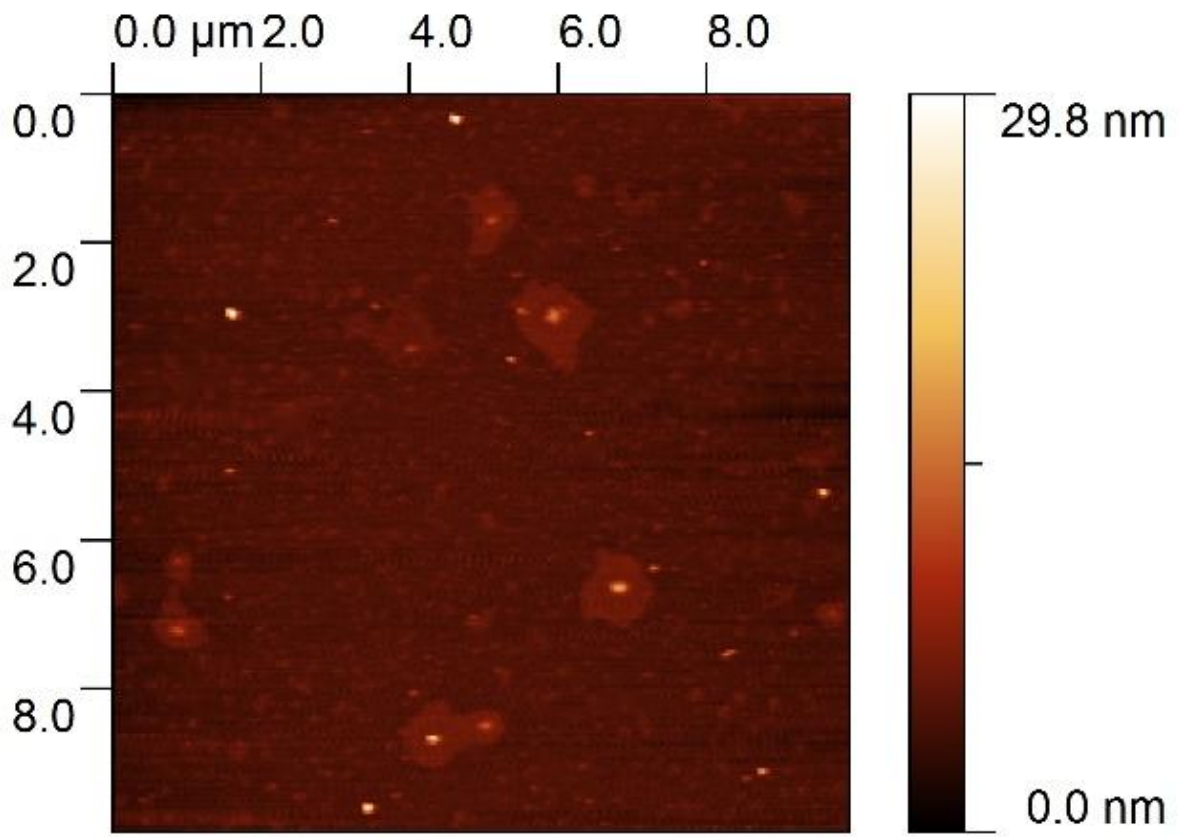
Figure 9.10. AFM scan of AuNP thin film on an SOI tribology chip.
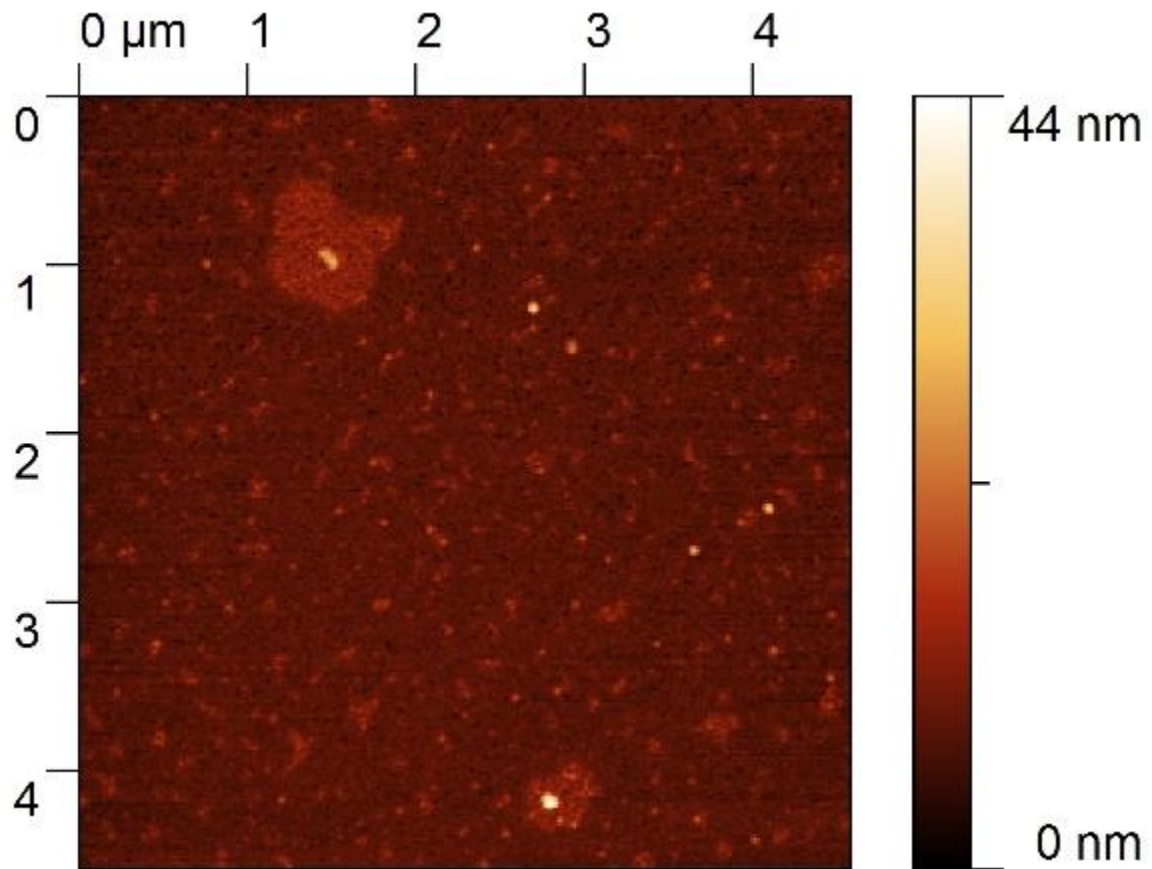
Figure 9.11. AFM scan of AuNP/CVD SiO$_2$ thin film on an SOI tribology chip.
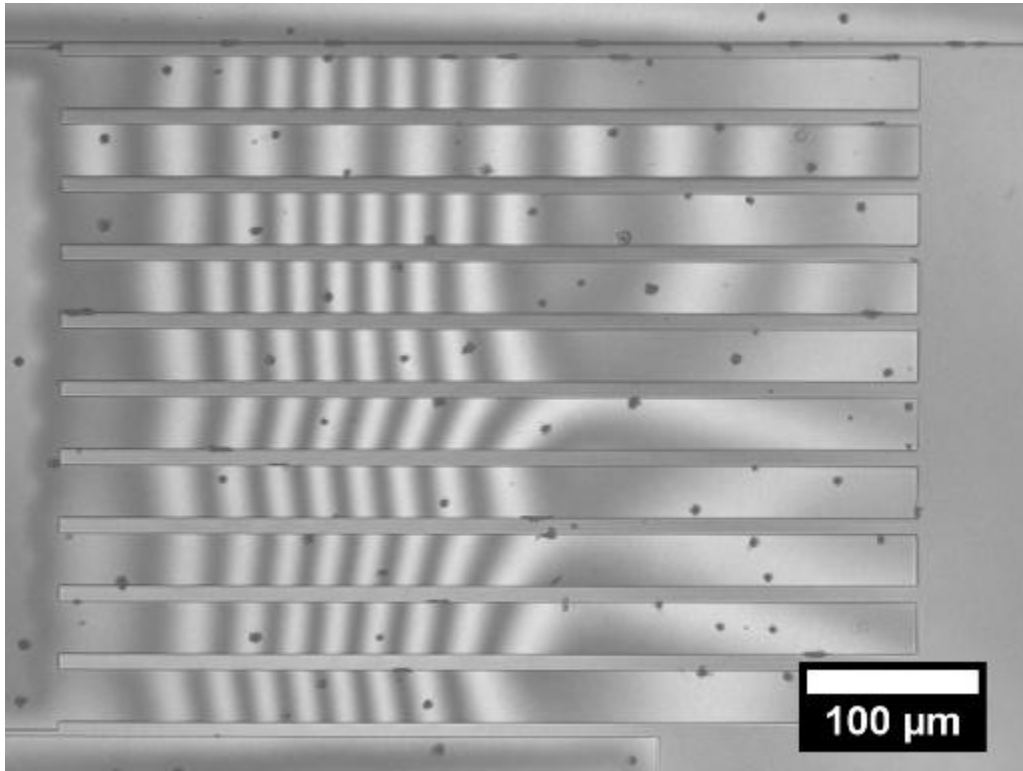
Figure 9.12. Interferogram of 500-µm cantilever beams coated with AuNP/CVD SiO$_2$.

approximately 10% which illustrates that the real contact surface area plays a large role in adhesion regardless of surface energy.

To further investigate the effect of reducing the surface energy on adhesion, a FOTS monolayer was deposited on top of the AuNP/CVD SiO_2 film in Fig. 9.12. Rough SiO_2-coated silicon substrates accompanied the microtribology chip in order to confirm FOTS deposition. The contact angle following FOTS deposition increased to 103°, which is slightly lower than the 108° expected for a complete FOTS monolayer. The reduced contact angle could be a result of sticky FOTS agglomerations that form when too many molecules were available for monolayer deposition. Such agglomerations have been exhibited in numerous FOTS examinations (Maboudian et al. 2002; Ashurst et al. 2006). Interestingly, there was virtually no difference in adhesion between tribology chips coated with AuNP/CVD SiO_2 or AuNP/CVD SiO_2/FOTS thin films. Fig. 9.13 presents an interferogram of a previously unactuated CBA found on the same tribology chip as the CBA in Fig. 9.12. The average crack length and adhesion energy of the array in Fig. 9.13, coated with AuNP/CVD SiO_2/FOTS, were 285.5 ± 239.9 μm and 1.24 ± 1.27 mJ/m^2, respectively. These results can said to be approximately equal to those collected from the AuNP/CVD SiO_2 coated cantilever beams.

To compare the effect of AuNP/CVD SiO_2 films with tribology chips coated only with silica, Fig. 9.14 presents an interferogram of cantilever beams coated only by the CVD SiO_2 thin film. Interestingly, the beam array presented in Fig. 9.14 exhibits slightly increased adhesion compared to native SiO_2 coated beams. The particular array shown in Fig. 9.14 exhibits an average crack length of 84.2 ± 2.5 μm and an average apparent work of adhesion of 38.0 ± 4.0 mJ/m^2. The decreased crack length when compared to previous samples coated with native SiO_2
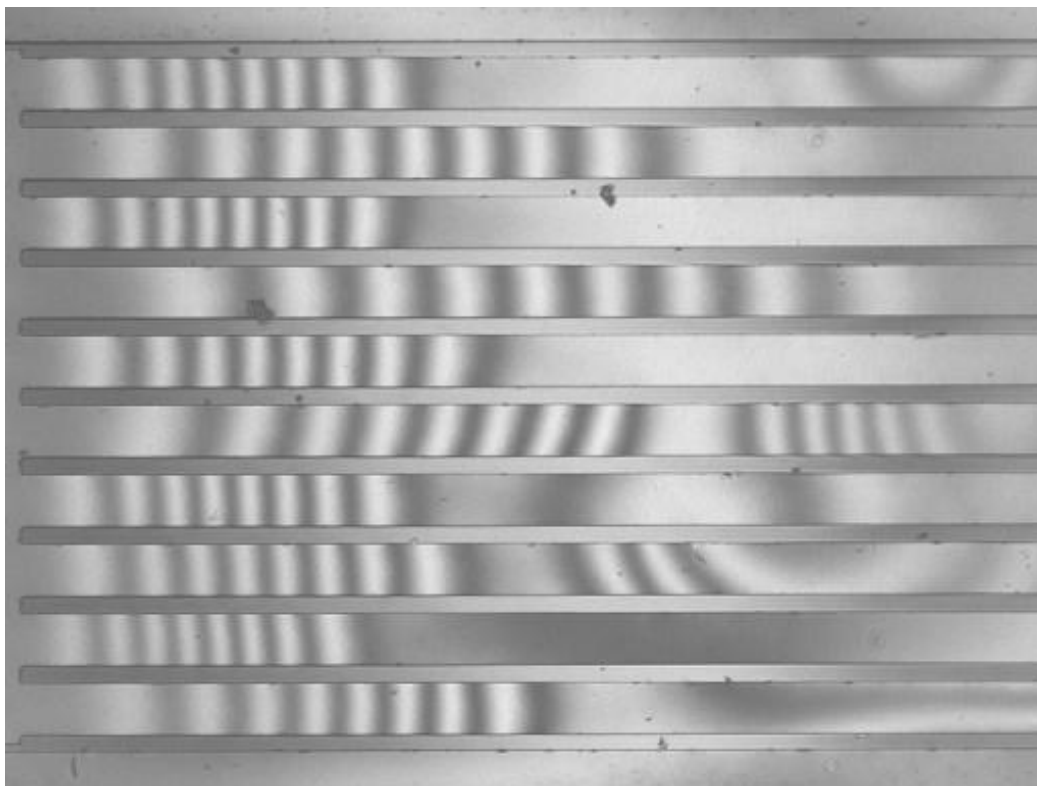
Figure 9.13. Interferogram of 500-µm cantilever beams coated with AuNP/CVD SiO$_2$/FOTS.
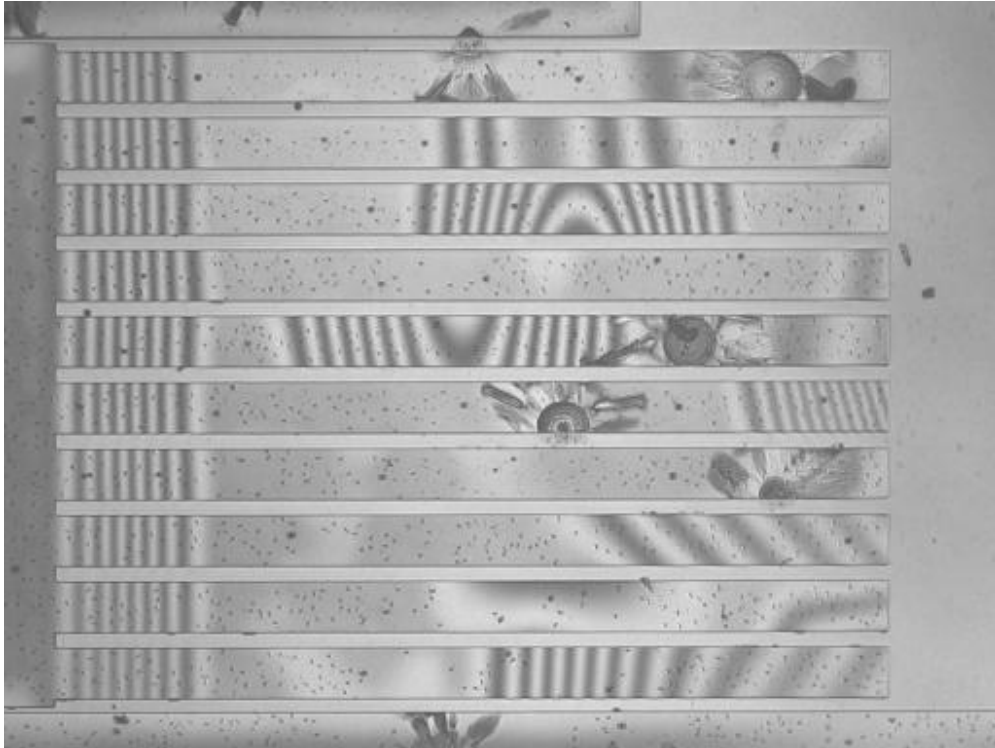
Figure 9.14. Interferogram of 500-μm cantilever beams coated with only CVD SiO_2 layer.

films could simply be a result of the ambient conditions (relative humidity) in the laboratory during the time of actuation. In this study, the effect of AuNP/CVD composite coatings on friction was not investigated due to the results discussed in Chapter 7. When the adhesion energy is reduced, the coefficient of static friction is also inherently reduced.

9.5 VPD experimental setup and details

In the case of superhydrophobic coatings, a special VPD apparatus was used to produce the coatings on silicon substrates. The apparatus consists of a stainless steel coating chamber, a high vacuum pump and four lines for reaction precursor injection connected by a number of pneumatic valves. The chamber, precursor lines and precursor canisters are all equipped with thermocouples and heating tape in order to accurately control the temperature digitally. LABVIEW software is utilized to operate the various pneumatic valves for precise, and even automated, control of precursor injections into the deposition chamber. Bottled nitrogen is utilized as a carrier gas for each of the precursors. Figs. 9.15 and 9.16 present photographs of the front and back of the VPD apparatus. Fig. 9.17 provides a simplified illustration of the chemical delivery systems shown in Fig. 9.16.

The primary difference in this study is that AuNPs were not used as the surface roughness material for superhydrophobic films. Instead, a vapor phase deposition of Al_2O_3 nanoparticles is performed using trimethylaluminum (TMA, $Al_2(CH_3)_6$) as a precursor. The reaction of TMA to form alumina particles follows Eqn. (9.2) (Lakomaa et al. 1996; Gosset et al. 2002):

$$Al_2(CH_3)_6(v) + 3H_2O(v) \rightarrow Al_2O_3(s) + 6CH_4(v) \tag{9.1}$$

Precursor containers
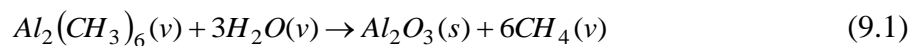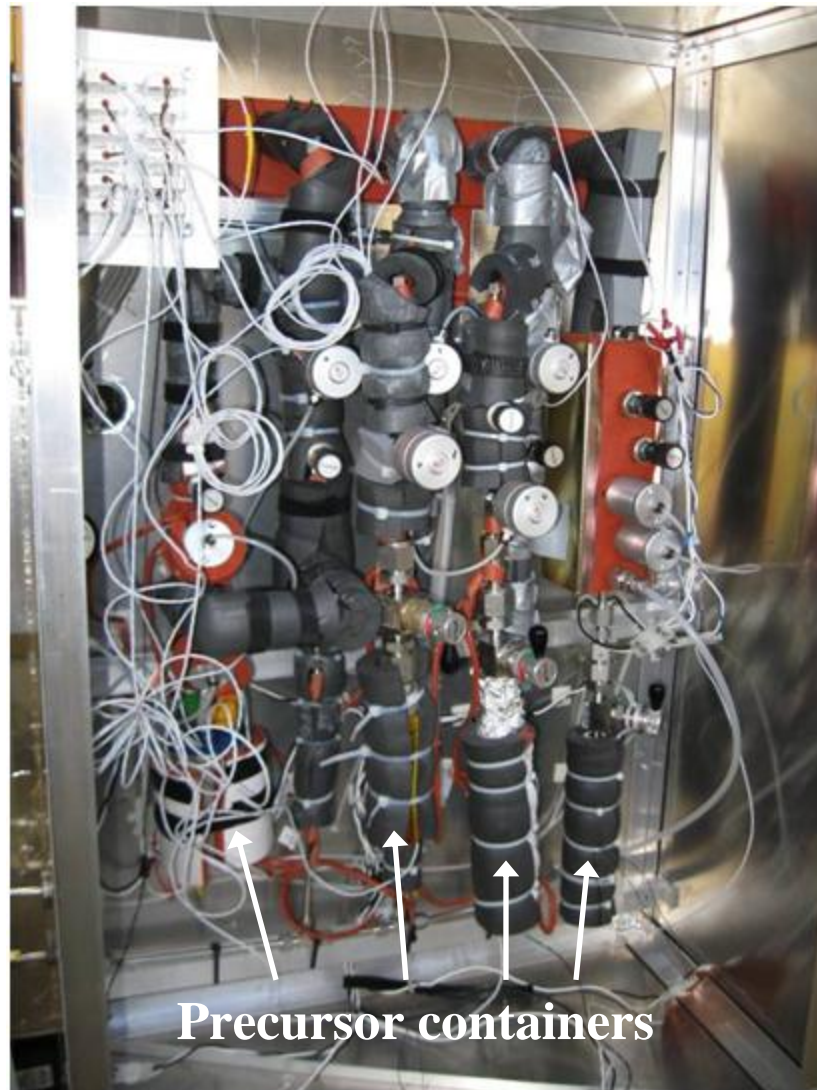
Figure 9.15. Digital photograph of the backside of the ROGER-1 VPD apparatus showing gas carrier lines and precursor chemical containers.

Pressure gauges

Coating chamber door
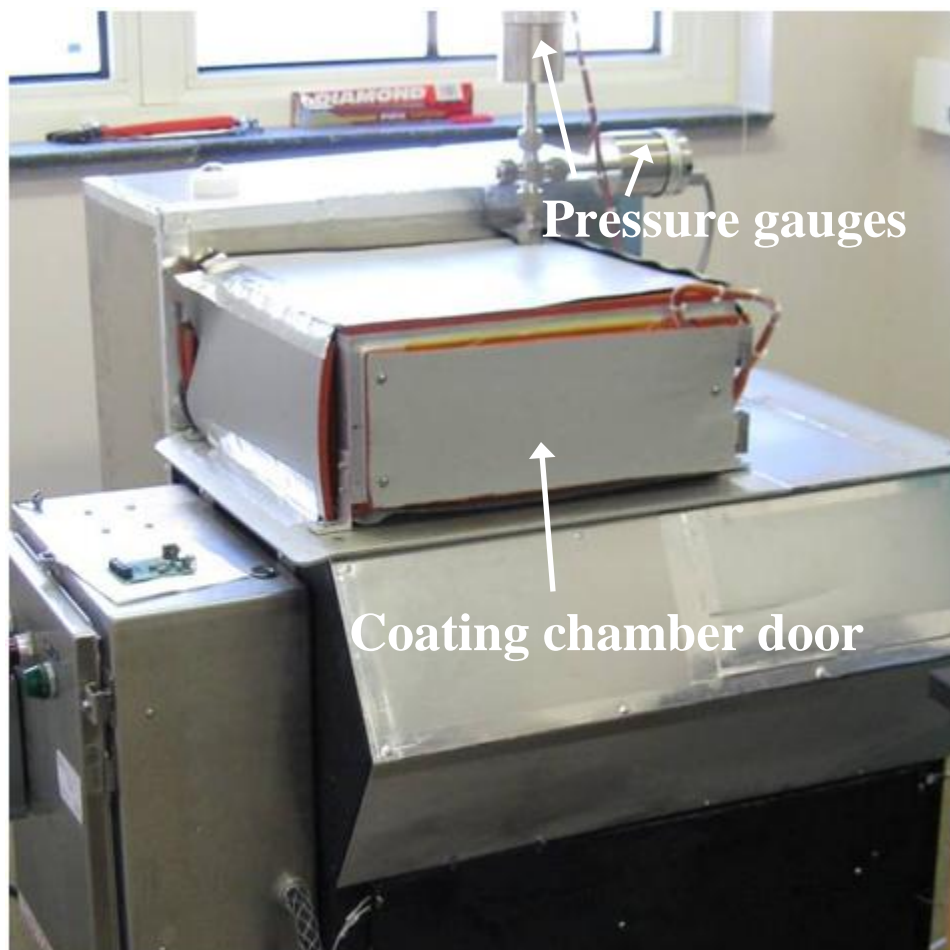
Figure 9.16. Digital photograph of the front of the ROGER-1 VPD apparatus.
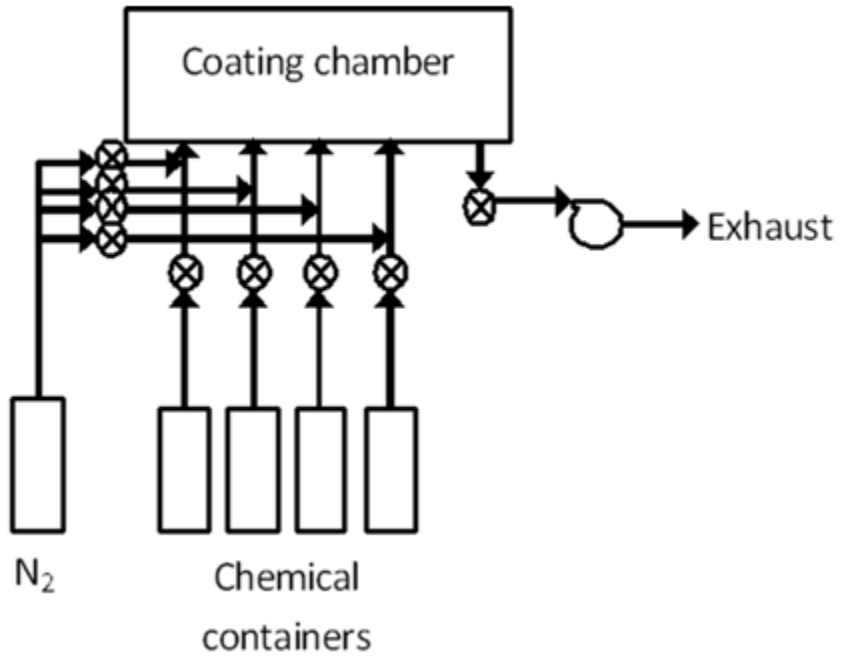
Figure 9.17. Simple schematic diagram of the ROGER-1 VPD apparatus. "X" indicates a

pneumatic valve controlled by LABVIEW software.

During the reaction, vapor drawn from a canister containing liquid TMA reactions with water vapor to form solid alumina particles and methane gas. The alumina particles create significantly more roughness than AuNP films, which would be too large for microtribological purposes. Fig. 9.18 presents an AFM scan of the rough Al_2O_3 deposited onto a Si (100) substrate. The associated line scan performed using Gwyddion imaging software, in Fig. 9.19, illustrates that the particulates formed on the surface are roughly 400 to 800 nm tall. The RMS roughness of the sample in Fig. 9.18 is 182 nm, compared to a roughness of about 0.2 nm for the original Si (100) substrate sample. Following alumina deposition, the particles are linked together by SiO_2 formation and then coated with a hydrophobic FOTS coating. These hydrophobic film samples were also characterized by AFM, ellipsometry and water erosion durability.

Various types of superhydrophobic films were created using ROGER-1, all with Al_2O_3 nanoparticles as a rough, base coating. Table 9.1 presents the names of various coating techniques along with brief descriptions of the processes. All of the superhydrophobic coatings examined in this work were completed with a coating of FOTS in order to provide a low energy surface, as described in the proceeding section. Recipes B and C utilize SiO_2 layers as linkers to entrap the nanoparticles. Recipe D, rather than SiO_2, uses a dual functionality of aminopropyl- and epoxypropyl-trimethoxysilane precursors which enclose the nanoparticles. Recipes E and F take advantage of SiO_2 formation catalyzed by pyridine. The pyridine catalysis allows for low temperature SiO_2 film formation (Du et al. 2007). The ALD in recipe E refers to atomic layer deposition, in which the film deposition process takes place in very short, sequential steps (or "half-reactions") in order to create very thin and uniform layers. Meanwhile, the chemical vapor deposition (CVD) used in recipe F creates a thicker, slightly more unorganized, silica layer. For

249
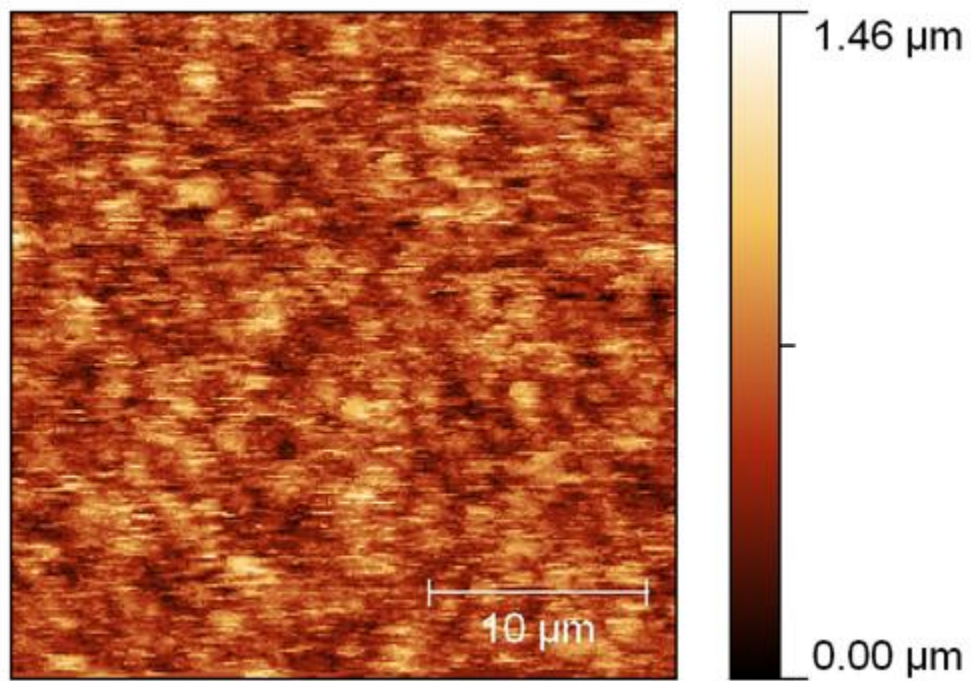
Figure 9.18. 30 x 30 μm AFM scan of Al_2O_3 particles on Si (100).
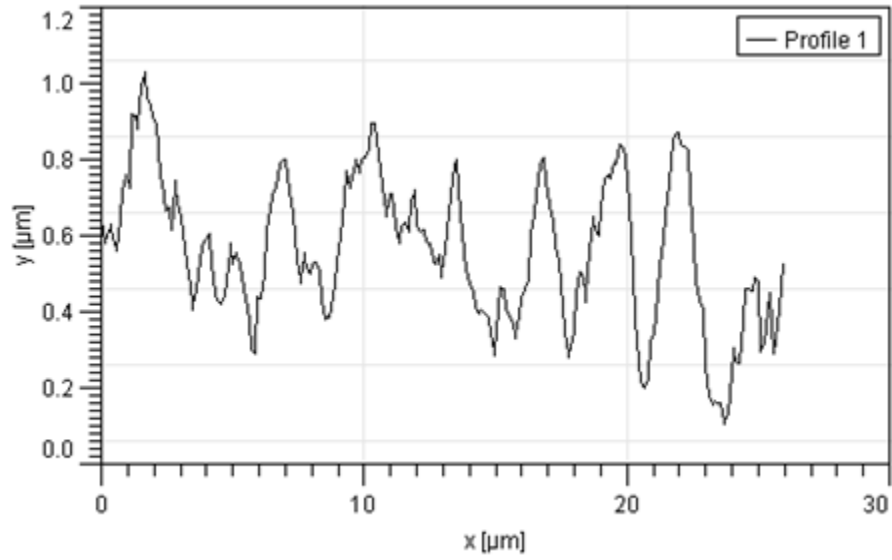
Figure 9.19. Line scan of Al_2O_3 particles on Si (100) imaged in Figure 9.18.

Recipe	Coating name	Brief process description
A	TMA Baseline	Unlinked Al_2O_3 nanoparticles (no SiO_2 layer) covered by a FOTS monolayer
B	TMA/Linker	Al_2O_3 nanoparticles linked together with a thin SiO_2 layer and coated with FOTS
C	TMA/Linker300	Al_2O_3 nanoparticles linked together with a much thicker SiO_2 layer and coated with FOTS
D	Amine/Epoxy	Al_2O_3 nanoparticles linked by a coupling film combining amino- and epoxy-functionalization and coated with FOTS
E	ALD Pyridine Oxide	Al_2O_3 nanoparticles linked together by a pyridine-catalyzed ALD SiO_2 layer and coated with FOTS
F	CVD Pyridine Oxide	Al_2O_3 nanoparticles linked together by a pyridine-catalyzed CVD SiO_2 layer and coated with FOTS

Table 9.1. Table of superhydrophobic coating names and brief descriptions.

this study, all superhydrophobic film depositions were performed by Jeff Chinn at Integrated Surface Technologies (Menlo Park, CA).

The VPD apparatus utilizes well known gas phase reactions to produce thin films of materials on surfaces placed within the deposition chamber. The first reaction which encapsulates a nanoparticle-coated surface within a thin layer of SiO_2 involves the hydrolysis of a silicon precursor, tetrachlorosilane ($SiCl_4$). The gas phase reaction of water with $SiCl_4$ is given by Eqn. (9.1) (Jia and McCarthy 2003; Anderson and Ashurst 2008b; Anderson and Ashurst 2008c). This reaction occurred by a cyclic process in which, starting at a base pressure of about 10 mTorr, very small partial pressures of $SiCl_4$ and water are allowed to react. By performing the reaction in cycles with very small injections, the topography of the SiO_2 layer can be controlled compared to CVD processes in which the partial pressures of the reactants exceed 10 Torr (Anderson and Ashurst 2008c).

Following the deposition of a thin, but very hydrophilic, SiO_2 layer, a hydrophobic FOTS monolayer film is deposited. This reaction occurred by first injecting about 2.4 Torr of water into the chamber, allowing water vapor to adsorb onto the surface, and pumping out the water down to the base pressure. 100 mTorr of FOTS was then introduced to the chamber and allowed to react with the surface water molecules for 30 min before the system was purged with nitrogen, pumped down, and vented to the atmosphere with nitrogen. The temperatures of the precursor canisters and lines, as shown in Table 9.2, are elevated to assist in increasing the vapor pressure of the precursors and avoid condensation throughout the lines. However, these reactions could take place at room or slightly elevated temperatures resulting in only increased injection times to achieve sufficient precursor partial pressures. The reactions themselves take place at only 35 °C within the coating chamber, much lower than vapor phase SAM reactions in previous studies

Component	Maintained temperature (°C)
Coating chamber	35.0
TMA canister	40.0
Water canister	45.0
$SiCl_4$ canister	25.0
FOTS canister	90.0
TMA line	40.0
Water line	45.0
$SiCl_4$ line	25.0
FOTS line	80.0

Table 9.2. Operation temperatures for ROGER-1 coating chamber,

precursor canisters and gas lines.

(Mayer et al. 2000). For a more detailed description about the operation of ROGER-1, refer Appendix B.

9.6 Durability of AuNP/VPD superhydrophobic coatings

Another ultimate goal utilizing the ROGER-1 apparatus is to create durable, superhydrophobic coatings for electronic devices such as cellular phones. The water durability of various hydrophobic coating recipes, produced by Integrated Surface Technologies, was also examined. Table 9.3 presents the water erosion time for the six superhydrophobic coating recipes examined in this work. The table indicates that Al_2O_3 particles either unbound or very weakly linked to the surface (recipes A and B) are easily eroded and coating exhibit drastic contact angle changes in less than 1 h. When a thicker SiO_2 linking film is deposited, the water erosion time until failure increases by a factor of 20. The amine/epoxy linking system (recipe D) shows good improvement in water durability; however, this film requires high temperature (> 100 °C) for film deposition. The two types of pyridine-catalyzed SiO_2 deposition, however, can be accomplished at room temperature and provide very durable coatings. The water erosion for these two coatings (recipes E and F) were suspended after 80 hours without experiencing any decline in contact angle.

As seen in Table 9.3, Recipes E and F − the most durable superhydrophobic coatings examined thus far − utilize pyridine as a catalyst to produce very thin and ordered layers of silicon oxide. The catalysis of silicon oxide formation using pyridine is a well known reaction and has been widely studied (Klaus and George 2000; Du et al. 2005; Du et al. 2007). One consideration is what happens to the pyridine after the reaction. FTIR spectroscopic analysis can offer suggestions to whether or not residual pyridine may become an issue. Fig. 9.20 presents

255

Recipe	Coating name	Water erosion time until failure (h)
A	TMA Baseline	0.25
B	TMA/Linker	0.50
C	TMA/Linker300	10
D	Amine/Epoxy	35
E	ALD Pyridine Oxide	>80
F	CVD Pyridine Oxide	>80

Table 9.3. Water erosion times until coating failure for various

superhydrophobic coating recipes.
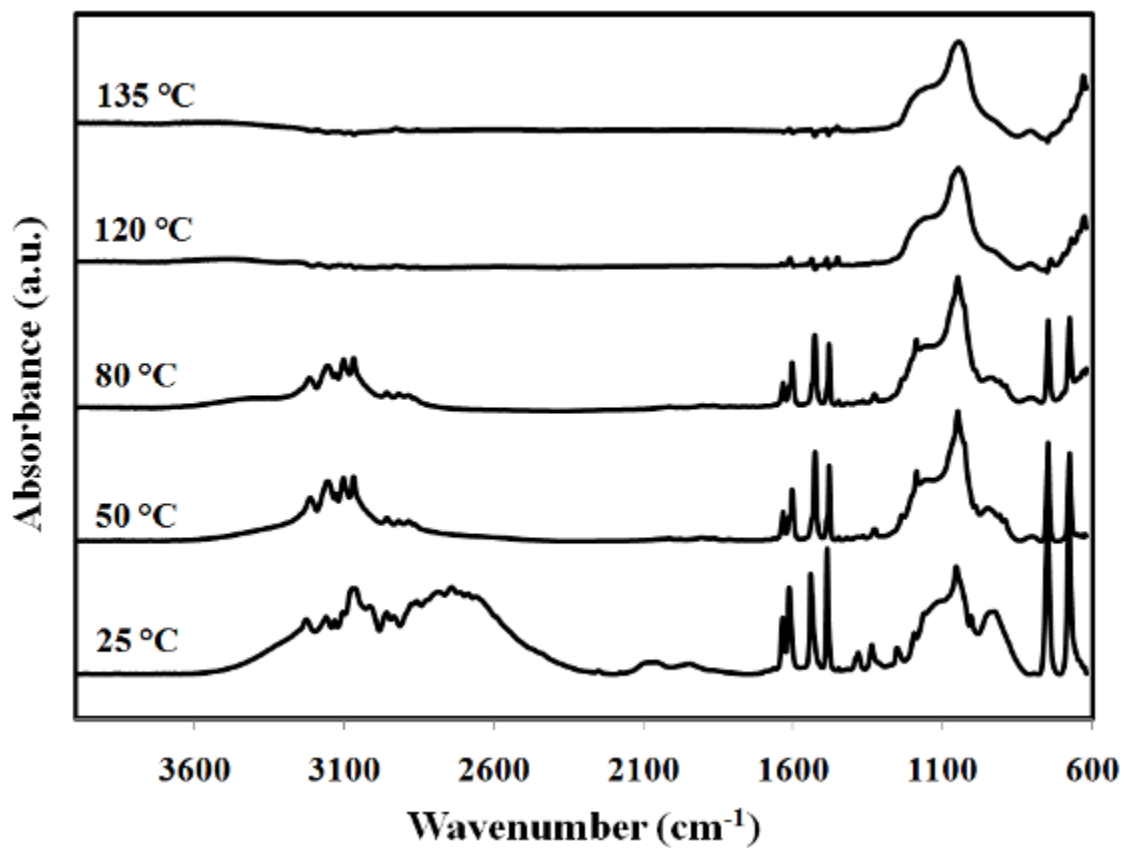
Figure 9.20. FTIR spectra of pyridine absorbed on a silica seed layer after heating to various

temperatures.

ATR-FTIR spectroscopy scans of pyridine vapor which has been absorbed on the surface of a silica seed layer deposited on a ZnSe ATR crystal at room temperature. At 25 °C, sharp peaks exist between about 1500 and 1650 cm^{-1}. These four peaks are characteristic of pyridine and pyridium ions (Barzetti et al. 1996). The ATR crystal was heated to 50 °C and allowed to cool back to room temperature before the spectrum was taken again. After heating to 80 °C, very little change, other than the loss of water, is experienced by the sample. However, after heating to 120 °C, there is a drastic decrease in the characteristic pyridine peaks, suggesting that surface pyridine molecules can be removed by heating the thin films.

The loss of pyridine from heating to 120 °C in Fig. 9.20 removes only absorbed pyridine molecules on the surface of the film. Therefore, the "trapping" of pyridine by the SiO_2 layer was examined to ensure that residual pyridine could not escape from the interior of the film. A ZnSe ATR crystal was first coated in-house with a silica seed layer. The crystal was then shipped to Integrated Surface Technologies where a pyridine-catalyzed SiO_2 layer was deposited. The FTIR spectrum of the initial pyridine-containing film was first acquired at room temperature (r.t.). This spectrum was then used as a background to acquire the difference spectra after heating to 80 and 120 °C. Fig. 9.21 presents the resulting FTIR spectra. The initial background spectrum shows the characteristic peaks for pyridine around 1600 cm^{-1} and the characteristic SiO_2 peaks around 1100 cm^{-1}. After heating to 120 °C, there is no noticeable difference in either of these wavenumber regions. The only noticeable difference is the loss of water around 3000 cm^{-1}. This result indicates that pyridine that exists inside the vapor deposited silica film is not released due to heating and will remain trapped within the film.
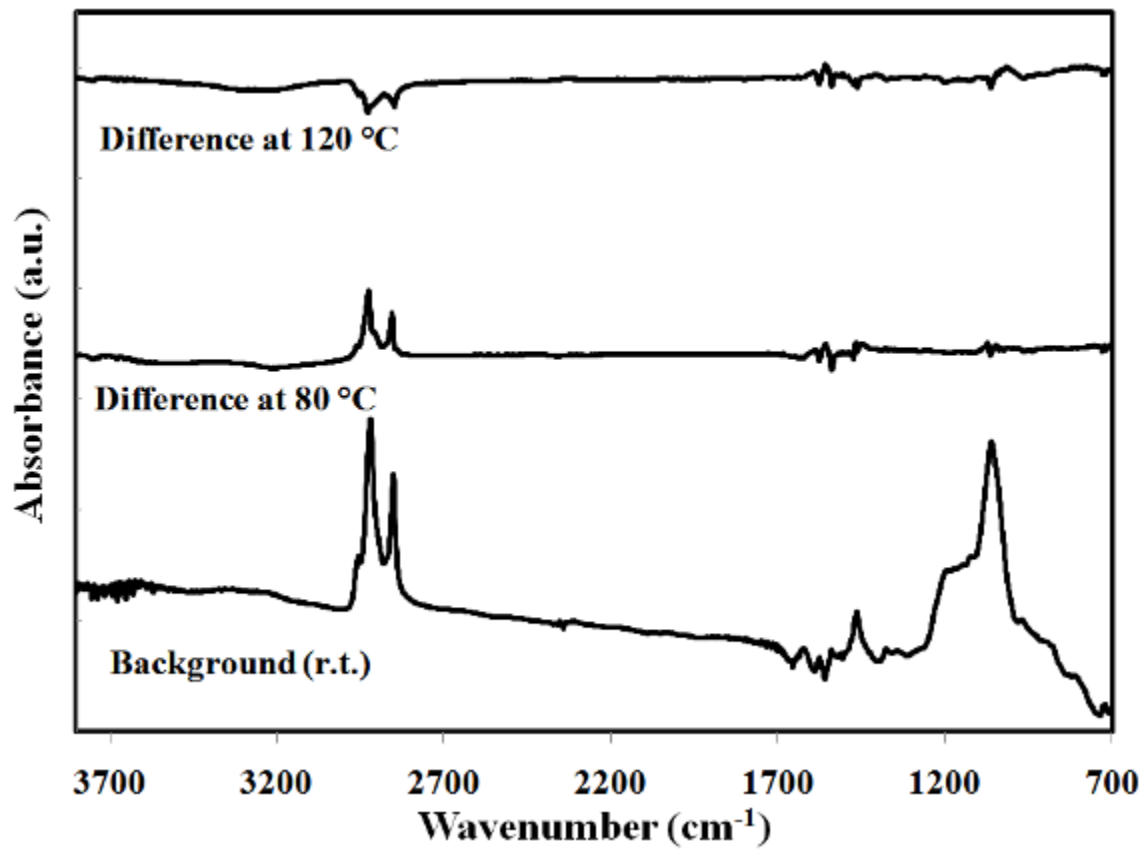
Figure 9.21. FTIR spectrum of pyridine-containing SiO_2 layer at room temperature and difference spectra after heating to 80 and 120 °C.

9.7 Effect of roughness and asperity density on hydrophobicity

One of the most famous examples of a superhydrophobic surface is that of a lotus leaf which exhibits contact angles of ca. 161° (Sun et al 2005a; Sun et al. 2005b). Lotus leaves consist of a combination of two-scale roughness: a micro-scale roughness around 10 μm and a nano-scale roughness of less than 100 nm (Sun et al. 2005a). It is widely presumed that the superhydrophobic nature of lotus leaves arise from the combination of this two-scale roughness along with a waxy secretion that alone has a contact angle of 110° (Sun et al. 2005b), similar to that of many SAMs including FOTS which has a contact angle of 108°. The coatings produced in ROGER-1 combine the roughness of Al_2O_3 nanoparticle films along with the hydrophobic nature of self-assembled monolayers.

Recently, a third consideration, asperity coverage and density, has been considered to be an important factor in the creation of superhydrophobic surfaces (Extrand 2002). This fact became apparent when the water contact angle for various samples were plotted with surface RMS roughness values calculated using Gwyddion from AFM scans of the surface coatings. Fig. 9.22 presents this data which illustrates that superhydrophobic surfaces (> 160°) can be achieved over a very wide range of surface roughness values (35-450 nm). However, every surface with an RMS roughness above about 200 nm exhibited superhydrophobic properties. Anderson (2009) discussed that roughness was not enough information to characterize superhydrophobicity and illustrated that surfaces with comparable RMS roughness values can have drastically different asperity coverages. Therefore, Anderson (2009) developed an algorithm in which height data from AFM scans, the same data used to quantify roughness, is re-binned and analyzed using imaging software in order to determine the coverage of asperities on a given surface. Fig. 9.23 presents data from two AFM scans, each with RMS roughness values of
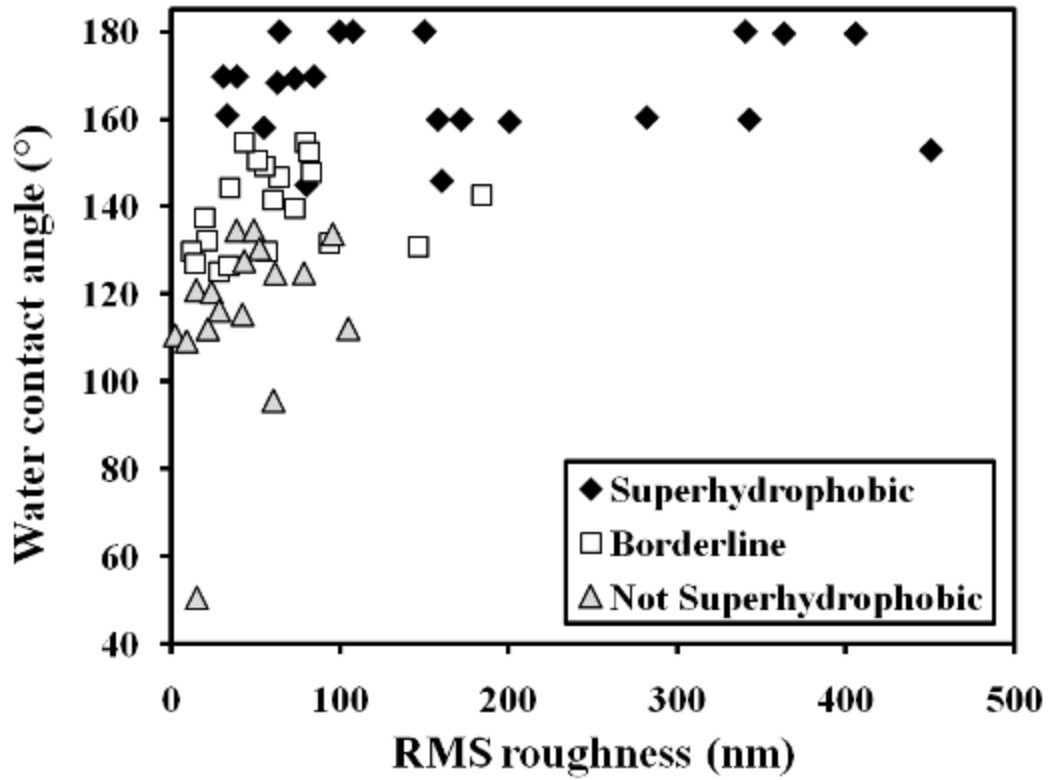
Figure 9.22. Water contact angle for various coatings plotted against

RMS roughness from AFM surface scans.
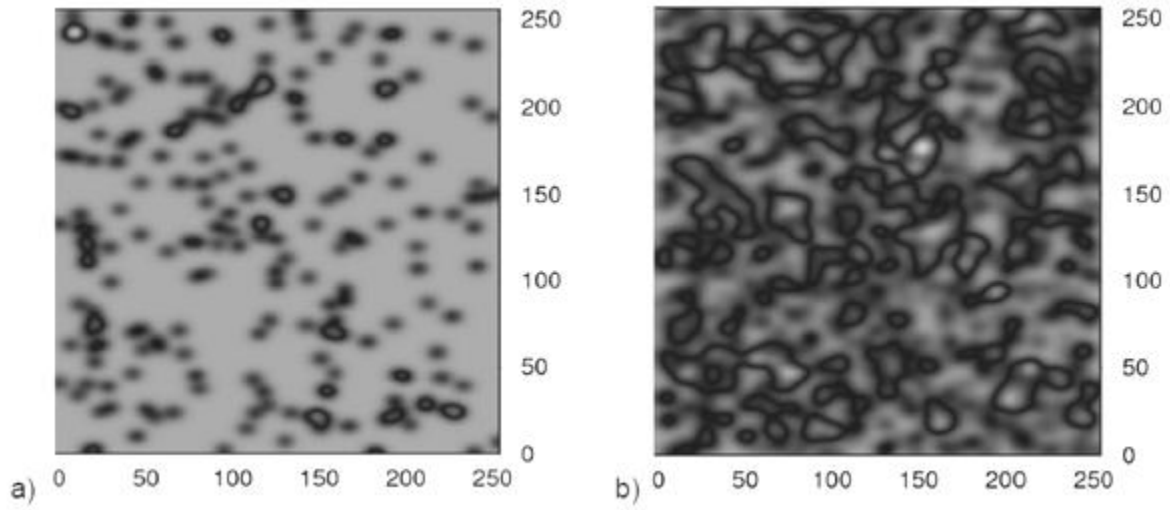
Figure 9.23. Re-binned AFM data with equal RMS roughness values (3.3 nm)

and varying asperity coverages.

3.3 nm, which illustrate completely different asperity coverage densities. The surface in Fig. 9.23(a) has a coverage of 23% while the surface in Fig. 9.23(b) exhibits a coverage of 43%. The asperities with heights greater a baseline height are indicated by the darker color.

By performing the re-binning algorithm on a variety of sample coatings, the asperity coverage (or density) could be plotted against water contact angle as shown in Fig. 9.24. The data indicates that while coatings over a wide range of coverage densities can exhibit either superhydrophobic or non-superhydrophobic properties, there exists a range between 30-50% coverage where the superhydrophobic samples exist. This makes perfect sense fundamentally, as one would expect an optimal coverage density to exist assuming a monolayer base height. Low coverage densities, such as shown in Fig. 9.23(a), exhibit larger areas where asperities are not detected. These regions would have higher surface energies and real contact areas, resulting in greater adhesion and lower hydrophobicity. As the coverage density increases, these higher surface energy regions shrink as fewer real areas of contact exist, resulting in increased hydrophobicity. If the coverage continues to increase beyond about 50%, although the higher surface energy surface available decreases, the actual number of real contact points begins to increase offering more regions for adhesion to occur. This also results in lower hydrophobicity. Theoretically, a surface with 0% asperity coverage would exhibit similar interactions as a coated surface with 100% asperity coverage density. Fig. 9.25 illustrates this intuitive trend by showing how the surface energy and real contact area is affected by coverage density. The inverse of the trend exhibited in the figure could nearly be placed upon the data in Fig. 9.24.

In order to better characterize the combined effect of RMS roughness and coverage density on the hydrophobicity of surfaces, Fig. 9.26 plots the RMS roughness-to-coverage density ratio with water contact angle. The plot indicates that any surface with an RMS/density
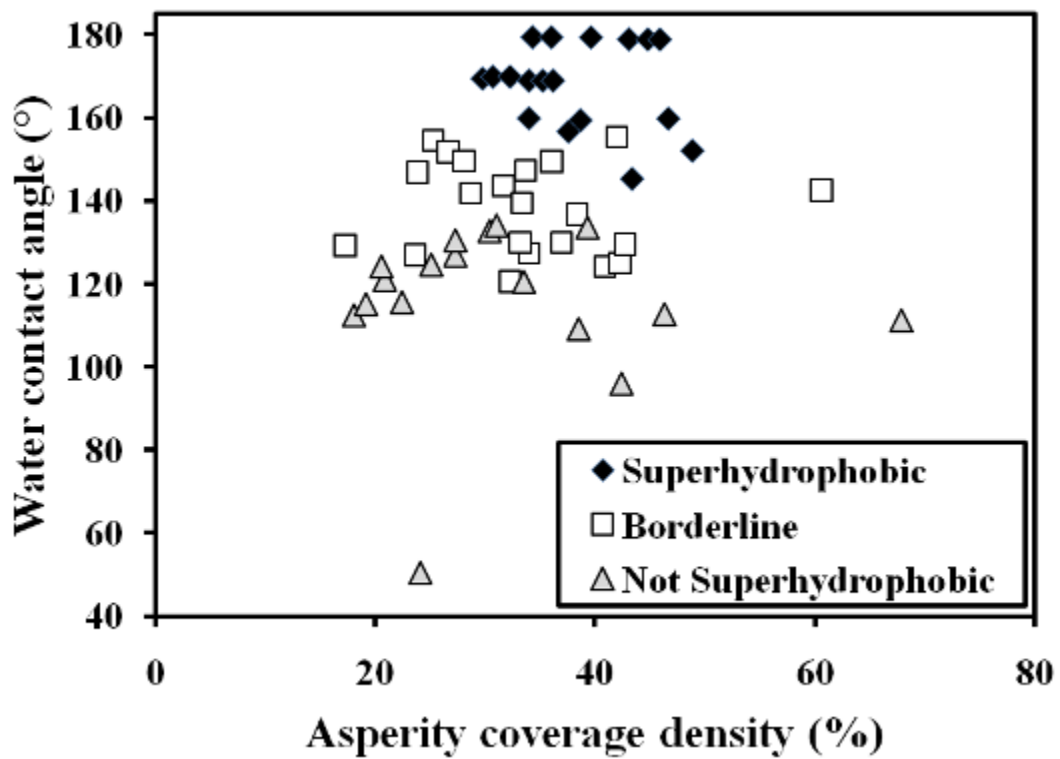
Figure 9.24. Water contact angle for various coatings plotted against

asperity coverage density from AFM surface scans.
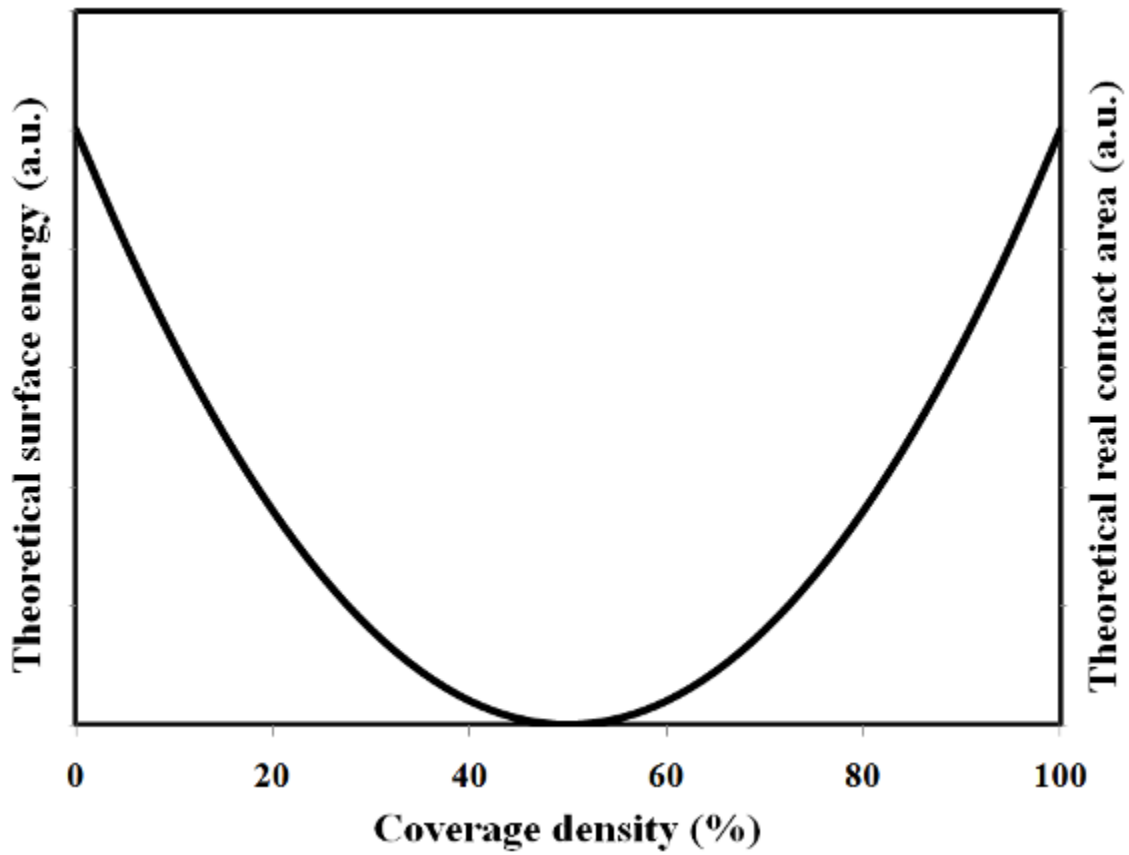
Figure 9.25. Theoretical effect of asperity coverage density on surface energy

and real contact area. Not based on actual data.
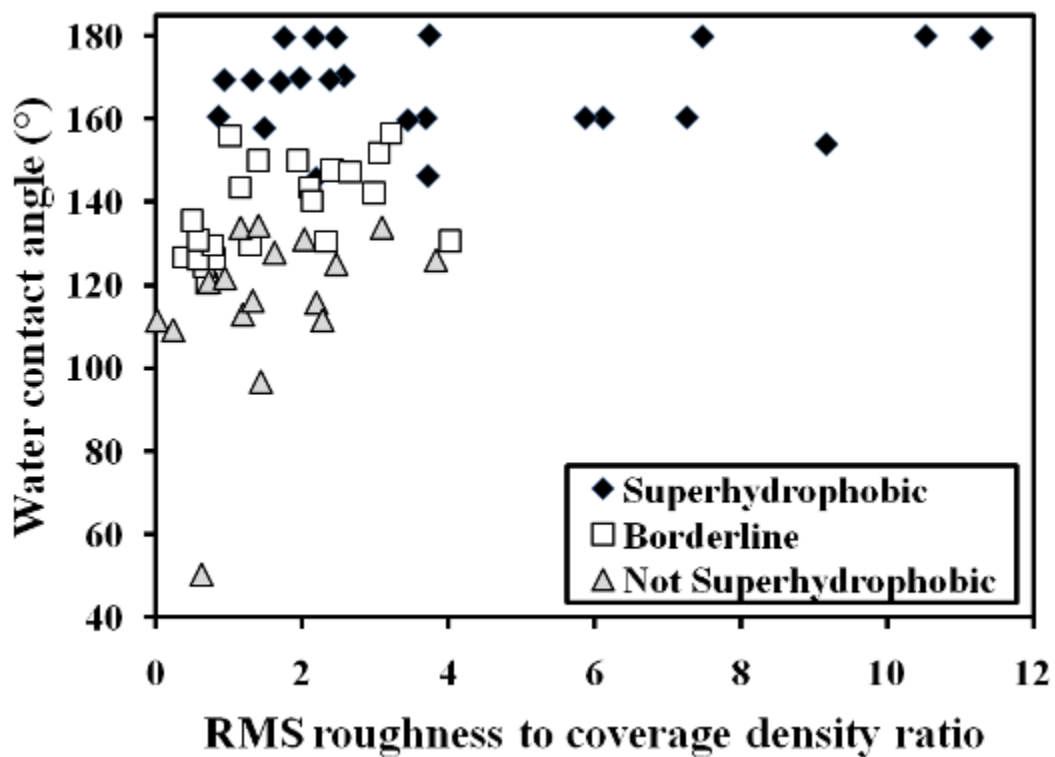
Figure 9.26. Effect of RMS to coverage density ratio on water contact angle.

ratio greater than 4 exhibits superhydrophobicity. Therefore, this value can become a new standard for superhydrophobic films that may be developed in future studies even though coatings with ratios less than 4 can also yield superhydrophobic properties. Figs. 9.27 through 9.32 present AFM scans of the six recipes provided in Table 9.4. Table 9.4 then provides information generated from the scans such as RMS roughness, coverage density, RMS to density ratio, and initial water contact angle. As the data suggests, the pyridine-catalyzed coatings exhibit RMS to density ratios of less than 3; however, they still provide superhydrophobicity and are very durable based on water erosion testing. This is likely due to the fact that the pyridine catalyzed oxide films exhibit lower surface energy than typical silicon oxide films, and therefore, requiring less surface roughness to produce superhydrophobic properties. The results presented here have opened the door for Auburn and IST to collaboratively examine new superhydrophobic coatings in the future.

9.8 Conclusions

In this chapter, chemical vapor deposition (CVD) was utilized to deposit solid and smooth SiO_2 thin films over rough AuNP films in the attempt to create extremely durable composite films for microtribology control. AFM, ellipsometry and goniometry analysis provided confirmation that smooth SiO_2 layers can be deposited over rough AuNP films without the SiO_2 providing significant film roughness. Silicon cantilever beams coated with the CVD SiO_2 layer (without any surface roughness) exhibited extremely high adhesion similar to native oxide coated beams. However, when rough AuNP thin films were first introduced and then coated by a top layer of CVD SiO_2, the adhesion decreased drastically even though the CVD SiO_2 was still very high in surface energy (hydrophilic). This interesting result illustrates that the
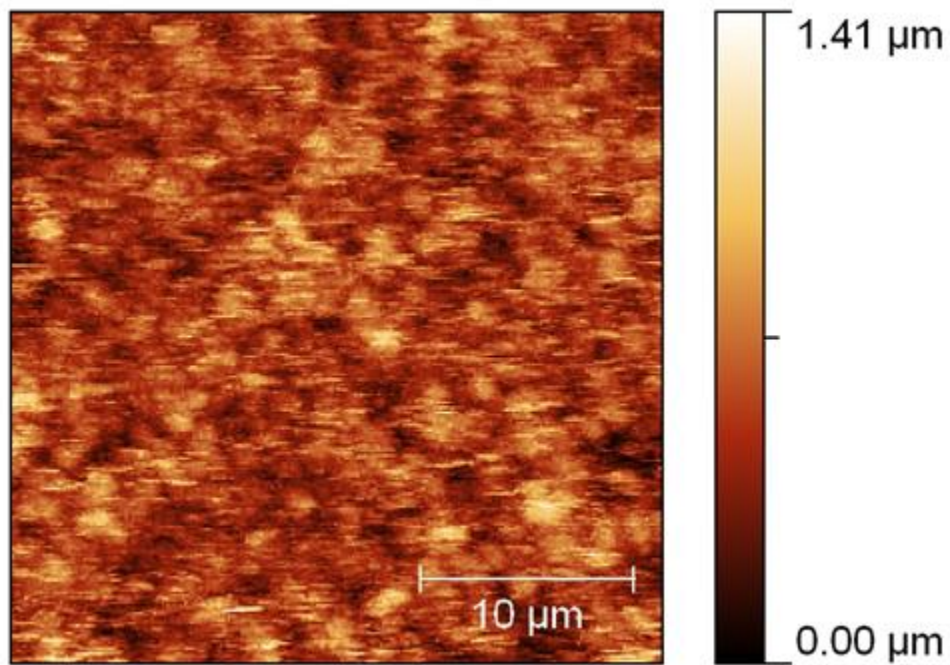
Figure 9.27. AFM scan of TMA Baseline (Recipe A) surface coating.
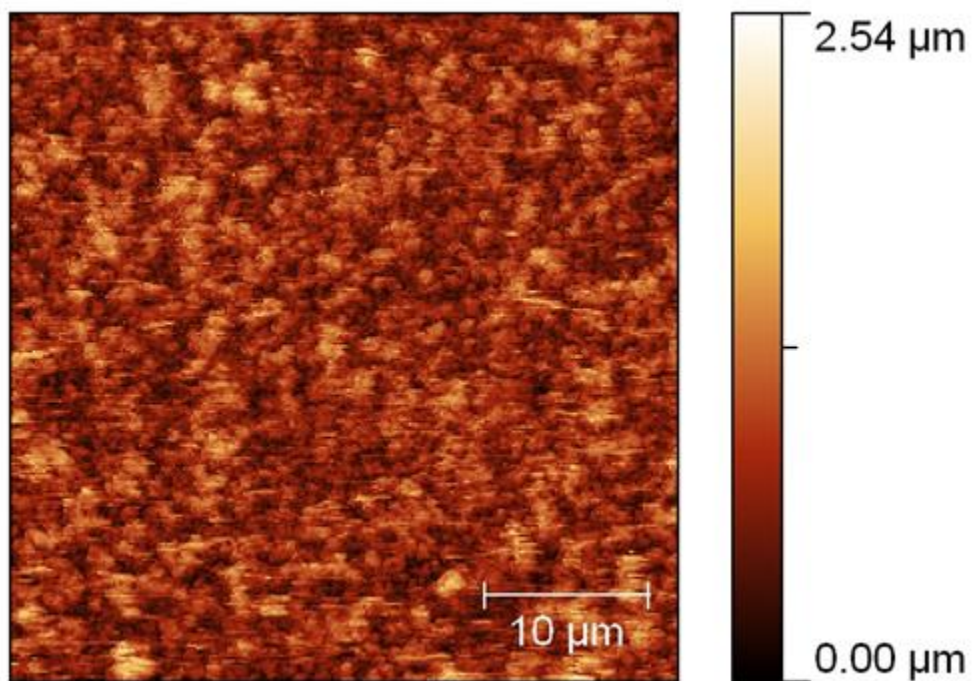
Figure 9.28. AFM scan of TMA/Linker (Recipe B) surface coating.
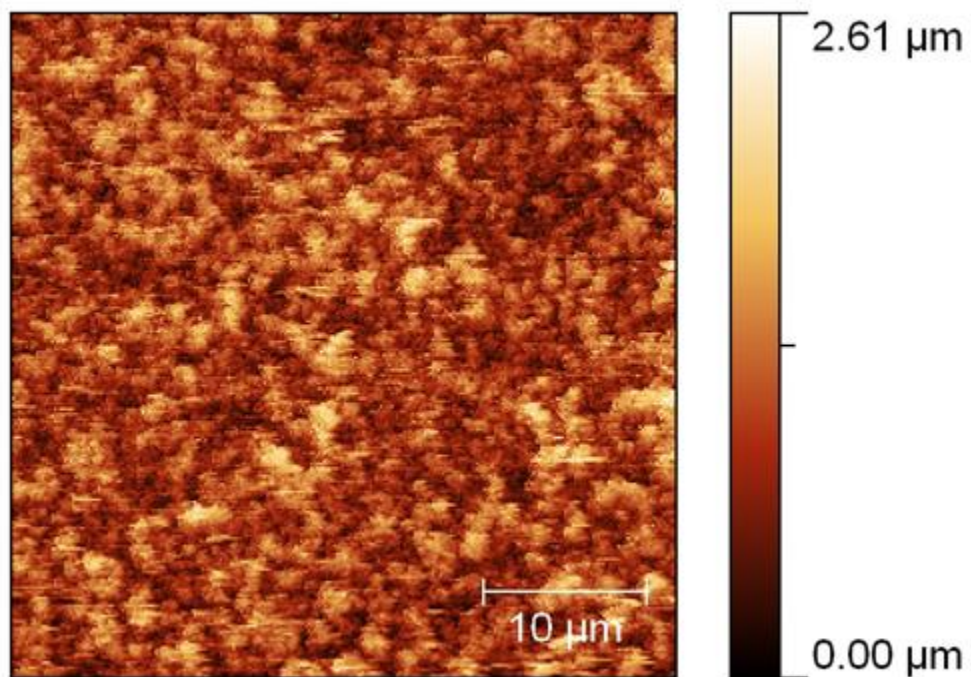
Figure 9.29. AFM scan of TMA/Linker300 (Recipe C) surface coating.
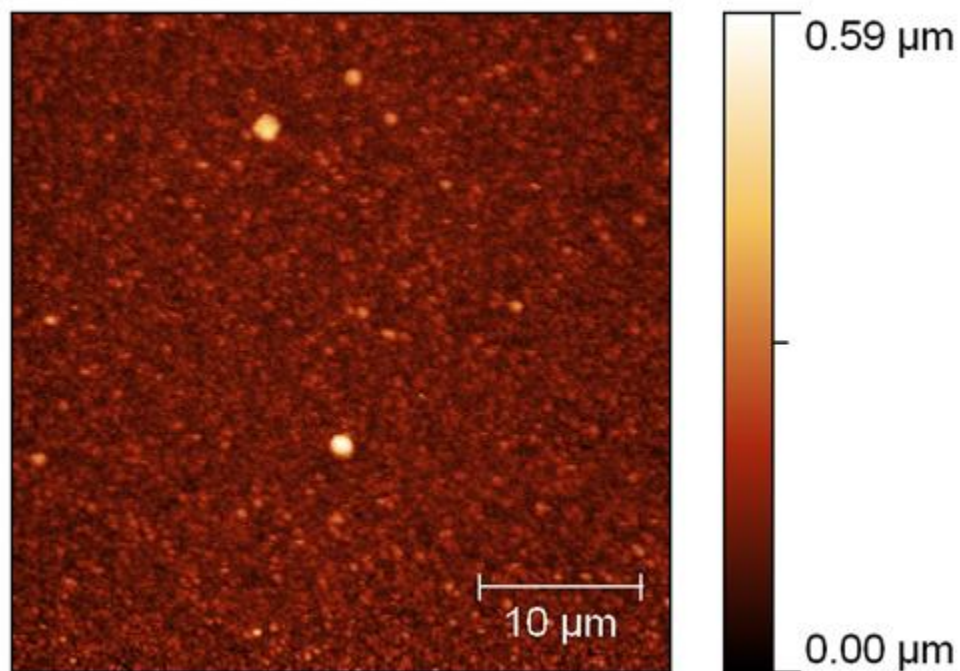
Figure 9.30. AFM scan of Amine/Epoxy (Recipe D) surface coating.

271
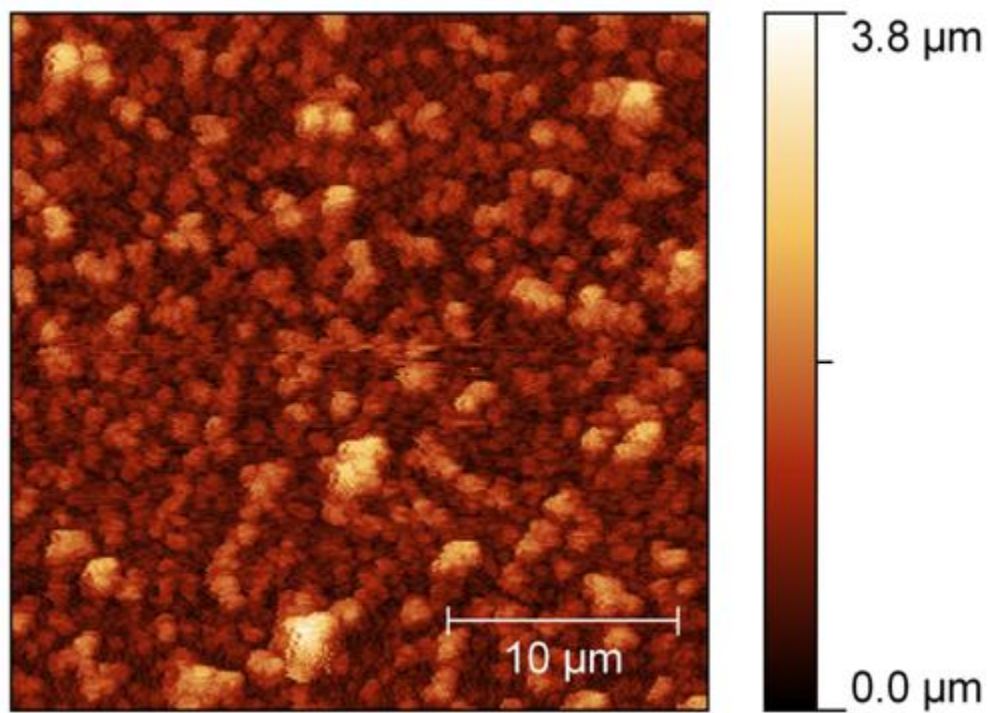
Figure 9.31. AFM scan of ALD Pyridine Oxide (Recipe E) surface coating.
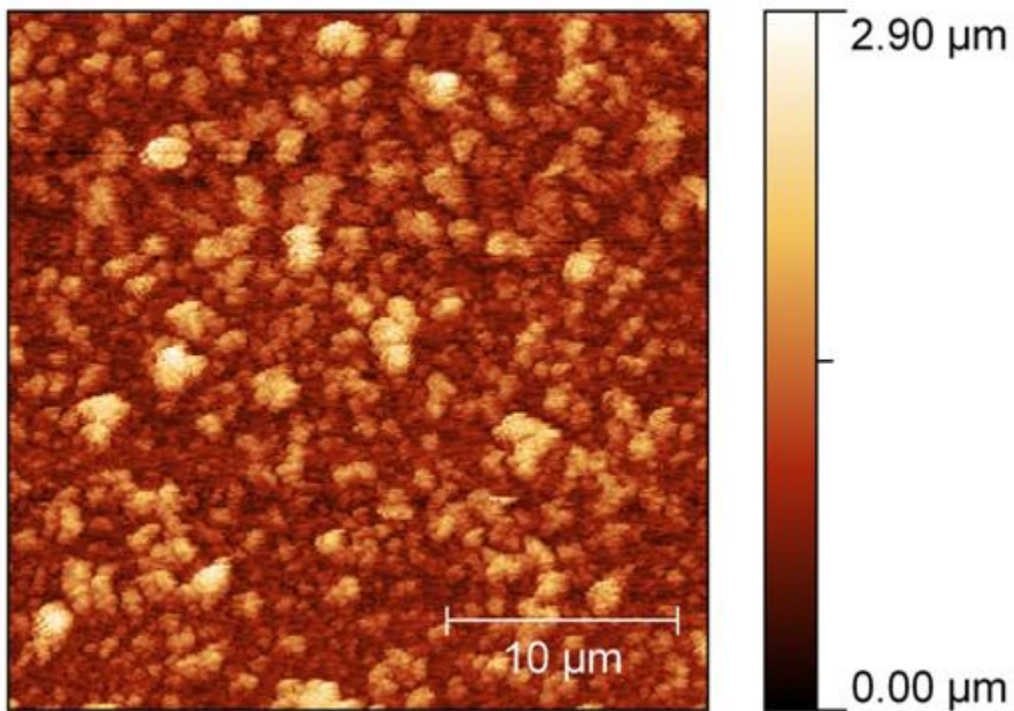
Figure 9.32. AFM scan of CVD Pyridine Oxide (Recipe F) surface coating.

Recipe	Coating name	RMS (nm)	Coverage density (%)	RMS to density ratio (nm)	Initial water contact angle (°)
A	TMA Baseline	160	47	3.4	130
B	TMA/Linker	281	46	6.1	> 160
C	TMA/Linker300	343	47	7.3	> 160
D	Amine/Epoxy	164	42	3.9	> 160
E	ALD Pyridine Oxide	113	45	2.5	> 160
F	CVD Pyridine Oxide	80	38	2.1	> 160

Table 9.4. RMS, coverage density, RMS to density ratio, and water contact angles for

superhydrophobic recipes examined in this work.

reduction in real contact area provided by the rough films plays a larger role in reducing adhesion than the actual surface energy. This was further illustrated by the addition of a FOTS monolayer which had little to no effect in further reducing the adhesion of the rough composite films.

The durability of AuNP/CVD SiO_2 composite films was examined only by the water droplet erosion technique which was illustrated in Chapter 8 to provide more film disruptive force than the mechanical contact between two microstructured surfaces. Due to the hydrophilic nature of the top CVD SiO_2 layer, a FOTS monolayer was incorporated onto the films in order to acquire measurable contact angles. Interestingly, the composite films exhibited extreme durability by maintaining a constant contact angle of about 120° for well over 40 hours of water droplet erosion. This result suggested that AuNP/CVD SiO_2 films are much more robust than the SAM/AuNP films examined in Chapter 8.

In addition, this chapter introduced a vapor particle deposition (VPD) technique to create and deposit superhydrophobic thin films. In collaboration with IST, different superhydrophobic recipes were investigated to determine their durability to water erosion and their film characteristics including RMS roughness and asperity surface coverage. The results illustrate that any of the surfaces investigated with RMS-to-asperity coverage ratios of greater than 4 will exhibit superhydrophobic properties. However, films with these high ratios may not provide the most durable of coatings. Therefore, IST and Auburn University will continue to investigate a large number of coating recipes in order to produce reliable and durable superhydrophobic thin films which may someday be used to make consumer and electronic devices resistant to water contact and damage.

CHAPTER 10

CONCLUSIONS AND AVENUES FOR FUTURE WORK

10.1 Morphology of GXL-deposited nanoparticle films

The work presented in Chapter 6 illustrated that the surface coverage and morphology of a GXL-deposited nanoparticle film is highly dependent on the surface upon which the deposition occurs as well as the ligand molecule used for particle stabilization in solution. Dodecanethiol-stabilized gold nanoparticle films achieved varying surface coverages on surfaces which exhibited varying degrees of oleophobicity based on hexadecane contact angle measurements. Very little is actually known about how nanoparticle films will deposit on various surfaces. Therefore, the work presented in Chapter 6 is introductory research which has opened the door for a very thorough and fundamental study on the effect of surface properties on nanoparticle film morphology.

Future work is proposed which investigates the deposition of nanoparticle films systematically changing the substrate surface modifications, the stabilizing ligands, and nanoparticle concentrations and sizes. The use of additional surface modification molecules, such as SAMs functionalized with various groups, will provide additional data points by creating surfaces with varying surface energies (i.e., oleophobicity or hydrophobicity). The choice of stabilizing ligand can also play a huge role in how nanoparticle films deposit on particular surfaces. For example, the ligand used in Chapter 6 was dodecanethiol, which consists of a long

hydrocarbon chain of sixteen carbon atoms. However, gold nanoparticles can also be stabilized with alkanethiols consisting of much shorter hydrocarbon chains such as pentanethiol and hexanethiol. The oleophobic effect of the SAM-coated surfaces is expected to be much less for particles capped with shorter alkanethiol molecules. Hydrophobic ligand tails can also be examined.

The surface coverage of nanoparticle films is also dependent on the initial concentration of the nanoparticle dispersion used for GXL particle deposition. The nanoparticle films investigated in Chapter 6 were produced using equal dispersions of nanoparticles. However, utilizing dispersions of lesser or greater nanoparticle concentrations should provide different surface coverages and morphologies. For instance, if a more concentrated dispersion was deposited onto an FDTS-coated substrate, the surface coverage may be greater than 0.59 as achieved in Chapter 6. A dispersion containing fewer nanoparticles should result in decreased surface coverage compared to the 0.59 value.

By systematically investigating the variables discussed above, a significant amount of data can be collected. The ultimate goal of this work would be to develop a model or correlation which would assist in predicting the surface coverage or morphology of a nanoparticle film by inputting particle size, concentration, and information about both the stabilizing ligand and the surface. This information can then in turn be used to engineer nanoparticle-coated surfaces for a variety of applications ranging from superhydrophobic surfaces, photovoltaic nanoparticle films, coatings for MEMS, microreactor catalysis, and coatings for biomedical applications.

10.2 Nanoparticle-based coatings for MEMS

The ultimate goal of this dissertation was to develop a process that could be integrated within current MEMS fabrication methods in order to provide nanoparticle films to increase surface roughness and reduce adhesion. The preliminary results discussed in Chapter 5 illustrated that the GXL particle deposition process can easily be integrated between MEMS device fabrication and critical point drying by making only minor modifications to CPD equipment. The GXL process allowed for the deposition of uniform and conformal AuNP films which effectively increased surface roughness and reduced the real contact area between silicon cantilever beams and the underlying substrate, which significantly reduced the apparent work of adhesion by several orders of magnitude. However, the early AuNP coatings were not durable towards the mechanical contact made between the two surfaces.

Before investigating methods to create more durable AuNP coatings for MEMS, the effect of adding surface roughness and reducing real contact area using GXL-deposited AuNPs was examined. The results were very intuitive in that they fit the expected trends. Introducing surface roughness significantly decreased the apparent work of adhesion of cantilever beams to a particular point, after which the adhesion began to increase due to the formation of large – but inherently flat – AuNP islands. These islands may have increased the surface roughness, but had significant real contact areas. By further adding particles to increase the surface roughness, the apparent work of adhesion began to decrease once again due to a reduction in real contact area. As expected, a reduction in the work of adhesion correlates with a reduction in real contact area between two surfaces.

Chapter 7 investigated how surface roughness and surface coverage (i.e., projected area and real contact area) affect the adhesion and friction between microstructures. Varying

concentrations of gold nanoparticles were deposited onto SOI tribology chips in order to achieve varying degrees of RMS roughness and surface coverage. These studies illustrated that surface roughness does play a significant role in the reduction of adhesion. However, the most dramatic effect was exhibited when the real contact surface area between coated surfaces was estimated. A clear trend exists between adhesion energy and the estimated real contact area. Providing surface roughness as to reduce the real area of contact between two surfaces to a minimum appears to reduce the adhesion energy between the surfaces to a minimum. Interestingly, a similar trend exists between real contact area and the coefficient of static friction. This suggests, very intuitively, that adhesion dominates at the microscale.

Chapters 8 and 9 investigated methods to immobilize rough AuNP films on silicon surfaces to create more durable and robust coatings for MEMS. Thiol- (MPTS) and amine-functionalized (APhTS) monolayers were first used to immobilize AuNPs on the surface of silicon cantilever beams. The functionalized monolayers, deposited in liquid phase prior to GXL particle deposition, effectively tethered and immobilized AuNPs to the surface and prevented the removal of particles by ultrasonication. The monolayer-immobilized AuNPs were also shown to be more robust to mechanical contact between a cantilever beam and substrate while reducing the adhesion by two orders of magnitude.

In Chapter 9, chemical vapor deposition (CVD) techniques were used to link and encase AuNP films in a thin film of solid SiO_2. The CVD SiO_2 layers were shown to be virtually smooth, allowing the underlying AuNP films to increase surface roughness. Although the CVD SiO_2 were still hydrophilic and high in surface energy, the real contact area provided by the rough AuNP/CVD SiO_2 surface coating allowed for adhesion to be reduced by at least one order of magnitude. These films were further investigated by the addition of a third component – a top

self-assembled monolayer of FOTS also deposited via CVD – which had no significant effect on adhesion. In terms of durability, the AuNP/CVD SiO$_2$/FOTS composite thin films have proven to be the most durable and robust anti-stiction coating investigated in this study. The water erosion time of AuNP/CVD SiO$_2$/FOTS thin films was more than 40 times greater than that of MPTS/AuNP films.

10.3 Nanoparticle-based coatings for superhydrophobicity

The work presented in this dissertation on vapor phase deposited superhydrophobic thin films was performed in collaboration with Integrated Surface Technologies (IST). Thin films were deposited at IST in Menlo Park, California and sent to Auburn University for characterization and analysis. The superhydrophobic films couple the low surface energy of fluorinated monolayer films with moderate surface roughness (> 100 nm RMS). Durability analysis of superhydrophobic films using novel water erosion techniques illustrates that ALD and CVD techniques of depositing pyridine-catalyzed silicon oxide films over rough alumina particle coatings provides very durable superhydrophobic thin films. FTIR analysis suggests that while surface pyridine molecules can be removed from the coatings by heating, interior pyridine molecules can be trapped within the film so that they do not become a health hazard.

A unique algorithm has also been utilized to estimate the coverage density of superhydrophobic thin films – a quantitative measure similar to real contact surface area. Characterization of large numbers of superhydrophobic samples suggests that an optimal coverage density exists between 30 and 50%. In addition, analysis shows that RMS roughness of greater than 200 nm will produce superhydrophobic nature. The work described in this

dissertation on superhydrophobic thin films is very introductory and the project will become the focus of succeeding graduate student research projects.

10.4 Ideas for future work

In addition to the additional research projects described in Section 10.1 regarding the engineering of thin film morphology and topography, a number of avenues for future work exist in the realms of nanoparticle-based thin films for MEMS and superhydrophobic surfaces.

One of the original plans in my preliminary defense was to incorporate the use of various nanoparticle shapes into thin films for tribology control. Collaborative efforts were attempted with Dr. Brian Korgel's research group at the University of Texas at Austin. These efforts attempted to use gas-expanded liquids to deposit pyramidal-shaped copper indium selenide (CuInSe) photovoltaic nanoparticles onto MEMS devices and tribology chips. Fig. 10.1 presents an SEM image of the pyramid particles deposited onto a silicon substrate. Unfortunately, the CuInSe nanoparticles were unstable in organic solvents and were basically unusable two weeks after synthesis. Therefore, these efforts were ceased. In the future, opportunities may arise to once again revisit the use of different nanoparticle shapes to achieve anti-stiction coatings as the field of nanoparticle synthesis progresses.

Another early idea which was not successfully investigated was the effect of various nanoparticle sizes on microstructure adhesion. Various attempts were made to transfer aqueous-dispersed gold nanoparticles of 10, 20 and 30 nm in diameter into organic solvents which could be used for the GXL precipitation process. However, none of the attempts to phase transfer the nanoparticles were successful. Indeed, it is widely accepted that larger nanoparticles (> 10 nm)
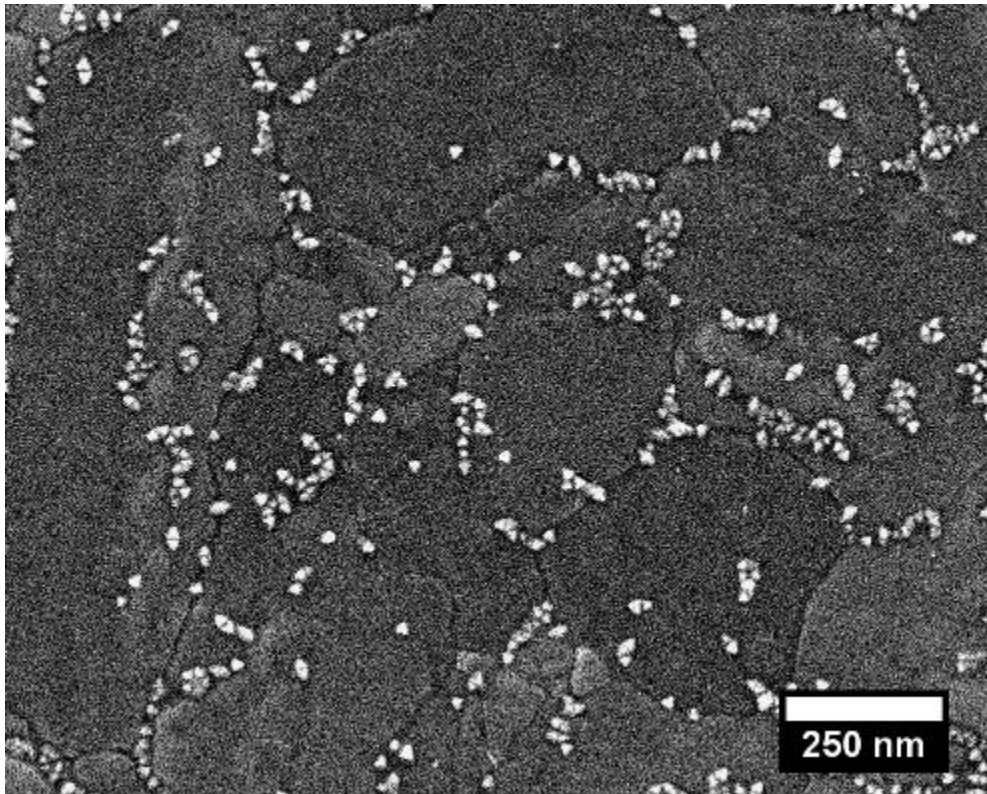
Figure 10.1. SEM micrograph of CuInSe nanopyramids on silicon.

synthesized in aqueous solutions are much more difficult than smaller nanoparticles to extract into an organic phase (Yao et al. 2001). Someday, it may yet be possible to extract larger nanoparticles into an organic solvent for GXL nanoparticle precipitation. It is suggested that future studies focus more on the extraction process so that the effect of nanoparticle size on real contact area and adhesion energy can be investigated.

Bibliography

Abe, T., Messner, W. C., and Reed, M. L. (1995). "Effects of elevated temperature treatments in microstructure release procedures." Journal of Microelectromechanical Systems **4**: 66-75.

Adamson, A. W. and Gast, A. P. (1990). "Capillarity." In: Physical Chemistry of Surfaces, 6th ed, New York: John Wiley & Sons, Inc., pp. 4-47.

Ali, M. B., Bessueille, F., Chovelon, J. M., Abdelghani, A., Jaffrezic-Renault, N., Maaref, M. A., and Martelet, C. (2008). "Use of ultra-thin organic silane films for the improvement of gold adhesion to the silicon dioxide wafers for (bio)sensor applications." Materials Science and Engineering C **28**: 628-632.

Alley, R. L., Cuan, G. J., Howe, R. T., and Komvopoulos, K. (1992). "The effect of release-etch processing on surface microstructure stiction." Proceedings of the 1992 Solid-State Sensor and Actuator Workshop, Hilton Head, SC: 202-207.

Alley, R. L., Mai, P., Komvopoulos, K., and Howe, R. T. (1993). "Surface roughness modification of interfacial contacts in polysilicon microstructures." Transducers '93: 288-291.

Anand, M., McLeod, M. C., Bell, P. W., and Roberts, C. B. (2005). "Tunable solvation effects on the size-selective fractionation of metal nanoparticles in CO_2 gas-expanded liquids." Journal of Physical Chemistry B **109**: 22852-22859.

Anand, M., You, S.-S., Hurst, K. M., Saunders, S. R., Kitchens, C. L., Ashurst, W. R., and Roberts, C. B. (2008). "Thermodynamic analysis of nanoparticle size selective fractionation using gas-expanded liquids." Industrial & Engineering Chemistry Research **47**: 553-559.

Anderson, A. and Ashurst, W. R. (2008a). "Investigation of the ability of a silica seed layer to imporive the thermal and aqueous immersion stability of alkylsilane monolayers on silicon oxide surfaces," Thin Solid Films **516**: 7538-7546.

Anderson, A. and Ashurst, W. R. (2008b). "Investigation of a vapor-deposited thin silica film: morphological and spectral characterization." Langmuir **24**: 7947-7954.

Anderson, A. and Ashurst, W. R. (2008c). "Investigation of a vapor deposited thin silica film as a novel substrate for *in situ* Fourier transform infrared spectroscopy." Journal of Vacuum Science and Technology A **26**: 1357-1361.

Anderson, A. and Ashurst, W. R. (2009). "Enabling organosilicon chemistries on inert polymer surfaces with a vapor-deposited silica layer," Langmuir **25**: 11541-11548.

Anderson, A. (2009). "Designer silica layers for advanced applications: processing and properties." Ph.D. Thesis, Auburn University (Auburn, AL).

Anguita, J. and Briones, F. (1998). "HF/H_2O vapor etching of SiO_2 sacrificial layer for large-area surface-micromachined membranes." Sensors and Actuators A **64**: 247-251.

Aresta, M., Quaranta, E., Dibenedetto, A., Tommasi, I., and Marciniec, B. (2000). "CO_2-catalysed carbamation of aminofunctional silanes," Applied Organometallic Chemistry **14**: 871-873.

Ashurst, W. R., Yau, C., Carraro, C., Howe, R. T., and Maboudian, R. (2000). "Alkene based monolayer films as anti-stiction coatings for polysilicon MEMS." Proceedings of the 2000 Solid-State Sensor and Actuator Workshop, Hilton Head, SC: 42-47.

Ashurst, W. R., Yau, C, Carraro, C., Maboudian, R., and Dugger, M. T. (2001a). "Dichlorodimethylsilane self-assembled monolayer for MEMS: a comparison to the octadecyltrichlorosilane self-assembled monolayer." Journal of Microelectro-mechanical Systems **10**: 41-49.

Ashurst, W. R., Yau, C., Carraro, C., Lee, C., Kluth, G. J., Howe, R. T., and Maboudian, R. (2001b). "Alkene based monolayer films as anti-stiction coatings for polysilicon MEMS." Sensors and Actuators A **91**: 239-248.

Ashurst, W. R. (2003). "Surface engineering for MEMS reliability," Ph.D. Thesis, University of California (Berkeley, CA).

Ashurst, W. R., Carraro, C., and Maboudian, R. (2006). "Thin film processes in MEMS and NEMS technologies." In: Encyclopedia of Chemical Processing, Lee, S. (ed.), Taylor & Francis.

Aswal, D. K., Lenfant, S., Guerin, D., Yakhmi, J. V., and Vuillaume, D. (2005). "Fowler-Nordheim tunneling and electrically stressed breakdown of 3-mercaptopropyltrimethoxysilane self-assembled monolayers," Nanotechnology **16**: 3064-3068.

Bachmann, D., Kuhne, S., and Hierold, C. (2006). "Determination of the adhesion energy of MEMS structures by applying Weibull-type distribution function." Sensors and Actuators A **132**: 407-414.

Bai, T. and Cheng, X. (2006). "Investigation of the tribological behavior of 3-mercaptopropyl trimethoxysilane deposited on silicon." Wear **261**: 730-737.

Bai, T. and Cheng, X. (2008a). "Nano-tribological characteristics of lanthanum-based thin films sulfonated self-assembled monolayer of 3-mercaptopropyl trimethoxysilane." Journal of Rare Earths **26**: 93-98.

Bai, T. and Cheng, X. (2008b). "Preparation and characterization of 3-mercaptopropyl trimethoxysilane self-assembled monolayers." Journal of University of Science and Technology Beijing **15**: 192-196.

Bain, C. D. and Whitesides, G. M. (1989). "Formation of monolayers by the coadsorption of thiols on gold: variation in the length of the alkyl chain." Journal of the American Chemical Society **111**: 7164-7175.

Banga, R., Yarwood, J., Morgan, A. M., Evans, B., and Kells, J. (1995). "FTIR and AFM studies of the kinetics and self-assembly of alkyltrichlorosilanes and (perfluoroalkyl)trichlorosilanes onto glass and silicon." Langmuir **11**: 4393-4399.

Bannikova, A., Podvigalkina, G. and Khalezova, G. (1969). "Deposition of silicon oxide films by hydrolysis of tetrachlorosilicon vapors." Instruments and Experimental Techniques: 492-493.

Bao, M. and Wang, W. (1996). "Future of microelectromechanical systems (MEMS)." Sensors and Actuators A **56**: 135-141.

Barbier, V., Tatoulian, M., Li, H., Arefi-Khonsar, F., Ajdari, A., and Tabeling, P. (2006). "Stable modification of PDMS surface properties by plasma polymerization: application to the formation of double emulsions in microfluidic systems," Langmuir **22**: 5230-5232.

Bargeman, D. and Vader, F. V. (1972). "Van der Waals forces between immersed particles." Journal of Electroanalytical Chemistry **37**: 45-52.

Barzetti, T., Selli, E., Moscotti, D., and Forni, L. (1996). "Pyridine and ammonia as probes for FTIR analysis of solid acid catalysts." Journal of the Chemical Society, Faraday Transactions **92**: 1401-1407.

Battjes, K. P., Barolo, A. M., and Dreyfuss, P. (1991). "New evidence related to reactions of aminated silane coupling agents with carbon dioxide." Journal of Adhesion Science and Technology **5**: 785-799.

Bellatreccia, F., Della Ventura, G., Piccinini, M., Cavallo, A., and Brilli, M. (2009). "H_2O and CO_2 in minerals of the hauyne-sodalite group: an FTIR spectroscopy study," Mineralogical Magazine **73**: 399-413.

Bhat, R. R., Genzer, J., Chaney, B. N., Sugg, H. W., and Liebmann-Vinson, A. (2003). "Controlling the assembly of nanoparticles using surface grafted molecular and macromolecular gradients." Nanotechnology **14**: 1145-1152.

Bhushan, B. (1990a). "Magnetic media tribology: state of the art and failure challenges." Wear **136**: 169-197.

Bhushan, B. (1990b). Tribology and Mechanics of Magnetic Storage Devices. Springer, New York.

Bhushan, B. (1998). "Micro/nanotribology: State of the Art and its Applications." Tribology Issues and Opportunities in MEMS. Klower Academic Publishers, Dordrecht, Netherlands.

Bhushan, B. (1999). "Introduction – Measurement Techniques and Applications." Handbook of Micro/Nano Tribology. CRC Press, Boca Raton, FL.

Bhushan, B. (2003). "Adhesion and stiction: mechanisms, measurement techniques, and methods for reduction." Journal of Vacuum Science and Technology B **21**: 2262-2296.

Bourlinos, A. B., Herrera, R., Chalkias, N., Jiang, D. D., Zhang, Q., Archer, L. A., and Giannelis, E. P. (2005). "Surface-functionalized nanoparticles with liquid-like behavior." Advanced Materials **17**: 234-237.

Brenner, D. W. (2001). "Mysteries of friction and wear unfolding: CMS advances the field of tribology." Advanced Materials and Processes Technology **5**: 3-6.

Brzezinski, B., Labowski, M. and Zundel, G. (1995). "Disulphide bond formation by glutathione via the glutathione-trimethylamine-*N*-oxide complex," Journal of Molecular Structure **354**: 127-130.

Brzoska, J. B., Shahidzadeh, N. and Rondelez, F. (1992). "Evidence of a transition temperature for the optimum deposition of grated monolayer coatings." Nature **360**: 719-721.

Brzoska, J. B., Benazouz, I., and Rondelez, F. (1994). "Silanation of solid substrates − a step toward reproducibility." Langmuir **10**: 4367-4373.

Bunker, B. C., Carpick, R. W., Assink, R. A., Thomas, M. L., Hankins, M. G., Viogt, J. A., Sipola, D., de Boer, M. P., and Gulley, G. L. (2000). "The impact of solution agglomeration on the deposition of self-assembled monolayers." Langmuir **16**: 7742-7751.

Burnham, N. A. and Kulik, A. J. (1999). "Surface Forces and Adhesion." Handbook of Micro/Nano Tribology. CRC Press, Boca Raton, FL.

Cabuz, C., Cabuz, E. I., Ohnstein, T. R., Neus, J., and Maboudian, R. (2000). "Factors enhancing the reliability of touch-mode electrostatic actuators." Sensors and Actuators A **79**: 245-250.

Carraro, C., Yauw, O. W., Sung, M. M., and Maboudian R. (1998). "Observation of three growth mechanisms in self-assembled monolayers." Journal of Physical Chemistry B **102**: 4441-4445.

Cassie, A. B. D. and Baxter, S. (1944). "Wettability of porous surfaces." Transactions of the Faraday Society **40**: 546-551.

Cha, K. H. and Kim, D. E. (2001). "Investigation of the tribological behavior of octadecyltrichlorosiane deposited on silicon." Wear **251**: 1169-1176.

Chang, F. Y., Chao, K. J., Cheng, H. H., and Tan, C. S. (2009). "Adsorption of CO_2 onto amine-grafted mesoporous silicas," Separation and Purification Technology **70**: 87-95.

Cléchet, P., Martelet, C., Belin, M., and Zarrad, H. (1994). "Lubrication of silicon micromechanisms by chemical grafting of long-chain molecules." Sensors and Actuators A **44**: 77-81.

Collier, C. P., Vossmeyer, T., and Heath, J. R. (1998). "Nanocrystal Superlattices." Annual Review of Physical Chemistry **49**: 371-404.

Culler, S. R., Naviroj, S., Ishida, H., and Koenig, J. L. (1983). "Analytical and spectroscopic investigation of the interaction of CO_2 with amine functional silane coupling agents on glass fibers." Journal of Colloid and Interface Science **96**: 69-79.

De Boer, M. P., Clews, P. J., Smith, B. K., and Michalske, T. A. (1998). "Adhesion of polysilicon microbeams in controlled humidity ambient." Microelectro-mechanical structures for Materials Research Symposium: 131-136.

De Boer, M. P., and Michalske, T. A. (1999). "Accurate method for determining adhesion of cantilever beams." Journal of Applied Physics **86**: 817-827.

DelRio, F. W., de Boer, M. P., Knapp, J. A., Reedy, E. D., Clews, P. J., and Dunn, M. L. (2005). "The role of van der Waals forces in adhesion of micromachined surfaces." Nature Materials **4**: 629-634.

DelRio, F. W., Dunn, M. L., Boyce, B. L., Corwin, A. D., and de Boer, M. P. (2006). "The effect of nanoparticles on rough surface adhesion." Journal of Applied Physics **99**: 104304.

Deng, K., Collins, R. J., Mehregany, M., and Sukenik, C. N. (1995a). "Performance impact of monolayer coating of polysilicon micromotors." Proceedings of the IEEE Micro Electro Mechanical Systems Workshop: 368-373.

Deng, K., Collins, R. J., Mehregany, M., and Sukenik, C. N. (1995b). "Performance impact of monolayer coatings on polysilicon micromotors." Journal of the Electrochemical Society **142**: 1278-1285.

Doms, M., Feindt, H., Kuipers, W. J., Shewtanasoontorn, D., Matar, A. S., Brinkhues, S., Welton, R. H., and Mueller, J. (2008). "Hydrophobic coatings for MEMS applications." Journal of Micromechanics and Microengineering **18**: 055030.

Dowson, D. (1998). History of Tribology. Professional Engineering Publishing, London.

Du, Y., Du. X. and George, S. M. (2005). "SiO$_2$ film growth at low temperatures by catalyzed atomic layer deposition in a viscous flow reactor." Thin Solid Films **491**: 43-54.

Du, Y., Du. X. and George, S. M. (2007). "Mechanism of pyridine-catalyzed SiO$_2$ atomic layer deposition studied by Fourier transform infrared spectroscopy." Journal of Physical Chemistry C **111**: 219-226.

Extrand, C. W. (2002). "Model for contact angles and hysteresis on rough and ultraphobic surfaces." Langmuir **18**: 7991-7999.

Fan, L. S., Tai, Y. C., and Muller, R. S. (1988). "Integrated movable electrostatic micromechanical structure for sensors and actuators." IEEE Transactions on Electron Devices **35**: 666-669.

Fan, L. S., Tai, Y. C., and Muller, R. S. (1989). "IC-processed electrostatic micromotors." Sensors and Actuators A **20**: 41-47.

Feynman, R. (1992). "There is plenty of room at the bottom." Journal of Microelectromechanical Systems **1**: 60-66.

Frantz, P. and Salmeron, M. (1998). "Preparation of mica surfaces for enchanced resolution and cleanliness in the surface forces apparatus." Tribology Letters **5**: 151-153.

Gere, J. M. and Timoshenko, S. P. (1997). Mechanics of Materials, PWS Publishing, Boston.

Giersig, M. and Mulvaney, P. (1993). "Preparation of ordered colloid monolayers by electrophoretic deposition." Langmuir **9**: 3408-3413.

Goodenough, F. (1991). "Airbags boom when IC accelerometer sees 50g." Electronic Design **8**: 45.

Goss, C. A., Charych, D. H., and Majda, M. (1991). "Application of (3-mercaptopropyl)trimethyoxysilane as a molecular adhesive in the fabrication of vapor-deposited gold electrodes on glass substrates." Analytical Chemistry **63**: 85-88.

Gosset, L. G., Damlencourt, J.-F., Renault, O., Rouchon, D., Hollinger, Ph., Ermolieff, A., Trimaille, I., Ganem, J.-J., Martin, F., and Semeria, M.-N. (2002). "Interface and material characterization of thin Al_2O_3 layers deposited by ALD using TMA/H_2O." Journal of Non-Crystalline Solids **303**: 17-23.

Guckel, H., Sniegowski, J. J., Christenson, T. R., Mohney, S., and Kelly, T. F. (1989). "Fabrication of micromechanical devices from polysilicon films with smooth surfaces." Sensors and Actuators **20**: 117-122.

Guckel, H., Sniegowski, J. J., Christenson, T. R., and Raissi, F. (1990). "The application of fine-grained polysilicon to mechanically resonant transducers." Sensors and Actuators A **21-23**: 346-351.

Hampe, E. M. and Rudkevich, D. M. (2003). "Exploring reversible reactions between CO_2 and amines," Tetrahedron **59**: 9619-9625.

Hariharan, P., Oreb, B. F., and Eiju, T. (1987). "Digital phase-shifting interferometry: a simple error-compensating phase calculation algorithm." Applied Optics **26**: 2504-2506.

Hata, K., Futaba, D. N., Mizuno, K., Namai, T., Yumura, M., and Iijima, S. (2004). "Water-assisted highly efficient synthesis of impurity-free single-walled carbon nanotubes." Science **19**: 1362-1364.

Henck, S. A. (1997). "Lubrication of Digital Micromirror Devices[TM]." Tribology Letters **3**: 239-247.

Houston, M. R., Maboudian, R., and Howe, R. T. (1995). "Ammonium fluoride anti-stiction treatments for polysilicon microstructures." Transducers '95: 210-213.

Houston, M. R., Maboudian, R., and Howe, R. T. (1996). "Self-assembled monolayer films as durable anti-stiction coatings for polysilicon microstructures." Proceedings of the 1996 Solid-State Sensors and Actuator Workshop, Hilton Head, SC: 42-47.

Howe, R. T. (1988). "Surface micromachining for microsensors and actuators." Journal of Vacuum Science and Technology B **6**: 1809-1813.

Hsu, T.-R. (2002). <u>MEMS & Microsystems: Design and Manufacture</u>. McGraw-Hill Companies, Inc., New York.

Hu, M., Noda, S., Okubo, T., Yamaguchi, Y., and Komiyama, H. (2001). "Structure and morphology of self-assembled 3-mercaptopropyltrimethoxysilane layers on silicon oxide." <u>Applied Surface Science</u> **181**: 307-316.

Hurst, K. M., Saunders, S. R., Liu, J., Anand, M., You, S.-S., and Roberts, C. B. (2007). "Metal and semiconductor deposition and size fractionation using CO_2-expanded liquids and supercritical CO_2 processing." <u>Proceedings of Super Green 2007: The 5th International Symposium on Supercritical Fluids, Seoul, South Korea</u>: KL-12, pp. 1-8.

Hurst, K. M., Roberts, C. B., and Ashurst, W. R. (2009a). "A new method to determine adhesion of cantilever beams using beam height experimental data." <u>Tribology Letters</u> **35**: 9-15.

Hurst, K. M., Roberts, C. B., and Ashurst, W. R. (2009b). "A gas-expanded liquid nanoparticle deposition technique for reducing the adhesion of silicon microstructures." <u>Nanotechnology</u> **20**: 185303.

Ishizaki, T., Saito, N., Sato, Y., and Takai, O. (2007). "Probing into adsorption behavior of human plasma fibrinogen on self-assembled monolayers with different chemical properties by scanning probe microscopy," <u>Surface Science</u> **601**: 3861-3865.

Israelachvili, J. N. (1992). "Van der Waals forces between surfaces." In: <u>Intermolecular and Surface Forces</u>, 2nd ed., London: Academic Press, pp. 176-209.

Itoh, H., Naka, K., and Chujo, Y. (2004). "Synthesis of gold nanoparticles modified with ionic liquid based on the imidazolium cation." <u>Journal of the American Chemical Society</u> **126**: 3026-3027.

Janssen, D., de Palma, R., Verlaak, S., Heremans, P., and Dehaen, W. (2006). "Static solvent contact angle measurements, surface free energy and wettability determination of various self-assembled monolayers on silicon dioxide." Thin Solid Films **515**: 1433-1438.

Jensen, B. D., de Boer, M. P., Masters, N. D., Bitsie, F., and LaVan, D. A. (2001). "Interferometry of actuated microcantilevers to determine material properties and test structure nonidealities in MEMS." Journal of Microelectromechanical Systems **10**: 336-346.

Jessop, P. G. and Subramaniam, B. (2007). "Gas-expanded liquids." Chemical Reviews **107**: 2666-2694.

Jia, X. and McCarthy, T. J. (2003). "Controlled growth of silicon dioxide from "nanoholes" in silicon-supported tris(trimethylsiloxy)silyl monolayers: rational control of surface roughness at the nanometer length scale." Langmuir **19**: 2449-2457.

Kang, C.-K. (2007). "Preliminary study of tribology: uniform control of the density control of the functionalized gold nanoparticles on a modified silicon surface." M.S. Thesis, Auburn University (Auburn, AL).

Khatri, O. P., Adachi, K., Murase, K., Okazaki, K., Torimoto, T., Tanaka, N., Kuwabata, S., and Sugimura, H. (2008). "Self-assembly of ionic liquid (BMI-PF$_6$)-stabilized gold nanoparticles on a silicon surface: chemical and structural aspects. Langmuir **24**: 7785-7792.

Khuri, A. I. (2003). Advanced Calculus with Applications in Statistics, 2nd ed., Hoboken, New Jersey: Wiley-Interscience.

Kim, B. H., Chung, T. D., Oh, C. H., and Chun, K. (2001). "A new organic modifier for anti-stiction." Journal of Microelectromechanical Systems **10**: 33-40.

Kim, J., Novick, B. J., DeSimone, J. M., and Carbonell, R. G. (2006). "Ultrathin film deposition by liquid CO_2 free meniscus coating – uniformity and morphology." Langmuir **22**: 642-657.

Kitchens, C. L. (2004). "Metallic nanoparticle synthesis within reverse micellar microemulsion systems." Ph.D. Thesis, Auburn University (Auburn, AL).

Kitchens, C. L., Roberts, C. B., Liu, J., Ashurst, W. R., Anand, M., White II, G. V., Hurst, K. M., and Saunders, S. R. (2009). "Application of gas-expanded liquids for nanoparticle processing: experiment and theory." In: Gas-Expanded Liquids and Near-Critical Media: Green Chemistry and Engineering, Hutchenson, K. W., Scurto, A. M. and Subramaniam, B. (eds.), American Chemical Society: Washington, DC, pp. 290-308.

Klaus, J. W. and George, S. M. (2000). "Atomic layer deposition of SiO_2 at room temperature using NH_3-catalyzed sequential surface reactions." Surface Science **447**: 81-90.

Knapp, J. A. and de Boer, M. P. (2002). "Mechanics of microcantilever beams subject to combined electrostatic and adhesive forces." Journal of Microelectromechanical Systems **11**: 754-764.

Knieling, T., Lang, W., and Benecke, W. (2007). "Gas phase hydrophobisation of MEMS silicon structures with self-assembled monolayers for avoiding in-use sticking." Sensors and Actuators B **126**: 13-17.

Komvopoulos, K. (1996). "Surface engineering and microtribology for microelectro-mechanical systems." Wear **200**: 305-327.

Komvopoulos, K. (2003). "Adhesion and friction forces in microelectromechanical systems: mechanisms, measurement, surface modification techniques, and adhesion theory." Journal of Adhesion Science and Technology **17**: 477-517.

Korgel, B. A. and Fitzmaurice, D. (1998). "Condensation of ordered nanocrystal thin films." Physical Review Letters **80**: 3531-3534.

Kozlowski, F., Lindmair, N., Scheiter, T. H., Hierold, C., and Lang, W. (1995). "A novel method to avoid sticking of surface micromachined structures." Transducers '95: 220-223.

Kulkarni, S. A., Mirji, S. A., Mandale, A. B., Gupta, R. P., and Vijayamohanan, K. P. (2005). "Growth kinetics and thermodynamic stability of octadecyltrichlorosilane self-assembled monolayer on Si (100) substrate." Materials Letters **59**: 3890-3895.

Kushmerick, J. G., Hankins, M. G., de Boer, M. P., Clews, P. J., Carpick, R. W., and Bunker, B. C. (2001). "The influence of coating structure on micromachine stiction." Tribology Letters **10**: 103-108.

Kwok, D. Y., Gietzelt, T., Grundke, K., Jacobasch, H.-J., and Neumann, A. W. (1997). "Contact angle measurements and contact angle interpretation. 1. Contact angle measurements by axisymmetric drop shape analysis and a goniometer sessile drop technique." Langmuir **13**: 2880-2894.

Lacroix, L. M., Lejeune, M., Ceriotti, L., Kormunda, M., Meziani, T., Colpo, P., and Rossi, F. (2005). "Tuneable rough surfaces: a new approach for elaboration of superhydrophobic films." Surface Science **592**: 182-188.

Lakomaa, E.-L., Root, A. and Suntola, T. (1996). "Surface reactions in Al_2O_3 growth from trimethylaluminium and water by atomic layer epitaxy." Applied Surface Science **107**: 107-115.

Laoharojanaphand, P., Lin, T. J. and Stoffer, J. O. (1990). "Glow discharge polymerization of reactive functional silanes on poly(methyl methacrylate)," Journal of Applied Polymer Science 40: 369-384.

Leal, O., Bolivar, C., Ovalles, C., Garcia, J. J., and Espidel, Y. (1995). "Reversible adsorption of carbon dioxide on amine surface-bonded silica gel," Inorganica Chimica Acta 240: 183-189.

Lee, E. P. and Xia, Y. (2008). "Growth and patterning of Pt nanowires on silicon substrates." Nano Research 1: 129-137.

Lee, J. H., Chung, H. H., Kang, S. Y., Baek, J. T., and Yoo, H. J. (1996). "Fabrication of surface micromachined polysilicon actuators using dry release process of HF gas-phase etching." Proceedings of IEEE Electron Devices: 761-764.

Legtenberg, R., Tilmans, H. A. C., Elders, J., and Elwenspoek, M. (1994). "Stiction of surface micromachined structures after rinsing and drying: model and investigation of adhesion mechanisms." Sensors and Actuators A 43: 230-238.

Legtenberg, R. (1996). "Electrostatic actuators fabricated by surface micromachining techniques." Ph.D. Thesis, University of Twente (Enschede, Netherlands).

Li, Q.-G., Zheng, J.-W., and Liu, Z.-F. (2001). "Site-selective assembly of gold nanoparticles on silicon using AFM nano-oxidation technique." Chemical Journal of Chinese Universities 22: 1218-1220.

Li, Z., Liu, Z., Zhang, J., Han, B., Du, J., Gao, Y., and Jiang, T. (2005). "Synthesis of single-crystal gold nanosheets of large size in ionic liquids." Journal of Physical Chemistry B 109: 14445-14448.

Lin, X. M., Jaeger, H. M., Sorensen, C. M., and Klabunde, K. J. (2001). "Formation of long-range-ordered nanocrystal superlattices on silicon nitride substrates." Journal of Physical Chemistry B **105**: 3353-3357.

Liu, J., Qin, Z., Wang, G., Hou, X., and Wang, J. (2003). "Critical properties of binary and ternary mixtures of hexane + methanol, hexane + carbon dioxide, methanol + carbon dioxide, and hexane + carbon dioxide + methanol." Journal of Chemical and Engineering Data **48**: 1610-1613.

Liu, J., Anand, M., and Roberts, C. B. (2006). "Synthesis and extraction of β-$_D$-glucose-stabilized Au nanoparticles processed into low-defect, wide-area thin films and ordered arrays using CO_2-expanded liquids." Langmuir **22**: 3964-3971.

Liu, J., Zhong, L., Wickramasuriya, J., and Vasudevan V. (2009). "µWave: Accelerometer-based personalized gesture recognition and its applications." Pervasive and Mobile Computing **5**: 657-675.

Maboudian, R. (1998). "Surface processes in MEMS technology." Surface Science Reports **30**: 207-269.

Maboudian, R., Ashurst, W. R., and Carraro, C. (2002). "Tribological challenges in micromechanical systems." Tribology Letters **12**: 95-100.

Maboudian, R. and Carraro, C. (2004). "Surface chemistry and tribology of MEMS." Annual Review of Physical Chemistry **55**: 35-54.

Maboudian, R. and Howe, R. T. (1997). "Critical review: Adhesion in surface micromechanical structures." Journal of Vacuum Science and Technology B **15**: 1-20.

Maboudian, R., Ashurst, W. R., and Carraro, C. (2000). "Self-assembled monolayers as anti-stiction coating for MEMS: characteristics and recent progress." Sensors and Actuators A **82**: 219-223.

Madou, M. J. (1997). Fundamentals of Microfabrication. CRC Press, Boca Raton, FL.

Majewski, P. J. and Fuchs, T. M. (2007). "Variation of the surface charge of silica particles by functionlised self-assembled monolayers." Advanced Powder Technology **18**: 303-310.

Mastrangelo, C. H. and Hsu, C. H. (1992). "A simple experimental technique for the measurement of the work of adhesion of microstructures." Proceedings of the 1992 Solid-State Sensor and Actuator Workshop, Hilton Head, SC: 208-212.

Mastrangelo, C. H. and Hsu, C. H. (1993). "Mechanical stability and adhesion of microstructures under capillary forces. I. Basic theory." Journal of Microelectro-mechanical systems **2**: 33-43.

Mastrangelo, C. H. and Saloka, G. S. (1993). "A dry-release method based on polymer columns for microstructure fabrication." Proceedings of the IEEE Micro Electro Mechanical Systems Workshop, Fort Lauderdale, FL: 77-81.

Mastrangelo, C. H. (1997). "Adhesion-related failure mechanisms in micromechanical devices." Tribology Letters **3**: 223-238.

Mayer, T. M., de Boer, M. P., Shinn, N. D., Clews, P. J., and Michalske, T. A. (2000). "Chemical vapor deposition of fluoroalkylsilane monolayer films for adhesion control in microelectromechanical systems." Journal of Vacuum Science and Technology B **18**: 2433-2440.

McLeod, M. C., Anand, M., Kitchens, C. L., and Roberts, C. B. (2005a). "Precise and rapid size selection and targeted deposition of nanoparticle populations using CO_2 gas expanded liquids." Nano Letters **5**: 461-465.

McLeod, M. C., Kitchens, C. L., and Roberts, C. B. (2005b). "CO_2-expanded liquid deposition of ligand-stabilized nanoparticles as uniform, wide-area nanoparticle films." Langmuir **21**: 2414-2418.

Meng, Q., Mehregany, M., and Mullen, R. L. (1993). "Theoretical modeling of microfabricated beams with elastically restrained supports." Journal of Micro-electromechanical Systems **2**: 128-137.

Miller, S., Sniegowski, J. J., LaVigne, G., and McWorther, P. J. (1996). "Friction in surface micromachined microengines." Proceedings of SPIE Smart Electronics and MEMS, San Diego, CA **2722**: 197-204.

Motte, L., Billoudet, F., Lacaze, E., Douin, J., and Pileni, M. P. (1997). "Self-organization into 2D and 3D superlattices of nanosized particles differing by their size." Journal of Physical Chemistry B **101**: 138-144.

Mulhern, G. T., Soane, D. S., and Howe, R. T. (1993). "Super-critical carbon dioxide drying of microstructures." Transducers '93: 296-299.

Mullen, R. L., Mehrengany, N., Omar, M. P., and Ko, W. H. (1991). "Theoretical modeling of boundary conditions in microfabricated beams." Proceedings of Investigation of Micro Structures, Sensors, Actuators, Machines and Robots (MEMS '91), Nara, Japan: 154-159.

Muller, R. S. (1990). "Microdynamics." Sensors and Actuators A **21**: 1-8.

Offenberg, M., Elsner, B., and Laermer, F. (1994). "Vapor HF etching for sacrificial oxide removal in surface micromachining." Technical Digest of the Electro-chemical Society Fall Meeting: 1056.

Ohara, P. C. and Gelbart, W. M. (1998). "Interplay between hole instability and nanoparticle array formation in ultrathin liquid films." Langmuir **14**: 3418-3424.

Ohlidal, I. and Franta, D. (2000). "Ellipsometry of thin film systems." Progress in Optics **41**: 181-282.

Ohnishi, S., Hato, M., Tamada, K., and Christenson, H. K. (1999). "Presence of particles on melt-cut mica sheets." Langmuir **15**: 3312-3316.

Ohring, M. (2002). "Substrate surfaces and thin-film nucleation." In: Materials Science of Thin Films: Deposition & Structure, 2nd ed., San Diego: Academic Press, pp. 357-415.

Orpana, M. and Korhonen, A. O. (1991). "Control of residual stress of polysilicon thin films by heavy doping in surface micromachining." Transducers '91: 957-960.

Patton, S. T., Cowan, W. D., Eapen, K. C., and Zabinski, J. S. (2000). "Effect of surface chemistry on the tribological performance of a MEMS electrostatic lateral output motor." Tribology Letters **9**: 199-209.

Patton, S. T. and Zabinski, J. S. (2002). "Failure mechanisms of a MEMS actuator and other small scale devices." Tribology International **35**: 373-379.

Patton, S. T., Voevodin, A. A., Vaia, R. A., Pender, M., Diamanti, S. J., and Phillips, B. (2008). "Nanoparticle liquids for surface modification and lubrication of MEMS switch contacts." Journal of Microelectromechanical Systems **17**: 741-746.

Petersen, K. (1982). "Silicon as a mechanical material." Proceedings of IEEE Electron Devices **70**: 420-457.

Petersen, K. (1995). "MEMS: what lies ahead." Proceedings of 8th International Conference on Solid-State Sensors and Actuators, Stockholm, Sweden 1: 894-897.

Resnick, P. J. and Clews, P. J. (2001). "Whole wafer critical point drying of MEMS devices." Proceedings of the SPIE International Society of Optical Engineering 4558: 189-196.

Roach, P., Shirtcliffe, N. J., and Newton, M. I. (2007). "Progress in superhydrophobic surface development." Soft Matter 4: 224-240.

Rozlosnik, N., Gerstenberg, M. C. and Larsen, N. B. (2003). "Effect of solvents and concentration on the formation of a self-assembled monolayer of octadecylsiloxane on silicon (001)." Langmuir 19: 1182-1188.

Rymuza, Z. (1999). "Control tribological and mechanical properties of MEMS surfaces. Part I: critical review." Microsystem Technologies 5: 173-180.

Schwartz, D. K. (2001). "Mechanisms and kinetics of self-assembled monolayer formation." Annual Review of Physical Chemistry 52: 107-137.

Sieval, A. B., Linke, R., Heij, G., Meijer, G., Zuilhof, H., and Sudholter, E. J. R. (2001). "Amino-terminated organic monolayers on hydrogen-terminated silicon surfaces," Langmuir 17: 7554-7559.

Sigman, M. B., Saunders, A. E., and Korgel, B. A. (2004). "Metal nanocrystal superlattice nucleation and growth." Langmuir 20: 978-983.

Smith, B. C. (1996). Fundamentals of Fourier Transform Infrared Spectroscopy, CRC Press: New York.

Sniegowski, J. J. and de Boer, M. P. (2000). "IC-compatible polysilicon surface micromachining." Annual Review of Materials Science 30: 299-333.

Srinivasan, U., Houston, M. R., Howe, R. T. and Maboudian, R. (1997). "Self-assembled fluorocarbon films for enhanced stiction reduction." <u>Transducers '97</u>: 210-213.

Srinivasan, U., Houston, M. R., Howe, R. T., and Maboudian, R. (1998a). "Alkyltrichlorosilane-based self-assembled monolayer films for stiction reduction in silicon micromachines." <u>Journal of Microelectromechanical Systems</u> **7**: 252-260.

Srinivasan, U., Foster, J. D., Habib, U., Howe, R. T., Maboudian, R., Senft, D. C., and Dugger, M. T. (1998b). "Lubrication of polysilicon micromechanisms with self-assembled monolayers." <u>Proceedings of the 1998 Solid-State Sensor and Actuator Workshop, Hilton Head, SC</u>: 156-161.

Sugimura, H. and Nakagiri, N. (1997). "Nanoscopic surface architecture based on scanning probe electrochemistry and molecular self-assembly." <u>Journal of the American Chemical Society</u> **119**: 9226-9229.

Sun, T. L., Feng, L., Gao, X. F., and Jiang, L. (2005a). "Bioinspired surfaces with special wettability." <u>Accounts of Chemical Research</u> **38**: 644-652.

Sun, M. H., Luo, C. X., Xu, L. P., Ji, H., Qi, O. Y., Yu, D. P., and Chen, Y. (2005b). "Artificial lotus leaf by nanocasting." <u>Langmuir</u> **21**: 8978-8981.

Sung, M. M., Carraro, C., Yauw, O. W., Kim, Y., and Maboudian, R. (2000). "Reversible liquid-liquid transitions in the early stages of monolayer self-assembly." <u>Journal of Physical Chemistry B</u> **104**: 1556-1559.

Tanner, D. M., Miller, W. M., Peterson, K. A., Dugger, M. T., Eaton, W. P., Irwin, L. W., Senft, D. C., Smith, N. F., Tangyunyong, P., and Miller, S. L. (1999). "Frequency dependence of the lifetime of surface micromachined microengine driving a load." <u>Microelectronics Reliability</u> **39**: 401-414.

Tanner, D. M. (2000). "Reliability of surface micromachined microelectromechanical actuators." Proceedings of the 22nd International Conference in Microelectronics, Nis, Yugoslavia, 97-104.

Tas, N., Sonnenberg, T., Jansen, H., Legtenberg, R., and Elwenspoek, M. (1996). "Stiction in surface micromachining." Journal of Micromechanics and Microengineering **6**: 385-397.

Tillman, N., Ulman, A., Schildkraut, J. S., and Penner, T. L. (1988). "Incorporation of phenoxy groups in self-assembled monolayers of trichlorosilane derivatives. Effects on film thickness, wettability, and molecular orientation." Journal of the American Chemical Society **111**: 6136-6144.

Tourillon, G., Dreesen, L., Volcke, C., Sartenaer, Y., Thiry, P. A., and Peremans, A. (2007). "Total internal reflection sum-frequency generation spectroscopy and dense gold nanoparticle monolayer: a route for probing adsorbed molecules." Nanotechnology **18**: 415301 (7pp).

Vakarelski, I. U., McNamee, C. E., and Higashitani, K. (2007). "Deposition of silica nanoparticles on a gold surface via a self-assembled monolayer of (3-mercaptopropyl)trimethoxysilane." Colloids and Surfaces A **295**: 16-20.

Van Kessel, P., Hornbeck, L. J., Meier, R. E., and Douglass, M. R. (1998). "A MEMS-based projection display." Proceedings of IEEE Meeting **86**: 1687-1704.

Venables, J. (2000). Introduction to Surface and Thin Film Processes, Cambridge: Cambridge University Press.

Wang, J., Yang, S., Liu, X., Ren, S., Guan, F., and Chen, M. (2004). "Preparation and characterization of ZrO_2 thin film on sulfonated self-assembled monolayer of 3-mercaptopropyl trimethoxysilane." Applied Surface Science **221**: 272-280.

Wang, W. Y., Wang, Y. L., Bao, H. F., Xiong, B., and Bao, M. H. (2002). "Friction and wear properties in MEMS." Sensors and Actuators A **97-98**: 486-491.

Wang, Y. and Lieberman, M. (2003). "Growth of ultrasmooth octadecyltrichlorosilane self-assembled monolayers on SiO_2." Langmuir **19**: 1159-1167.

Watt, I. M. (1997). The principles and practice of electron microscopy, 2nd ed., Cambridge University Press: New York.

Wenzel, R. N. (1936). "Resistance of solid surfaces to wetting by water." Industrial & Engineering Chemistry **28**: 988-994.

Williams, J. A. (2001). "Friction and wear of rotating pivots in MEMS and other small scale devices." Wear **250**: 965-972.

Wu, K., Bailey, T. C., Willson, C. G., and Ekerdt, J. G. (2005). "Surface hydration and its effect on fluorinated SAM formation on SiO_2 surfaces." Langmuir **21**: 11795-11801.

Wuister, S. F. and Meijerink, A. (2003). "Synthesis and luminescence of (3-mercaptopropyl)-trimethoxysilane capped CdS quantum dots." Journal of Luminescence **102-103**: 338-343.

Xu, L., Liao, J., Huang, L., Ou, D., Guo, Z., Zhang, H., Cunwang, G., Gu, N., and Liu, J. (2003). "Surface-bound nanoparticles for initiating metal deposition." Thin Solid Films **434**: 121-125.

Yakimova, R., Petoral Jr., R. M., Yazdi, G. R., Vahlberg, C., Spetz, A. L., and Uvdal, K. (2007). "Surface functionalization and biomedical applications based on SiC," Journal of Physics D: Applied Physics **40**: 6435-6442.

Yamanoi, Y., Yonezawa, T., Shirahata, N., and Nishihara, H. (2004). "Immobilization of gold nanoparticles onto silicon surfaces by Si-C covalent bonds." Langmuir **20**: 1054-1056.

Yao, H., Momozawa, O., Hamatani, T., and Kimura, K. (2001). "Stepwise size-selective extraction of caroxylate-modified gold nanoparticles from an aqueous suspension into toluene with tetraoctylammonium cations." Chemistry Materials **13**: 4692-4697.

Yee, Y., Chun, K., Lee, J. D., and Kim, C. J. (1996). "Polysilicon surface-modification technique to reduce sticking of microstructures." Sensors and Actuators A **52**: 145-150.

Yonezawa, T. and Toshima, N. (2001). "Polymer-stabilized metal nanoparticles." In: Advanced Functional Molecules and Polymers, Nalwa, H. S. (ed.). Gordon and Breach: London, pp. 65-86.

Yu, S. H., Colfen, H., and Mastai, Y. (2004). "Formation and optical properties of gold nanoparticles synthesized in the presence of double-hydrophilic block copolymers." Journal of Nanoscience and Nanotechnology **4**: 291-298.

Zhang, F. and Srinivasan, M. P. (2004). "Self-assembled molecular films of aminosilanes and their immobilization capacities." Langmuir **20**: 2309-2314.

Zhang, F. and Srinivasan, M. P. (2005). "Ultra thin films of oligoimide through molecular assembly." Colloids and Surfaces A **257-258**: 295-299.

Zhang, F. and Srinivasan, M. P. (2008). "Layer-by-layer assembled gold nanoparticle films on amine-terminated substrates." Journal of Colloid and Interface Science **319**: 450-456.

Zhou, Y., Wang, C. Y., Zhu, Y. R., and Chen, Z. Y. (1999). "A novel ultraviolet irradiation technique for shape-controlled synthesis of gold nanoparticles at room temperature." Chemistry Materials **11**: 2310-2312.

Zhuang, Y. X., Hansen, O., Knieling, T., Wang, C., Rombach, P., Lang, W., Benecke, W., Kehlenbeck, M., and Koblitz, J. (2007). "Vapor-phase self-assembled monolayers for

anti-stiction applications in MEMS." <u>Journal of Microelectro-mechanical Systems</u> **16**: 1451-1460.

Zhuravlev, L. T. (1987). "Concentration of hydroxyl groups on the surface of amorphous silicas," <u>Langmuir</u> **3**: 316-318.

Zisman, W. A. (1964). "Contact angle, wettability and adhesion." In: <u>Advances in Chemistry Series 43</u>. American Chemical Society: Washington.

SCRIPT FOR AUTOMATED WORK OF ADHESION CALCULATION

The following script was written to automate the determination of the crack length of a cantilever beam directly from interferometry data. The script also automatically performs the work of adhesion calculation method described in Chapter 4. The first portion of the script allows for the user input of data such as the Young's modulus of the beam material, cantilever beam thickness, and the lower bound value for the crack length which shortens the time required for the script to run. Please note that this script will only work for adhered cantilever beams that are not experiencing an external load such as an electrostatic force. In the script, apostrophes (') indicate comments that are not utilized by the scripting environment program, MEMScript.

Fig. A.1 presents a screen shot of the MEMScript environment performing the crack length determination step. The screen shot displays the cantilever beam being analyzed, with the user inputs such as Young's modulus and first crack length iteration (300 μm). The "Script Output" portions on the left hand side of the image present the experimentally determined beam profile data collected interferometrically and the iterations on the crack length including the error values for the particular crack length values. The error values are indicating that as the iterated crack length is approaching the actual value (near 350 μm as indicated by the beam profile), the error is decreasing. Fig. A.2 presents another screen shot once the script is complete. The "Script Output" section presents the determined crack length and apparent work of adhesion of

the beam following the calculation method presented in Chapter 4. The determined crack length for the particular beam was about 360.4 µm and the calculated work of adhesion was 0.635 mJ/m^2. The output also presents the determined coefficients for the non-dimensionalized 3rd order polynomial which are used to determine the work of adhesion: a_1 = 5.227 and a_2 = -8.155, respectively, for the particular example beam.

Crack length and work of adhesion calculation script

'List of user inputs
ustring fname_base, "sample_name", "Base name of files to be used"
ustring beam, "1", "Beam number"
uglobal crack_min, 100, "Lower bound crack length (microns) – increment of 20"
uglobal crack_max, 2000, "Maximum bound crack length (microns)"
uglobal E, 160000000000, "Young's modulus of material (Pa)"
uglobal t, 2.5, "Beam thickness (microns)"
uglobal mag, 10, "Magnification used"

```
include init.mac
begin
setdir "C:\memscript\data"
global lambda 532
global 2v2pi 0.029544
global gain 1
call init

array out
array out2
array position
array zfinal
alloc scale2
let scale2 = 0.465*10/mag
```

'The following section of the script allows for the selection of a beam and grabs five Hariharan
'images which are then used to determine the profile of the beam and create the data set used for
'analysis.

```
string fname

for i=4 to 0 i-1
{
        let fname = fname_base,"_",@d i+0,".tif"
        rdimg fname
        sgrab images[i]
        if (i==4)
        {
                sdisp sequence[i]
                moire_select test
        }
        linescanx test, out
}
psi out, out2, lambda/1000/4/3.1415
for j=0 to assize[out2]-1 j+1
```

```
{
        let position[j] = scale2*j
        let zfinal[j] = out2[j] + abs[out2[asize[out2]-1]]
        chart position[j], zfinal[j], 1
}
wait
```

'The following section of the script iteratively determines the crack length of the beam,
'regardless of arc or s-shape.

```
alloc s
array coefs
array x_fit
array y_fit
array h_error
alloc sum_error
array avg_error
let crack_min = crack_min*mag/5

if (crack_min==2000)
{
        let crack_max = asize[position]-1
}
else
{
        let crack_max = crack_max*mag/5
}
for i=0 to crack_min i+1
{
        let avg_error[i] = 10
}
for i=crack_min to crack_max i+1
{
        clr_array x_fit
        clr_array y_fit
        let s = position[i]
        for j=0 to asize[position]-1 j+1
        {
                let x_fit[j] = position[j]
                if (x_fit[j]<s)
                {
                let y_fit[j] = zfinal[0]*(2*position[j]^3/s^3 − 3*position[j]^2/s^2 + 1)
                }
                else
                {
                let y_fit[j] = 0
```

```
        }
                let h_error[j] = (zfinal[j] - y_fit[j])^2
        }
        let sum_error = 0
        for ii=0 to asize[h_error]-1 ii+1
        {
                let sum_error = sum_error + h_error[ii]
        }
        let avg_error[i] = sum_error/asize[y_fit]
        refresh
}
alloc tempmin 10
alloc s_found
for k=crack_min to crack_max k+1
{
        if (avg_error[k]<tempmin)
        {
                let tempmin = avg_error[k]
                let s_found = position[k]
        }
}
print "Crack length = ",s_found," microns"
wait
refresh
chrtclr
```

'The following section of the script non-dimensionalizes the lateral beam position data and
'performs the 3rd order polynomial fit as discussed in Chapter 3. It uses the coefficients of the
'polynomial fit to calculate the apparent work of adhesion.

```
array eta
array deflection

for i=0 to s_found*mag/5 i+1
{
        let eta[i] = position[i]/s_found
        let deflection[i] = zfinal[i]
        chart eta[i], deflection[i], 1
}
alloc errv
poly_fit eta, deflection, coefs, errv, 3
for i=0 to asize[eta]-1 i+1
{
        let x_fit =  eta[i]
        let y_fit = coefs[3]*eta[i]^3 + coefs[2]*eta[i]^2 + coefs[1]*eta[i] + coefs[0]
        chart x_fit[i], y_fit[i], 2
```

```
}
alloc term1
alloc term2
alloc work
alloc m

let term1 = (E)*3*(t^3)/2/(s_found^4)
let term2 = (coefs[3]^2) + (coefs[3]*coefs[2]) + (1/3)*(coefs[2]^2)
let work = term1*term2/1000
let m = zfinal[0] – coefs[3]/coefs[0]

if (s_found==position[asize[position]-1])
{
        print "The beam is arc-shaped with m = ",m
}
else
{
        print "The beam is S-shaped"
}
print "The work of adhesion is: ",work," mJ/m^2"
```
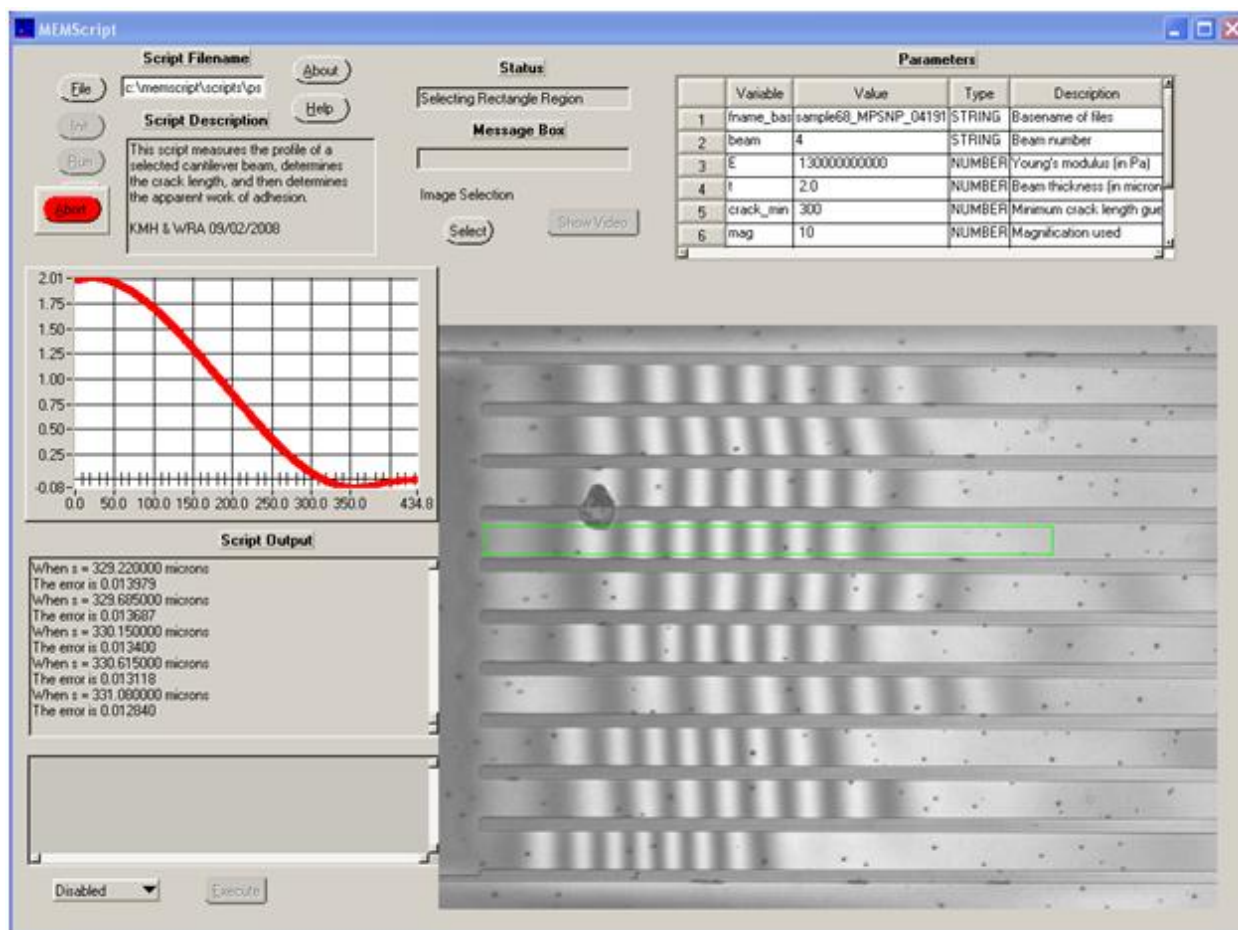
Figure A.1. Screen shot of MEMScript environment running the crack length and work of
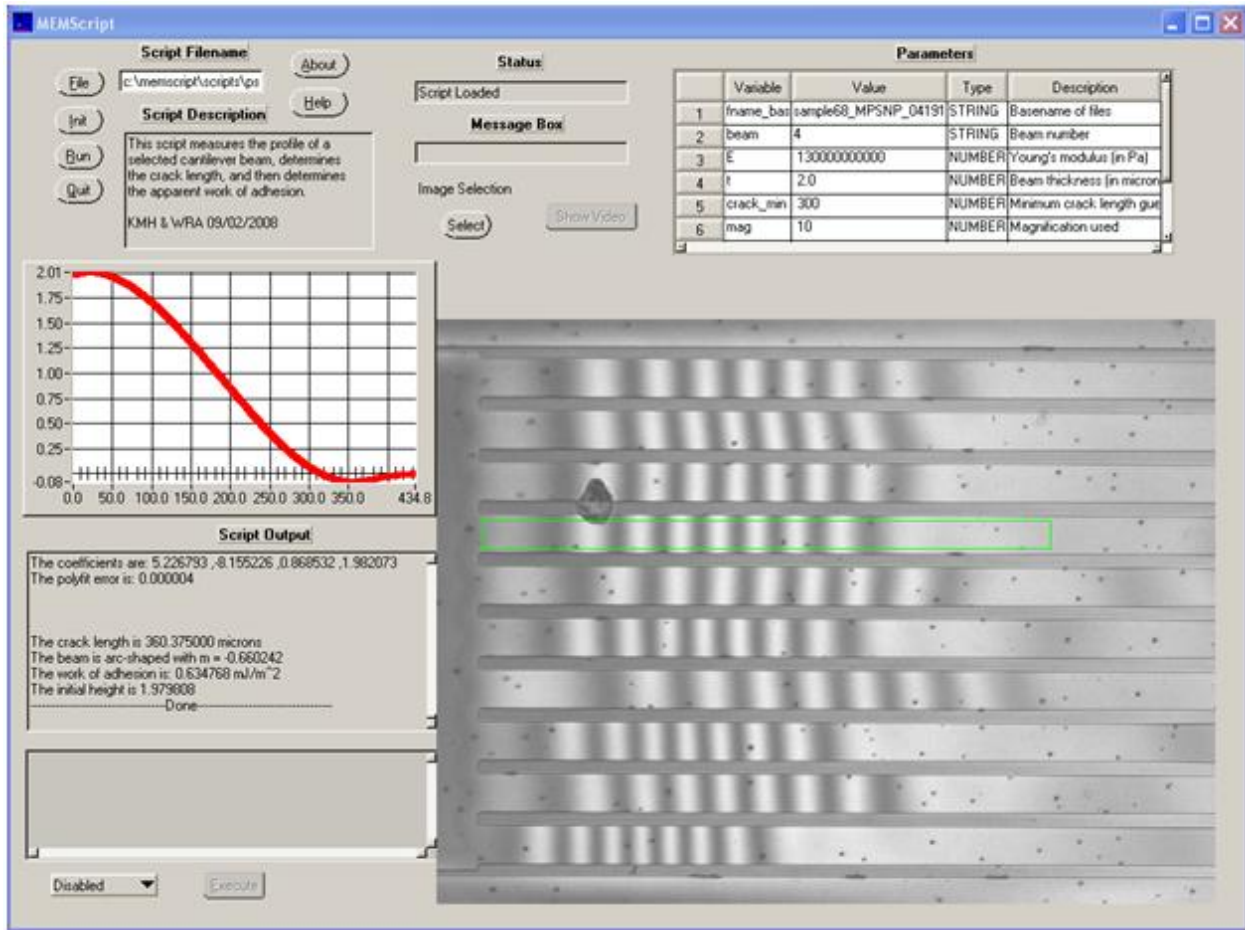
adhesion determination script.

Figure A.2. Screen shot of MEMScript environment at completion of work of adhesion script.

APPENDIX B

OPERATION OF ROGER-1 VPD APPARATUS

This section discusses the operation of ROGER-1, the VPD apparatus used to coat silicon surfaces with rough SiO_2 films and hydrophobic monolayers in the vapor phase. The operation of the VPD unit utilizes LABVIEW software in order open/close pneumatic valves for precursor injection into the coating chamber. Fig. B.1 presents a screen shot of LABVIEW illustrating the four precursor bottles, lines and lines for nitrogen carrier gas and venting. The red circles in Fig. B.1 indicate pneumatic valves which can be manually opened/closed by clicking on the circles. When a pneumatic valve is open, the circle changes from red to green. The software also provides the coating chamber pressure to a resolution of 0.01 Torr. The minimum base pressure achievable under ultra high vacuum is 50 mTorr.

In addition to the ability to manually operate the valves, automated operation of the unit can also be performed using "recipes" developed in Microsoft Excel. The recipes utilize a "0 or 1" off/on method to operate the pneumatic valves for specified amounts of time. Fig. B.2 presents an example recipe file for an automated purging cycle of the coating chamber and gas carrier lines. The first three columns in the recipe give the step description, step number, and the number of seconds the operation in each row is performed. The remainder of the columns indicates which pneumatic valves are opened during each step, as labeled in LABVIEW. For instance, the second row labeled "Back Fill Purge 1 of 5" opens valve N2-5 to allow nitrogen
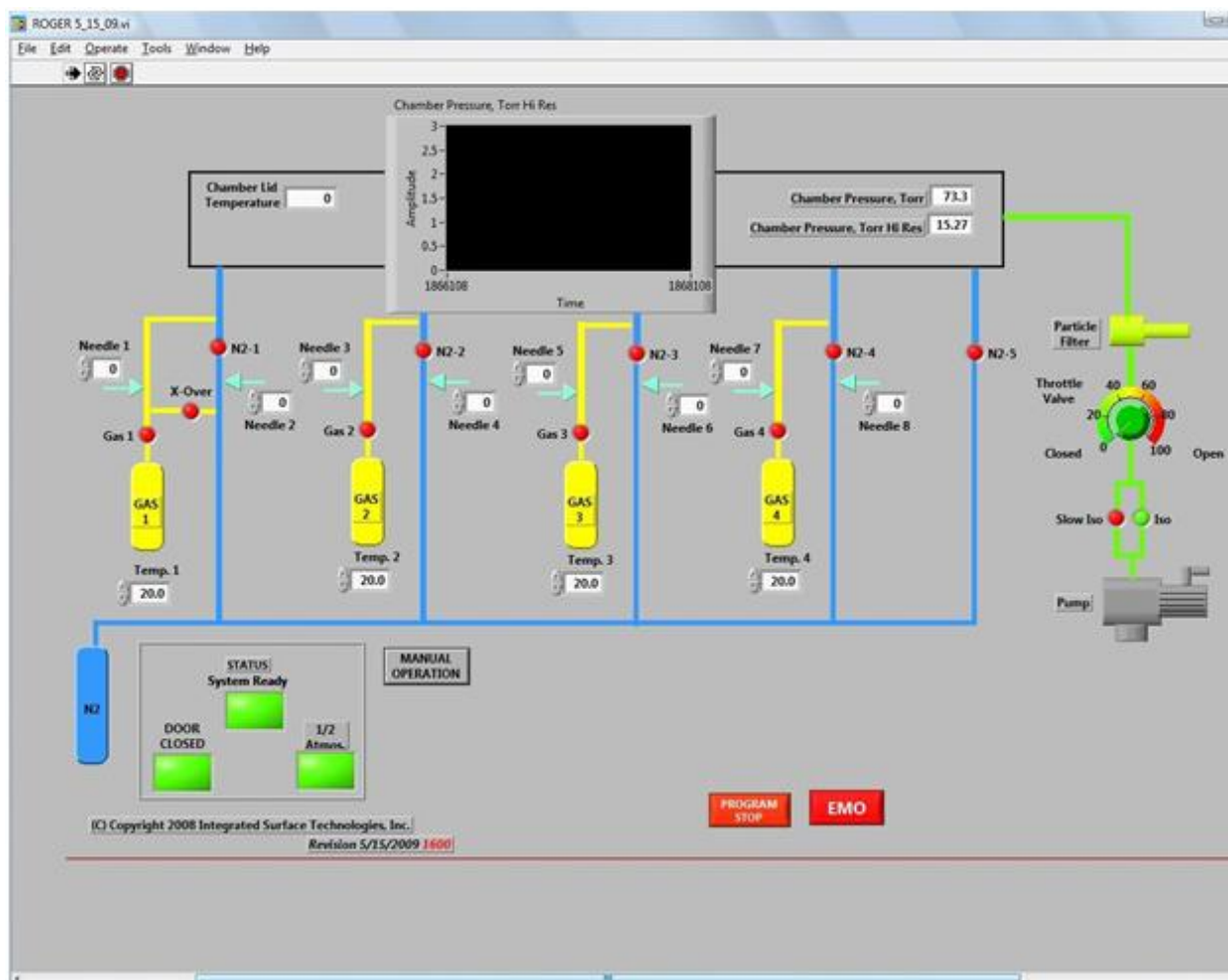
Figure B.1. Screen shot of LABVIEW software for control of ROGER-1.

Note	Step	Time	Gas 1	N2 1	Xover 1	Gas 2	N2 2	Gas 3	N2 3	Gas 4	N2 4	Slow ISO	ISO	N2 5
Start in Safe State	1	0.25												
Back Fill Purge 1 of 5	2	7												1
Pump Down 1 of 5	3	20											1	
Back Fill Purge 2 of 5	4	7												1
Pump Down 2 of 5	5	20											1	
Back Fill Purge 3 of 5	6	7	1			1		1		1				1
Pump Down 3 of 5	7	20											1	
Purge Lines #1	8	10	1			1		1		1				1
Pump Line Purge	9	20											1	
Purge Lines #2	10	10	1			1		1		1				1
Pump Line Purge	11	20											1	
Purge Lines #1	12	10	1			1		1		1				1
Pump Line Purge	13	20											1	
Purge Lines #2	14	10	1			1		1		1				1
Pump Line Purge	15	20											1	
Purge Lines #1	16	10	1			1		1		1				1
Pump Line Purge	17	20											1	
Purge Lines #2	18	10	1			1		1		1				1
Pump Line Purge	19	20											1	
Purge Lines #1	20	10	1			1		1		1				1
Pump Line Purge	21	20											1	
Purge Lines #1	22	10	1			1		1		1				1
Pump Line Purge	23	20											1	
Purge Lines #2	24	10	1			1		1		1				1
Pump Line Purge	25	20											1	
Purge Lines #1	26	10	1			1		1		1				1
Pump Line Purge	27	20											1	
Purge Lines #1	28	10	1			1		1		1				1
Pump Line Purge	29	20											1	
Purge Lines #2	30	10	1			1		1		1				1
Pump Line Purge	31	20											1	
Purge Lines #1	32	10	1			1		1		1				1
Pump Line Purge	33	20											1	
Purge Lines #1	34	10	1			1		1		1				1
Pump Line Purge	35	20											1	
Purge Lines #2	36	10	1			1		1		1				1
Pump Line Purge	37	20											1	
Purge Lines #1	38	10	1			1		1		1				1
Pump Line Purge	39	20											1	
Purge Lines #2	40	10	1			1		1		1				1
Pump Line Purge	41	20											1	
Start in Safe State	42	0.25												

Figure B.2. Example recipe file for automated operation of ROGER-1.

into the coating chamber for a total of 7 sec. The next step labeled "Pump Down 1 of 5" closes valve N2-5 and opens the ISO valve to the vacuum pump for 20 seconds, before closing the valve and proceeding to the next step. During vapor phase deposition reactions, the particular gas line valves may be opened by placing a "1" within that gas precursor valve's column. The valve may be opened for any given amount of time. After two reactants are injected into the chamber in this manner, reactions typically take place for a specified amount of time in which no pneumatic valves are open (entire row is blank or contains "0"). At the end of each recipe, the operation generally returns to manual mode so that the coating chamber can be vented by opening valve N2-5, and the coated sample can be removed.

The temperatures of the chamber, precursor bottles and gas lines are also controlled and maintained electronically using TrendViewer software. Fig. B.3 presents a screen shot of the TrendViewer software package. The central chart presents the color-coded temperature trends. The top right window lists the temperature presets (or setpoints) and the actual temperatures read by the thermocouples. This software is used to maintain control over the temperatures of the entire system to ensure repeatability. The typical temperatures used in this work can be found in Table 9.1.
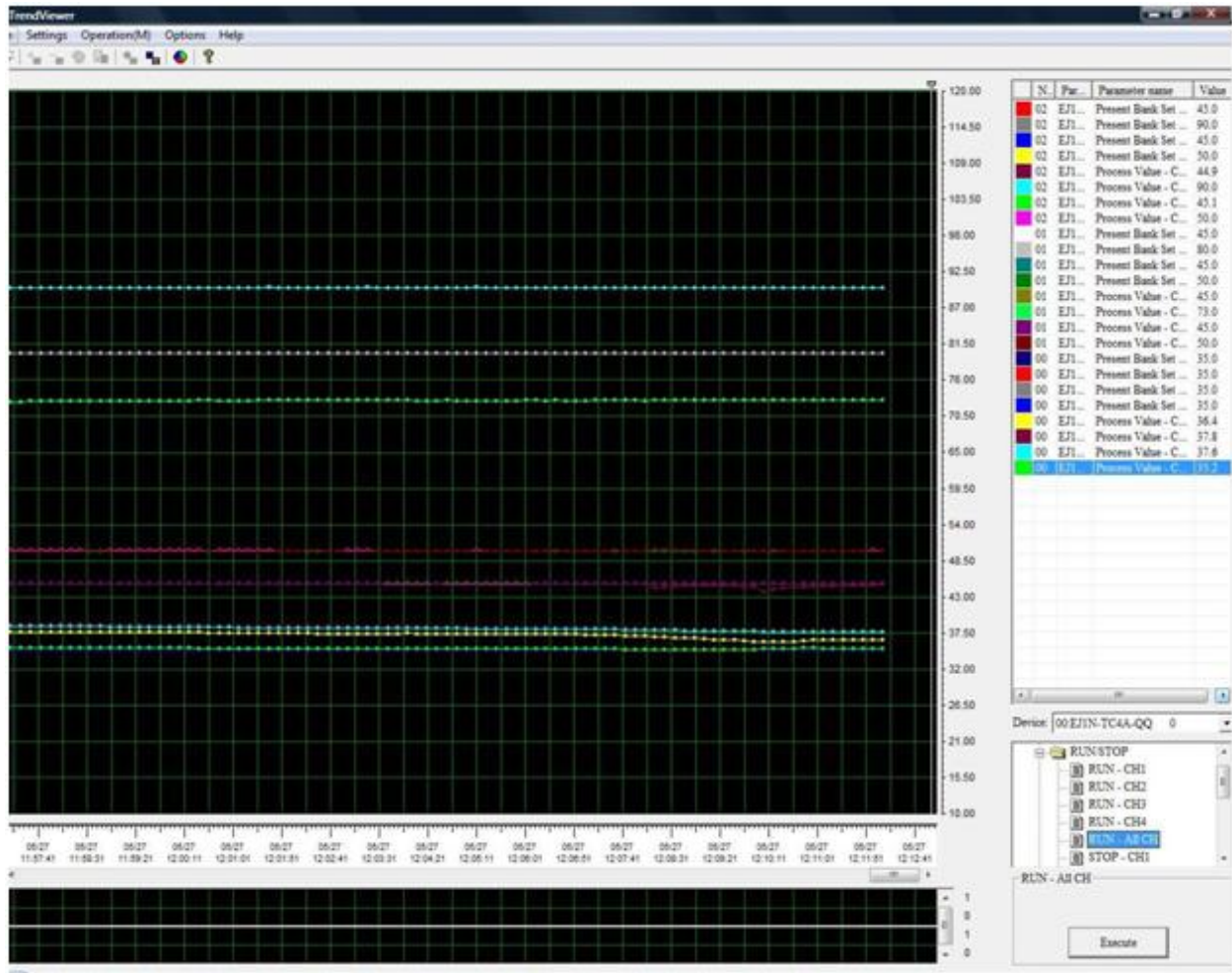
Figure B.3. Screen shot of Trend Viewer package controlling the system temperatures.